Katerina Spranger

Wadham College

Supervisor

Professor Yiannis Ventikos

COMPUTATIONAL MODELLING OF VASCULAR INTERVENTIONS: **Endovascular Device Deployment**

A thesis submitted for the degree of Doctor of Philosophy

Trinity 2014

Моей семье
(To my family)

A thesis submitted for the degree of Doctor of Philosophy.

Computational Modelling of Vascular Interventions:
Endovascular Device Deployment

By Katerina Spranger, Wadham College.

Submitted Trinity 2014.

Abstract

Minimally invasive vascular interventions with stent deployment have become a popular alternative to conventional open surgery in the treatment of many vascular disorders. However, the high initial success rates of endovascular repairs have been overshadowed by reported complications that cause re-interventions and, in the worst case, morbidity and mortality. The dangerous complications could be mitigated by better choice of device design and by the appropriate positioning of the implant inside the vessel. However, there is currently no possibility for the interventionist to predict the resulting position and the expanded shape of the device for a given patient, before the actual procedure, within the clinical setting.

Motivated by this unmet clinical need and the lack of suitable methods, this thesis develops a methodology for modelling virtual deployment of implantable devices inside patient vessels, that features fast computational execution times and can be used in clinical practice. This novel deployment method was developed based on a spring-mass model and was tested in different deployment scenarios, expanding stents inside vessels in the order of seconds. Further, the performance of the novel method was optimised by calibrating a set of parameters with the help of a genetic algorithm, which utilises the outcomes of a finite element analysis as a learning reference. After the calibration, the developed stenting method demonstrated acceptable accuracy as compared to the "gold standard" of the finite element simulation. Finally, on a real patient case, 4 alternative stenting scenarios were investigated by comparing the subsequent blood flow conditions, via computational haemodynamics. The obtained results suggested that device design, dimensions, stiffness and positioning have important implications on the post-procedural haemodynamics of the vessel. Ultimately, the presented results can play a transformative role in aiding clinical decision-making and also give rise to overall improvements in implant design and deployment procedure.

Statement of Originality

I hereby declare that this submission is my own work and to the best of my knowledge it contains no materials previously published or written by another person, or substantial proportions of material which have been accepted for the award of any other degree or diploma at the University of Oxford or any other educational institution, except where due acknowledgement is made in the thesis.

Any contribution made to the research by others, with whom I have worked at the University of Oxford or elsewhere, is explicitly acknowledged in the thesis.

I also declare that the intellectual content of this thesis is the product of my own work, except to the extent that assistance from others in the project's design and conception or in style, presentation and linguistic expression is acknowledged.

Katerina Spranger
9 October 2014

Acknowledgements

This thesis is dedicated to my family and they shall be the first ones to thank here. I am extremely grateful to my beloved parents who not only provided unconditional love and support in difficult moments of these four years, but also for raising me in awe of knowledge, determination and daring, being themselves a living example. Special thanks goes to my clever brother for being such a blessing, to my sweet grandparents for always believing in me and to my extended family for love and care.

My scientific family consisted of Professor Yiannis Ventikos to whom I am extremely grateful for supervising me during this DPhil journey. Further, a big thank you goes to all members of the Fluidics and Biocomplexity group, particularly to Alisa Selimovic, Daniel Zajarias-Fainsod, John Vardakis, Katia Mandaltsi, Malie Ngoepe, Pedro Aparicio, Paul Watton and Tom Peach. You guys made my time spent inside (and outside) the lab especially fun.

This work would not have been possible without the clinical input from Professor James Byrne (University of Oxford) and Dr. Hendrik von Tengg-Kobligk (Inselspital Bern). I would also like to especially acknowledge my collaborators and friends Claudio Capelli, Giorgia Bosi and Silvia Schievano (University College London), which provided great help with the validation of this work, as well as my German colleague Philipp Hoegen (University of Heidelberg).

Last but not least, I want to thank my dearest friends for always being there for me.

This work was supported by the Centenary Year Graduate Scholarship from the Department of Engineering Science and the Keeley Senior Scholarship from the Wadham College.

This thesis template was created by Brett Tully (2010) *'Allostasis of Cerebral Water: Modelling the Transport of Cerebrospinal Fluid'*, PhD Thesis, University of Oxford.

Dissemination

Peer-Reviewed Journal Papers

K. Spranger and Y. Ventikos. Which spring is the best? Comparison of methods for virtual stenting. *IEEE Transactions on Biomedical Engineering*, 61 (7):1998–2010, 2014.

K. Spranger, C. Capelli, G. Bosi, S. Schievano and Y. Ventikos. Comparison and calibration of a real-time virtual stenting algorithm using Finite Element Analysis and Genetic Algorithms. *Computer Methods in Applied Mechanics and Engineering*, 293: 462–480, 2015.

T. W. Peach, M. Ngoepe, K. Spranger, D. Zajarias-Fainsod and Y. Ventikos. Personalizing flow diverter intervention for cerebral aneurysms: From computational hemodynamics to biochemical modeling. *International Journal for Numerical Methods in Biomedical Engineering (IJNMBE)*, 30 (11): 1387–1407, 2014.

K. Spranger, P. Hoegen, H. von Tengg-Kobligk and Y. Ventikos. Implications of stent graft choice and placement position on the haemodynamics of the aorta: Case study with aortic dissection type B. (under review), 2014.

Conference Papers

K. Spranger, M. Reynolds, D. Chen, M. Müller-Eschner, H. von Tengg-Kobligk and Y. Ventikos. Computational modelling of vascular interventions. *Proceedings of the Biomedical Engineering '11 Conference*. September 2011.

D. Zajarias-Fainsod, K. Spranger, E. Holland, A. Selimovic, H. Chen, M. Ngoepe, T. Peach, T. Baptista, A. Chiarini, J. Penrose, J. Byrne, P. N. Watton and Y. Ventikos. Modelling intracranial aneurysms treated with flow

diverters: correlation of intra-aneurysm sac flow dynamics with thrombus evolution. *Proceedings of the 8th European Solid Mechanics Conference (ESMC) 2012*. July 2012.

K. Spranger, J. M. T. Penrose, A. Chiarini, P. N. Watton and Y. Ventikos. Comparison of computational methods for simulating stent deployment. *Proceedings of the Virtual Physiological Human Conference (VPH) 2012*. September 2012.

K. Spranger. Modelling of Vascular Interventions with Stent Deployment. *5th Summer School of Biomechanics and Modeling in Mechanobiology*. Graz, Austria, September 2012.

K. Spranger. Computational Modelling of Vascular Interventions. *Medical Engineering Centres (MEC) Annual Meeting*. Ascot, September 2013.

K. Spranger and Y. Ventikos. Methods for virtual stent deployment. *Proceedings of the 11th Interdisciplinary Cerebrovascular Symposium / Intracranial Stent Meeting (ICS) 2014*. June 2014.

K. Spranger, C. Capelli, G. Bosi, S. Schievano and Y. Ventikos. Validation and calibration of a real-time virtual stenting algorithm using Finite Element Analysis and Genetic Algorithms. *Proceedings of the 7th World Congress of Biomechanics (WCB) 2014*. July 2014.

Competitions

Finalist of *TATA Idea Idol 2013*, Saïd Business School, February 2013

Finalist of the *European Student Startups 2013* competition, London School of Economics, May 2013

Winner of the "Pitching for Success: Best Potential Investment" session at the *Venturefest 2013*, Saïd Business School, June 2013

1st Place in the *Falling Walls Lab 2013 London* – innovative ideas competition, sent as UK representative to the *Falling Walls Berlin* Final, September 2013

3rd place at the *Falling Walls Berlin* – International Conference on Future Breakthroughs in Science and Society and awarded with the title "Young Innovator of the Year 2013", November 2013

CONTENTS

List of Figures

LIST OF TABLES

ACRONYMS

CVD	Cardiovascular disease
AAA	Abdominal aortic aneurysm
TAA	Thoracic aortic aneurysm
CFD	Computational fluid dynamics
CSM	Computational Solid Mechanics
FEA	Finite Element Analysis
FM	Fast method
GA	Genetic Algorithm
SG	Stent graft
FD	Flow diverter
PED	Pipeline Embolization Device
LSA	Lineal Spring Analogy
STSA	Semi-torsional Spring Analogy
TSA	Torsional Spring Analogy
ICA	Internal carotid artery
LSA	Left subclavian artery
MRI	Magnetic Resonance Imaging
PC-MRI	Phase contrast MRI
WSS	Wall Shear Stress
BC	Boundary conditions

CHAPTER 1

INTRODUCTION

This chapter describes the motivation for the research work presented in this thesis. After briefly describing the current standard of care in minimally invasive vascular interventions and what is potentially missing, I state the aim and scope of the project and its potential for improving current clinical practice. The chapter ends with an overview of the entire thesis and a detailed description of the content and structure of the coming chapters.

1.1 MOTIVATION FOR THE RESEARCH

Minimally invasive vascular interventions have become a popular alternative to conventional open surgery for treating many vascular disorders, including aneurysms, aortic dissections and atherosclerotic stenoses. A minimally invasive endovascular repair is performed through a small incision, usually made in the femoral artery. From this incision, a prosthesis or *stent*[1] is pushed to a target location, under fluoroscopic guidance and using a catheter, where it is subsequently deployed inside the diseased vessel. Compared to open surgery, endovascular repair leads to better treatment outcomes, including fewer complications, less blood loss, shorter surgery times and shorter hospital stays, etc., mainly attributed to its minimally invasive nature (Adriaensen et al., 2002; Lylyk et al., 2009).

However, the strong rationale and initial successes of minimally invasive endovascular repairs have subsequently been shadowed by reported complications.

[1] For the sake of conciseness and brevity, the general term "stent" will be used in the sequel to denote endovascular devices such as stents, stent grafts and flow diverters.

For example, there have been cases of stroke, thromboembolism and luminal restenosis, that can cause re-interventions and, in the worst case, increased morbidity and mortality (D'Urso et al., 2011; Mas et al., 2006). In the case of intracranial aneurysms, major concerns are attributed to occasional haemorrhagic events that follow an initially successful treatment (Byrne et al., 2010). In approximately 1% of cases, there is an incidence of the subsequent rupture of the treated cerebral aneurysms occurring between a few days and 3-4 months after treatment (Kulcsar et al., 2011). With respect to post-procedural stroke, the new rate of 6% has been recently established by the "Pipeline Embolization Device in the Intracranial Treatment of Aneurysms (PITA)" trial (Fiorella et al., 2009), which is unacceptably high and could threaten the general use of flow diverters in the future.

It is known that a number of factors play an important role in the outcome of the stent deployment procedure; the key players being

- incidence of arterial injury,
- vessel geometry,
- vessel haemodynamics,
- design and placement position of the stent, etc. (Kiousis et al., 2009).

Specifically, it has been reported that neointimal hyperplasia[2] can initiate from **arterial injury** sustained during intervention and cause significant stenosis (Schwartz and Henry, 2001). Additionally, several studies have suggested that vessel injuries can also originate after the procedure due to the **non-uniform expansion** of the stent, which occurs, e.g., when the excessive axial contraction of the stent damages the thin endothelial layer of the vessel (Kiousis et al., 2009). The adverse effects can become aggravated by particularities of the **vessel geometry**. For example, in tortuous vessels, straightening of the vessel curves can occur due to the longitudinal stiffness of the stent, creating kinks (Zhu et al., 2003). At the end of these kinks, rigid stent extremes introduce a drastic increase in longitudinal stiffness compared to the soft vessel tissue and can become an origin of stenosis (Wu et al., 2007b). On the other hand, the **incomplete contact** between the stent-filaments and the

[2] "Neointimal hyperplasia is a formation of a new or thickened layer of tunica intima (the inner layer) of a blood vessel formed by migration and proliferation of cells from the media, as a vascular response to injury" (Med, 2007).

arterial wall increases the risk of neointimal hyperplasia (Jamous et al., 2004) and in-stent thrombosis (Cook et al., 2007). Moreover, it is thought that **haemodynamic** parameters, such as wall shear stress, vorticity, jetting, recirculation, fluctuations in pressure, etc., might be of even greater consequence than local mechanics of device contact. For instance, malapposition of the stent to the vessel wall could create unfavourable vorticity or even turbulence in the blood flow, fostering the initiation of thrombosis (Wu et al., 2007b).

The dangerous complications caused by the arterial injury and inadequate device apposition could be mitigated by improving the **positioning** of the implant inside the vessel (Hirabayashi et al., 2004) and by better choice of the stent **design** (Lieber et al., 2002). However, there is currently no possibility for a clinician to predict the resulting position and the expanded shape of the device for a given patient before the intervention in the clinical setting. Firstly, the unique vessel geometry of each patient makes any *ad hoc* predictions of how a particular device is going to 'sit' inside the diseased site extremely tentative. Secondly, *in vivo* assessment of stent deployment is particularly challenging since the majority of the nitinol stents currently employed are not or only poorly visible under fluoroscopic imaging (Karmonik et al., 2005). Thirdly, the precise positioning of the device is often complicated by its shortening or migration after placement, for example, due to insufficient radial stiffness (Saad et al., 2003).

Furthermore, choosing the optimal **stent design** for a particular patient is not straightforward. The devices available on the market differ substantially in their design and mechanical characteristics that affect the deployment performance. For example, there are currently six FDA-approved devices for abdominal aneurysm repair and three types of stents for thoracic aneurysm repair. These devices are very different in design (modular versus unibody), materials (nitinol versus stainless steel), deployment mechanisms (balloon-expanded versus self-expanding) and fixation mechanisms (radial force, hooks and barbs) (Prasad et al., 2013). Apart from the design, **dimensions** of the stent are important in selecting a suitable device. A stent that is too large will result in overly high radial force that can damage the vessel's endothelial layer, triggering pressure necrosis or other dangerous conditions (Kleinstreuer et al., 2008). On the other hand, the insufficient radial force of an undersized device may result in its migration, leading to serious complications (Saad et al., 2003).

Hence, the ability to predict a deployed configuration of the stent before the actual intervention would provide a clinician with crucial information that is currently unavailable, even in the state-of-the-art medical centers. A computational system that faithfully represents stent deployment in a virtual environment could therefore offer the desired predictive capability. Such a system would help in evaluating the efficacy of different devices and selecting the most appropriate treatment option for each pathological case.

Further, obtaining the released stent geometry beforehand would enable quantitative analysis of the consequences of the stent deployment procedure, such as the stresses exerted on the vessel wall, providing early indicators for possible complications. Indeed, the studies mentioned above indicated that non-physiologic stresses and strains on the vessel wall can trigger unfavorable adaptations of vessel tissue such as atherosclerosis (Moore and Berry, 2002; Wentzel et al., 2003). Moreover, predicting the deployed configuration of the device inside the vessel can constitute the base for a subsequent investigation of the haemodynamic change induced by the intervention. The post-procedural haemodynamic analysis could provide early indications of such complications as endoleakage[3] (Golzarian and Valenti, 2006), endotension[4] (Gawenda et al., 2003), thrombus formation, etc.

1.2 AIM AND SCOPE

This project aims to develop a computational framework of minimally invasive stent placement that is able to provide clinicians with information required for improved treatment of common cardiovascular diseases such as aneurysms and dissections. As stated above, the most important consequences of stent deployment are haemodynamic alteration and stress exerted on the vessel wall. The project will therefore focus on the development of a methodology predicting the position and the expanded shape of the stent when released within patient-specific vessel geometries, with a computational time in the order of minutes, as well as investigating haemodynamic implications of the stenting procedure.

Providing such a system can play a transformative role in aiding clinical decision-making on intravascular interventions on a patient-specific basis and give

[3] Endoleakage is persistent perfusion of the aneurysmal sac (Golzarian and Valenti, 2006).

[4] Endotension is the pressure transmission into the aneurysmal sac through the graft material or blood clots (Gawenda et al., 2003).

rise to overall improvements in implant design and deployment procedure.

Specific goals of the project include:

- Development of a computationally **fast** method for virtual device deployment. One of the essential requirements for a virtual stenting method to be utilised in clinical practice is its computational speed. In contrast to common finite element method studies focusing on a single aspect, the stenting algorithm would be integrated in a complex clinical workflow and thus has to provide solutions close to real-time. Fast turnover times would ensure that other components of the workflow remain executable and would give a clinician the opportunity to explore multiple deployment scenarios quickly.
- **Validation** of the developed method. To ensure trustworthiness of the virtual results, the developed method has to be validated. In particular, the results of stent deployment procedure with the developed method have to be compared with a trusted alternative in equal intervention scenarios, especially with respect to the reported configurations of deployed devices. Additionally, important numerical measurements such as reaction and contact forces have to lie in the physically adequate range.
- Incorporation of **flexible vasculature**. It is known that stent placement can result in dilation of the vessel, vessel straightening and other deformations of the vessel geometry (Huang et al., 2011). Geometric changes have enormous implications on post-procedural vessel remodelling, haemodymanic conditions and, hence, procedure outcomes. Therefore, being able to account for a possible vessel deformation is an extremely valuable and important aspect of the envisioned deployment model.
- Integration with **haemodynamics**. The ultimate consequences of a stent placement procedure become apparent by performing the haemodynamic analysis subsequent to virtual device placement. Three-dimensional computational fluid dynamics (CFD) analysis can supply useful data that is currently lacking or is too laborious to measure in clinical practice, for example, important metrics of blood flow such as velocity profiles, pressure fields, wall shear stress, etc. Hence, performing post-stenting CFD studies can predict haemodynamic changes and truly help evaluate the suitability of a particular intervention scenario for a given patient, including the choice of device.

1.3 OVERVIEW OF THE THESIS

This thesis consists of eight chapters and has the following structure:

Chapter 2 provides the necessary background knowledge. It outlines some relevant aspects of the human cardiovascular system, focusing on healthy vessels and widespread vascular diseases. Then, the minimally invasive treatment methods are introduced, in particular those involving the deployment of intravascular stents. The chapter finishes with a description of different types of stents and their mode of operation.

Chapter 3 provides a literature review of the previous work in the field. I report on two classes of existing approaches to virtual stent deployment and their limitations in the context of the goals of this project. The first class of finite element analysis (FEA) methods are overly slow to constitute a base for a clinical tool, taking from several days to several hours to run. On the other hand, the second class of rapid stenting techniques feature major simplifications in important aspects of the deployment process, especially in stent representation and vessel behaviour. At the end of the chapter, a brief review of the relevant studies investigating vessel haemodynamics is included, since it constitutes the essential next step in modelling virtual vascular interventions.

Chapter 4 presents the methods that were used to **develop the novel fast stent deployment method** in this thesis. The chapter starts by describing different stages involved in modelling virtual stent deployment and how they were addressed in the present work. The weighting of the different sections reflects the importance to the present project and the amount of contribution offered by the thesis. Hence, the core of the chapter is dedicated to methods that were developed for reconstruction of vascular devices and for modelling their expansion mechanics. In particular, the chapter focuses on the stent expansion process and develops expansion algorithms based on three different spring analogy techniques. Further, methods for handling the vessel are described, from geometry reconstruction to modelling its contact with the stent. Finally, the chapter outlines some of the established methods that were used as a basis for computational experiments presented in the following chapters.

Chapter 5 **tests the performance of the developed expansion algorithms**. For that purpose, a number of deployment experiments have been carried out and evaluated in search of the most appropriate fast stenting method. The performance of

the expansion algorithms was tested on two different devices and five different vessel geometries, including real patients cases, to finalise the developed fast deployment method.

Chapter 6 is dedicated to a **validation study of the developed fast deployment method**. The developed fast method was compared with the gold standard, the finite element analysis, in a set of computational experiments. The results showed good agreement between the two methods. Further, this chapter describes a methodology for calibration and optimisation of the fast method with the help of genetic algorithms.

Chapter 7 presents the next step in modelling vascular interventions and **investigates haemodynamic conditions** of the treated vessel before and after the stent deployment procedure. On the basis of a real patient's case, different scenarios of an intervention were explored virtually, and their consequences for haemodynamic changes were evaluated using computational fluid dynamics, illustrating the importance of the choice of device, deployment positioning and overall pre-operative planning.

Chapter 8 concludes the thesis by discussing limitations of the presented work and outlining future research directions.

CHAPTER 2

CARDIOVASCULAR DISEASES: BACKGROUND

This chapter initiates the reader into the fascinating world of vessels and minimally invasive vascular repairs. First, it touches upon some relevant aspects of the human cardiovascular system, focusing on healthy vessels and widespread vascular diseases. Thereafter, minimally invasive treatment methods are introduced, in particular those involving the deployment of intravascular stents. The chapter closes with a description of different types of stents and their mode of operation.

2.1 THE CARDIOVASCULAR SYSTEM

The heart is the first and most tireless muscle of the human body. It starts beating about three weeks after conception and will beat approximately 3 billion times during an average lifetime, 72 times per minute or 100,000 times per day (Sehnert and Stainier, 2002). Each heartbeat pumps blood around the body through a complex branching network of elastic vessels that build up the cardiovascular system. As vital and sophisticated as this system is, it is also extremely vulnerable. According to the latest medical statistics published by the World Health Organisation, cardiovascular diseases (CVDs) currently constitute the world's largest killers, being responsible for 17.1 million deaths annually. In Europe, CVDs cause nearly half of all deaths (Allender et al., 2008) and in the USA, one out of three Americans is estimated to have one or more types of CVDs (Lloyd-Jones et al., 2009). Similar demographics prevail throughout the western world.

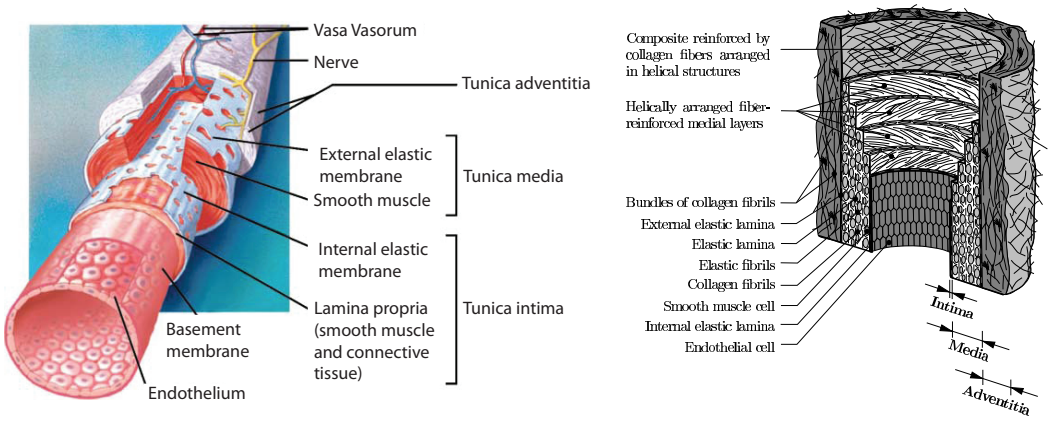

(a) (b)

Figure 2.1: Structure of a medium-size muscular arterial wall consisting of three layers. Image (a) was adapted from Lasheras (2007) and image (b) from Holzapfel et al. (2000).

The term CVD refers to any dysfunctional condition of the heart or blood vessels such as high blood pressure, heart failure, strokes, vasospasm, atherosclerotic stenoses and congenital defects. The causes of CVDs are profoundly multifactorial, with influencing factors ranging from genetics (Yusuf et al., 2001) to large vessel haemodynamics (Ventikos et al., 2009) up to psychosocial factors (Rozanski et al., 1999).

Most CVDs are related to ailments of blood vessels and especially to disorders of the arterial wall (Kiousis et al., 2009). In order to understand their nature, it is firstly necessary to gain understanding of the structure and physiology of a healthy artery, briefly outlined below.

2.1.1 Healthy arterial structure

In general, walls of healthy human arteries consist of three distinguishable layers: the *tunica intima*, the *tunica media* and the *tunica adventitia* (see Figure 2.1). The inner layer of the artery is called tunica intima and consists of a single layer of endothelial cells placed on a thin membrane and a subendothelial layer composed of connective tissue, elastic fibrils and collagenous bundles (Lasheras, 2007). In arteries of healthy young subjects, the intima is very thin and plays an insignificant role in the mechanical behaviour of arterial tissue (Holzapfel et al., 2000).

The tunica media is the middle layer of the arterial wall, containing a three-dimensional matrix of smooth muscle cells, elastin fragments and collagen fibers (Lee, 1995). These components are interconnected and oriented in a way to form a continuous fibrous helix, so that some fibrils are in a nearly circumferential orientation (Holzapfel et al., 2000). It is due to this arrangement that the media exhibits its high strength, resilience and resistance to loads. It is thereby responsible for most of the mechanical characteristics of the arterial tissue, making it structurally the most significant layer (Lasheras, 2007).

The outermost layer is the adventitia, which is mainly made up of fibroblasts and fibrocytes (cells that produce collagen and elastin), histological ground substance[1], crimped collagen fibers, blood vessels that supply the vessel itself[2] and nerves that stretch all the way to the media (Lasheras, 2007). The wavy collagen fibrils are arranged in a helical structure, strengthening the wall, and are largely responsible for stability and support of the artery (Holzapfel et al., 2000).

Mechanical Behaviour. Human arteries are flexible complex structures and feature a nonlinear stress-strain response that is predominantly attributed to the presence of elastin and collagen constituents (Holzapfel et al., 2000).

Elastin is a rubber-like, highly extensible protein that gives elasticity to arterial tissue. Its fibers possess an elastic modulus of around 0.6 megapascals (MPa) and can stretch up to 2.5-fold of their initial length, displaying essentially a linear stress-strain response, displayed in Figure 2.2 (Shadwick, 1999). In contrast to elastin, collagen fibers function as a stiff protective sheath with an elastic modulus of 500 MPa (note that it is nearly $\times 10^3$ higher than that of elastin!) (Lasheras, 2007). Collagen acts as the main load-carrying element of the arterial wall and prevents its overstretching through the highly nonlinear stress-strain response, depicted in Figure 2.2 (Shadwick, 1999).

The overall mechanical behaviour of an artery is nonlinear. It is characterised by the initial compliance of the artery at low pressures due to elastin, while the exponential stiffening effect at higher pressures is attributed to the gradual recruitment and straightening of wavy collagen fibers, as shown in Figure 2.2 (Shadwick, 1999; Holzapfel et al., 2000).

[1] "Ground substance is the amorphous intercellular material in which the cells and fibers of connective tissue are embedded" (Med, 2007).

[2] These blood vessels are called *vasa vasorum*; they are absent in cerebral arteries.

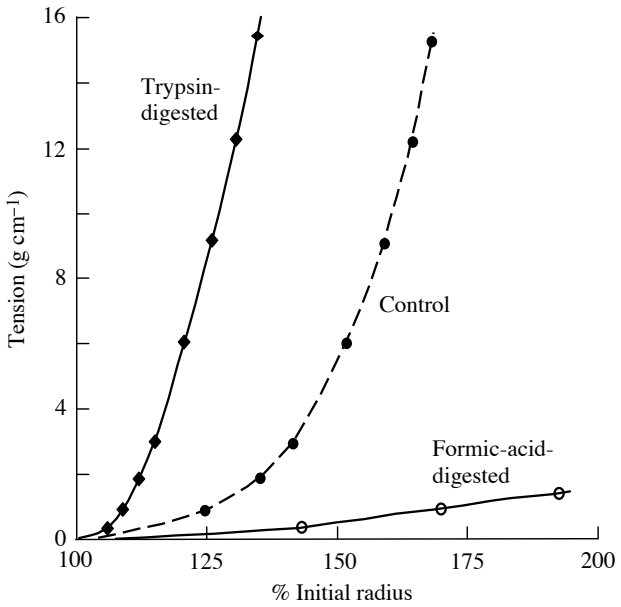

Figure 2.2: The tension-length response of human iliac arteries. The response of collagen fibers is captured by the curve with diamonds and the response of elastin by the curve with open circles. The broken curve with filled circles shows the combined elastin-collagen response for the complete artery (image from Shadwick 1999).

2.1.2 Diseases of arterial walls

Unfortunately, no matter how sophisticated the cardiovascular system is, its repair mechanisms are sometimes insufficient to prevent the onset of various cardiovascular ailments. The most common CVDs are diseases of the vessel walls such as aneurysms, arterial dissections, stenoses, briefly outlined below.

Aneurysms. An aneurysm is a pathological dilatation of the artery resulting from the arterial wall weakening. Rupture of an aneurysm can lead to haemorrhage and stroke. The outpouching in the artery occurs due to elastin degradation, which is characteristic to the aneurysmal wall consisting primarily of collagen with either a fragmented or absent medial elastic lamina (Humphrey and Canham, 2000). Aneurysms are often classified according to their shape in two broad categories: fusiform and saccular aneurysms. Saccular ("berry-like") aneurysms most commonly originate in cerebral arteries, particularly those surrounding the Circle of Willis at the base of the brain (Figure 2.3, a), whereas fusiform ("spindle-shaped") predominantly form in the abdominal aorta (Figure 2.3, b).

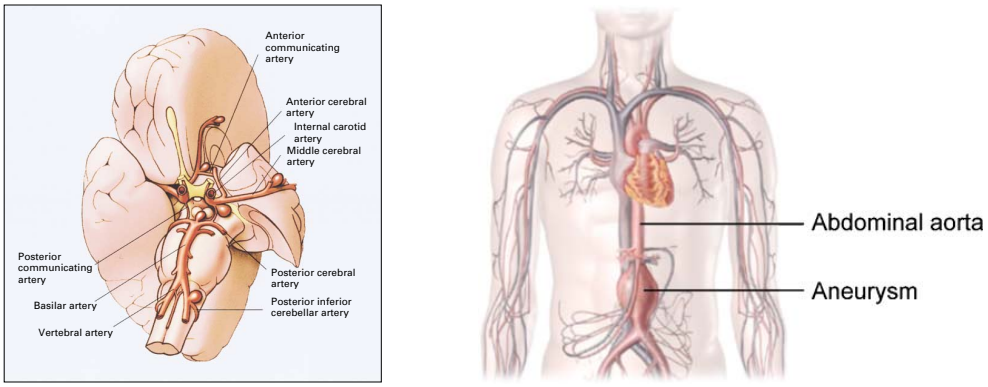

(a) (b)

Figure 2.3: (a) Cerebral aneurysms most commonly occur at the arteries surrounding the Circle of Willis and have a saccular shape in the majority of cases (> 90%) (image from Schievink 1997). (b) AAAs form in the abdominal area of the aorta and usually feature a fusiform shape (image from Lasheras 2007).

Cerebral or *intracranial aneurysms* (Figure 2.4, a) are quite common among adults and an estimated 2–5% of the adult population live with undiagnosed cerebral aneurysms worldwide (Van Gijn and Rinkel, 2001). The etiology of this disease has not been fully understood; however, it is thought to be associated with a complex interplay of multiple factors including blood flow, arterial wall composition, cell populations, genetics and signalling pathways (Ventikos et al., 2009). Once an aneurysm is formed, haemodynamic forces of blood flow may cause its enlargement coupled with a further degradation of the arterial wall, which in the worst-case scenario may lead to rupture of the aneurysmal sac (Lasheras, 2007). Although only less than 1% of detected cerebral aneurysms rupture per year (Juvela et al., 2000), the incidence of rupture has dreadful consequences of subarachnoid haemorrhage[3]: 45% of ruptured aneurysms result in death in the first 30 days, and 30% of survivors face moderate to severe morbidity (Brisman et al., 2006). Despite of the grave consequences of aneurysmal rupture, there is currently no accurate means of determining its probability, and the decision on the need for clinical intervention is based predominantly on the aneurysm size (Ventikos et al., 2009). Even before rupture, cerebral aneurysms can cause complications by exerting pressure on the surrounding tissue, inducing symptoms such as “headache, palsy of the third nerve or brain-stem compression” (Schievink, 1997).

[3] “A subarachnoid haemorrhage (SAH) is bleeding between the middle membrane covering of the brain and the brain itself” (Med, 2007).

(a) (b)

Figure 2.4: Angiograms of (a) cerebral fusiform aneurysm of the basilar artery (images from Crowley et al. 2009) and (b) abdominal aortic aneurysms (image from The Vascular Care Centre: `www.vascularcarecentre.com`).

Abdominal Aortic Aneurysms, or *AAAs* (Figure 2.4, b), very rarely appear in individuals under the age of 50, but their prevalence increases dramatically after 55 years, culminating shortly after 80 (Lasheras, 2007). According to a large screening study of individuals over 60 years of age, AAAs are found in 8.9% of male and in 2.2% of female subjects (Singh et al., 2001).

As is the case with intracranial aneurysms, the causes of AAAs are poorly understood. The widely accepted hypothesis is that their formation is linked to the specific changes in the vessel geometry such as length, diameter and other structural changes that are associated with the process of aging. In turn, these alterations lead to modifications in the haemodynamics, for example, creating unsteady flow separation and weak turbulence. The disordered flow conditions may induce a gradual degradation of the wall of the abdominal aorta, whereby its diameter progressively increases, forming an aneurysm (Lasheras, 2007).

For a developed abdominal aneurysm, the maximum potential rupture rate (actual rupture rate plus elective surgery rate) is reported to lie around 2.1% annually for small AAAs (3.0 – 4.4 cm) and 10.2% per year for large aneurysms (4.5 – 5.9 cm) (Scott et al., 1998). Due to the absence of a reliable method of rupture risk assessment, a surgical intervention is advised at the moment for AAAs with a diameter larger than 5 cm and for those with the annual growth exceeding 0.5 cm (Brown et al., 2003).

(a) (b) (c)

Figure 2.5: Arterial dissections. (a) Schematic representation of an arterial dissection (image from `www.jeffersonhospital.org`). (b) Dissection of the thoracic aorta: contrast medium flows from the true lumen of the aorta (T) across the entry tear (arrow) into the false lumen (F) (image from Dake et al. 1999). (c) Dissection of the carotid artery: the true lumen is severely narrowed, as indicated by the arrow (image from Phatouros et al. 2000b).

Dissections. Arterial dissections are characterised by a separation of layers within the arterial wall (Figure 2.5). Blood enters the intima-media space and forces the layers apart, propagating the dissection further. When a dissection occurs in the aorta, high blood pressure can tear the aorta completely open and lead to heavy and expeditious blood loss. Thus, *aortic dissection* is an acute medical condition with a high-level mortality of 80%, and in half of the cases, there is not even enough time for the patient to reach a hospital (Isselbacher, 2006). While it remains unclear how the event starts, in most instances there is a preceding malformation of the aortic structure as well as systemic hypertension (Hagan et al., 2000). Other arteries that may be affected by a dissection include coronary arteries, carotid arteries, vertebral arteries, etc.

Stenoses. Stenosis is a constriction of an arterial lumen which reduces the lumen area, decreases the blood flow and thus the transport of oxygen and nutrients to distal organs (see Figure 2.6). It often occurs as a result of the accumulation of *atherosclerotic plaque* on arterial walls, which is a composition of fatty substances, calcium, collagen fibers, cellular waste products and fibrin (a clotting material in

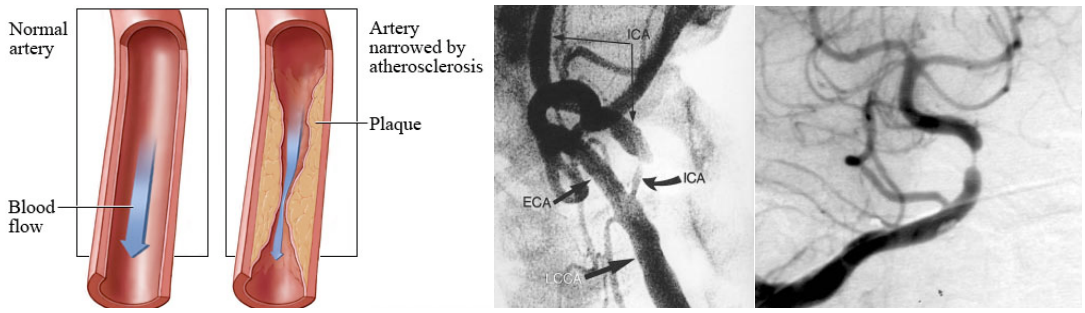

(a) (b) (c)

Figure 2.6: (a) Schematic representation of stenosis due to atherosclerotic plaque (image from `www.health.com`). (b) Angiogram showing stenosis of 80% in the left internal carotid artery (ICA), indicated by the curved arrow (image from Vitek et al. 2000). (c) Angiogram showing severe stenosis of the proximal basilar artery (image from Marks et al. 2005).

the blood) (Holzapfel et al., 2000). A progression of stenosis can cause ischemia[4], infarct of organs that artery supplies or even a stroke (Bose et al., 2007).

Although there are many other ailments of the vessel wall, this project will focus on those outlined above, which constitute the most common cardiovascular disorders.

2.2 MINIMALLY INVASIVE INTERVENTIONS

The advent of minimally invasive vascular interventions has revolutionised the treatment of common vascular diseases, becoming a preferable option compared to conventional open surgery. A minimally invasive endovascular repair involves small incisions made to expose the arteries, from where, under fluoroscopic guidance and with the help of specially designed introducer systems (guidewires, catheters, etc.), a prosthesis or *stent* is deployed inside the diseased vessel, as schematically shown in Figure 2.7 (Prinssen et al., 2004).

Originally, minimally invasive interventions were mainly suggested in difficult cases and for older patients, for which conventional open surgery would be overly invasive (Prasad et al., 2013). However, due to the expeditious evolution in devices,

[4] "Ischemia is a decrease in the blood supply to a bodily organ, tissue, or part caused by constriction or obstruction of the blood vessels, leading to a shortage of oxygen, glucose and other blood-associated fuels" (Med, 2007).

(a) (b) (c) (d)

Figure 2.7: Stent deployment in treatments of (a) abdominal aortic aneurysm (image from `www.medgadget.com`); (b) cerebral aneurysm (image from Alfke et al. 2004); (c) aortic dissection (image from `www.thoracicaorticdissection.com`); and (d) stenosis (image from `www.sciencephoto.com`).

procedure improvements and promising outcomes, they are now recommended for a wider cohort of patients. This general acceptance is due to the fact that endovascular repairs lead to more effective operative procedures, with a smaller incidence of systemic complications, less blood loss, shorter surgeries and shorter hospital stays, as compared to an open surgery. These advantages together with lower rates of post-operative mortality and morbidity make minimally invasive vascular interventions a compelling choice for an increasing number of patients (Adriaensen et al., 2002; Molyneux et al., 2002).

2.2.1 Endovascular stents

In most cases, minimally invasive vascular repairs involve the deployment of a stent inside the treated vessel. Stents are tubular structures that consist of a grid-like skeleton and possibly a polymer-based sheath (Stoeckel et al., 2002).

Implanted at the neck of an aneurysm, such a prosthesis diverts blood from flowing into the aneurysmal sac, thereby reducing the pressure on the arterial wall. Moreover, the reduction in the flow to the sac leads to stagnation inside and formation of a stable clot that isolates the aneurysm, preventing its rupture (schematic representation in Figure 2.7 [a-b] and real angiography in Figure 2.8 [a-b]). Additionally, the aim is that after the treatment, the natural absorption of the thrombus results in progressive shrinkage of the aneurysm. As a consequence, the increased constriction of the neighbouring tissue due to the presence of the aneurys-

mal sac can be gradually alleviated, which is especially relevant in the case of cerebral aneurysms exerting pressure on neuronal tissue.

Sometimes, the stenting procedure is used in combination with coiling embolisation. In this method, a stent is firstly deployed at the neck of the aneurysm, securing the positioning inside the vessel, after which soft metallic coils (Guglielmi Detachable Coils) are packed into the aneurysmal sac, being pushed in between the stent struts (Lanzino et al., 2005). The goal is to partially fill the aneurysm with the coils and thereby facilitate formation of a local thrombus, which would lead to obliteration of the aneurysmal lumen. However, because of the more complicated and time-consuming nature of this method (due to the need to deal with single coils), using stenting alone to treat aneurysms is desirable.

In the case of aortic dissections, minimally invasive stent graft deployment has also become a popular alternative to an open surgical graft placement (Dake et al., 1999). Stent grafts are deployed inside the true lumen of the aorta aiming at covering the primary intimal tear and thereby obliterating the flow into the false lumen, as shown in Figure 2.7 (c) and 2.8 (c) (Eggebrecht et al., 2005). The effect of stent grafting resembles that of surgical removal of the dissection tear. The result is comparable because the stent graft can seal the entry tear in the intima and prevent blood from flowing into the false lumen, steering it to only enter the true lumen (Dake et al., 1999). This can prevent severe ischemia or infarction of the organs supplied by the dissected artery and, in addition, promote complete occlusion of the false lumen and formation of thrombosis (Dake et al., 1999).

Another method gaining popularity in treatment of symptomatic stenoses is angioplasty[5] with stent deployment. When deployed within stenotic regions, stents push the vascular wall outwards and, thus, restore lumen cross section and blood flow, as schematically shown in Figure 2.7 (d) and Figure 2.8 (d) (Mas et al., 2006). The endarterectomy[6] procedure, that previously used to be the standard treatment for severe symptomatic stenoses, is no longer the first choice for many patients, the main disadvantages being early relapses and vessel dissections due to the high invasiveness of the method (Weber et al., 2005).

[5] "Angioplasty is a minimally invasive procedure in the reconstruction of blood vessels damaged by disease or injury, often performed by inflating a balloon within the vessel lumen at the site of narrowing to reconstitute flow" Med (2007).

[6] "Endarterectomy is the surgical removal of the intimal lining of an artery to clear a major artery that may be blocked by plaque accumulation" Med (2007).

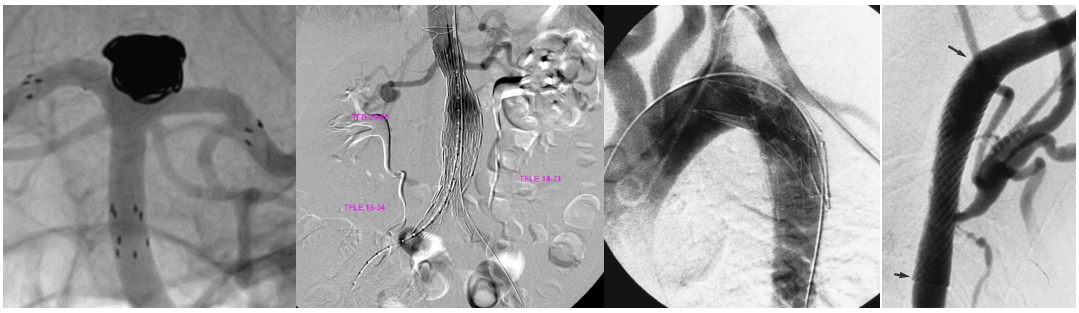

(a) (b) (c) (d)

Figure 2.8: (a) Angiography of an intracranial aneurysm treated by two stents, with black dots indicating their proximal and distal margins (image from Fiorella et al. 2010). (b) Stent graft placed over an abdominal aneurysm (image from `www.surgeryinfo.org`). (c) Stent graft placed over the primary entry tear of an aortic dissection (image from Dake et al. 1999). (d) Stenting of a stenosed cerebral artery with arrows indicating the proximal and distal margins (image from Phatouros et al. 2000a).

Stents have become increasingly popular and are also used in treatments of other conditions, such as kidney or liver disease. However, these conditions fall out of scope of this thesis, which will only focus on the most common vessel wall diseases discussed above and the types of stents associated with them.

2.2.2 Key parameters of stents

Stents are introduced into a vessel in a slim configuration to enable their pushing through the vasculature to a desired location. Deployed by shape-memory effects or by an inflating balloon, they expand and should fit the diameter of the artery's healthy part. Balloon-expandable stents are expanded by a plastic deformation through an inflation of a balloon placed inside the device. They are usually made of stainless steel, which is a particularly corrosion-resistant and easily deformable material (Stoeckel et al., 2002).

In contrast to balloon-expandable, self-expanding stents are manufactured in the expanded shape, to be later crimped and placed in a delivery system. Upon release, they "spring back" to a load free configuration under the elastic forces of the material. Currently, most self-expanding devices are made of nitinol (a nickel-titanium alloy), which is a superelastic material that features an elastic response to small deformations, while larger strains (of up to 10%) can be achieved superelas-

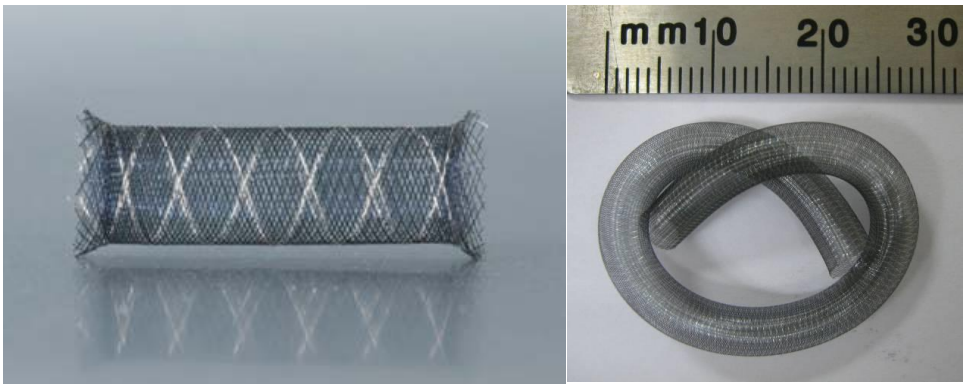

(a) (b)

Figure 2.9: Flow diverters. (a) Silk stent produced by Balt Extrusion, Montmorency, France (image from Pierot 2011) and (b) Pipeline Embolization Device (PED) manufactured by Covidien, Irvine, California (image from `www.fda.gov`).

tically due to its shape-memory effect (Stoeckel et al., 2002). Figure 2.10 illustrates in a sequence of screenshots the expansion process of a nitinol stent induced by an increase in temperature. First, the crimped stent located in a sealed glass tube was heated (a). The expansion started to be visible after around 10 seconds (b) and progressed for another 10 seconds (c-f), after which no diameter change was observed. During this free expansion process, the stent recovered its initial shape completely (Zhou, 2009; Zhou and You, 2009). Note that during clinical procedures, the expansion of a stent is usually triggered by the retraction of a constraining sheath, using the superelastic properties of nitinol, and not by temperature increase (stress- rather than temperature-induced martensite).

Out of many different types of implants, this project will focus on the self-expanding stents for the treatment of cerebral aneurysms and the stent grafts used for aortic aneurysms and dissections. Although these devices are targeting different diseases, the mechanisms underlying their functioning are the same.

Apart from material, other characteristics of the stent design, such as porosity (defined as the proportion of an open area to the total area of the stent), are of extreme importance. The appropriate preoperative choice of these features is necessary to avoid such problems as stent loosening, obstruction of branching vessels and thrombus formation in the healthy part of the vessel (Flórez-Valencia et al., 2002). For example, in treatment of cerebral aneurysms, the stent has to be flex-

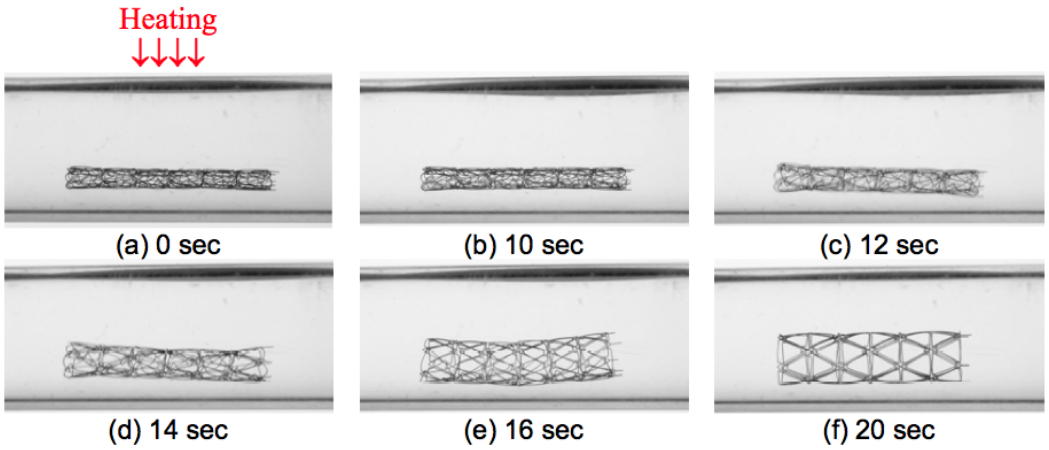

Figure 2.10: The expansion process of a nitinol stent (image from Zhou 2009).

ible enough to follow tortuous intracranial vessels and, at the same time, provide sufficient coverage to occlude the aneurysmal sac. The newest flow-diverting systems that have been introduced in clinical practice for this purpose are the Pipeline Embolization Device (PED; Covidien Irvine, California, USA) and the Silk stent (Balt Extrusion, Montmorency, France), shown in Figure 2.9. They were especially designed for the treatment of fusiform and wide-neck intracranial aneurysms, which were posing a lot of problems when treated with previous generations of devices (Pierot, 2011). Figure 2.11 depicts the stages of deployment procedure for the PED device.

2.3 Concluding Remarks

This chapter provided the background on cardiovascular diseases and a current method of their treatment by minimally invasive endovascular stenting. The high prevalence of cardiovascular conditions is expected to increase in the future due to the aging population in most of the western world. Such demographic developments and the popularity of vascular repairs by stent deployment necessitate a rigorous analysis of the consequences of these procedures. In particular, having seen that human arteries have complex mechanisms of remodelling (especially active after the placement of a stent), it appears plausible that stenting procedures should be performed in the least disruptive way. Although not much is known about ways to guarantee a successful device placement in the long run, some data is available on what should be avoided during the intervention. Hence, the sophistication of

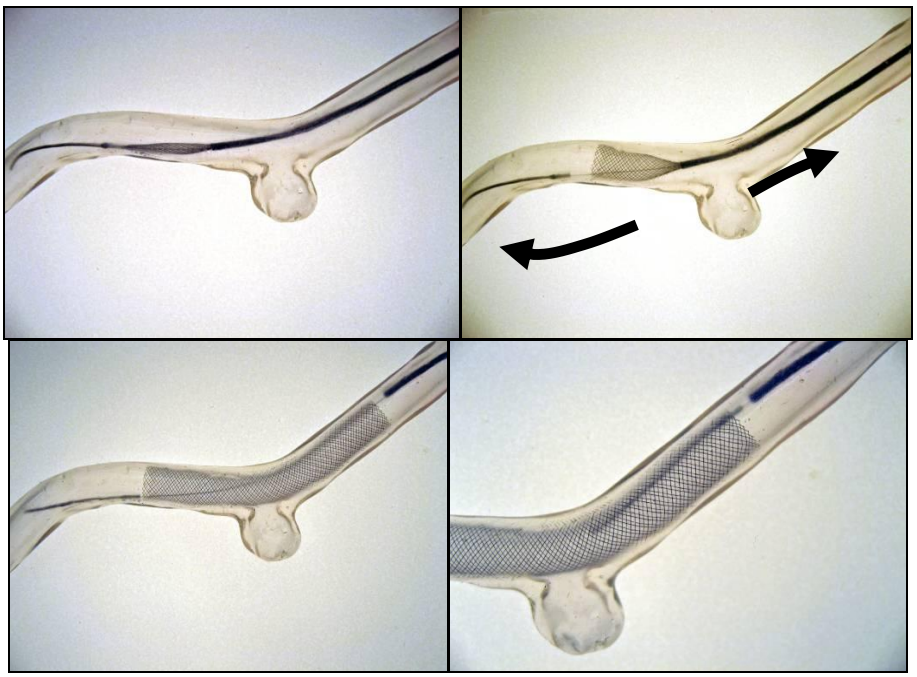

Figure 2.11: Stages of deployment of the PED device: PED advanced 10-15 mm beyond aneurysm, the distal end of the implant expanded, PED implant fully deployed across aneurysm, withdrawal of the delivery system (image from `www.fda.gov`).

the vascular system provides another motivation for mindful placement of stents, well-planned interventions and better selection of patients, serving therefore as an additional inspiration for the present research work.

With respect to stents for cardiovascular disorders, they can be classified into three broad categories according to the area of implantation, namely, (1) tiny cerebral stents and flow diverters for treating intracranial aneurysms, (2) abdominal stent grafts for treating aortic dissections, AAAs and TAAs; and finally, (3) balloon-expandable coronary stents to combat stenoses by angioplasty. This thesis will be focusing on the first two categories due to the greater need for pre-procedural planning in these areas and the prevalence of self-expanding devices. Although, the devices employed in these two domains differ substantially in their design and architecture, most of them are made of nitinol and thus feature the same principles of operation. Their expansion from the crimped state will constitute the primary subject of the modelling undertaking of the subsequent chapters.

The next chapter is dedicated to the literature review, listing existing work on virtual stent deployment.

CHAPTER 3

EXISTING WORK ON MODELLING VIRTUAL STENT DEPLOYMENT: LITERATURE REVIEW

This chapter reports on attempts that have been made up to date in modelling virtual stent deployment. The literature review revealed two major trends in the field that address the problem from different angles. The first class of methods includes detailed finite element models, which are very precise and are often designed to study a specific aspect of the problem, thereby providing a thorough analysis of the studied question. Another class of approaches includes rapid stenting techniques that are meant to support clinical decision-making. The latter category is directly relevant to the scope of this project and focuses on developing techniques capable of simulating the deployment of prostheses in real-time mode. The methods used by these approaches are reported in detail in the sequel of the chapter. At the end of the chapter, a brief review of the relevant studies investigating vessels haemodynamics is also included, since it constitutes the essential next step in modelling virtual vascular interventions.

3.1 EXISTING APPROACHES

Over the past decade, a lot of effort has been dedicated to the investigation of the physical behaviour of vascular prostheses and their usage in minimally invasive vascular interventions by means of computational modelling. The developed approaches can be roughly divided into finite element methods and rapid virtual stenting techniques.

3.1.1 Finite element methods

Finite element analysis (FEA) is a powerful method which has been extensively used to study the mechanical behaviour of stent devices and their deployment process inside virtual vessels. Previous work on analysing the stent mechanics ranged from the structural analysis of stent cells (Theriault et al., 2006) to investigations of device materials (Migliavacca et al., 2005) to examining longitudinal flexibility and bending behaviour of different stent designs (Ma et al., 2013; Wu et al., 2007c).

With respect to stent deployment, the simulation of the deployment process requires, firstly, modelling the expanding and the crimping behaviour of the prosthesis and, secondly, the interaction between the implant and the vessel wall when they come into contact. Some studies have especially focused on expansion behaviour, inspecting the shape change and recoil, maximum stress, strain and the radial strength of the stent. Such studies have been performed either on an entire stent (Migliavacca et al., 2005) or on single parts of a stent (Theriault et al., 2006), which, under the assumption that the prosthesis consists of repeating elements, allows to considerably reduce the computational cost of the simulations.

There have been several proposals on how to realise the expansion and folding of a stent numerically. In case of balloon-expandable stents, the deployment can be carried out by placing an initially folded prosthesis inside an artery and expand it to a radius greater than that of the vessel under control conditions (Wu et al., 2007b; Gijsen et al., 2008). The expansion process has been simulated either by applying a direct pressure to the internal surface of the stent (Migliavacca et al., 2005) or by using the contact between the device and an expanding cylindrical surface (Hall and Kasper, 2006). Another proposal has been to explicitly model the balloon and the contact between its external surface and the internal surface of the stent. Thereafter, the stent was indirectly expanded as a result of applying pressure to the internal surface of the balloon (Chua et al., 2003).

With respect to the self-expanding stents, their deployment within an artery usually starts by folding them to a small radius with a subsequent insertion into the vessel. Following that, the radial constraint is removed releasing the strain energy of the implant which causes its expansion (Wu et al., 2007a). The removal of the constraint can be achieved, for example, via the use of contact between the external surface of the stent and an analytical cylindrical surface with a changing radius (Rebelo et al., 2009).

Many of the studies examining the interaction between the expanding prosthesis and the vascular tissue used an idealised vessel geometry, for instance, a straight cylindrical tube (Chua et al., 2003; Migliavacca et al., 2004). For modelling stenotic arteries, some researches have additionally included an explicit layer of atherosclerotic plague attached to the part or the entire internal surface of the artery (Migliavacca et al., 2004; Wu et al., 2007a). The artery and plaque were assumed to have either linear elastic material properties (Rebelo et al., 2009) or hyperelastic material properties (Migliavacca et al., 2004; Wu et al., 2007a).

When more sophisticated vessel geometries were considered, the analysis of the stent-vessel interactions has led to interesting predictions about the potential treatment outcomes. For example, the study of Wu et al. (2007a) modelled the prosthesis release inside a curved segment of a Y-shaped artery and reported a number of potential problems. Although the curved tissue of the vessel bent the stent, straightening of the vessel geometry also occurred and there was a prolapse of parts of the vessel wall between the stent filaments. In its turn, the stent was non-conformable to the vessel, especially the stent extremes departed from the walls at the inner curvature of the vessel. The authors conclude that such a configuration is prone to (re-)stenosis at the stent extremities, especially at hinge points, where the level of stress reaches the maximum value and where a sharp transition occurs between the rigid ends of the stent and the soft vessel tissue.

More recently, Gijsen et al. (2008) and Rebelo et al. (2009) used realistic vessel geometries which were obtained from MRI data to simulate stent-artery interaction. Gijsen et al. (2008) reported that the stresses exerted by a deployed stent on the arterial wall concentrate behind stent struts in those locations where the vessel wall is thinner (see Figure 3.1). The maximum values of the stress behind stent struts corresponded to vessel regions that displayed clinical signs of neointimal hyperplasia. Moreover, the stents showed larger deformation in the proximal part, with stresses close to the estimated fatigue fracture stress. Such levels of stress are alarming since the breakage of stent struts could injure the surrounding vessel tissue and could trigger the development of in-stent stenosis, as well as potential embolic events further downstream. Moreover, the continuous stresses exerted on the damaged vessel tissue could ultimately lead to vessel perforation. Additionally, when analysing stent-artery interactions, Rebelo et al. (2009) underlined the significance of utilising real patient-specific vessel configurations. They reported that the peak maximum

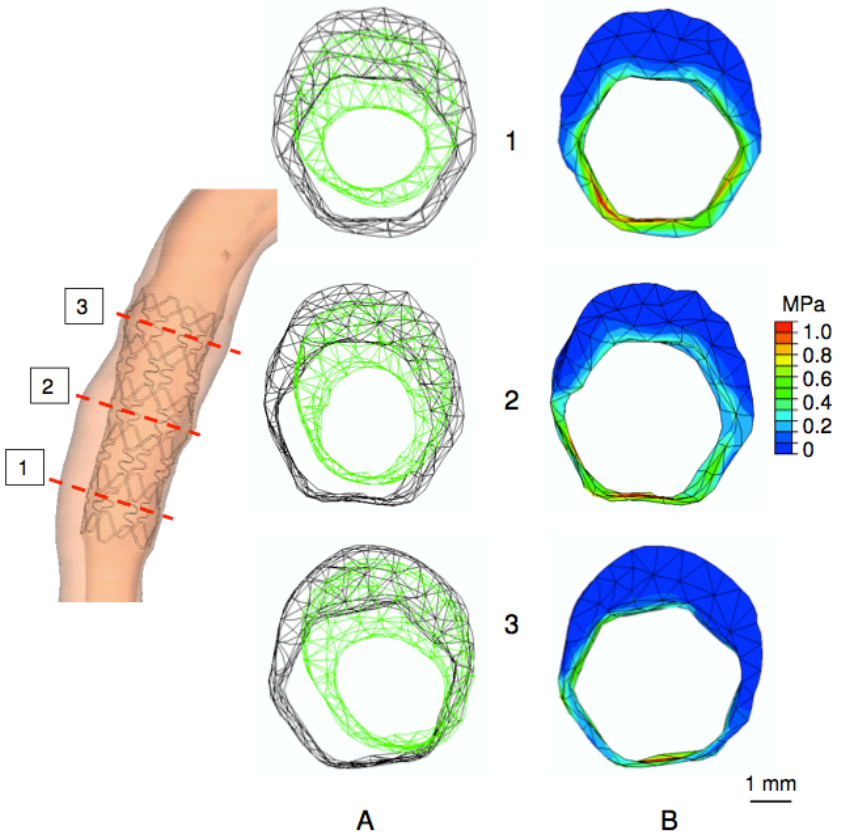

Figure 3.1: Column A: configuration of the vessel cross section at the beginning of the stent expansion process (green) and at the maximum inflation pressure of 1.0 MPa (black) for three different locations in the vessel (shown on the left side). Column B: the corresponding contour maps of von Mises stresses in the vessel wall (image from Gijsen et al. 2008).

principal strains measured in the device deployed at the curved vessel segment were roughly three times higher than those measured in the straight segment.

Another study by De Bock et al. (2012) focused on the procedure of stent assisted coiling in cerebral aneurysms and investigated the consequences of stent design and vessel geometry. The authors simulated virtual placement of three different stents in three different vessel geometries using FEA and analysed the stent apposition to the vessel wall and the impact of implanted stents on straightening of the vessel. The results suggested that devices with open cell design cover the aneurysm neck in a better way compared to both the stiff and flexible closed cell stents and induce less straightening of the vessel. The open cell design has, however, less struts apposing well to the vessel wall compared to the flexible and stiff closed cell de-

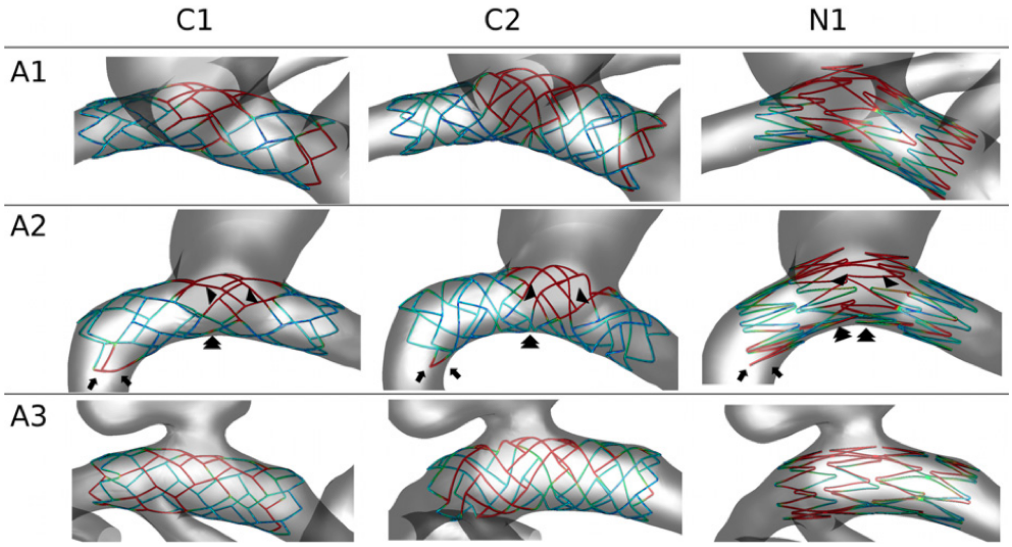

Figure 3.2: Deployed stents (C1, C2, N1) and their apposition to the vessel wall when deployed in three different vessels (A1, A2, A3). The colour of the stent indicates the distance to the vessel wall, ranging from blue (0 mm) to red (40.2 mm) (image from De Bock et al. 2012).

sign. Figure 3.2 shows the resulting configurations, for two generic closed-cell designs (stiff C1, flexible C2) and a design resembling the open cell Neuroform (Stryker Neurovascular, Fremont, California, USA) design (N1). These findings provide important general heuristics on the choice of stents for different pathological configurations and illustrate the added-value of computational modeling in pre-procedural treatment planning.

Finally, probably the most sophisticated FEA setup for analysing intravascular interventions was recently presented by Ma et al. (2012). The study developed a complex model of the PED flow diverter and simulated its mechanical deployment in patient-specific aneurysmal geometries, however, under the assumption of rigid vessel walls. The specific contribution of the study was to implement interlaced wires of the braided PED device, as well as to account for other components of the deployment process such as microcatheter, pusher and distal coil (constraining the stent distal end). Based on the resulting vessel wall apposition of the deployed device (see Figure 3.3), the authors concluded that flow diverters conform better than the widely-used Wallstent (Boston Scientific, Natick, MA) but worse than laser-cut stents.

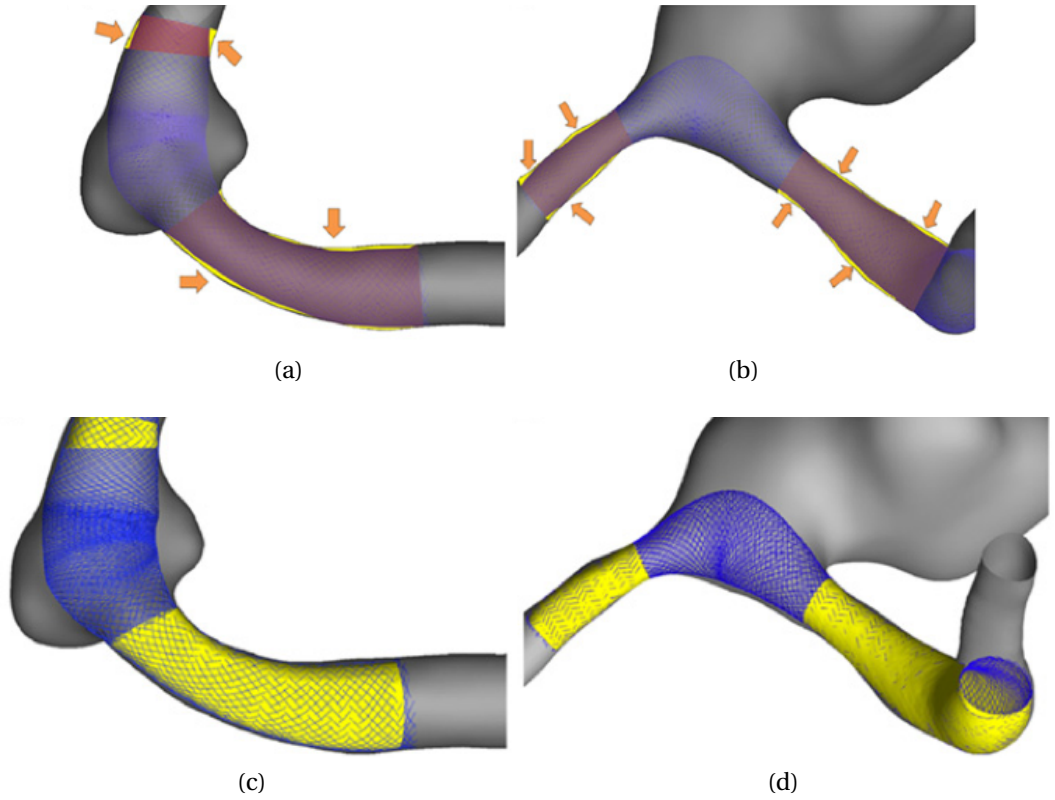

Figure 3.3: Conformity of the deployed flow diverter to the target vessel. Panels (a) and (b): vessel segments featuring device malapposition are marked in yellow. Panels (c) and (d): yellow surfaces show areas of the parent vessel that are covered by stent struts (image from Ma et al. 2012).

In summary, FEA simulations can produce very accurate results for particular cases and can be used for thorough analysis of many aspects of intravascular stent placement. However, this accuracy comes together with high computational cost and considerable complexity of models, especially when applied to patient-specific geometries. Thus, the major drawback of the FEA approaches with respect to clinical applicability is their speed, which involves execution times from several hours to a couple of days (excluding setup time), depending on the complexity of simulations, in most cases on clusters with multiple cores (parallelised simulations). Additionally, FEA models are usually implemented in Abaqus (Dassault Systemes Simulia Corp., Providence, RI, USA) or other FEA software packages, with each model requiring a complex set-up that cannot be expected to be performed by a clinician or a nurse. Although highly accurate, these methods are aimed to thoroughly examine the device mechanical behaviour, the contact with the arterial wall and alter-

ations in blood flow from a mechanical perspective and are not destined for direct application in daily clinical routine, which dictates fast turnover times and where a stand-alone method would be preferred.

3.1.2 Fast stenting techniques

This category of modelling approaches is of great relevance to the present study and focuses on developing techniques capable of simulating the deployment of stent devices in real time. In this respect, they are different from the previously presented studies, since they allow small sacrifices of accuracy for the sake of fast execution, which constitutes an essential requirement for clinical preoperative planning. An exhaustive literature survey has revealed only three approaches for stent deployment simulations that aim at evaluating different stent placement scenarios on a patient-specific, clinically relevant basis.

The first approach allowing the prediction of the stent released shape was presented by Cebral and Lohner (2005) and in the follow-up study of Appanaboyina et al. (2008) and uses the framework of deformable models. In these studies, the patient-specific vessel geometries were reconstructed from anatomical images and discretised with a finite element grid. To simulate the deployment of the prosthesis, first a generated cylindrical surface was placed along the centerline of the target vessel. The deformation of the cylinder was determined by the combination of internal forces that were smoothing the stent structure and external forces that were attracting the stent vertices to the arterial wall (see Figure 3.4). During the simulated deployment process, the interplay of the internal and external forces drew the

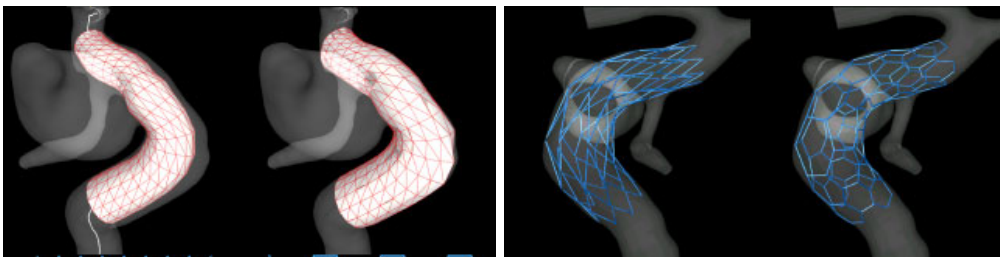

Figure 3.4: Stages of virtual stent deployment (from left to right): cylindrical surface placed along the centerline of the vessel, final deployed cylindrical surface, two stent designs drawn on the cylindrical surface after deployment (image from Appanaboyina et al. 2008).

cylinder to the arterial walls. The deformation was calculated by solving the elasticity equations on the triangulated cylindrical surface using finite elements. The vessel was assumed rigid and the deformation process terminated as soon as the majority of the nodes on the cylindrical surface reached the vessel wall. Thereafter, different stent designs were projected onto the deformed cylinder by drawing them as a set of connected lines.

Although specific designs of stents is considered in this study, physical and geometrical features of the design, such as length of struts and angle between the struts, were not accounted for during the expansion process. Overall, this method is essentially based on deforming a regular cylindrical mesh inside the parent vessel, from which the final configuration of the stent is recovered. Such mapping of the stent geometry as a texture over a cylinder can introduce substantial inaccuracies in final stent configurations, especially in regions of high arterial curvatures.

Another method has been proposed by Flórez-Valencia et al. (2002, 2007) and is based on deformable 2-simplex meshes. A 2-simplex mesh has exactly 3 neighbours per vertex and is topologically dual to triangular meshes (Delingette, 1999). A simplex deformable mesh is defined by a collection of vertices $\{\mathbf{v}_i\}$, with each vertex deforming according to the interplay of internal ($\mathbf{f}_i^{int}$) and external ($\mathbf{f}_i^{ext}$) forces, formally written as the evolution equation:

$$\mathbf{v}_i^{t+1} = \mathbf{v}_i^t + \gamma(\mathbf{v}_i^t - \mathbf{v}_i^{t-1}) + \mathbf{f}_i^{int} + \beta\mathbf{f}_i^{ext}, \tag{3.1}$$

where $\mathbf{v}_i^t$ stands for the position of vertex $\mathbf{v}_i$ at the time point t, $\beta \in [0,1]$ is the weighting parameter for the external force and γ is a damping component.

The geometry of both the vessel and the stent is modelled as generalised cylinders, represented as a centerline with orthogonal planar contours of specific radii. First, the initial stent deployment is carried out by aligning the skeleton of the straight model of the stent with the vessel axis, while keeping the contour planes orthogonal to the axis line (see Figure 3.5, left and middle). Thereafter, the deployed configuration of the vessel is obtained using simplex-mesh deformable model, with the extended version of Equation (3.1). The idea behind the modification is that the vertices on the surface of the stent tend to follow the bending of the centerline, which is reported to them as the "axial" force. Additionally, each vertex tends to position itself on a circle around the centerline, giving rise to the "radial" force component. Thus, the new iterative equation for a vertex i features additional axial

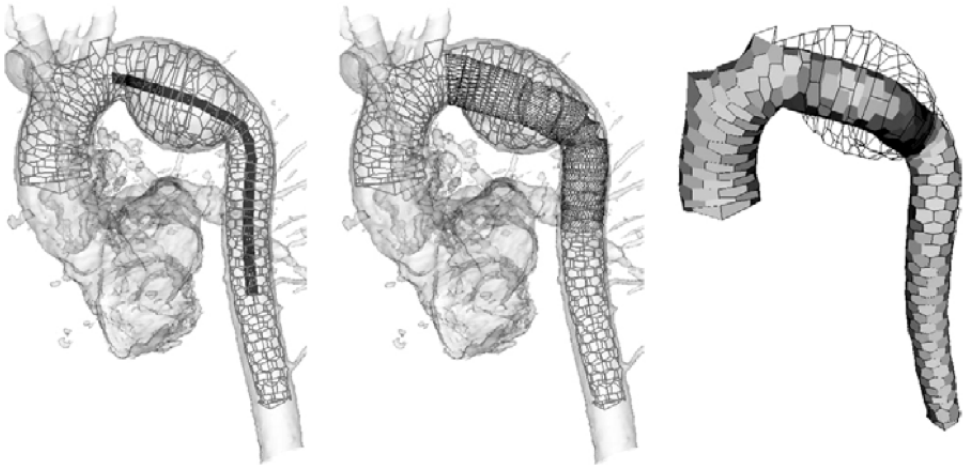

Figure 3.5: Virtual placement of a stent in a patient-specific aortic aneurysm. Left: vessel mesh with a folded stent. Middle: stent in the deployed configuration. Right: surface rendering of the vessel to match the surface of the deployed stent (image from Flórez-Valencia et al. 2007).

($\mathbf{f}^{axial}$) and radial ($\mathbf{f}^{radial}$) force components resulting from the centerline bending:

$$\mathbf{v}_i^{t+1} = \mathbf{v}_i^t + \gamma(\mathbf{v}_i^t - \mathbf{v}_i^{t-1}) + \lambda(\mathbf{f}_i^{int} + \beta\mathbf{f}_i^{ext}) + (1-\lambda)(\mathbf{f}^{axial}(\mathbf{v}_i^t) + \mathbf{f}^{radial}(\mathbf{v}_i^t)), \qquad (3.2)$$

where $\lambda \in [0,1]$ is a parameter weighting importance of the local and centerline forces. However, in the proposed method this equation is only applied to the vessel, not the stent. The initially deployed stent is not subject to any more deformation and is visualised by struts drawn smoothly around its surface. In contrast to a static stent, the vessel is set to be moving towards the cylindrical surface of the stent and locally fit its shape according to Equation 3.2 (see Figure 3.5, right).

In summary, the stent model is initialised as a cylinder placed along the centerline of a vessel, which is deformed to comply with the vessel. Similarly to the previous approach, this method deforms a cylindrical mesh and does not sufficiently account for either the geometrical properties of the device design or its interaction with the vessel morphology. Moreover, it is very counterintuitive and physically implausible that the mechanically more rigid vessel is modelled to be deforming according to the stent surface that is assumed to be static, rather than other way around.

The third and the most sophisticated method that explicitly models stent design was proposed by Larrabide et al. (2010, 2008); Flore et al. (2009). Here again, vessels

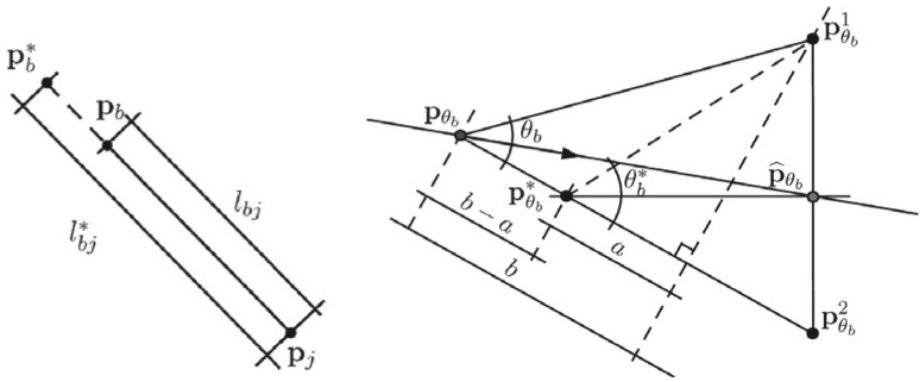

(a) Strut length force ($\mathbf{f}_l$) (b) Strut angle force ($\mathbf{f}_a$)

Figure 3.6: Shape-constraining forces acting on the vertices of the stent mesh (image from Larrabide et al. 2010).

were assumed rigid and their geometrical configurations were reconstructed from 3D-angiography medical data. The modelling of stent release, as in the previous approach, was based on a variation of deformable simplex meshes (Montagnat and Delingette, 2005, Equation 3.1), extended to incorporate geometrical characteristics of the stent.

In order to include the stent design into the model, a second design-specific mesh (consisting of vertices $\mathbf{p}_b$) was defined on the set of vertices of the simplex mesh (set of vertices $\mathbf{p}_i$). This additional mesh was meant to capture the geometrical features of the deployed device, such as stent struts, length of the struts and angles between the struts, that define soft constraints on the deformation of the simplex mesh. Thus, the new set of forces responsible for the device shape is added, which consists of the strut length force ($\mathbf{f}_l$) and angle force ($\mathbf{f}_a$), along with the internal smoothing force ($\mathbf{f}_s$), resulting in the following evolution equation for a simplex mesh point $\mathbf{p}_i$:

$$\mathbf{p}_i^{t+1} = \mathbf{p}_i^t + (1-\gamma)(\mathbf{p}_i^t - \mathbf{p}_i^{t-1}) + (\mathbf{f}_s(\mathbf{p}_i^t) + \chi\mathbf{f}_l(\mathbf{p}_b^t) + \psi\mathbf{f}_a(\mathbf{p}_b^t) + \mathbf{f}_{exp}(\mathbf{p}_i^t)) + \mathbf{f}_{ext}(\mathbf{p}_i^t), \quad (3.3)$$

where t stands for the iteration number, and γ, χ and ψ are weighting parameters.

The internal stent expanding force $\mathbf{f}_{exp}$ is reproduced with springs positioned along the radial direction, with the rest position at the load-free radius of the stent. Whereas the external force $\mathbf{f}_{ext}$ originates from the vessel wall boundary opposing the expansion of the stent, and is set to be equal in magnitude but with an opposite

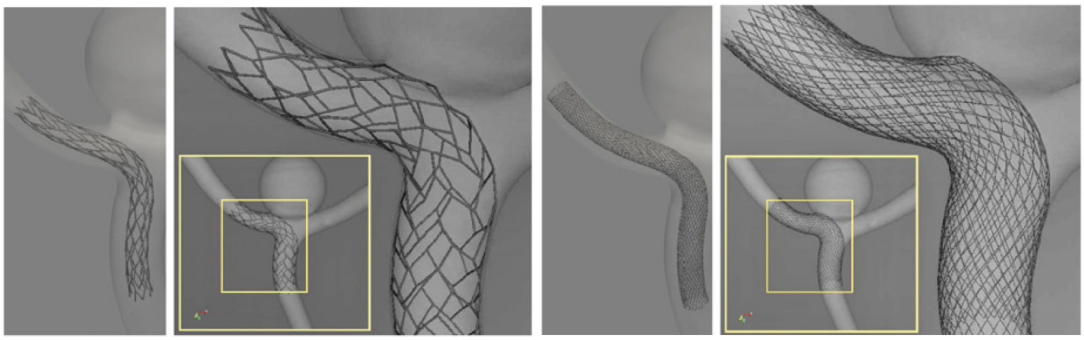

Figure 3.7: Virtual release of two stents in an aneurysmal vessel geometry (Larrabide et al. 2010).

sign to the stent expansion force. This effectively means that expansion stops when a particular mesh point is closer to the vessel wall than a given value ϵ. In addition, the smoothing force $\mathbf{f}_s$ ensures a smooth distribution of simplex points. Finally, the length constraint force $\mathbf{f}_l$ is set to be proportional to the average difference between reference length (l^*_{bj}) and current length (l_{bj}) in order to preserve the initial lengths of struts (see Figure 3.6, a). Similarly, strut angle force $\mathbf{f}_a$ is preserving the load-free angles between the struts (θ^*_b in Figure 3.6, b). Figure 3.7 illustrates the results of deployment experiments with two different stents.

Although this method explicitly models real stent geometries by capturing them as soft constraints, the model operates under the assumption of the rigid vessel wall. This simplification eliminates the possibility of vessel deformation resulting from stent placement, together with the associated alterations in the haemodynamic environment, which is of extreme importance for evaluation of treatment outcomes. Moreover, this method was designed to only focus on cerebral aneurysmal cases, without considering other areas of stenting and other diseases, especially those where substantial vessel deformation is known to occur (such as stent grafting of the thoracic aorta).

In summary, in contrast to FEA studies, the fast methods feature significant simplifications in crucial aspects of the stenting process. These simplifications undermine the trustworthiness of the results produced by the simulations and thus their very usability. More precisely, in all of the described approaches the vessel wall was treated as a rigid body (Flórez-Valencia et al., 2007; Appanaboyina et al., 2008; Larrabide et al., 2010), which eliminates the possibility of vessel deformation together with potential alterations in the haemodynamic environment. Moreover, the stent

expansion process was mechanically unrealistic, especially in the studies that did not account for the parameters of the stent design.

3.2 VESSEL HAEMODYNAMICS

Computational Fluid Dynamics (CFD) studies of vessel haemodynamics have become a popular way to gain understanding of the role of mechanical forces in the inception and evolution of many vascular diseases (Lawford et al., 2008). This popularity is especially augmented by the difficulty of conducting direct *in vivo* measurements of the relevant haemodynamic parameters, particularly in cerebral vessels.

When a diseased vessel is analysed with CFD, the obtained flow patterns could display abnormalities that provide clues into the possible progression of disease. For example, Cebral et al. (2005) performed a study of 62 patients with cerebral aneurysms with known incidence of rupture. After performing CFD simulations for all cases, the aneurysms were put in different categories based on the characteristics of the flow pattern, with the purpose of correlating it with the occurrence of rupture. Based on the obtained results, the authors suggested that unruptured aneurysms are commonly associated with simple stable flow patterns, large impingement regions (the region of collision between the inflow jet and the aneurysmal wall) and large jet sizes. In contrast, ruptured aneurysms often display disturbed flow patterns, small impingement regions and narrow jets.

Other studies focused on healthy vessel geometries that were known to subsequently form a pathology with the purpose of finding haemodynamics cues responsible for the genesis of the disease. For example, Doenitz et al. (2010) witnessed the *de novo* development and rupture of an intracranial aneurysm within 44 days. The authors conducted CFD studies of the basilar artery before and after the formation of aneurysm (see Figure 3.8). Based on the investigation of the haemodynamic parameters such as velocity, pressure and wall shear stress (WSS), they found particularly low WSS in the region where aneurysm eventually formed. They concluded that regions of high WSS have no relevance to aneurysm formation. Finally, they proposed a mechanism of inception for fast growing aneurysms, which is linked to areas of permanently low WSS with the reduced ability of the vessel wall to withstand pressure changes. When pressure increases, these areas can undergo geometrical changes, leading to changes in flow patterns and lowering the already low WSS.

(a) (b)

Figure 3.8: 3-D models of the basilar artery (a) on day 1 and (b) on day 44 (image from Doenitz et al. 2010).

Drops in the WSS result in endothelial damage and decreased stability of the vessel wall, that can eventually induce aneurysm development, growth and rupture.

However, some earlier studies have hypothesised high WSS to be responsible for the genesis of cerebral aneurysms. For example, Shojima et al. (2004) performed CFD analysis of 20 middle cerebral artery aneurysms. The results of their analysis suggested that the inception of aneurysms is linked to high values of WSS, whereas the progression and rupture are associated with low WSS that can cause degenerative changes in the aneurysm wall. Overall, the current state of the knowledge on the etiology and pathogenesis of the intracranial aneurysms was summarised in a review paper by Singh et al. (2009). The authors put together a table systematising the most important findings and studies in the field, depicted in Figure 3.9.

With respect to aortic dissections, several aspects of the dissection pathology have been subjects to CFD investigations. For example, Cheng et al. (2010) performed analysis of flow patterns within the aorta of a patient with a type B[1] dissection. Their results showed that the dissected aorta features a highly helical flow with strong recirculation and possibly turbulent regions. Around 80% of the flow injects into the false lumen, which may facilitate further propagation of the dilatation of the aorta (see Figure 3.10). Close to the initial tear, the vessel wall displayed regions

[1] Type B aortic dissection involves the descending aorta or the arch, without the ascending aorta.

Hemodynamic factors	Intracranial aneurysm			Proposed mechanism(s)	References
	Initiation	Growth	Rupture		
Dynamic					
Wall shear stress (WSS)	High	Low	Low	Increased WSS increases the production of MMP-13 which in turn leads to vessel wall damage. Decreased WSS increases iNOS synthesis—NO induced damage to vessel wall. Low WSS increases endothelial proliferation and apoptosis	Boussel et al. [11], Fukuda et al. [30], Gao et al. [7], Jou et al. [31], Malek et al. [21], Meng et al. [32], Shojima et al. [9], Ujiie et al. [33]
Oscillatory shear index (OSI)	High/Low	High	High	Degenerative changes in endothelium	Glor et al. [35], Goubergrits et al. [34], Mantha et al. [15]
Jet of blood stream	Impingement	Impingement	Impingement	Localized endothelial cell injury	Foutrakis et al. [36], Cebral et al. [14], Cebral et al. [37]
Flow pattern	—	—	Complex	Statistical association	Cebral et al. [14, 37]
Hydrostatic					
Pressure	High	High	High	Passive yield/water hammer effect	Inci and Spetzler [38], Morimoto et al. [8] Steiger et al. [39]

Figure 3.9: Studies indicating the importance of haemodynamics in the etiopathogenesis of intracranial aneurysms (table from Singh et al. 2009).

of high WSS that could induce further propagation of the dissection.

Another study of Chen et al. (2013b) investigated the communication between the true and false lumen of an aortic dissection with two re-entries. The authors found complex patterns of blood flow exchange, whereby at systole around 30% of the flow injected into the false lumen through the primary entry tear and the first re-entry, after which it flowed back to the true lumen through the second re-entry.

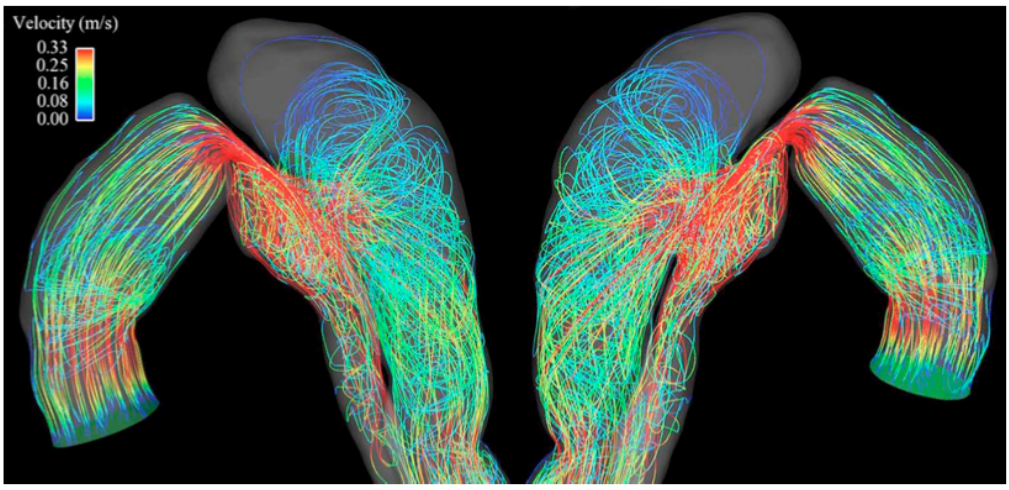

Figure 3.10: Particle paths of blood flow in the aortic dissection model (image from Cheng et al. 2010).

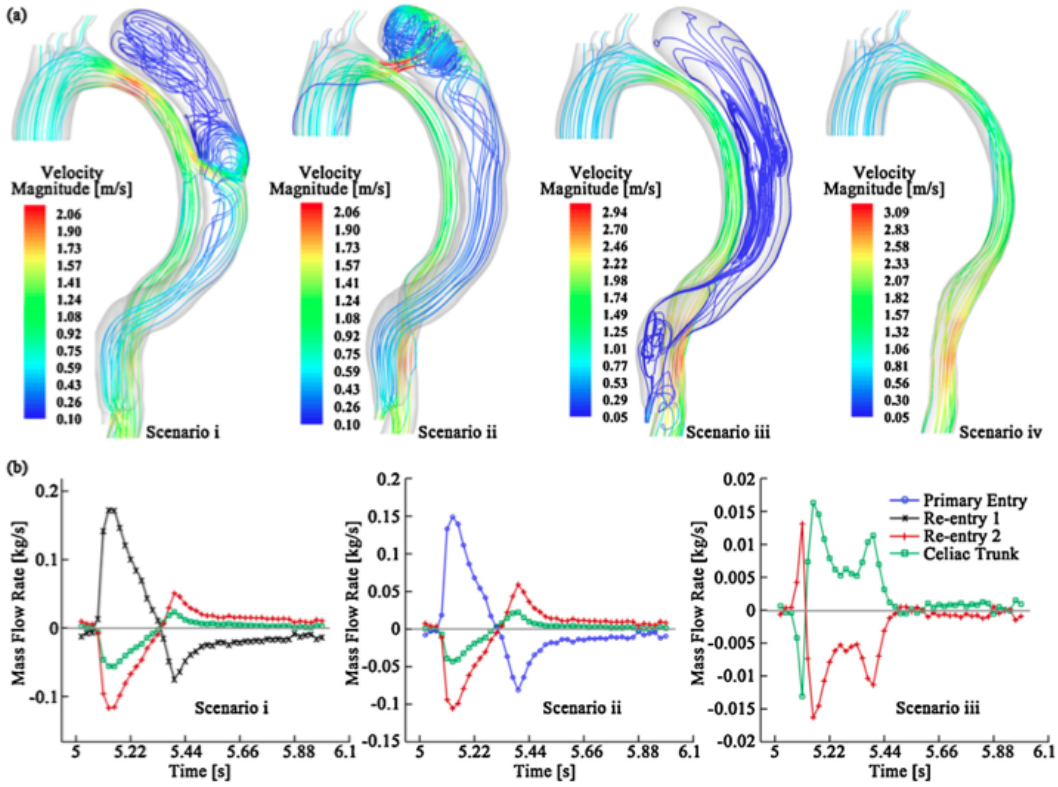

Figure 3.11: Changes in flow patterns corresponding to occlusions of different entries. (a) Flow patterns at systolic peak in 4 occlusion scenarios, which virtually close (i) the primary entry, (ii) re-entry 1, (iii) both the primary entry and re-entry 1 and (iv) all the tears along the flap; (b) diagrams of inter-luminal blood communication showing that the flow into the false lumen was best reduced by scenario iii, which sealed both the primary tear and the first re-entry (image from Chen et al. 2013a).

On the other hand, at diastole only around 5% of the flow entered through the primary tear. During one cardiac cycle, flow rates of the primary entry, two re-entries and the outlet of celiac trunk were 7.55%, 6.59%, -8.79% and 5.35% of the overall inlet inflow. The authors conclude that "the dissection not only diverts blood, it also largely disturbs the flow, inducing very high velocities near the entries and possibly turbulent flow patterns within the lumens, which reduces the available head for perfusion of the downstream organs."

Finally, some studies have analysed alterations in flow patterns when certain entries of the dissected aorta are occluded. These studies provide an initial understanding of blood flow and pressure changes in an aortic dissection as a preliminary preparation for aortic repair. For example, Karmonik et al. (2011) reported that the

pressure in the false lumen drops when the tear entrance is occluded. Performing similar analysis, Chen et al. (2013a) suggested that in cases of multiple dissection entries, stent grafts that cover all tear entries offer the most effective reduction in inter-luminal blood communication and thus can best promote thrombus formation in the false lumen (see Figure 3.11).

Computational studies specifically relevant to this project are those investigating alterations in haemodynamics due to the presence of the stent. With respect to intracranial stenting, the recent series of studies by Cebral and Lohner (2005) and Appanaboyina et al. (2009) presented an extensive methodology for simulating post-procedural vessels haemodynamics, which includes virtual stenting as well as CFD. After the virtual stenting procedure, the authors observed changes in flow patterns inside the aneurysmal sac due to the stent placement. Namely, prior to stent placement, the flow was entering the aneurysmal sac at the distal part of the neck and rotating inside in the clockwise direction. After the deployment procedure, the flow entered at the proximal end of the neck and was rotating in the counter-clockwise direction, which was in line with previous observations in phantom experiments. However, their stent deployment method is the one proposed by Appanaboyina et al. (2008), which was described in the previous section. Since the method is based on the deformation of a cylinder, on the surface of which stent design features are subsequently drawn, it by no means guarantees realistic configurations of a deployed device. Nor can it account for potential alterations of the vessel geometry, since vessel walls were assumed rigid. However, even though stent configurations were simplified, the study demonstrated that covering the neck of an aneurysm with a mesh reduces the inflow into the aneurysmal sac and changes the flow patterns, which is an important computational confirmation of the capability of the stenting procedure to reduce flow.

From the same group, there has been a slightly controversial publication that appeared in the American Journal of Neuroradiology in 2011. Cebral et al. (2011) performed a CFD analysis of 7 pre- and post-stented vessels treated with PED flow diverter. The data included 3 cases with post-procedural rupture and 4 successfully treated aneurysms, in order to compare haemodynamic indices and quantify the effects of flow diverter deployment. Based on their analysis, the authors reported that although reduction in aneurysm velocity was achieved, demonstrating the effectiveness of the stent in preventing most of the blood from entering the aneurys-

mal sac, the treatment also induced an increase in pressure inside the aneurysm (> 20 mmHg) in subsequently ruptured cases. In contrast, those aneurysms that did not rupture after flow diverter placement did not exhibit such dramatic pressure rises (< 3 mmHg). The pressure increase was supposed to be related to (1) alterations in geometry of the parent artery, such as reduction of a proximal stenosis, and (2) to "the flow diversion into higher resistance parent artery pathways combined with cerebral autoregulation, leading to higher pressure gradients." The authors concluded that placement of flow diverters may lead to the increase in pressure inside the aneurysm, followed by a post-treatment rupture, especially in cases of giant aneurysms.

However, this study was heavily criticised by Fiorella et al. (2011). The concerns were mainly attributed to the apparent overestimation of the physiologic pressure gradients, that were an order of magnitude higher than reported in previous *in vivo* and *ex vivo* experiments. The overestimation could occur due to a number of reasons such as assumed flow rates, the rigid wall assumption or the CFD solver. In their response, Cebral et al. argued that their CFD solver had been validated against in vitro measurements and that, although flow rates were assumed and not patient-specific, they were plausible. The controversy led to a CFD Challenge conducted with the aim of assessing the variability of solutions provided by 25 different CFD groups (Steinman et al., 2013). The results of the challenge demonstrated a remarkable consistency in the pressure drop predictions across a wide variety of CFD solvers and solution strategies. However, flow patterns within the aneurysmal sac were found to display higher variability and the solution was very sensitive to assumptions about the flow rate.

Another study combining virtual stenting and CFD was that of Bernardini et al. (2011). The authors tested models of a self-expanding Neuroform stent (Boston Scientific, Natick, MA, USA) deployed inside idealised aneurysmatic cerebral vessels. After performing virtual deployment with a fast virtual stenting method, a FE method and subsequent CFD analysis, the results predicted a reduction of WSS and velocity (by almost 50%) after stent placement, showing the usefulness of the device. However, the fast stenting algorithm the study used was that proposed by Larrabide et al. (2010) and reported in the previous section, which was developed only for cerebral vasculature and under the rigid wall assumption. When compared with the stent released shape obtained by a FE method with a flexible vessel, there

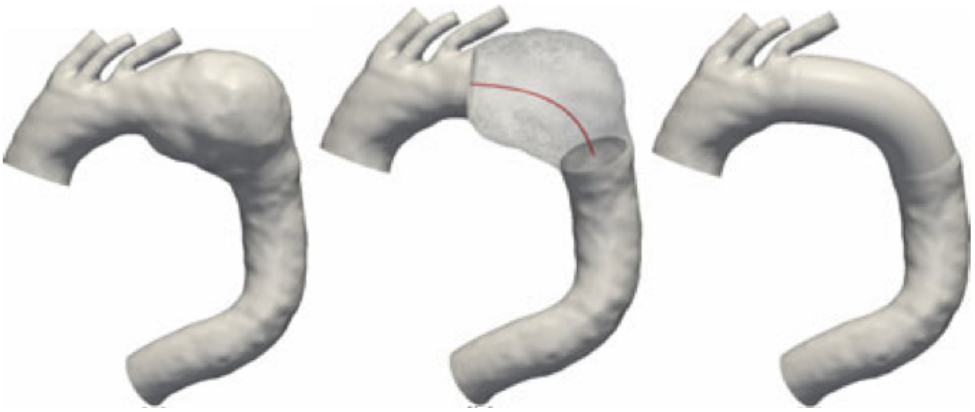

(a) (b) (c)

Figure 3.12: Reconstruction of an aortic geometry with TAA after stent grafting. (a) Initial vessel geometry, (b) removal of the aneurysm, (c) geometry after stent grafting (image from Xiong and Taylor 2010).

were noticeable discrepancies in released configurations of the device and the vessel, especially, the longitudinal straightening of the vessel in the stented part, as the authors reported. These geometrical differences led to discrepances in haemodynamic variables inside the aneurysmal sac, showing the importance of taking vessel distensibility into account.

With respect to stenting of AAAs, TAAs and aortic dissections, there have been studies investigating haemodynamic changes induced by the procedure, however, with an inadequate stent deployment part. Namely, these studies mainly focused on the CFD part and either simply occluded the tear entries in cases of dissected aorta (Karmonik et al., 2011; Chen et al., 2013a) or modelled the stent expansion in an *ad hoc* way. For example, Xiong and Taylor (2010); Xiong et al. (2012) conducted a series of studies of post-procedural vessel haemodynamics for different aortic pathologies. To reconstruct the vessel geometry after stent grafting, the authors used a purely geometrical approach, whereby the pathological vessel segment was clipped and substituted with a surface of a virtual stent graft, aligned with the centerline of the removed part. Afterwards, the mapping of a 2-D strut pattern on the stent graft surface was performed (see Figure 3.12). This deployment method does not simulate the deployment process and does not account for mechanical interaction between the stent and the vessel, leading to implausible geometries upon which the CFD analysis is based. An interesting result of the study, however, was the

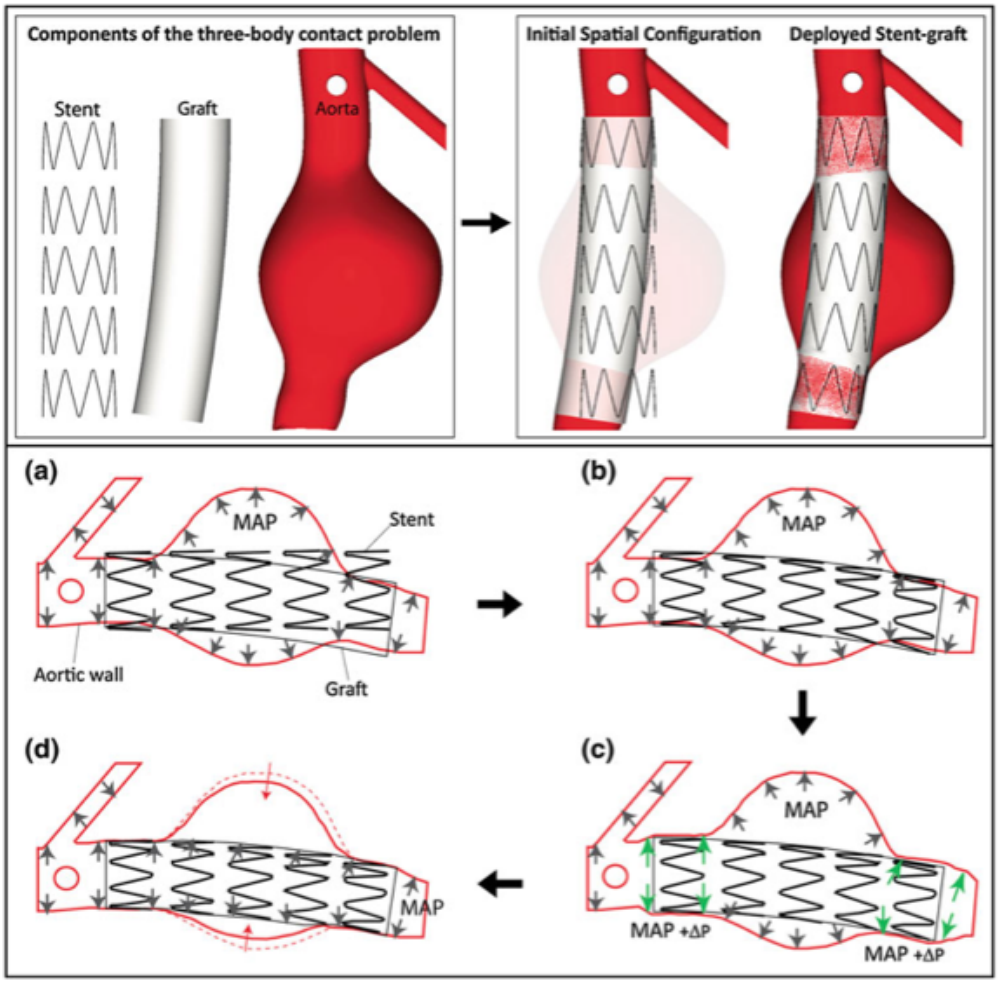

Figure 3.13: Deployment of the stent graft within the aorta. (a) Initial configuration of aorta, unloaded stent and bent graft following the main curvature of the vessel, no contact is activated. (b) The stent is crimped, bent and expanded until contact between the inner surface of the graft and the outer surface of the stent is established. (c) The proximal and distal landing zones of the vessel are expanded via an incremental pressure to make room for the stent graft. (d) The incremental pressure is released and contact between the aortic wall and stent-graft is established (image from Prasad et al. 2013).

investigation of the impact of the stent struts on the haemodynamic indices. Their results indicate that the "strut patterns do not have a significant impact on the magnitudes of the forces as their contributions to the surface integration are minimal." However, the struts influenced the local shear stress in the vicinity.

Another recent study by Prasad et al. (2013) investigated positional stability of

aortic endografts. In the performed experiments, the authors varied sizes of devices and aortic geometries, investigating the implications of fixation length, aortic curvature, friction coefficients and oversizing on device stability. However, stent graft deployment was implemented by means of contact between the inner surface of the graft and the outer surface of stent (see Figure 3.13, b) and did not represent a realistic process. Given the results, the authors concluded that unfavorable neck anatomy is responsible for poor contact at the fixation zone, which is therefore linked to unfavorable outcomes. Furthermore, their analysis demonstrated that a higher coefficient of friction leads to better positional stability. Finally, they showed that increasing device oversizing improves contact but may increase the level of circumferential stresses in the aortic neck to a point that may trigger neck dilation.

Finally, a CFD study by Figueroa et al. (2009) investigated the implications of vessel curvature on displacement forces acting on a stent graft. Here again, the stent graft was not deployed, but geometrically implanted and then manipulated in order to investigate the implications on acting forces.

3.3 CONCLUDING REMARKS

This chapter gave an overview of existing approaches to modelling virtual stent deployment in arteries. The reported previous attempts to simulate the deployment process feature considerable limitations when judged upon their suitability for preoperative rehearsals.

The discussed FEA methods are overly slow to constitute a base for a clinical tool, taking from several days to several hours to run, depending on the complexity of the model. Hence, they are not suitable for the purpose of this project. However, FEA is considered to be the “gold standard” in the field, offering accurate results and reliable measurements. Therefore, it could be used as a benchmark for comparison to assess the accuracy of the envisioned novel fast deployment method.

The reported rapid stenting methods operate under the assumption of rigid vessel wall. Even though the assumption may be justified in cases of intracranial stenting, it eliminates the very possibility of obtaining crucial information that is absent in medical imaging data and investigating the potential dangers of the stent placement procedure. Hence, incorporating flexible vasculature into the envisioned stent deployment model would provide an important contribution to the field.

In the published literature, the studies usually focus on either the virtual stent placement or the haemodynamics of the vessels, but the two methods are rarely coupled in a clinically suitable assembly. The mentioned study of Larrabide et al. (2010) is an exception. However, their approach is limited to only cerebral cases and does not account for vessel deformation. Hence, coupling virtual stenting with a subsequent CFD analysis would provide a possibility to conduct a complete *in silico* investigations before performing vascular interventions *in vivo*, especially in the abdominal area. In particular, incorporating vessel deformation would enable detection of cases where stents would cause dangerous deformation in the vessel geometry and preventing these scenarios from being pursued.

The next chapter describes the methodology adopted and developed in this project for modelling virtual stent deployment.

CHAPTER 4

VIRTUAL STENT DEPLOYMENT: METHODOLOGY

This chapter presents the methodology that was used to develop the novel fast stent deployment method. The chapter starts by describing different stages involved in modelling virtual stent deployment and how they were addressed in the present work. The weighting of the different sections reflects the importance to the present project and the amount of contribution offered by the thesis. Hence, the core of the chapter is dedicated to methods that were developed for pre-processing of vascular devices and for modelling their expansion mechanics. In particular, the chapter focuses in detail on the stent expansion process and develops expansion algorithms based on three different spring analogy techniques. Further, methods handling the vessel are described, from geometry reconstruction to modelling its contact with the stent. Finally, the chapter outlines some of the established methods that were used as a base for computational experiments presented in the coming chapters.

This chapter describes the methodology that was used to develop the novel fast virtual stent deployment method. The aim of the novel deployment method was to target interventions performed under radiological guidance both in the aortic and intracranial areas. Hence, the methodology had to be general enough to be able to include a broad range of devices, such as stent grafts and flow diverters. With this in mind, the computational techniques presented here are both sufficiently generic and computationally inexpensive.

The envisioned stent deployment system would become part of the clinical routine and serve as a decision support system. The architecture of the system is schematically represented in Figure 4.1. It consists of multiple components, some

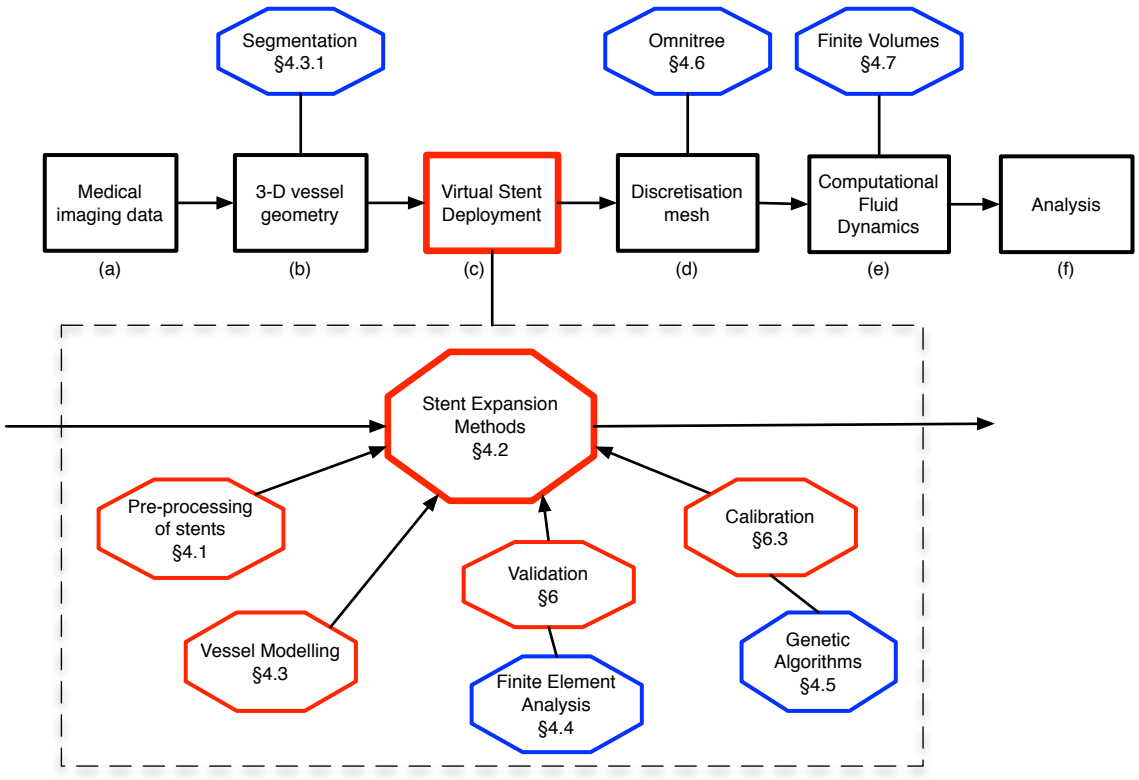

Figure 4.1: Integration of the envisioned Virtual Deployment system into clinical workflow: from obtaining clinical imaging data to analysis of haemodynamics in vessels after the stent deployment procedure. The dashed box illustrates the internal architecture of the Virtual Deployment system, showing in red methods developed in this thesis and in blue established methods that were utilised at a particular stage of development.

of which rely on already established methods (depicted as blue blocks), others are novel and will be developed in the coming sections and chapters (red blocks). The workflow starts with obtaining medical imaging data (box a) and transforming them into the 3-D geometrical vessel models (b) in the process of segmentation. The created 3-D vessel geometry constitutes the input into the Virtual Stent Deployment system (c), the development of which forms the core of this thesis. Its internal structure is shown within the dashed box in the image and features many components, such as modules for pre-processing of stents, vessel modelling, etc. The output of the virtual deployment process constitutes as the 3-D shape of the expanded device and the vessel. From these data, a discretisation mesh for subsequent haemodynamic analysis is constructed (d). The results of the CFD (e) are analysed to aid clinical decision (f).

The presented workflow diagram shapes the structure of this chapter, with the blue and red diagram blocks forming the coming sections and subsections. The weightings of the different sections reflect the importance to the present project and the amount of contribution offered by the thesis. Hence, the core of the chapter is dedicated to methods for pre-processing of vascular devices (diagram block **Pre-processing of stents**, described in Section 4.1) and modelling their expansion mechanics (**Stent Expansion Methods**, described in Section 4.2). Three different expansion methods are presented with the underlying theory and application to the stent deployment algorithms. Further, methods handling the vessel are reported, from geometry reconstruction (**Segmentation**, Section 4.3.1) to modelling its contact with the stent (**Vessel Modelling**, Section 4.3). Additionally, the chapter briefly outlines the two established methods of Finite Element Analysis (Section 4.4) and Genetic Algorithms (Section 4.5) that will be employed in the coming Chapter 6 for the validation of the developed novel fast stent deployment method. Finally, methods for computational grid generation (**Omnitree**, Sections 4.6) used for the subsequent haemodynamic analysis (**Finite Volumes**, Section 4.7) are briefly described.

4.1 Pre-processing of Stents

This section outlines the initial steps required to create a model of the stent and prepare it for the expansion process. I will briefly describe the reconstruction of the stent geometry, computation of the local coordinate system, computation of the crimped configuration and the initial positioning of the device inside the target vessel.

4.1.1 Geometry reconstruction

The data on commercial stents is usually not available and getting the information from manufacturers often proves difficult, given the IP issues involved. The most straightforward way to reconstruct the geometry of the device is to draw the stent manually with the help of a CAD software; however, this procedure can be extremely tedious and thus impractical. One possible solution to avoid the manual process is to reconstruct the stent design from an X-ray computed tomography

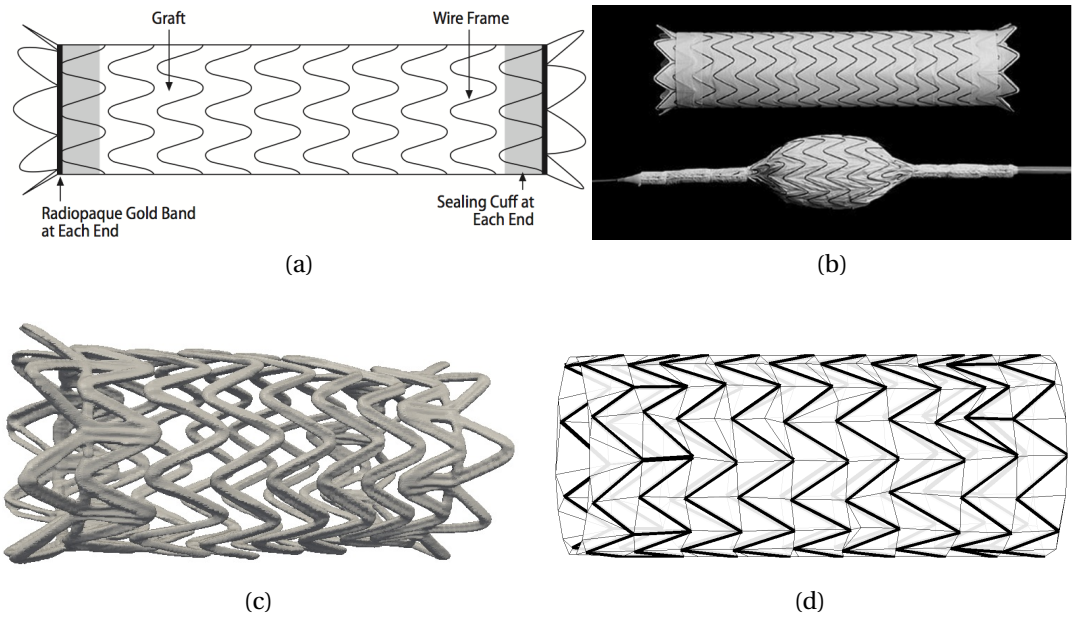

Figure 4.2: (a) Schematic representation of a stent graft, consisting of an external nitinol wire supporting structure that is attached circumferentially along the surface (image from `www.goremedical.com`). (b) Gore TAG thoracic endoprosthesis in the load-free and partially expanded configurations (image from Wheatley et al. 2006). (c) 3-D reconstruction of the scanned stent graft with dimensions 40 mm×10 cm. (d) Computational representation of the stent graft.

(CT)[1] scan, saved as an STL file[2]. This method is especially suitable for devices with high-porosity[3] wiring and low pore density[4], such as aortic stent grafts.

Stent graft reconstruction. The creation of the computational representation of stent devices is demonstrated on the example of the Gore TAG Thoracic Endoprosthesis (model TGT4010) which can be seen as a typical representative of an aortic stent graft (see Figure 4.2, b). The endoprosthesis is comprised of an external self-expanding nitinol wire structure (stent struts) that is attached circumferentially along the entire surface of the graft, as schematically illustrated in Figure 4.2, a). The

[1] "X-ray computed tomography (CT) is an imaging method in which a cross-sectional image of the structures in a body plane is reconstructed by a computer program from the x-ray absorption of beams projected through the body in the image plane (Med, 2007)."

[2] An STL (STereoLithography) file represents an unstructured triangulated surface of an object, describing each triangle with coordinates of its vertices (ordered by the right-hand rule) and the normal of the triangle in a three-dimensional Cartesian coordinate system.

[3] Porosity is defined as the ratio of the metal-free surface of a device to the total surface area.

[4] Pore density is defined as the number of pores per unit surface area.

device is 40 mm in diameter and 10 cm in length.

In case CAD design files of a stent geometry were available, no scanning of the device was required and the process was reduced to the creation of a 3-D geometry from the available surface mapping. For example, CAD design files constitute input into a stent cutting machine and are usually two-dimensional. They were simply wrapped around a cylinder to obtain a 3-D representation by assigning the x-coordinate to be the circumferential position around a cylinder of a given stent radius.

In cases the CAD files were unavailable, the design of the device was reconstructed from an X-ray computed tomography scan of the device with the spatial resolution of around 150 μm (see Figure 4.2, c). With respect to the strut wires, they were approximated by their centerlines, i.e., they were initially modelled without an explicit thickness to enable fast deployment. After the centerline representation of the stent struts has been obtained, it was supplemented with a background mesh, that emulates the device sheath and prevents an excessive expansion and distortion of the stent during the simulated deployment.

The merging of the two meshes – stent struts and background mesh – could be achieved in two ways: using an isotropic triangulation in which the stent geometry has been given a "best-fit" representation within the background mesh, or creating an anisotropic mesh using triangulation constraints, i.e., requiring mesh elements to incorporate the stent struts. Figure 4.2 (d) depicts the final computational model of the stent graft geometry.

Flow diverter reconstruction. Due to the low porosity, high pore density and regular struts architecture, the easiest way to model a typical flow diverter (FD), or devices of a similar design, was to use CAD software to replicate the design of the device. After a 2-D representation has been created with CAD, the sheet was wrapped around a cylinder to get a 3-D structure. Figure 4.3 shows an example geometry for the commercially available Pipeline Embolization Device (PED, Covidien, Irvine, California). At the moment, PED is the only FD device that has been approved by the FDA. It is a self-expanding device with braided structure, mainly composed of Cobalt-Chromium-Nickel (Co-Cr-Ni) alloy strands. Since the device does not have a sheath, there was no need for an additional background mesh. However, each rhomboid of the stent struts was additionally subdivided into two triangles, by means of adding

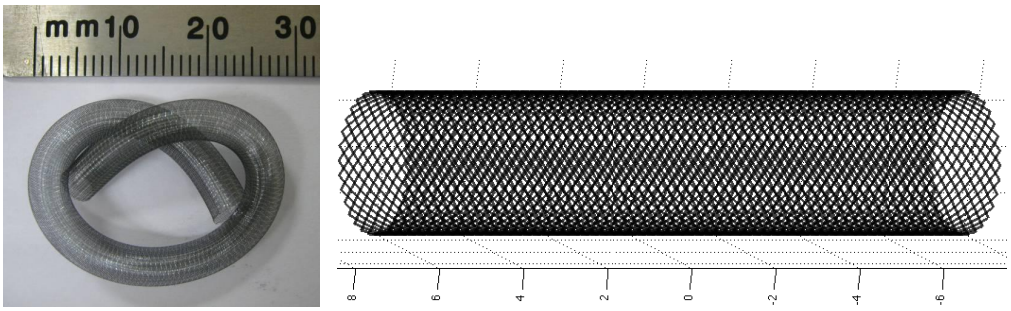

(a) (b)

Figure 4.3: (a) Pipeline Embolization Device (PED, ev3, Irvine, California) (image from Pierot 2011). (b) Reconstructed 3-D struts mesh representing the PED flow diverter with the diameter of 3 mm and the length of 14 mm.

one horizontal background spring to ensure adequate triangulation.

Data structures. The information about the stent devices was stored as a data structure[5] with multiple parameters, the most important of which are the following

- matrix $\boldsymbol{V}$ of coordinates of stent vertices, with the dimension $n \times 3$; each row has the form $\boldsymbol{v}_i = (x_i, y_i, z_i)$ for a vertex i, where i is a global index of the vertex running for $i = 1...N$ and N is a total number of nodes;
- stent struts table that stores pairs of nodes making up stent struts in the form $[v_i, v_j]$;
- background mesh table that stores triples of nodes making up the background mesh in the form $[v_i, v_j, v_k]$.

From the above information more parameters were computed and stored in the stent structure in order to be quickly accessed during the simulation process. For example, another very useful parameter was the connectivity table that was computed from struts pairs or background triples. The background connectivity table $Conn$ was listing for each vertex its direct neighbours in the mesh in the form $i : [n_k, n_l, ..., n_m]$. The connectivity table was computed for both stent struts' nodes and background nodes. To note is that the vertices belonging to the stent struts constitute a subset of the background vertices. More details on stent parameters will be

[5]The stent data structure was implemented as a class with properties that store particular pieces of information and methods that allow calculation and manipulation of the device structure.

provided in the coming sections, for instance, stiffness of struts or geometrical features like diameter and length.

4.1.2 Local coordinates

For later manipulations of stent geometry, such as the calculation of the crimped and expanded configuration, it was convenient to establish a local coordinate system for the device in order to decouple the mechanical component of computations from the stent positioning in the global coordinate system. The local coordinates were set along the principal axes of the stent that also correspond to the principal components of the stent nodes' data, i.e., dimensions of the largest possible variance in the data. For example, for an elongated tubular structure, like a stent, the dimension with the largest variance is its longitudinal direction (see Figure 4.4).

The principal components of the data were determined with a common mathematical technique called Principal Component Analysis (PCA). PCA is an orthogonal linear transformation that can establish new basis vectors for the data in a way that the first coordinate, or the first principal component, bears the greatest variance

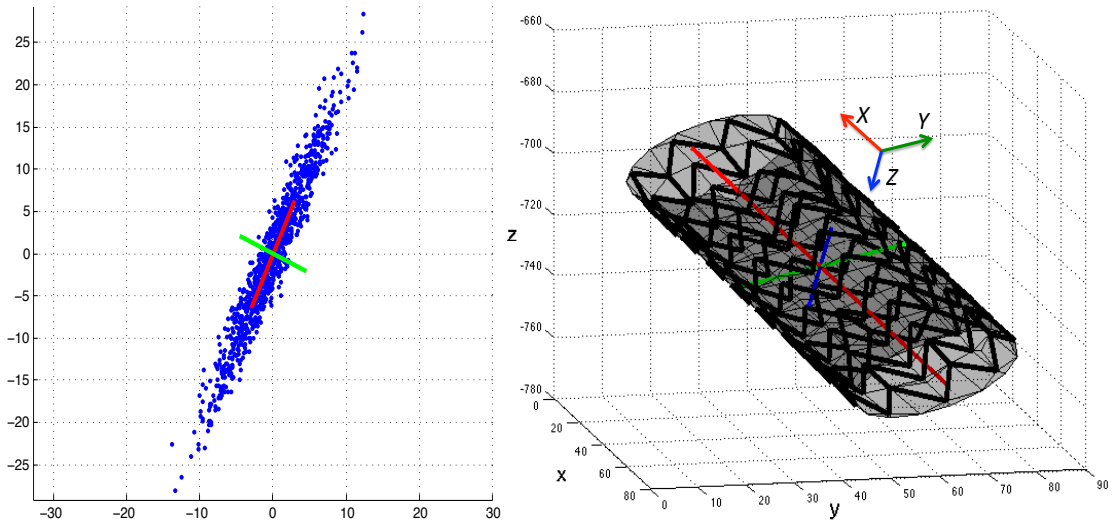

(a) (b)

Figure 4.4: (a) Two principal components (red and green lines) of the data (blue points). (b) PCA on stent vertices with the 1st, 2nd, 3rd components in red, green and blue, respectively, which are set to build the stent's local coordinate system indicated by the capital *X, Y, Z* (global axes are indicated by the small x, y, z).

in the data. The second principal component is orthogonal to the first and corresponds to the dimension of the second greatest variance and so on. Mathematically, the transformation is carried out by finding the eigenvalues and eigenvectors of the symmetric covariance matrix **C** defined as the following, for the case of n points $v_i = (x_i, y_i, z_i), i = 1...N$:

$$\mathbf{C} = \begin{pmatrix} \mathbf{C}_{xx} & \mathbf{C}_{xy} & \mathbf{C}_{xz} \\ \mathbf{C}_{yx} & \mathbf{C}_{yy} & \mathbf{C}_{yz} \\ \mathbf{C}_{zx} & \mathbf{C}_{zy} & \mathbf{C}_{zz} \end{pmatrix}, \tag{4.1}$$

where $\mathbf{C}_{xy}$ represent covariances between the components x_i and y_i defined as

$$\mathbf{C}_{xy} = \frac{1}{N}\sum_{i=1}^{n}(x_i - \mu_x)(y_i - \mu_y), \tag{4.2}$$

and where μ_x stands for the mean of x: $\mu_x = \frac{1}{N}\sum_{i=1}^{N} x_i$.

Finding the eigenvalues ($\boldsymbol{\lambda}$) and the corresponding eigenvectors of the matrix **C** can be achieved by solving the following characteristic equation for $\boldsymbol{\lambda}$:

$$\det(\mathbf{C} - \boldsymbol{\lambda}\mathbf{I}) = 0, \tag{4.3}$$

where **I** is the identity matrix and det stands for the determinant. Having solved the equation, an orthogonal basis can be formed by placing the eigenvectors in descending order with respect to eigenvalues (largest first), where the first eigenvector captures the dimension of the largest data spread, i.e., the largest variance of the points from the mean value.

Matlab offers a predefined function `princomp(X)` to perform the PCA analysis on data `X`. It is used for the stent in the following way, whereby the data consist of the stent vertices:

```
[coeff, score] = princomp(stentVertices);
```

where `coeff` returns the principal component (PC) coefficients, i.e., the vectors of the new coordinate system, and `score` gives the coordinates of each point of `X` in the new basis. In order to get the coordinates in the global system, one has to multiply the coordinates in the new basis (`score`) by the PC coefficients (`coeff`) and add back the mean of the data:

```
global = repmat(meanX, n, 1) + score * coeff';
```

As the above transformation shows, PC coefficients can also be seen as a rotation matrix (`coeff'`) that has to be multiplied with the local or undisplaced configuration (`score`) to obtain the rotated (here global) configuration (symbol ' indicates the transpose of a matrix).

After the PCA has been performed on the stent vertices, the first component gives the centerline of the stent, whereas the second two lie in its circumferential plane (see Figure 4.4, b). The information obtained with PCA was also used to obtain stent dimensions such as length and radius; namely, the length was determined as the range of values in the first PC dimension, while the radius as the distance of a vertex to its projection onto a centerline.

4.1.3 Crimped configuration

During the minimally invasive stent deployment, the vascular prosthesis is firstly crimped and placed into a delivery system. Upon release in a target vessel location, it "springs" back to a load-free configuration under the elastic forces of the material. The most widely used material for self-expanding devices is nitinol (nickel-titanium alloy), which is a superelastic material that features the elastic response to small deformations of up to 10% due to its shape-memory effect (Stoeckel et al., 2002).

Thus, we have to start the deployment simulation with the crimping of the device. In order to compute the crimped configuration, an automatic procedure has been developed, which determines the displacements of the folded stent nodes with respect to the load-free configuration. All calculations were performed in the local coordinate system of the stent, and the crimping was carried out around the z-axis which was aligned with the centerline of the device.

The crimping algorithm consisted of two steps: (1) calculation of preliminary node coordinates of the crimped stent and (2) their correction to retain the length of the struts unchanged. Assuming that the stent nodes are arranged circumferentially on a circle around the centerline of the stent, the first step made use of the following parametric circle definition:

$$\begin{aligned} x &= a + r \cdot cos(t) \\ y &= b + r \cdot sin(t) \end{aligned}$$

where the parameter t ranges between 0 and 2π and geometrically represents the angle that the ray from (a,b) to (x,y) formes with the x-axis. Using this equation,

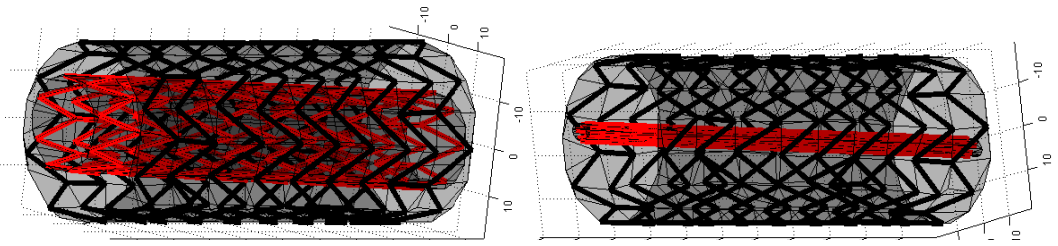

(a) (b)

Figure 4.5: Crimping of the stent graft (black) with the dimensions 40 mm × 10 cm to (a) 50% and (b) 10% of its initial radius (red).

each stent node was parametrised, i.e., the parameter t was obtained, knowing the nodal coordinates (x, y), the stent initial radius (r) and the location of the center (a, b). Having found t, the new (x_c, y_c) coordinates of the crimped device were calculated by deciding on the radius of the crimped configuration. The z-coordinate was initially assigned unchanged, which resulted in a distortion of the struts' length.

When crimping the stent, it was important to retain the length of the struts unchanged since for a typical ring stent, most of the crimping effect results from decrease in the angles between the struts. The correction of the struts' lengths was performed in two phases: first, the whole crimped stent was scaled along the z-axis by stretching because all struts became shorter after the preliminary crimping step. Choosing the scaling constant as $0.2 \cdot (1 - crimpingPercent)$ yielded the best performance. Thereafter, the node coordinates were explicitly recalculated for each pair of nodes building a strut, so that the resulting length equals the initial value. This step was performed in the iterative manner, where the newly calculated node coordinate was only partially assigned as a weighted sum of the old and the new value. Iterating helped to avoid a potential elimination of the correction if the node happened to be chosen for a correction in another strut, since nodes belong to multiple struts. The iteration terminated when the desired precision was achieved. The example crimping of the stent graft is shown in Figure 4.5 and the pseudocode of the two steps of the crimping procedure is summarised below.

1. Compute center coordinates (a, b) in the xy-plane, stent radius r and stent crimped radius $r_c = crimpingPercent \cdot r$

2. For each stent node $n = (x, y, z)$ do
   - calculate parameter t = arctan($\frac{y-b}{x-a}$) ;
   - compute preliminary coordinates of crimped stent (x_c, y_c, z_c) as $x_c = a + r_c \cdot cos(t); \quad y_c = b + r_c \cdot sin(t); \quad z_c = z$

Correction of the struts' length:

3. Scale the stent along the z-axis: $z_c = (1 + 0.2 \cdot (1 - crimpingPercent))) \cdot z$
4. For each strut pair (n_i, n_j) with the initial length l do:
   - Find the upper node in the pair by comparing the z-coordinates
   - Correct the upper node n_i by computing its new z-coordinate as $z_{i_c} = \sqrt{(l^2 - (x_{i_c} - x_{j_c})^2 - (y_{i_c} - y_{j_c})^2)} + z_{j_c}$

The fact worth mentioning is that the struts' length correction also resulted in the foreshortening effect, whereby the stent becomes longer when crimped and shorter when deployed, which is observed in real stents, especially in case of flow diverters.

4.1.4 Initial positioning

After the stent has been crimped, which simulates its folding and placement in a catheter, the next step in the minimally invasive procedure is the positioning of the catheter in a desired location of the vessel with the help of a guidewire. Both the guidewire and the catheter are flexible enough to be able to follow the curvature of the vessel they are being pushed through. Once the target destination is reached, such as a neck of an aneurysm or the initial tear in the case of an aortic dissection, the catheter is being pulled out to release the stent which starts expanding under the elastic forces of nitinol it is made of.

In order to simulate the initial placement of the device before its release out of the catheter, an automated positioning method has been developed. This method

deforms the crimped device in a way to let it follow the curvature of the vessel centerline. The alignment with the centerline was implemented in two steps: (1) first, all vertices of the stent were divided into layers depending on their longitudinal position in the stent local coordinates; (2) afterwards, each layer of the stent was deformed according to the curvature of the vessel centerline, i.e., according to the deviation of the corresponding vessel centerline point from the straight line, starting at the centerline node corresponding to the distal landing zone. Below is the detailed pseudocode of an algorithm which computes the coordinates of the deformed configuration of the stent aligned with the vessel centerline (`deformedVertexGlob`).

1. **Calculate the stent layers' matrix** which stores indices of all vertices lying in each of the corresponding layers, depending on their longitudinal position (`stentLayersMatrix`). The distance between the layers in the stent longitudinal direction is set depending on the stent design. For regular wiring, for instance, it is set to be the longitudinal distance between two vertices of any chosen strut pair.

2. **Determine the necessary centerline points**: calculate the location and length of the centerline segment needed to accommodate the crimped device and identify the corresponding centerline points. If the centerline vector does not have a sufficient resolution in a needed segment (to allocate a point for each of the stents layers), interpolate the given curve nodes to obtain the number of points corresponding to stent layers.

3. **Deform according to the curvature of the centerline**:
   For each `layer` from distal to proximal do

   - get indices of the stent nodes (`layerInd`) that belong to the current `layer` from the stent layers' matrix (`stentLayersMatrix`)
     `layerInd=stentLayersMatrix(layer)`
   - calculate the rotation matrix `R` that represents the rotation of the relevant centerline segment. The segment can be chosen to lie between the centerline points that correspond to the previous and the current stent layer. Then, the rotation matrix `R` can be determined by cal-

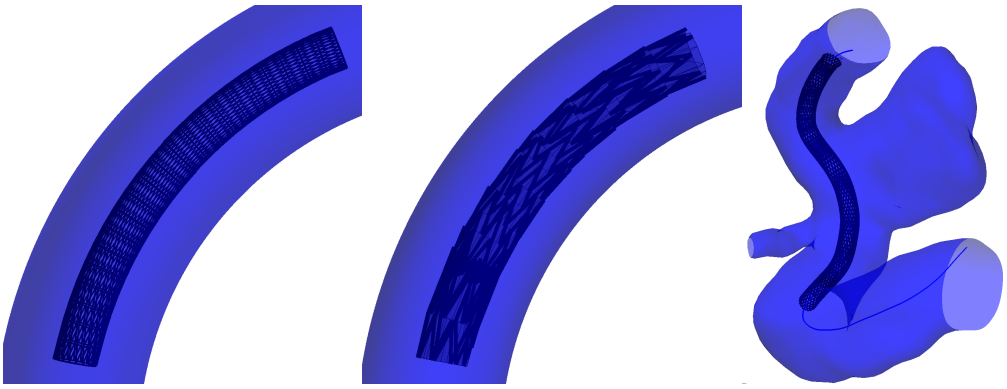

(a) (b) (c)

Figure 4.6: The initial positioning of the crimped stent along the centerline of the vessel. (a) 30%-crimped generic stent; (b) 30%-crimped Gore Tag stent graft; (c) 20%-crimped PED flow diverter in a patient-specific geometry.

culating the principal components of the corresponding centerline points (`curvepoints`):

```
R = princomp(curvepoints)
```

- place the current stent layer (all vertices with indices `layerInd`) in the center of the egocentric coordinate system by subtracting its mean:

```
shiftedVertexEgo=vertexEgo(layerInd)-
                 mean(vertexEgo(layerInd))
```

- deform all nodes of the current layer according to the deformation of the centerline segment, i.e., rotate the (shifted) egocentric coordinates with the rotation matrix `R`. Then, the obtained configuration has to be placed back onto the centerline in order to obtain the final global coordinates, i.e., it has to be translated with the mean of the corresponding centerline points (`curvepoints`):

```
deformedVertexGlob(layerInd)=shiftedVertexEgo*R+
                             mean(curvepoints)
```

The results of the algorithm are shown in Figure 4.6 which illustrates the place-

ment of three different crimped stents along the centerline of the vessel. After the deformation, the length of the struts contains a small error. This error was corrected in a similar way as it has been done after the crimping procedure reported in the previous section.

4.2 MODELLING STENT EXPANSION

In a process of computational modelling, one inevitably faces a tradeoff between the accuracy of computations and their speed. Some methods can offer visually appealing results in a very fast time frame but do not represent physically realistic mechanisms. On the other hand, there are very accurate methods that capture physical processes but are very time-consuming, as has been discussed in Chapter 3. Additionally, since we are interested in interventions performed under radiological guidance in both the abdominal and intracranial areas, the stenting method should be general enough to include a broad range of devices, such as stent grafts and flow diverters. This requirement narrowed down the investigated computational techniques to those that are both sufficiently generic and computationally inexpensive.

This section explores different computational methods in order to determine the most suitable approach for modelling the process of stent expansion. First, I briefly describe the overall theoretical framework of the *dynamic mesh* approaches and then zoom into the details of three exemplar methods. After outlining the theory behind each of the investigated methods, I show how to apply them to the stent expansion problem. The three versions employed are the lineal spring analogy, the semi-torsional spring analogy and the torsional spring analogy. All three versions are approximative methods; however, they feature increasing complexity and precision of iterative equations. The ultimate goal of the coming two chapters is to investigate their suitability for modeling the stent expansion process and finding out whether the more computationally intensive version is justified by a concomitant increase in precision.

4.2.0.1 Theoretical framework

The methods under investigation fall within the category of *dynamic meshes*, which were originally employed in the field of computational aerodynamics. Dynamic meshes were proposed as a means of dealing with the *moving boundary problems*

– the class of problems that involve the deformation of the computational domain during the course of the simulation. They arise, for example, in fluid-structure interaction, like modelling of the pulsatile blood flow in arteries undergoing systemic deformations. One solution for coping with mesh deformation is to perform remeshing of the domain during the simulation after the deformation has occurred. Another approach is to fix the quality of the existing mesh that has been deformed, which is a preferable option for those computational problems where the movement of the mesh structure itself is unknown and has to be found in the solution (Moyle and Ventikos, 2008).

To handle a dynamic mesh, it is often viewed as a continuous or discrete system with fictitious mass, damping and stiffness properties (Farhat et al., 1998). The movement of such a system obeys the equation of dynamic equilibrium:

$$\mathbf{M}\ddot{\mathbf{q}} + \mathbf{D}\dot{\mathbf{q}} + \mathbf{K}\mathbf{q} = 0, \tag{4.4}$$

where $\mathbf{M}, \mathbf{D}$ and $\mathbf{K}$ are the system's fictitious mass, damping and stiffness matrices, respectively; $\dot{\mathbf{q}}$ is a time-derivative of the displacement vector $\mathbf{q}$:

$$\mathbf{q}(t) = \xi(t) - \xi(0), \tag{4.5}$$

where t represents the time and ξ is the vector of nodal coordinates (Farhat et al., 1998).

The equation of dynamic equilibrium (Equation 4.4) is often accompanied by the displacement boundary condition

$$\mathbf{q}(t) = \bar{\mathbf{q}}(t) \tag{4.6}$$

on Γ_m, where $\bar{\mathbf{q}}(t)$ indicates the known displacement vector of the moving boundary Γ_m. Usually, the grid points originally located on the moving boundary Γ_m stay attached to this boundary at the same relative locations, and the new positions of the nodes inside the mesh are determined through the integration of Equation (4.4) with the boundary condition (Equation 4.6).

The first way to generate a dynamic mesh is by overlaying the given grid with a continuous elastic medium that is subsequently discretised. In this case, Equation (4.4) stems from the discretisation of the classical elastodynamics equation

$$\rho \frac{\partial^2 q}{\partial t^2} - \nabla \cdot \tau = 0, \tag{4.7}$$

where q is the displacement of the structure, ρ is the density of the material, τ is the stress tensor expressed in terms of $\tau = E : \epsilon(q)$, with the tensor of elasticities E and the strain tensor ϵ.

Alternatively, in the discrete case, the dynamic mesh can be directly assembled by equipping the grid with additional elements, i.e., by

- adding a fictitious mass at each vertex of the mesh,
- attaching a fictitious spring to each edge connecting two vertices
- and adding a fictitious dashpot at each edge connecting two vertices.

Very often in applications, the system described in Equation (4.4) is reduced to its quasi-static version resulting in a simplified form

$$\mathbf{Kq} = 0 \tag{4.8}$$

Numerical solution. Systems of linear equations in the form $K\mathbf{q} = \mathbf{f}$ are frequently solved with the *Jacobi method*. The Jacobi method is an iterative algorithm where the matrix K is split into two matrices, diagonal matrix K_d and the residual matrix K_r, so that $K = K_d + K_r$, under the assumption of dominant diagonal elements. More precisely:

$$K = \begin{bmatrix} k_{11} & k_{12} & \cdots & k_{1n} \\ k_{21} & k_{22} & \cdots & k_{2n} \\ \vdots & \vdots & \ddots & \vdots \\ k_{n1} & k_{n2} & \cdots & k_{nn} \end{bmatrix}, \quad \boldsymbol{q} = \begin{bmatrix} q_1 \\ q_2 \\ \vdots \\ q_n \end{bmatrix}, \quad \boldsymbol{f} = \begin{bmatrix} f_1 \\ f_2 \\ \vdots \\ f_n \end{bmatrix} \tag{4.9}$$

K is decomposed into a diagonal matrix K_d and the residual matrix K_r in the following way:

$$K = K_d + K_r, \quad \text{where} \quad K_d = \begin{bmatrix} k_{11} & 0 & \cdots & 0 \\ 0 & k_{22} & \cdots & 0 \\ \vdots & \vdots & \ddots & \vdots \\ 0 & 0 & \cdots & k_{nn} \end{bmatrix} \quad \text{and} \quad K_r = \begin{bmatrix} 0 & k_{12} & \cdots & k_{1n} \\ k_{21} & 0 & \cdots & k_{2n} \\ \vdots & \vdots & \ddots & \vdots \\ k_{n1} & k_{n2} & \cdots & 0 \end{bmatrix} \tag{4.10}$$

Hence,

$$K\mathbf{q} = K_d\mathbf{q} + K_r\mathbf{q} \tag{4.11}$$

This implies

$$\begin{aligned} K_d\mathbf{q} &= K\mathbf{q} - K_r\mathbf{q} \\ &= \mathbf{f} - K_r\mathbf{q} \end{aligned} \tag{4.12}$$

Finally, we can derive an expression for $\mathbf{q}$ which can serve as a base for iterative solutions $\mathbf{q}^{(k+1)}$

$$\mathbf{q} = K_d^{-1}(\mathbf{f} - K_r\mathbf{q}) \quad \Longrightarrow \quad \mathbf{q}^{(k+1)} = K_d^{-1}(\mathbf{f} - K_r\mathbf{q}^{(k)}), \tag{4.13}$$

where $k+1$ is the number of iteration. The algorithm is iterated until it converges, i.e., $\mathbf{q}^{(k+1)}$ is equal or close enough to $\mathbf{q}^{(k)}$. Alternatively to the system approach, the solution can also be found on the element-to-element basis, which takes the following form for an element i:

$$q_i^{(k+1)} = \frac{1}{k_{ii}}(f_i - \sum_{j \neq i} k_{ij} q_j^{(k)}), \quad i = 1, 2, ..., n \tag{4.14}$$

In the sequel, the Jacobi method was used to solve the system of stent forces, as will be described below.

4.2.1 Lineal Springs

4.2.1.1 Lineal spring analogy

The idea behind the spring analogy methods consists in replacing the mesh by fictitious springs, as schematically illustrated in Figure 4.7 (Blom, 2000). Each spring then behaves according to Hooke's law, stating that the extension of a spring is directly proportionate to the load applied to it, or mathematically:

$$\mathbf{F} = -k\mathbf{x}, \tag{4.15}$$

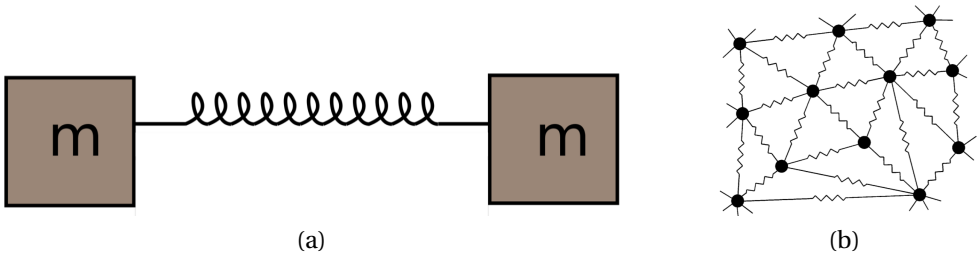

Figure 4.7: (a) Graphical interpretation of the lineal spring analogy. (b) Each edge of the 2-D mesh is modeled as a fictitious lineal spring (image from Meier et al. 2005).

where **x** is the displacement of the end of the spring from its equilibrium position, **F** is the restoring force exerted by the material and k is a spring constant.

When spring analogy is based on lineal springs, it is referred to as *lineal spring analogy* (LSA). In case the springs in the model are set to possess a certain positive equilibrium length, Hooke's law can be written for the fictitious force $\boldsymbol{F}_i$ acting on node i from its neighbours as

$$\boldsymbol{F}_i = \sum_{j=1}^{n_i} k_{ij}(\boldsymbol{\delta}_j - \boldsymbol{\delta}_i), \tag{4.16}$$

where $\boldsymbol{\delta}_i$ is the displacement of node i, k_{ij} is the stiffness of the segment spring between node i and j and n_i is the number of neighbours of node i (Blom, 2000).

Figure 4.8 illustrates the behaviour of a mesh consisting of springs elements when the deformation is prescribed to the farthest upper right node of the mesh. Assuming that in equilibrium the force acting on each node is zero, the new nodal displacement can be calculated at every time step as a weighted average of the displacements of the surrounding nodes. This gives the following iterative Equation (4.17), which can be derived from Equation (4.16) by setting the force to zero:

$$\boldsymbol{\delta}_i^{(k+1)} = \frac{\sum_{j=1}^{n_i} k_{ij}\boldsymbol{\delta}_j^{(k)}}{\sum_{j=1}^{n_i} k_{ij}}, \tag{4.17}$$

where index k represents the number of iterations.

Applying the iterative Equation (4.17) to all nodes of the mesh, the system is solved for displacements at the internal nodes, using the known displacements on boundary nodes and nodal coordinates of the previous iteration. After the sufficient number of iterations, the new nodal coordinates $\boldsymbol{x}^{new}$ are determined by adding the final displacement $\boldsymbol{\delta}^{final}$ to the old coordinates $\boldsymbol{x}^{old}$, which ensures the conformity of the mesh with the physical elastic properties of the deforming body:

$$\boldsymbol{x}_i^{new} = \boldsymbol{x}_i^{old} + \boldsymbol{\delta}_i^{k,final} \tag{4.18}$$

Stiffness setting. The value of the springs' stiffness has implications on how the boundary deformation is propagated to the inner parts of the mesh. Usually the stiffness of lineal springs is set proportional to the inverse of the spring length before the deformation, as originally proposed by Batina (1990). This value of the stiffness is sensible since mesh points that are located in close proximity to each other

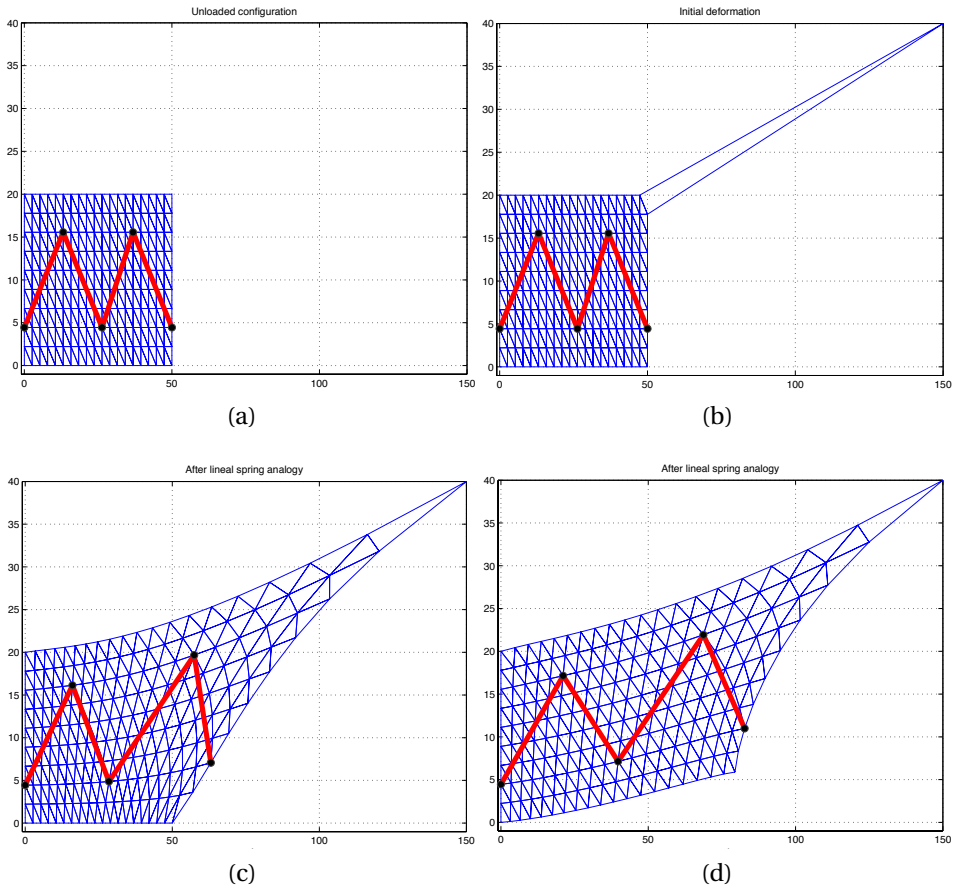

Figure 4.8: Mesh deformation with lineal spring analogy: (a) unloaded configuration; (b) prescribed initial deformation to the node at the upper right corner; (c-d) regularisation of the mesh by lineal spring analogy with different boundary conditions; result after 100 iterations.

should exhibit larger restoring force onto each other. Since collision of vertices is more prone to occur in high-density parts of the mesh, this stiffness setting helps to prevent collisions from happening, as has been proven by Blom (2000) for 1-D case.

An example of the mesh behaviour with such stiffness setting is illustrated in Figure 4.9. After the initial boundary deformation shown in the image (a), the mesh was regularised by 300 iterations of the LSA method with the stiffness value calculated prior to any deformations and held constant; the result shown in the image (b). Updating the stiffness during the iterative process made its value deformation-dependent and influenced the result in a drastic way. For example, the image (c) presents the resulting mesh when the stiffness was recalculated during the itera-

tive process after every 100 iterations. As can be seen, the regularisation performs poorer since springs connected to nodes that were subject to large deformations got a smaller value of the stiffness and hence started bearing more of the deformation, without distributing it to inner nodes. When the stiffness was updated in every iteration, there was no regularisation effect visible.

However, in some cases recalculation of the stiffness during the iterative process helps correcting the quality of the mesh that is necessary for some types of problems. This is especially the case for large deformations where inversion of mesh elements might occur. One approach to avoid this issue is an extension of the lineal springs framework called *semi-torsional spring analogy* (Blom, 2000; Zeng and Ethier, 2005), which is described in the following Section 4.2.2.

4.2.1.2 LSA-based stent expansion

As already mentioned, the spring analogy method has mainly been used in literature for regularisation of the mesh after boundary deformations. The regularisation is achieved by means of propagating the known boundary displacements into the inner parts of the mesh. However, if we think about a stent expanding inside an artery, there is no part of the stent structure where the deformation is known *a priori* as a boundary condition; thus, there is nothing to propagate. In this case, the computational problem consists in determining the deformation in the *entire* stent structure. To solve the stent problem, a method that draws inspiration from the

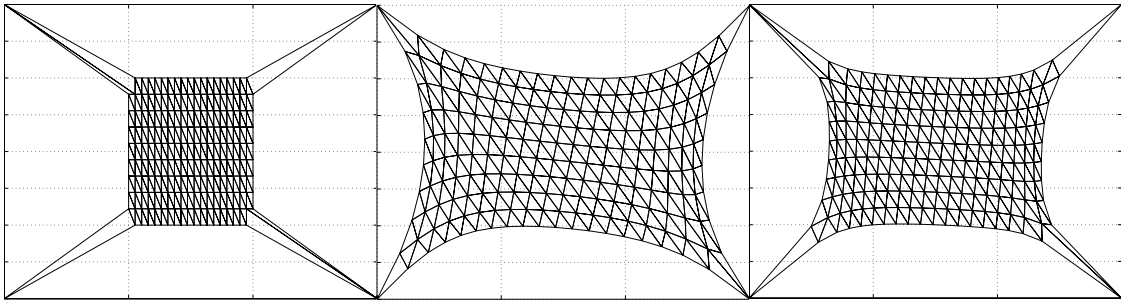

Figure 4.9: The effect of the stiffness setting: (a) initial boundary deformation; (b) result after 300 iterations of LSA method with constant stiffness calculated before the initial deformation; (c) result after 300 iterations with stiffness updated after every 100 iterations.

spring analogy was developed for determining mesh movements **without** known boundary deformations. Since crimping of the stent creates spring forces acting inside the structure, the idea was to allow the nodes in the mesh to move under these forces. The movement took into account the nodal intertwinement with its neighbours by means of the nodal stiffness, the value of which was set to be equal to the sum of the stiffness of all springs emanating from it.

Input for LSA expansion procedure:

1. Stent in the load-free configuration, especially, matrix of nodal coordinates $\boldsymbol{V}$.
2. Stent in the crimped configuration (matrix $\boldsymbol{V}_{cr}$), folded around its longitudinal dimension, as described in Section 4.1.3. All calculations were performed in the local coordinates of the stent, i.e., with respect to the stent egocentric coordinate system, found by the PCA, as reported in Section 4.1.2.
3. Stiffness of the mesh edges (springs) captured in the matrix $\boldsymbol{K}_{lineal}$.
4. Nodal stiffness of the mesh in the matrix $\boldsymbol{K}_{lineal-nodal} = \sum_{j=1}^{n_i} k_{ij}$.

Output: Current stent configuration after the device has been expanded.

When the stent is expanding freely without constraints, the output will ultimately reach the load-free configuration of the device, which is known in advance in this case. However, the final configuration is unknown in general, especially in cases where there are obstacles on the way of the expanding stent such as vessel walls (examples will follow in later sections). Hence, the procedure had to distinguish between the two different displacements (deltas):

1. The first one was responsible for the current configuration of the stent, i.e., it accounts for the remaining crimping status of the structure. This delta, that is called *crimping delta* δ^{cr}, was used to calculate restoring forces in the current crimped stent.
2. The second delta, called *expansion delta* δ^{exp}, was the actual displacement with which the stent was expanding in each iterative step. It was used to update the stent nodal coordinates in the process of deployment.

Procedure: During the deployment process, the two deltas fed into each other. Firstly, the initial δ^{cr} was determined, which measured the initial crimping deformation. The iterative process started with the calculation of the restoring forces inside the mesh based on the crimping delta δ^{cr}. Based on this information and stiffness of the vertices, one step of stent expansion was calculated which gave the displacement δ^{exp}. Afterwards, the current coordinates of stent vertices were updated, as well as δ^{cr}, so that they both corresponded to the current status of crimping in the stent structure (after update). The process was repeated until there was no change in the stent structure, i.e., no restoring forces were acting on the struts. The detailed pseudocode of the procedure is below.

Incremental LSA displacement algorithm for free stent expansion:
Input:

- Stent coordinates in the load-free configuration in the format for node i: $\boldsymbol{v}_i^{lf} = (x_i^{lf}, y_i^{lf}, z_i^{lf})$ calculated in the stent egocentric coordinate system.
- Stent nodal coordinates in the crimped configuration in the format $\boldsymbol{v}_i^{cr} = (x_i^{cr}, y_i^{cr}, z_i^{cr})$ calculated in the stent egocentric coordinate system.
- Stiffness of edges and vertices of the stent structure mesh. Matrix $\boldsymbol{K}_{lineal}$ of stiffness values k_{ij} of the spring edge $(i-j)$ is set to be inversely related to the length of $(i-j)$. Nodal stiffness for node i is determined as the sum of the stiffness of all edges emanating from this node: $\boldsymbol{K}_{lineal-nodal} = \sum_{j=1}^{n_i} k_{ij}$.

Output: Nodal coordinates of the current expanded stent.

---

1. **Calculate initial displacement of stent vertices** by subtracting the load-free coordinates of vertices from the current crimped coordinates. For a vertex i initial crimping delta $\boldsymbol{\delta}_i^{cr}$ is found by:

$$\boldsymbol{\delta}_i^{cr} = \begin{pmatrix} \delta_{x_i}^{cr} \\ \delta_{y_i}^{cr} \\ \delta_{z_i}^{cr} \end{pmatrix} = \begin{pmatrix} x_i^{cr} \\ y_i^{cr} \\ z_i^{cr} \end{pmatrix} - \begin{pmatrix} x_i^{lf} \\ y_i^{lf} \\ z_i^{lf} \end{pmatrix}$$

2. **Iterate** until there is almost no change in expansion delta $\boldsymbol{\delta}^{exp}$, i.e., stop when $max\{|\delta_{x_i}^{exp}|, |\delta_{y_i}^{exp}|, |\delta_{z_i}^{exp}|\} \leq \epsilon$, where i ranges over all internal nodes ($\epsilon = 10^{-6}$)

   - **Calculate restoring force** $\boldsymbol{F}_i$ for each node i from Equation (4.16)

$$\boldsymbol{F}_i = \sum_{j=1}^{n_i} k_{ij}(\boldsymbol{\delta}_j^{cr} - \boldsymbol{\delta}_i^{cr})$$

   - **Calculate expansion delta** $\boldsymbol{\delta}_i^{exp}$ for each node i from force and nodal stiffness

$$\boldsymbol{\delta}_i^{exp} = -\frac{\boldsymbol{F}_i}{\sum_{j=1}^{n_i} k_{ij}} = -\frac{\sum_{j=1}^{n_i} k_{ij}(\boldsymbol{\delta}_j^{cr} - \boldsymbol{\delta}_i^{cr})}{\sum_{j=1}^{n_i} k_{ij}} \tag{4.19}$$

   - **Update stent** nodal coordinates for each node i by adding the expansion delta

$$\begin{pmatrix} x_i^{cr} \\ y_i^{cr} \\ z_i^{cr} \end{pmatrix} := \begin{pmatrix} x_i^{cr} \\ y_i^{cr} \\ z_i^{cr} \end{pmatrix} + \begin{pmatrix} \delta_{x_i}^{exp} \\ \delta_{y_i}^{exp} \\ \delta_{z_i}^{exp} \end{pmatrix}$$

   - **Update crimping delta** values $\boldsymbol{\delta}_i^{cr}$ for each node i by adding expansion displacement $\boldsymbol{\delta}_i^{exp}$ to the previous $\boldsymbol{\delta}_i^{cr}$

$$\boldsymbol{\delta}_i^{cr} = \begin{pmatrix} \delta_{x_i}^{cr} \\ \delta_{y_i}^{cr} \\ \delta_{z_i}^{cr} \end{pmatrix} := \begin{pmatrix} \delta_{x_i}^{cr} \\ \delta_{y_i}^{cr} \\ \delta_{z_i}^{cr} \end{pmatrix} + \begin{pmatrix} \delta_{x_i}^{exp} \\ \delta_{y_i}^{exp} \\ \delta_{z_i}^{exp} \end{pmatrix}$$

3. **Determine the new coordinates** of the stent vertices in the global coordinate system from newly found egocentric coordinates.

Free expansion. When a self-expanding stent is released from a catheter during a minimally invasive procedure, the device springs open to its load-free configuration under the elastic forces of nitinol. Figure 4.10 illustrates the free expansion process for three different stents with the lineal spring analogy expansion method. Columns (a)-(f) capture progression in the stent opening after a certain number of computational iterations when the entire structure of the stent was let go simultaneously. The resulting expansion progression looks very similar to that of a real nitinol stent

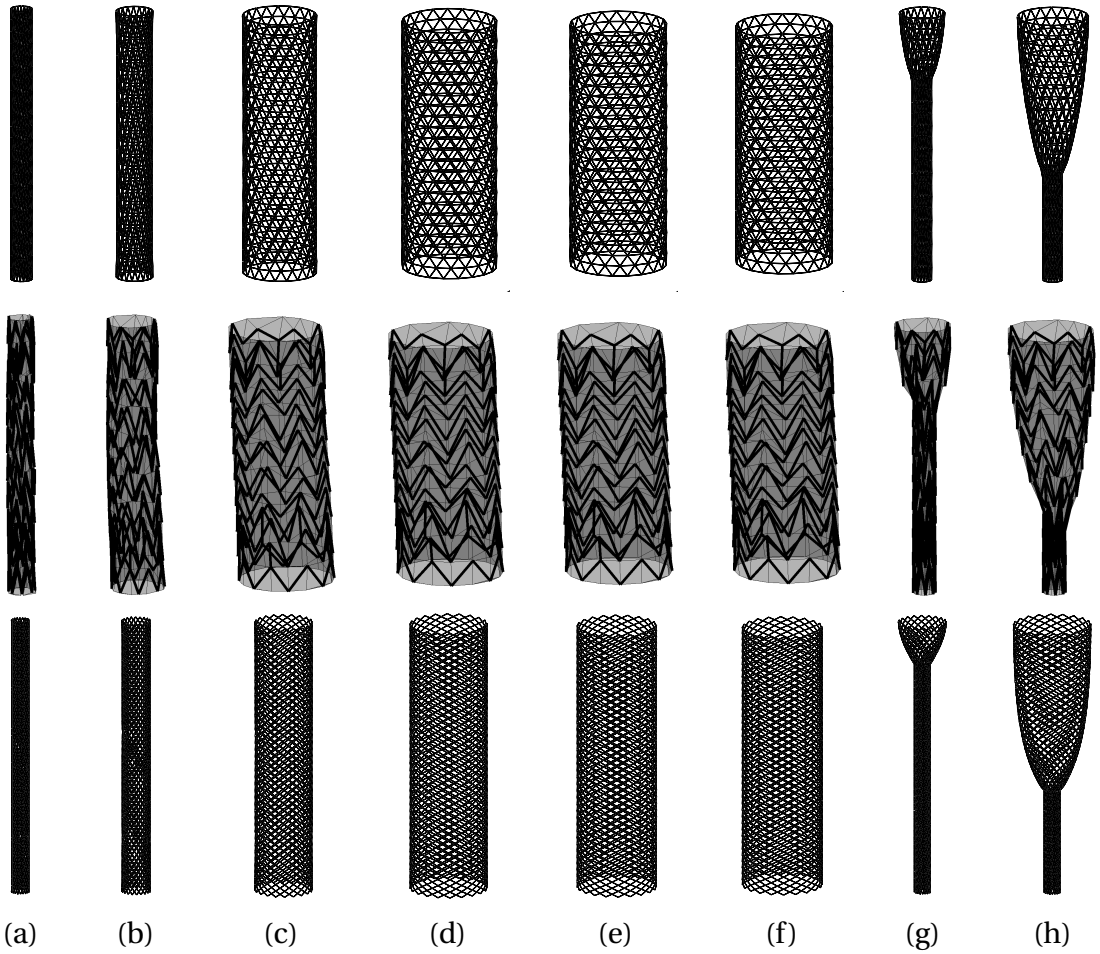

Figure 4.10: Free expansion of 3 different stents with the lineal spring analogy, shown in different rows, respectively. (a) Initial crimped stent, (b) after 10 iterations, (c) 50, (d) 150, (e) 250, (f) 500, (g-h) 30 and 70 iterations of layered expansion.

shown earlier in Figure 2.10. The last two columns of Figure 4.10 feature expansion initiated in the top layers of the stent and progressing to the bottom, which simulated the way in which a catheter/sheath is pulled out to release the stent during a real intervention.

4.2.2 Semi-Torsional Springs

The driving force of the lineal spring analogy is the restoring force created by the stiffness of an edge. In general, the stiffness of an edge is not associated with either angular displacement or area (volume) change of mesh elements. Hence, in problems that involve large deformations of the mesh elements, nothing in the lineal model is preventing the elements from losing their shape or from "snapping

through", as shown in Figure 4.11 (a). Such cases are possible because a lineal spring can prevent its two ends from colliding, but cannot stop a vertex from crossing an opposite edge. Thus, to preserve the validity of the mesh in such cases, several extensions have been proposed in the literature.

One of the proposed solutions is to introduce artificial nodes and additional lineal springs emanating from them that inhibit a vertex of the mesh from moving too close to the opposite edge. For example, the solution proposed by Bottasso et al. (2005) was to control the volume (or area) of a mesh element by allowing each vertex to move only within its ball – the so-called *ball-vertex* method. This is done by means of additional lineal springs that attach every vertex of the mesh to an artificial point which is constructed as a projection on the ball of edges or faces, in 2-D or 3-D, respectively. In 3-D case (see Figure 4.11, b), for each region R associated with the vertex i, an additional lineal spring is constructed that attaches i to its projection p on the plane of the face F_i opposite i. Figure 4.11 (b) illustrates this new spring (in red) for a tetrahedron R.

The additional ball-vertex springs give rise to the corresponding forces, which are included into the equilibrium equation for each vertex. Hence, the new vertex coordinates are computed under the influence of both the edge springs and the additional ball-vertex springs. Compared to the lineal spring case, the only difference

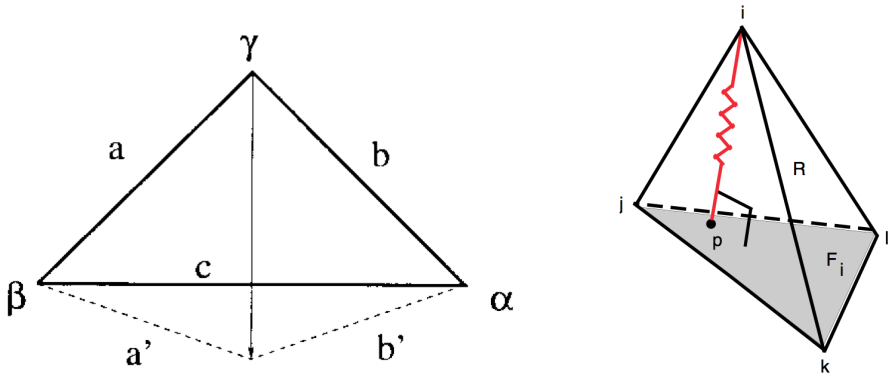

(a) (b)

Figure 4.11: (a) Possible snap-through of a triangular mesh cell indicated by dashed lines (image from Blom 2000). (b) The ball-vertex spring method with an additional lineal spring attaching each vertex i to the opposite face F_i in a tetrahedron R (image from Bottasso et al. 2005).

is that the springs force equation features the displacement of a virtual point, and not of an existing vertex (Bottasso et al., 2005).

Another solution is to extend the lineal spring analogy by incorporating the angle information into the spring stiffness, the so-called *semi-torsional spring analogy*, which is described in the next section.

4.2.2.1 Semi-torsional spring analogy

The idea of a semi-torsional spring analogy (STSA) is to inhibit element inversion by simulating a torsional spring connected to each vertex of the mesh. The torsion spring would account for the angular displacement of mesh elements and enable control over mesh deformation. Based on the lineal spring analogy, the behaviour of the torsion spring is modeled indirectly by integrating the element's angular values into the stiffness of the spring edge, giving rise to the *semi-torsional* stiffness. Figure 4.12 schematically demonstrates the idea behind the approach for a 2-D unstructured triangular mesh, showing torsional springs placed at the corners between the adjacent edges of a triangular element.

There have been different proposals in the literature as to how to define the

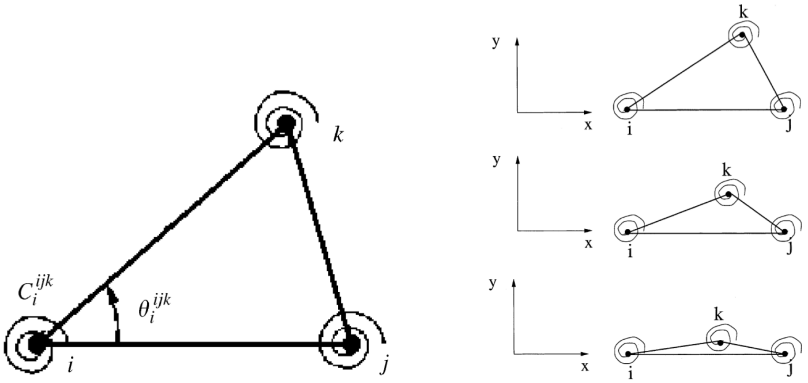

Figure 4.12: Schematic representation of the semi-torsional spring analogy. (a) Element collision and snap-through is prevented by torsional springs that are resisting the change of the angles at the vertices they are attached to (from Degand and Farhat 2002). (b) Torsional springs connected to each vertex of a triangular mesh element are stiffening the system when neighbouring nodes are close to collision, preventing thereby the inversion of elements (from Zeng and Ethier 2005).

semi-torsional stiffness. One of the early approaches for a triangular element was to simply divide the lineal stiffness of an edge in a triangular element by the angle this edge faces:

$$k_{ij}^{semi-torsional} = \frac{k_{ij}^{lineal}}{\theta}, \tag{4.20}$$

where θ is the angle facing the edge $(i-j)$ (Blom, 2000). However, this definition has been criticised for the fact that it assigns an inconsistent value for internal edges in a 2-D triangular mesh. This is due to the fact that an internal edge is shared between two mesh cells and possibly faces two angles that differ in magnitude (see Figure 4.13, b). Therefore, when considered for each of the two cells separately, the above definition gives different stiffness values to the one and very same edge (Zeng and Ethier, 2005).

Another definition, suggested by Zeng and Ethier (2005), was to determine the semi-torsional stiffness of an edge by gathering angular information from all facing edges in a sum, giving it thereby a consistent value. More precisely, the semi-torsional stiffness is defined as

$$k_{ij}^{semi-torsional} = \kappa \sum_{m=1}^{NE_{ij}} \frac{1}{\sin^2 \theta_m^{ij}}, \tag{4.21}$$

where NE_{ij} is the number of elements that include the edge $(i-j)$, θ_m^{ij} is the angle facing the edge $(i-j)$ on the m^{th} element, and κ is a coefficient setting the dimension of the stiffness; κ is set to 1 for now (see Figure 4.13, a).

Since the value of the sine approaches 0 as the angle approaches 0 or π, the facing edge becomes very stiff when neighbouring edges are close to collision. Thus, the above setting of the semi-torsional stiffness prevents further change in the angle, thereby avoiding element inversion.

Then the total stiffness value of an edge is defined as the sum of the lineal and the semi-torsional stiffness components

$$k_{ij} = k_{ij}^{lineal} + k_{ij}^{semi-torsional} \tag{4.22}$$

The sine of an angle $\sin\theta_m^{ij}$ can be determined directly without computing the angle by finding the angle between the normals of the corresponding planes. Let $\vec{v}_i$ denote the position of a vertex i, i.e., $\vec{v}_i = (x_i, y_i, z_i)$ and $\vec{n}_1$, $\vec{n}_2$ be the normals to the

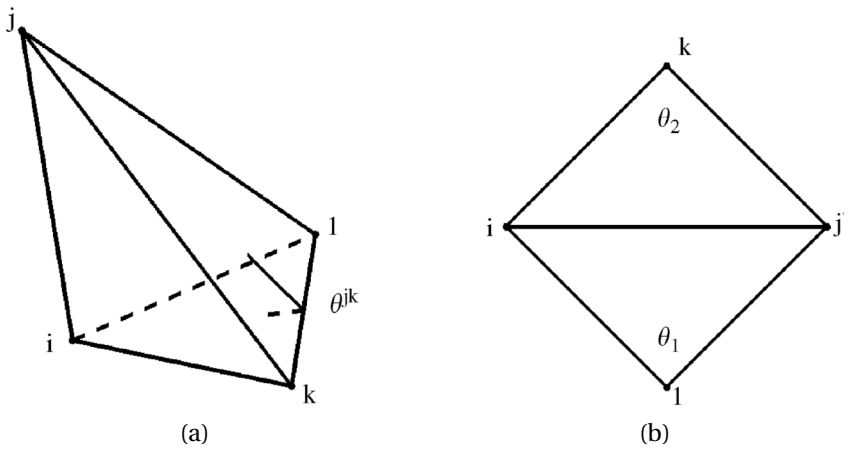

Figure 4.13: Schematic representation of facing angles. (a) In a tetrahedral element, the angle θ^{jk} facing the edge $(i-j)$ is the angle between the face Δ^{jkl} and the face Δ^{ikl} (image from Zeng and Ethier 2005). (b) In a 2-D triangular mesh, two angles θ_1 and θ_2 are facing the internal edge $(i-j)$ (image from Zeng and Ethier 2005).

faces Δ^{jkl} and Δ^{ikl}, respectively (Figure 4.13, a). The normals that can be found in the following way

$$\begin{aligned}\vec{n}_1 &= (\vec{v}_l - \vec{v}_j) \times (\vec{v}_k - \vec{v}_j) \\ \vec{n}_2 &= (\vec{v}_l - \vec{v}_i) \times (\vec{v}_k - \vec{v}_i)\end{aligned} \tag{4.23}$$

Then using the definition of the dot product, the normals are related to the angle as

$$\vec{n}_1 \cdot \vec{n}_2 = |\vec{n}_1||\vec{n}_2| \cos\theta_m^{ij}, \tag{4.24}$$

from where the sine square can be obtained using the trigonometric identity $\sin^2\theta_m^{ij} + \cos^2\theta_m^{ij} = 1$

$$\sin^2\theta_m^{ij} = 1 - \frac{(\vec{n}_1 \cdot \vec{n}_2)^2}{|\vec{n}_1|^2|\vec{n}_2|^2} \tag{4.25}$$

2-D Examples. When the stiffness of the mesh was enhanced with the angular information, its deformation behaviour changed. Figure 4.14 compares the deformation of the mesh for the semi-torsional case (blue colour) with the baseline lineal case (black). For the semi-torsional model, the governing equation was the same as in the lineal case (Equation 4.17), but the stiffness was set to include the semi-torsional component following Equation (4.22). It can be noted that the semi-torsional springs mesh exhibited smaller deformation due to its stiffer connections resulting from the addition of the semi-torsional stiffness to the lineal one.

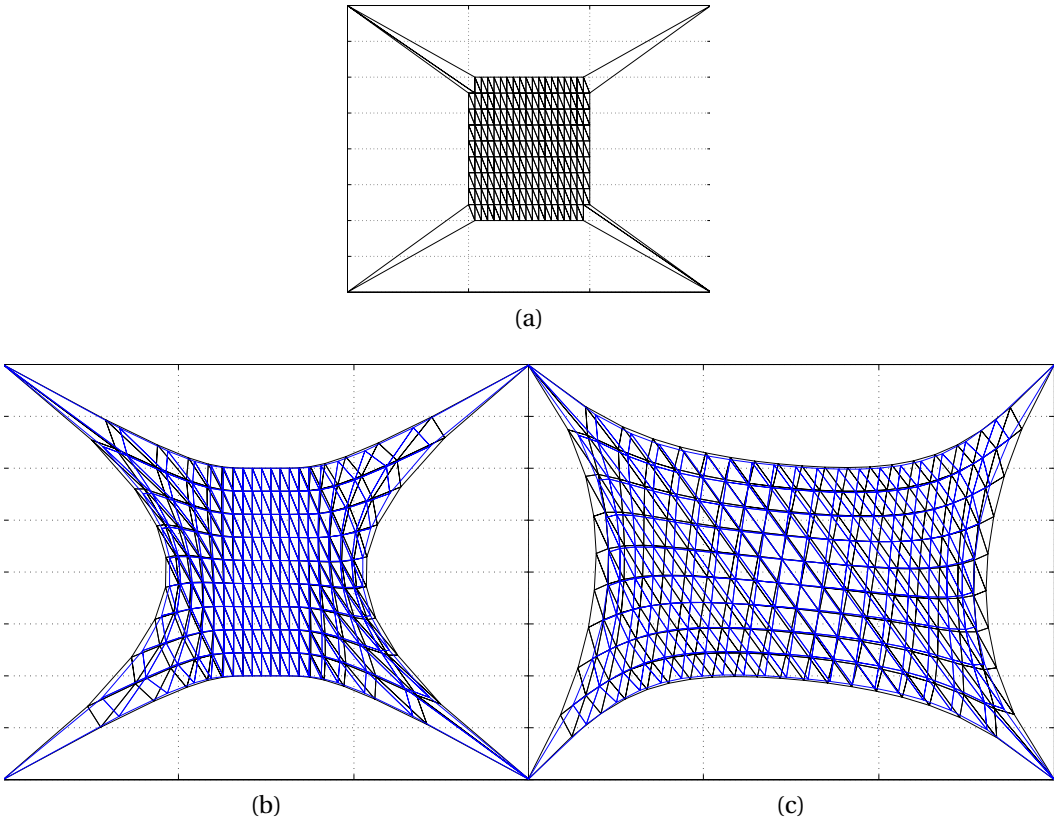

Figure 4.14: Comparison of lineal (black) and semi-torsional (blue) springs networks: (a) initial boundary deformation; (b) result after 10 iterations with constant stiffness calculated before the initial deformation; (c) after 300 iterations with constant stiffness calculated before the initial deformation. The semi-torsional springs mesh is stiffer and thus deforming less.

The real advantage of the semi-torsional model became visible in cases that involve large deformations with a possibility of element inversion. Figure 4.15 illustrates an example of a mesh that underwent a deformation as its top right node was being stepwise displaced inwards, 5 times by $\delta = [-2, -2]$. Nodes located on both axes were kept fixed and the displacement of the top vertex was carried out sequentially. After each displacement, the deformation was propagated with the spring model. As can be seen, element inversion occurred in the top right corner in the lineal model (b), which did not happen in the semi-torsional model that was able to successfully preserve the validity of the mesh for moderately large deformations (c). However, in case of very large deformations (6 times $\delta = [-2, -2]$), also this method was not enough, as seen in image (d) exhibiting element inversion.

4.2.2.2 STSA-based stent expansion

In order to apply the semi-torsional model to stent expansion, some additional parameters had to be calculated, the most important of which are:

- Table of angles that stores the list of all triples in the mesh that build angles. It was computed from the background mesh triangulation by means of translating it into three angles, i.e., each triple $[v_i, v_j, v_k]$ gives rise to three angles $[v_i, v_j, v_k], [v_k, v_i, v_j], [v_j, v_k, v_i]$.

- Semi-torsional stiffness that was added to the lineal stiffness component according to Equation (4.22). Since in the triangular stent mesh an internal edge always shares two elements, the governing equation for the semi-torsional stiffness was rewritten as

$$k_{ij}^{semi-torsional} = \kappa\left(\frac{1}{\sin^2\theta_1} + \frac{1}{\sin^2\theta_2}\right), \tag{4.26}$$

  where θ_1 is the angle facing the edge $(i-j)$ in the triangular element Δ^{ijl}, and θ_2 is the angle facing the edge $(i-j)$ in Δ^{ijk} and k, l, i and j are the nodes of the elements with coordinates $\vec{v}_i = (x_i, y_i, z_i)$ for an example vertex i, as illustrated in Figure 4.13 (b) (Zeng and Ethier, 2005).

  The stiffness coefficient κ had to be set appropriately in order to implement the overlay of torsional and lineal springs. κ was needed because of the dis-

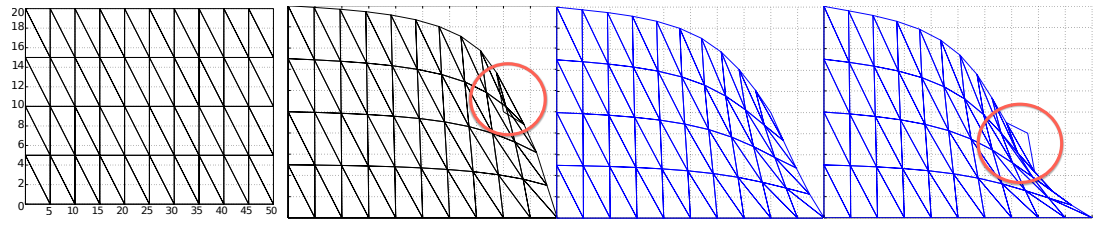

Figure 4.15: Comparison of lineal (black) and semi-torsional (blue) springs networks: (a) initial configuration; (b) result after deformation with the lineal model and updated stiffness: element inversion occurs in the top right corner (area inside the red circle); (c) result after deformation with the semi-torsional model and updated stiffness: mesh integrity is preserved better and no element inversion occurs; (d) result after large deformation with the semi-torsional model and updated stiffness: mesh integrity is not preserved, element inversion occurs (area inside the red circle).

crepancy in dimensionality in both types of stiffness. More precisely, the lineal stiffness k_{ij} was inversely proportional to segment lengths, whereas the semi-torsional stiffness would be dimensionless without κ. Thus, if the semi-torsional stiffness was simply added to the lineal stiffness, the relative importance of the lineal and semi-torsional force components would depend on the choice of length units (for example, either meters or millimeters), which clearly should not be the case. In order to avoid this undesirable effect, the semi-torsional stiffness was scaled with the length, i.e., κ was set to be inversely proportional to the length:

$$\kappa = \frac{1}{\ell},$$

where ℓ is the local characteristic length in the mesh, such as the average edge length of a triangular element.

- The sines of the angles were found directly, as proposed by Zeng and Ethier (2005)

$$\sin^2\theta_1 = \frac{|(\vec{v}_i - \vec{v}_l) \times (\vec{v}_j - \vec{v}_l)|^2}{|\vec{v}_i - \vec{v}_l|^2 |\vec{v}_j - \vec{v}_l|^2}$$
$$\sin^2\theta_2 = \frac{|(\vec{v}_i - \vec{v}_k) \times (\vec{v}_j - \vec{v}_k)|^2}{|\vec{v}_i - \vec{v}_k|^2 |\vec{v}_j - \vec{v}_k|^2} \tag{4.27}$$

The algorithm for free expansion of the stent was the same as in the lineal case, reported in Section 4.2.1.2 in LSA expansion procedure.

Figure 4.16 illustrates the results of free expansion for a PED stent with the semi-torsional spring analogy expansion method. Columns (a)-(f) capture progression in the stent opening after a certain number of computational iterations when the entire structure of the stent was let go simultaneously, while columns (g)-(i) show layered expansion. The resulting expansion progression looks very similar to that of the lineal model in Figure 4.10, third row.

4.2.3 Torsional Springs

The torsional springs model was proposed as an improvement over the lineal spring analogy since the latter is prone to element inversion in cases of large mesh deformations, as mentioned earlier. In order to control the angular deformations of the

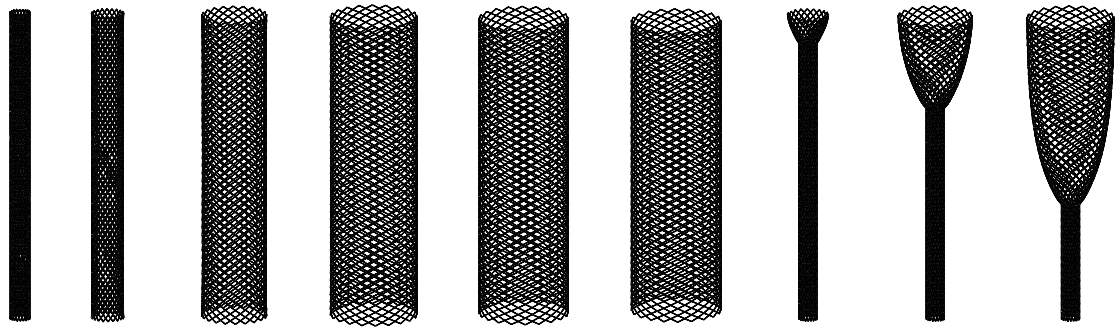

(a) (b) (c) (d) (e) (f) (g) (h) (i)

Figure 4.16: Free expansion of PED stent with semi-torsional spring analogy. (a) Initial crimped stent, (b) result after 10 iterations, (c) after 50 iterations, (d) after 150 iterations, (e) after 250 iterations, (f) after 500 iterations, (g) after 30 iterations of layered expansion, (h) after 100 iterations of layered expansion, (i) after 200 iterations of layered expansion.

mesh elements, additional torsional springs are attached to the vertices of each triangle. The difference to the previous approach is that torsional springs are not indirectly simulated by integrating the torsional stiffness component into the lineal stiffness of the springs, as in the semi-torsional method, but directly implemented, as will be shown below. In reality, torsional springs are flexible elastic objects that store mechanical energy when twisted (see Figure 4.17, a). The amount of force

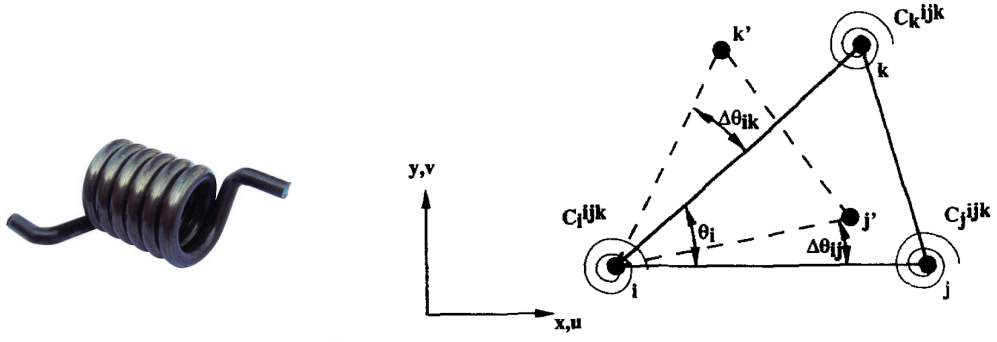

(a) (b)

Figure 4.17: (a) A torsional spring serves as an inspiration for the torsional spring analogy (image from `www.advanexusa.com`). (b) Graphical interpretation of the torsional spring analogy, whereby an artificial torsional spring is placed at each node of the mesh to control the angular deformation (image from Farhat et al. 1998).

(torque) such a spring exerts is proportional to the amount it is twisted, i.e., torsional springs obey the angular form of Hooke's law, as long as they are not twisted beyond their elastic limit:

$$\tau = -k\Delta\theta, \tag{4.28}$$

where τ denotes the torque exerted by the spring, $\Delta\theta$ is the angle of twist from its equilibrium position and k is the torsional stiffness of the spring. This time, the kinematics of real torsional springs are incorporated in the calculations of the method, as reported in the section below.

4.2.3.1 Torsional spring analogy

In the *torsional spring analogy* (TSA), when a torsional spring is connected to a node i of a triangular element Δ^{ijk}, the torsional stiffness C^{ijk} can be defined as

$$C_i^{ijk} = \frac{1}{1+\cos\theta_i^{ijk}} \times \frac{1}{1-\cos\theta_i^{ijk}} = \frac{1}{\sin^2\theta_i^{ijk}}, \tag{4.29}$$

where C_i^{ijk} is the stiffness of the spring that is attached to the vertex i which is connected with vertices j and k and, thus, associated with the angle θ_i^{ijk}, as proposed by Farhat et al. (1998). Hence, this torsional spring will create torques opposing the change in the angle, especially when the angle θ_i^{ijk} becomes close to zero or π.

The torsional stiffness defined in this way is dependent on the area of the corresponding triangular element. This can be seen when $\sin\theta_i^{ijk}$ is derived from the definition of the exterior vector product (the magnitude of which is the area of the parallelogram built on these vectors, geometrically) and expressed in terms of edge lengths l_{ij}, l_{jk} and the area A_{ijk} of the triangle Δ_{ijk} as follows:

$$\sin\theta_i^{ijk} = \frac{2A_{ijk}}{l_{ij}l_{ik}} \tag{4.30}$$

Thus, the torsional stiffness C_i^{ijk} takes the following form:

$$C_i^{ijk} = \frac{l_{ij}^2 l_{ik}^2}{4A_{ijk}^2} \tag{4.31}$$

Here, the derivation of the torsional method for the 2-D case will be shown and afterwards extended to the 3-D version, which is subsequently employed for the simulation of stent expansion.

Kinematics. Farhat et al. (1998) proposed a kinematic formulation that was developed under the assumption that only small displacements and rotations occur between two subsequent time steps. The assumption is necessary during the derivation to express the angular displacements in terms of nodal displacements in a linear way. Thus, the iterative algorithm based on this method has to sufficiently break down the large deformation that might occur in the course of the simulation into small ones in order to respect the assumption.

Coming back to Figure 4.17, the solid line depicts the displacement of a triangle Δ^{ijk} from its reference position, into a current configuration, shown by a dashed line in the image. The displacement components resulting from the displacement of the triangle vertices i, j and k are captured in the vector $\boldsymbol{q}$ defined in the following way

$$\boldsymbol{q}^{ijk} = \begin{bmatrix} u_i \\ v_i \\ u_j \\ v_j \\ u_k \\ v_k \end{bmatrix}$$

The resulting rotation increment is denoted by the vector $\boldsymbol{\Delta\theta}^{ijk}$

$$\boldsymbol{\Delta\theta}^{ijk} = \begin{bmatrix} \Delta\theta_i \\ \Delta\theta_j \\ \Delta\theta_k \end{bmatrix}$$

The rotation increment $\boldsymbol{\Delta\theta}^{ijk}$ can be defined in the matrix form as the following (details of the derivation are described in Appendix A.1)

$$\boldsymbol{\Delta\theta}^{ijk} = \boldsymbol{R}^{ijk}\boldsymbol{q}^{ijk}, \tag{4.32}$$

where the matrix $\boldsymbol{R}^{ijk}$ is composed in the following way

$$\boldsymbol{R}^{ijk} = \begin{bmatrix} b_{ik}-b_{ij} & a_{ij}-a_{ik} & b_{ij} & -a_{ij} & -b_{ik} & a_{ik} \\ -b_{ji} & a_{ji} & b_{ji}-b_{jk} & a_{jk}-a_{ji} & b_{jk} & -a_{jk} \\ b_{ki} & -a_{ki} & -b_{kj} & a_{kj} & b_{kj}-b_{ki} & a_{ki}-a_{kj} \end{bmatrix} \tag{4.33}$$

and the components of the $\boldsymbol{R}^{ijk}$ matrix are built as

$$a_{ij} = \frac{x_{ij}}{l_{ij}^2}, \quad b_{ij} = \frac{y_{ij}}{l_{ij}^2} \quad \forall(i,j)$$

Equilibrium. In order to express the moments produced by the torsional springs as forces acting on the mesh, these moments are first written in a matrix form, analogously to the angular version of Hooke's law (Equation 4.28):

$$\boldsymbol{M}^{ijk} = \boldsymbol{C}^{ijk}\boldsymbol{\Delta\theta}^{ijk},$$

where

$$\boldsymbol{M}^{ijk} = \begin{bmatrix} \boldsymbol{M}_i \\ \boldsymbol{M}_j \\ \boldsymbol{M}_k \end{bmatrix}; \quad \boldsymbol{C}^{ijk} = \begin{bmatrix} \boldsymbol{C}_i^{ijk} & 0 & 0 \\ 0 & \boldsymbol{C}_j^{ijk} & 0 \\ 0 & 0 & \boldsymbol{C}_k^{ijk} \end{bmatrix}$$

Substituting the expression for $\boldsymbol{\Delta\theta}^{ijk}$ defined in Equation (4.32), the torque can be found as

$$\boldsymbol{M}^{ijk} = [\boldsymbol{C}^{ijk}\boldsymbol{R}^{ijk}]\boldsymbol{q}^{ijk}$$

In order to attach the additional torsional springs into a lineal spring mesh, Farhat et al. (1998) have proposed the transformation of the moments $\boldsymbol{M}^{ijk}$ generated by torsional springs into a set of equivalent forces at each vertex gathered in vector $\boldsymbol{F}_{torsion}^{ijk}$ as

$$\boldsymbol{F}_{torsion}^{ijk} = \begin{bmatrix} F_{i_x} \\ F_{i_y} \\ F_{j_x} \\ F_{j_y} \\ F_{k_x} \\ F_{k_y} \end{bmatrix}_{torsion}$$

$\boldsymbol{F}_{torsion}^{ijk}$ can be found though moments $\boldsymbol{M}^{ijk}$ by a linear transformation with the help of the matrix $\boldsymbol{R}^{ijk^T}$ as follows (the detailed derivation is reported in the Appendix A.2)

$$\boldsymbol{F}_{torsion}^{ijk} = \boldsymbol{R}^{ijk^T}\boldsymbol{M}^{ijk}$$

Hence, in each triangle $\boldsymbol{\Delta}^{ijk}$, the contribution of the torsional springs connected to nodes of the triangular mesh elements can be expressed by discrete forces acting on these elements:

$$\boldsymbol{F}_{torsion}^{ijk} = [\boldsymbol{R}^{ijk^T}\boldsymbol{C}^{ijk}\boldsymbol{R}^{ijk}]\boldsymbol{q}^{ijk} = \boldsymbol{K}_{torsion}^{ijk}\boldsymbol{q}^{ijk} \tag{4.34}$$

Overlay of torsional and lineal springs. In order to overlay the lineal springs, that were defined for edges, and the newly created torsional springs, the torsional forces defined above have to be rewritten for each edge $(i-j)$:

$$\begin{aligned} \boldsymbol{F}^{ij}_{total} &= \boldsymbol{F}^{ij}_{lineal} + \boldsymbol{F}^{ij}_{torsion} \\ &= \boldsymbol{K}^{ij}_{lineal}\boldsymbol{q}^{ij} + \sum_{\boldsymbol{\Delta}^{ijk} \supset E_{ij}} [\boldsymbol{F}^{ij}_{torsion}]^{ijk} \\ &= \boldsymbol{K}^{ij}_{lineal}\boldsymbol{q}^{ij} + \sum_{\boldsymbol{\Delta}^{ijk} \supset E_{ij}} [\boldsymbol{K}^{ij}_{torsion}]^{ijk}\boldsymbol{q}^{ijk}, \end{aligned} \tag{4.35}$$

where $[\boldsymbol{F}^{ij}_{torsion}]^{ijk}$ indicates a subvector of $\boldsymbol{F}^{ijk}_{torsion}$ corresponding to the edge $(i-j)$ that is part of the triangular element $\boldsymbol{\Delta}^{ijk}$.

Dimensionality issues. In order to properly overlay torsional and lineal springs, some modifications to the original definition of torsional forces proposed by Farhat et al. (1998) had to be made. The reason for the alteration is the discrepancy in dimensionality in both types of forces, as pointed out by Bottasso et al. (2005). More precisely, the lineal spring forces are non-dimensional quantities, since lineal stiffnesses k_{ij} is inversely proportional to segment lengths and the forces are computed as $\boldsymbol{F}_i = \sum_{j=1}^{\nu_i} k_{ij}(\boldsymbol{\delta}_j - \boldsymbol{\delta}_i)$ (Equation 4.16). In contrast to that, the torsional forces are dimensional quantities. This is because torsional stiffness is determined as $\boldsymbol{K}^{ijk}_{torsion} = \boldsymbol{R}^{ijk^T}\boldsymbol{C}^{ijk}\boldsymbol{R}^{ijk}$ (Equation 4.34), where $\boldsymbol{C}^{ijk}$ is dimensionless and $\boldsymbol{R}^{ijk}$ is inversely proportional to the length (Equation 4.33). Hence, $\boldsymbol{K}^{ijk}_{torsion}$ is inversely proportional to length square $(1/m^2)$, resulting in torsional forces being inversely proportional to the length $(1/m)$.

Therefore, if the torsional spring forces were simply added to the lineal spring forces (Equation 4.35), the relative importance of the lineal and torsional springs would depend on the choice of length units (as was also the case for STSA). To avoid this, torsional spring forces were redefined as non-dimensional quantities by scaling the torsional stiffness with a dimensionality constant κ (Bottasso et al., 2005):

$$\boldsymbol{C}^{ijk} = \frac{\kappa}{\sin^2\theta^{ijk}_i}, \tag{4.36}$$

where scaling constant $\kappa = \frac{\ell}{c}$ was defined through the local characteristic length ℓ of the mesh, such as the average edge length of a triangular element, scaled with a chosen constant c.

4.2.3.2 TSA-based stent expansion

The governing equation for the 2-D triangular mesh element $\boldsymbol{F}^{ijk}_{torsion} = \boldsymbol{K}^{ijk}_{torsion}\boldsymbol{q}^{ijk}$ (Equation 4.34) in matrix form reads:

$$\begin{bmatrix} F_{i_x} \\ F_{i_y} \\ F_{j_x} \\ F_{j_y} \\ F_{k_x} \\ F_{k_y} \end{bmatrix}^{torsional} = \begin{bmatrix} \mathbf{k_{11}} & \mathbf{k_{12}} & k_{13} & k_{14} & k_{15} & k_{16} \\ \mathbf{k_{21}} & \mathbf{k_{22}} & k_{23} & k_{24} & k_{25} & k_{26} \\ k_{31} & k_{32} & k_{33} & k_{34} & \mathbf{k_{35}} & \mathbf{k_{36}} \\ k_{41} & k_{42} & k_{43} & k_{44} & \mathbf{k_{45}} & \mathbf{k_{46}} \\ k_{51} & k_{52} & \mathbf{k_{53}} & \mathbf{k_{54}} & k_{55} & k_{56} \\ k_{61} & k_{62} & \mathbf{k_{63}} & \mathbf{k_{64}} & k_{65} & k_{66} \end{bmatrix}^{torsional} \begin{bmatrix} u_i \\ v_i \\ u_j \\ v_j \\ u_k \\ v_k \end{bmatrix}$$

This extended form allows to notice that, firstly, the stiffness matrix $\boldsymbol{K}^{ijk}_{torsion}$ is symmetric and, secondly, that in the structure of $\boldsymbol{K}^{ijk}_{torsion}$ two different types of components can be distinguished. The first component type for a given vertex is the contribution of its own displacement to the force acting on it. The second distinguishable component is the contribution of displacements of other neighbours to the force generated on the node in question. In the matrix $\boldsymbol{K}^{ijk}_{torsion}$, the self-contribution takes the form of a 2×2 sub-matrix that is aligned along the diagonal. For example, for the vertex i it is the sub-matrix $\begin{bmatrix} \mathbf{k_{11}} & \mathbf{k_{12}} \\ \mathbf{k_{21}} & \mathbf{k_{22}} \end{bmatrix}$ (highlighted in bold in $\boldsymbol{K}^{ijk}_{torsion}$). Note that $\mathbf{k_{12}} = \mathbf{k_{21}}$ since $\boldsymbol{K}^{ijk}_{torsion}$ is symmetric.

The contribution of the neighbouring elements comprises the rest of the matrix. For example, the stiffness elements contributing to the force on the vertex j that results from the displacement of the neighbour k are captured in the following sub-matrix $\begin{bmatrix} \mathbf{k_{35}} & \mathbf{k_{36}} \\ \mathbf{k_{45}} & \mathbf{k_{46}} \end{bmatrix}$. Other way around, the elements contributing to the force on k due to the displacement of j are located in the sub-matrix $\begin{bmatrix} \mathbf{k_{53}} & \mathbf{k_{54}} \\ \mathbf{k_{63}} & \mathbf{k_{64}} \end{bmatrix}$. Note that again due to the symmetry of $\boldsymbol{K}^{ijk}_{torsion}$, $\mathbf{k_{35}} = \mathbf{k_{53}}, \mathbf{k_{45}} = \mathbf{k_{54}}, \mathbf{k_{36}} = \mathbf{k_{63}}, \mathbf{k_{46}} = \mathbf{k_{64}}$, which is to be expected in the case of reciprocal force two neighbours exert on each other.

This restructuring of the matrix $\boldsymbol{K}^{ijk}_{torsion}$ was convenient for computational implementation of the combined force from all neighbours based on the vertices connectivity matrix that was mentioned in Section 4.1.1. Thus, once the $\boldsymbol{K}^{ijk}_{torsion}$ has been assembled for a single triangular element, its stiffness components were re-

grouped into the stiffness matrix of the entire structure – $\boldsymbol{K}_{torsion}$ – by placing them on appropriate slots. Additionally, a new diagonal matrix $\boldsymbol{K_d}$ was constructed from diagonal elements of $\boldsymbol{K}^{ijk}_{torsion}$ and exemplified in Equation (4.10) when describing the Jacobi method earlier in the section. Further, another new matrix $\boldsymbol{K_d}_{torsion}$ for all vertices was constructed by extracting diagonal elements and eventually adding them in case of nodes shared by multiple triangles.

Numerical solution algorithm. To solve equation $\boldsymbol{Kq} = \boldsymbol{f}$, Farhat et al. (1998) proposed an iterative algorithm based on the Jacobi method, where $\boldsymbol{q}^{(n+1)}$ in the iteration $n+1$ is determined as follows:

$$\begin{aligned}
\overline{\boldsymbol{q}^{(n+1)}} &= -\boldsymbol{K_d}^{-1}(\boldsymbol{K}-\boldsymbol{K_d})\boldsymbol{q}^{(n)} + \boldsymbol{K_d}^{-1}\boldsymbol{f} \\
\boldsymbol{q}^{(n+1)} &= \omega^{(n+1)}_{optimal}\overline{\boldsymbol{q}^{(n+1)}} + (1-\omega^{(n+1)}_{optimal})\boldsymbol{q}^{(n)} \\
\omega^{(n+1)}_{optimal} &= \frac{\boldsymbol{r}^{(n)^T}[\boldsymbol{K}\boldsymbol{K_d}^{-1}\boldsymbol{r}^{(n)}]}{\|\boldsymbol{K}\boldsymbol{K_d}^{-1}\boldsymbol{r}^{(n)}\|_2} \\
\boldsymbol{r}^{(n)} &= \boldsymbol{f} - \boldsymbol{K}\boldsymbol{q}^{(n)}
\end{aligned}$$

where $\boldsymbol{K_d}$ stands for the diagonal part of $\boldsymbol{K}$ and $\omega^{(n+1)}_{optimal}$ is the optimal relaxation parameter. In every iteration $n+1$, $\omega^{(n+1)}_{optimal}$ aims at minimising the two-norm of the residual $\boldsymbol{r}^{(n+1)}$. The algorithm is an exact implementation of the Jacobi scheme with relaxation, which becomes apparent when the proposed expression for $\overline{\boldsymbol{q}^{(n+1)}}$ is rewritten in the following form:

$$\begin{aligned}
\overline{\boldsymbol{q}^{(n+1)}} &= -\boldsymbol{K_d}^{-1}(\boldsymbol{K}-\boldsymbol{K_d})\boldsymbol{q}^{(n)} + \boldsymbol{K_d}^{-1}\boldsymbol{f} \\
&= \boldsymbol{K_d}^{-1}(\boldsymbol{f} - (\boldsymbol{K}-\boldsymbol{K_d})\boldsymbol{q}^{(n)}) \\
&= \boldsymbol{K_d}^{-1}(\boldsymbol{f} - \boldsymbol{K_r}\boldsymbol{q}^{(n)}),
\end{aligned}$$

which is exactly Equation (4.13) of Jacobi method, after denoting the residual matrix $\boldsymbol{K_r} = \boldsymbol{K} - \boldsymbol{K_d}$.

To implement TSA for stent expansion, the Jacobi scheme was also employed to solve the system $\boldsymbol{K\delta} = \boldsymbol{f}$ on a vertex-by-vertex basis, making the following transfor-

mation:

$$\begin{aligned}
\boldsymbol{\delta}^{(n+1)} &= \boldsymbol{K_d}^{-1}(\mathbf{f} - \boldsymbol{K_r}\boldsymbol{\delta}^{(n)}) \\
&= \boldsymbol{K_d}^{-1}(\mathbf{f} - (\boldsymbol{K} - \boldsymbol{K_d})\boldsymbol{\delta}^{(n)}) \\
&= \boldsymbol{K_d}^{-1}(\mathbf{f} - \boldsymbol{K}\boldsymbol{\delta}^{(n)} + \boldsymbol{K_d}\boldsymbol{\delta}^{(n)}) \\
&= \boldsymbol{K_d}^{-1}\mathbf{f} - \boldsymbol{K_d}^{-1}\boldsymbol{K}\boldsymbol{\delta}^{(n)} + \boldsymbol{K_d}^{-1}\boldsymbol{K_d}\boldsymbol{\delta}^{(n)} \\
&= \boldsymbol{K_d}^{-1}\mathbf{f} - \boldsymbol{K_d}^{-1}\boldsymbol{K}\boldsymbol{\delta}^{(n)} + \boldsymbol{\delta}^{(n)}
\end{aligned}$$

Noting that the system should approach static equilibrium, i.e., $\boldsymbol{f} = \mathbf{0}$, and substituting in the above expression $\boldsymbol{K}\boldsymbol{\delta}^{(n)} = \boldsymbol{F}^{(n)}$, the final iterative algorithm for the torsional springs model can be summarised in the form below:

$$\begin{aligned}
&\boldsymbol{F}^{(n)} = \boldsymbol{K}_{lineal}\boldsymbol{\delta}^{(n)} + \boldsymbol{K}_{torsion}\boldsymbol{\delta}^{(n)} \\
&\overline{\boldsymbol{\delta}^{(n+1)}} = \boldsymbol{\delta}^{(n)} - (\boldsymbol{K_{d\ torsion}} + \boldsymbol{K}_{lineal-nodal})^{-1}\boldsymbol{F}^{(n)} \\
&\boldsymbol{\delta}^{(n+1)} = \omega\ \overline{\boldsymbol{\delta}^{(n+1)}} + (1-\omega)\ \boldsymbol{\delta}^{(n)}
\end{aligned} \tag{4.37}$$

Note that in every iteration, the torsional and the lineal spring forces were computed separately and added afterwards to obtain the total force $\boldsymbol{F}^{(n)} = \boldsymbol{K}_{lineal}\boldsymbol{\delta}^{(n)} + \boldsymbol{K}_{torsion}\boldsymbol{\delta}^{(n)}$. The separate computation was due to the different structural organisation of stiffness matrices $\boldsymbol{K}_{lineal}$ and $\boldsymbol{K}_{torsion}$, which resulted in a different mode of calculation for two types of forces. The organisation of the torsional stiffness matrices $\boldsymbol{K}_{torsion}$ and $\boldsymbol{K_{d\ torsion}}$ was described earlier in this section and the structure of $\boldsymbol{K}_{lineal}$ and $\boldsymbol{K}_{lineal-nodal}$ in Section 4.2.1. Since the Jacobi method was operating on the inverse diagonal matrix in every iteration, the diagonal components of both stiffness matrices had to be incorporated to overlay the effect of lineal and torsional springs, which was equivalent to adding the two matrices $\boldsymbol{K_{d\ torsion}} + \boldsymbol{K}_{lineal-nodal}$. The relaxation parameter ω was permanently set to 0.5, since this value resulted in the best convergence behaviour.

The deformation behaviour of the mesh equipped with torsional (and lineal) springs is demonstrated in Figure 4.18. To compare the resulting deformation to pure lineal and semi-torsional cases, the relevant figures from previous sections have been placed nearby (lineal in black, semi-torsional in blue and torsional in

turquoise). The initial mesh on the left most image underwent stepwise displacement in its top right node, 5 times by $\delta = [-2, -2]$. Nodes located on both axes were kept fixed and the stiffness was updated after each displacement cycle. As can be seen, the quality of the resulting mesh was satisfactory as its integrity was preserved and no element inversion occurred, which was comparable to the semi-torsional case and eliminated the problems that the lineal springs model faces.

Extension to 3-D stent case. In order to apply the torsional spring analogy to stent displacement, the algorithm was extended to 3-D. The main idea for the modification was to use the 2-D torsion spring analogy in the plane of each triangular element and then transfer the results to the 3-D stent world. More precisely, since the stent struts were modelled without taking thickness into account, each of the triangular elements lay in a 2-D space spun around its three points. Thus, it was possible to perform computations in the local coordinate system of the triangular elements, applying the 2-D torsional method, and then convert the obtained forces, displacements, etc., to the global coordinate system. Alternatively, one could convert the "local" stiffness matrix obtained for 2-D case into a global 3-D stiffness matrix, which was then used for calculation of forces and displacements in the global coordinate system. The latter way proved more convenient, since it did not require storing in memory all the local bases and conversion of displacements into these local coordinate bases, which was computationally more efficient. The schematic

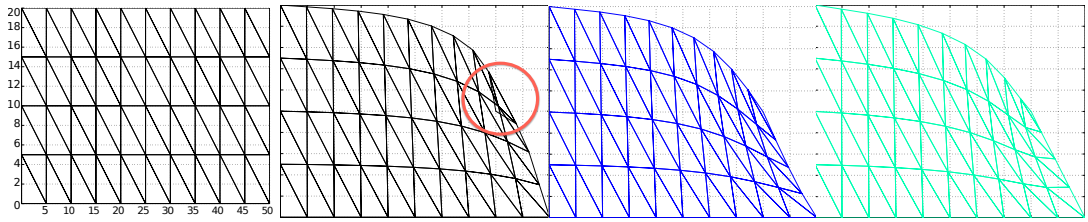

Figure 4.18: Comparison of lineal (black) and torsional (blue) springs networks: (a) initial configuration; (b) result after deformation with the lineal model and updated stiffness: element inversion occurred in the top right corner (area inside the red circle); (c) result after deformation with the semi-torsional model and updated stiffness: mesh integrity was preserved better and no element inversion occurred; (d) result after deformation with the torsional model and updated stiffness: mesh integrity was preserved better and no element inversion occurred, which was comparable with the result for the semi-torsional case (c).

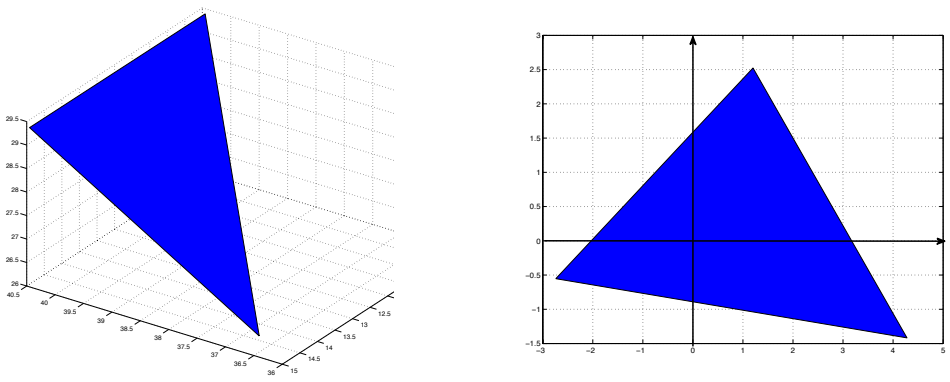

(a) (b)

Figure 4.19: (a) A 3-D configuration of the triangular element in the global coordinate system. (b) The same triangle in its local coordinate system, with local axes indicated with arrows.

way of switching coordinate systems is represented in Figure 4.19, where the first image illustrates the 3-D configuration of the triangular element and the second image shows the same triangle in its local coordinate system (with local axes indicated with arrows).

To implement this transformation, the local coordinate system basis had to be obtained first, together with local coordinates of the element nodes in that system. This was done with the PCA method discussed in Section 4.1.2. As already mentioned, the local coordinate system is actually a rotation matrix ($\boldsymbol{R}$) that can be used to switch between two coordinate systems. The matrix $\boldsymbol{R}$ was multiplied with local coordinates to obtain the global ones: $\boldsymbol{V}_{global} = \boldsymbol{V}_{local}\boldsymbol{R}^T$, and divided to go in the other direction. Similar to the 2-D case, the 2-D stiffness was first computed as described earlier in the section (Equation 4.34):

$$\boldsymbol{K}^{ijk}_{torsion-local} = \boldsymbol{R}^{ijk^T}\boldsymbol{C}^{ijk}\boldsymbol{R}^{ijk} \tag{4.38}$$

Then, the stiffness matrix was transformed back to the global coordinate system by multiplying it with the rotation matrix $\boldsymbol{R}$:

$$\boldsymbol{K}^{ijk}_{torsion-global} = \boldsymbol{R}\,\boldsymbol{K}^{ijk}_{torsion-local}\,\boldsymbol{R}^T \tag{4.39}$$

The last step was to restructure the stiffness matrix in two matrices: for self- and neighbours' contributions, as was done for the 2-D case, as well as determining the diagonal matrix to be later used for the iterative method.

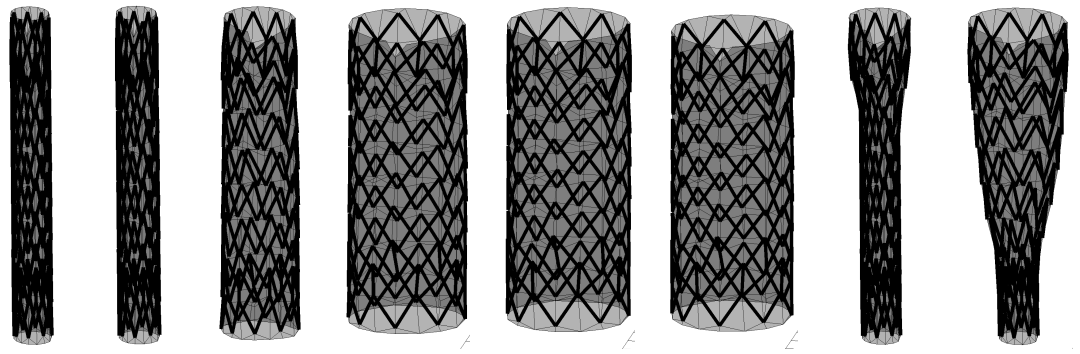

Figure 4.20: Free expansion of the stent graft with torsional spring analogy incremental algorithm. The sequence of images from left to right: (a) Initial crimped stent, (b) result after 10 iterations, (c) after 50 iterations, (d) after 150 iterations, (e) after 250 iterations, (f) after 500 iterations, (g) after 30 iterations of layered expansion, (h) after 100 iterations of layered expansion.

The stent expansion process used the same iterative method that was utilised in the 2-D case; one iteration is summarised in Equation (4.37). However, in order to apply the kinematic derivation for the torsional spring analogy, the requirement of small displacements had to be respected. To do that, the deformation process was split in a series of small deformations with regular updates of the stiffness according to the configuration in between. With respect to the force vector, as before, it contained a sum of both types of forces: lineal overlaid with torsional. Finally, to implement stent expansion, the LSA free expansion algorithm (described in Section 4.2.1.2) was modified to accommodate TSA by substituting the step 2 (Iterate) with the above iterative step (Equation 4.37).

Figure 4.20 illustrates the results obtained by the application of the described TSA method to the free expansion of a stent graft. Columns (a-f) capture progression in the stent opening after a certain number of computational iterations when the entire structure of the stent was let go simultaneously, while (g-h) feature layered expansion. The resulting expansion progression looks very similar to that of the lineal model in Figure 4.10, second row.

4.3 MODELLING THE VESSEL

This section outlines the steps required to create a computational model of the vessel which plays an essential role in the stent deployment procedure. The section briefly describes the reconstruction of the vessel geometry, its computational representation and implementation of contact with an expanding stent.

4.3.1 Segmentation

Clinical imaging data are usually packaged in the DICOM (Digital Imaging and Communications in Medicine) format, which has now become a standard for operating medical imaging information. Each DICOM file contains the pixel data of a patient recording, alongside of other attributes, like ID. A sequence of DICOM images that capture different "slices" of the scanned part of the body in 2-D can be combined, with the help of a specially dedicated software, to reproduce a 3-D representation of the scanned organ. Numerous software packages enable such reconstruction, called *segmentation*, some of which are directly integrated into imaging equipment.

In this work, the segmentation was performed using the Sheffield Image Registration Toolkit (ShIRT) which is a dedicated semi-automatic software allowing segmentation of the vessel geometries from the CT scans (Barber et al., 2007). The resulting meshes were smoothed and decimated to a size of approximately 50,000 vertices to make them applicable to virtual stent grafting. The outcome of the segmentation, which is a 3-D representation, was stored as an STL file or some other format, such as OBJ file, etc., that supports higher-order surfaces. Figure 4.21 (a) and (b) show one DICOM image and the reconstructed 3-D geometry, respectively.

4.3.2 Geometry reconstruction

Centerline. A very useful feature of the vessel geometry is its *skeleton* representation, or *centerline*. As discussed in Section 4.1.4, the vessel centerline is used in the preliminary step of the stent expansion process to obtain the initial positioning of the device. To achieve this, a common representation of the centerline is utilised, which includes an ordered list of points lying along the centerline. Usually each segmentation software has a means of computing a centerline of a vessel according to a definition used in that package. For example, the skeleton can be defined as a

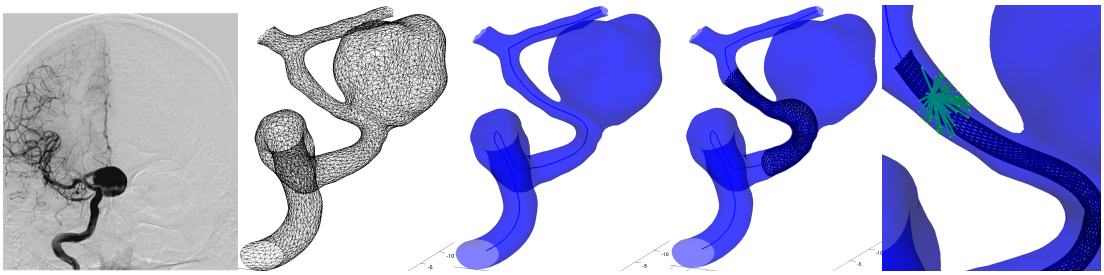

(a) (b) (c) (d) (e)

Figure 4.21: Workflow to reconstruct a vessel geometry: (a) DICOM image capturing the angiography of cerebral vessels of a patient (image from Pierot 2011); (b) 3-D vessel geometry obtained after the segmentation of the sequence of DICOM images; (c) 3-D vessel surface with centerline in black; (d) contact is detected when stent nodes have moved sufficiently close to the vessel wall; (e) stent-vessel neighbours visualised as green lines emanating from stent vertices to their potential vessel neighbours in contact (zoomed).

representation of the main line of symmetry of the object (see Figure 4.21, c), and it can be computed, e.g., by searching for points which constitute the centers of a set of maximal spheres that fit inside the vessel. Since the centerline can easily be exported together with the 3-D vessel surface from an ordinary segmentation software, it was taken for granted here and assumed as given for the input of the stent expansion algorithm.

Data structures. As was the case for the stent, the vessel information was stored in a data structure with multiple parameters. The structure could be as rich as needed, but the most essential features were the following

- matrix $\boldsymbol{V}$ with dimensions $n \times 3$ that contains the coordinates of the vessel vertices; each row has the form $\boldsymbol{v}_i = (x_i, y_i, z_i)$ for a vertex i, where i is a global index of the vertex running for $i = 1...n$, and n is the number of nodes;
- mesh connectivity table that stores triples of vertices making up the surface mesh in the form $[v_i, v_j, v_k]$;
- ordered list of centerline points in the form $\boldsymbol{c}_j = (x_j, y_j, z_j)$ for a centerline node j, where j is running for $j = 1...m$ and m is the number of centerline points.

From the above key features, more parameters were computed and stored in the vessel structure in order to be quickly accessed during the simulation process. For example, another very useful parameter was the connectivity table that was computed from mesh triples. The connectivity table $Conn$ listed for each vertex its direct neighbours in the mesh in the form $i : [n_k, n_l, ..., n_m]$. Additionally, the matrix $\boldsymbol{V}$ had a twin matrix representing the nodal coordinates in the local coordinate system of the stent (since all computations for the expansion process were performed in the stent egocentric coordinate system). This twin matrix was also stored in memory for faster access during the simulation.

4.3.3 Rigid contact

The mechanical behaviour of the vessel was implemented in two different ways. In some experiments, the vessel was treated as a rigid body (Chapters 5 and 6), in others the vessel was flexible (Chapter 7). Starting with the rigid-wall assumption allowed thorough examination and validation of the stent expansion process without interference of any additional parameters. In order to account for the presence of the vessel, the LSA free expansion procedure (Section 4.2.1) was modified to incorporate the possibility of contact with the rigid vessel. The pseudocode of the incremental LSA displacement algorithm for stent expansion inside vessels is depicted below.

The stent expansion process was performed on a vertex-to-vertex basis, and the coordinates of a vertex were updated after each iteration, as long as no contact between the vertex and the vessel occurred. The contact was defined to occur when the distance between the vertex of the stent and any of the vessel vertices became smaller than a chosen parameter ϵ. To detect contact, a contact check was performed in every iteration of the deployment loop before the update of the coordinates of stent vertices (step “Check contact”). After the contact was detected, the displacements of the stent vertex in contact were still calculated in future iterations, to enable possible readjustments resulting from the tension of the neighbouring nodes. However, its position could only change if it was located within the ϵ-boundary of the vessel inner surface. Figure 4.21 (d) illustrates the termination of the expansion process.

In order to detect contact in a rapid manner, a special matrix was calculated, which relates the vertices of the stent with those of the vessel in case they are likely

to come in contact at some point. The computation was performed before the beginning of the expansion process and after the crimped stent was positioned along the centerline of the vessel. The information was stored in a matrix of potential stent-vessel neighbours in the form of a list of vessel nodes for each stent vertex i, i.e., $i : [v_k, v_l, ..., v_m]$, where $[v_k, v_l, ..., v_m]$ is the list of potential vessel neighbours. Given the position of the crimped stent along the centerline of the vessel, for a node of the crimped stent, those nodes were set to be the potential points of contact that were located within a sphere of a chosen radius, which was set equal to the diameter of the vessel. Figure 4.21 (e) illustrates the potential vessel neighbours for one vertex of the stent by the green lines emanating from stent vertices to their potential vessel neighbours.

Incremental LSA displacement algorithm for stent expansion inside vessels:

1. **Calculate initial displacement of stent vertices** by subtracting the load-free (lf) coordinates of vertices from the current crimped coordinates (cr). For a vertex $\boldsymbol{v}_i = (x_i, y_i, z_i)'$ the initial crimping delta $\boldsymbol{\delta}_i^{cr}$ is found by:

$$\boldsymbol{\delta}_i^{cr} = \begin{pmatrix} \delta_{x_i}^{cr} \\ \delta_{y_i}^{cr} \\ \delta_{z_i}^{cr} \end{pmatrix} = \begin{pmatrix} x_i^{cr} \\ y_i^{cr} \\ z_i^{cr} \end{pmatrix} - \begin{pmatrix} x_i^{lf} \\ y_i^{lf} \\ z_i^{lf} \end{pmatrix}$$

2. **Iterate** until there is almost no change in the expansion delta $\boldsymbol{\delta}^{exp}$, i.e., stop when
$max\{|\delta_{x_i}^{exp}|, |\delta_{y_i}^{exp}|, |\delta_{z_i}^{exp}|\} \leq \epsilon$, where i ranges over all nodes ($\epsilon = 10^{-6}$)

   - **Calculate restoring force $\boldsymbol{F}_i$** for each node i from Equation (4.16)

$$\boldsymbol{F}_i = \sum_{j=1}^{n_i} k_{ij}(\boldsymbol{\delta}_j^{cr} - \boldsymbol{\delta}_i^{cr})$$

   - **Calculate expansion delta $\boldsymbol{\delta}_i^{exp}$** for each node i from force and nodal stiffness

$$\boldsymbol{\delta}_i^{exp} = -\frac{\boldsymbol{F}_i}{\sum_{j=1}^{n_i} k_{ij}}$$

   - **Check contact** between the newly determined stent coordinates and the vessel:

for each stent vertex v_i and each potential vessel contact vertex $p_j \in P_i$
if they are closer than ϵ: $\|(\boldsymbol{v}_i + \boldsymbol{\delta}_i^{exp}) - \boldsymbol{p}_j\| < \epsilon$
add i to set C of nodes in contact: $C := C \cup \{i\}$

- **Update stent** nodal coordinates for each node i not in contact, $i \notin C$

$$\begin{pmatrix} x_i^{cr} \\ y_i^{cr} \\ z_i^{cr} \end{pmatrix} := \begin{pmatrix} x_i^{cr} \\ y_i^{cr} \\ z_i^{cr} \end{pmatrix} + \begin{pmatrix} \delta_{x_i}^{exp} \\ \delta_{y_i}^{exp} \\ \delta_{z_i}^{exp} \end{pmatrix}$$

- **Update crimping delta** values $\boldsymbol{\delta}_i^{cr}$ for each node $i \notin C$, by adding expansion displacement $\boldsymbol{\delta}_i^{exp}$ to the previous $\boldsymbol{\delta}_i^{cr}$

$$\boldsymbol{\delta}_i^{cr} = \begin{pmatrix} \delta_{x_i}^{cr} \\ \delta_{y_i}^{cr} \\ \delta_{z_i}^{cr} \end{pmatrix} := \begin{pmatrix} \delta_{x_i}^{cr} \\ \delta_{y_i}^{cr} \\ \delta_{z_i}^{cr} \end{pmatrix} + \begin{pmatrix} \delta_{x_i}^{exp} \\ \delta_{y_i}^{exp} \\ \delta_{z_i}^{exp} \end{pmatrix}$$

3. **Output stent** nodal coordinates

4.3.4 Flexible contact

One of the goals of the developed stent deployment method was to be able to model the vessel tissue as non-rigid, in order to account for a potential deformation of the vessel geometry in the course of the deployment procedure. The mechanical response of the vessel tissue was approximated with a linear elastic model. In general, the distensibility of the large arteries is not purely elastic, but rather the vessels exhibit a complex viscoelastic stress-train response (see Section 2.1.1). However, viscoelastic effects were reported to be negligible within the physiological ranges of pressure (Tardy et al., 1991). Hence, the implemented model assumed the elastic behaviour of the vessel tissue for reasons of simplicity and computational efficiency.

Stiffness. Similarly to the stent, the vessel was represented as a mesh of linear springs with isotropic stiffness, and the deformation was propagated inside the mesh through linear elastic forces of the springs. To set the stiffness of vessel springs, a formula proposed by Lloyd et al. (2007) was utilised, which has been an-

alytically derived from the finite element method (FEM). The authors equated the stiffness matrices of the linearised spring-mass equations with the element stiffness matrix calculated using the FEM. The obtained approximative formula was proposed for arbitrary triangular meshes and related the springs' stiffness k_{ij} to the Young's modulus of the material E, the thickness of the material plane t and the areas of triangular elements A_e:

$$k_{ij} = \sum_e Et\frac{\sqrt{3}}{4}\frac{A_e}{A_0}, \tag{4.40}$$

where A_0 is the area of an equilateral triangle with the edge length equal to the length of the spring $(i-j)$. The sum is calculated over all adjacent triangular elements (e) that share the spring $(i-j)$, in order to model the stiffness contribution of material from all corresponding elements. Further, the *nodal* stiffness of the vessel mesh was defined as a sum of stiffness values of all springs emanating from this node: $\boldsymbol{K}_{i,nodal} = \sum_{j=1}^{n_i} k_{ij}$, where n_i is the number of direct neighbours of node i.

To set the stiffness of the stent springs in an analogous way for consistency, it was necessary to find the Young's modulus of the entire stent, which was not straightforward due to the complex design and distribution of nitinol wires. However, Zahora and Hanus (2003) provided an approximative equation for the Young's modulus of the entire stent. They modelled a stent as a chain of rings consisting of several semicircles and derived the stent stiffness formula based on geometrical parameters of strut wires and elasticity of the material. Assuming d is the diameter of the strut wire (m), r is the radius of a semicircle, n is the number of semicircles and E is the Young's modulus of elasticity of the material (Pa), the Young's modulus of the stent E' could be calculated as:

$$E' = \frac{3Ed^4}{8\pi^2 nr^4} \tag{4.41}$$

Contact. The contact between the stent and the vessel was implemented as a direct transfer of the residual nodal forces in the stent structure to the vessel mesh. The residual stent forces were acting as external stresses on the vessel, triggering the strain response of the vessel tissue. Since the vessel was represented as a mesh of lineal springs, the deformation was propagated inside the mesh through linear elastic forces of the vessel springs. Hence, the displacement of the vessel node i was computed as follows:

$$\boldsymbol{\delta}_i = \frac{\boldsymbol{F}_i^{ext} - \boldsymbol{F}_i^{int}}{\boldsymbol{K}_{i,nodal}}, \tag{4.42}$$

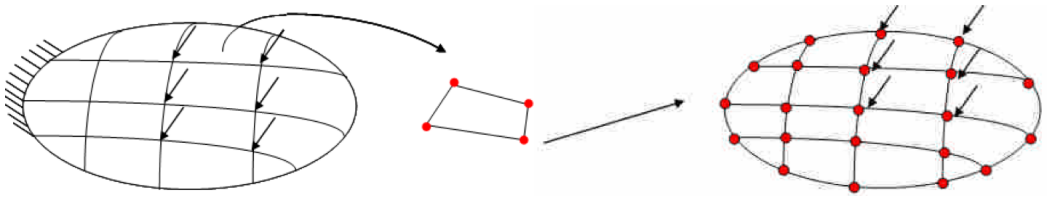

(a) (b)

Figure 4.22: Schematic illustration of the FEA process. (a) The object is subdivided into a set of finite elements joined by corresponding nodes (marked in red). (b) The governing equations of all the elements are assembled into a global matrix equation.

where the external force $\boldsymbol{F}_i^{ext}$ was computed as the sum over the residual forces of all stent vertices k that came into contact with the vessel vertex i ($k \perp i$), that is:

$$\boldsymbol{F}_i^{ext} = -\sum^{k \perp i} \boldsymbol{F}_k^{st}$$

The internal force $\boldsymbol{F}_i^{int}$ of the vessel vertex i was determined in a similar way to the stent:

$$\boldsymbol{F}_i^{int} = \sum_{j=1}^{n_i} k_{ij}(\boldsymbol{\delta}_j^{def} - \boldsymbol{\delta}_i^{def}),$$

where $\boldsymbol{\delta}_j^{def}$ is the displacement of the neighbouring node j, computed as the difference in vertex coordinates between the current to the initial vessel geometry. Finally, $\boldsymbol{K}_{i,nodal}$ was the nodal stiffness of the vessel vertex i ($\boldsymbol{K}_{i,nodal} = \sum_{j=1}^{n_i} k_{ij}$).

Modelling flexible vasculature required modification of the stent expansion procedure described in the pseudocode above (Incremental LSA displacement algorithm for stent expansion inside vessels). In particular, the steps following the contact check in the iterative procedure had to be altered. Firstly, the contact check was performed between the current stent and the current potentially deformed vessel (and not the initial undeformed vessel). Secondly, the vessel update procedure had to be included after the stent update step. The new vessel nodal coordinates were determined by adding the newly determined nodal displacements (Equation 4.42) to the coordinates from the previous iteration.

4.4 Finite Element Analysis

This section briefly outlines the finite element analysis (FEA) method which was used for the validation of the novel fast stent deployment method developed in this

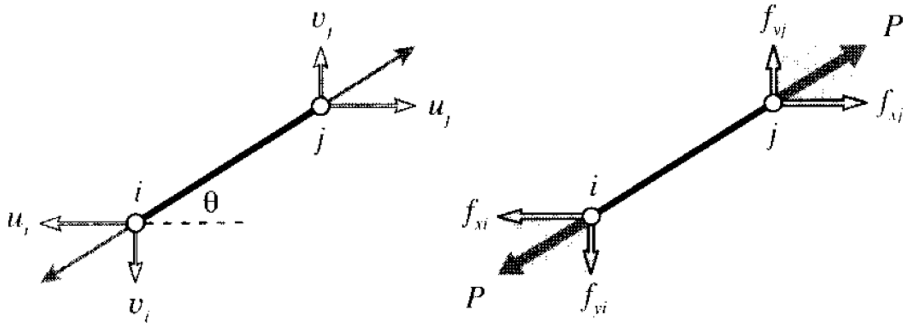

(a) (b)

Figure 4.23: Individual truss element. (a) Displacement components u and v of end nodes i and j (image from Roylance 2001). (b) Components of axial force P and nodal force components f (image from Roylance 2001).

thesis (see diagram in Figure 4.1). The implementation of the FEA model was a collaborative effort[6], performed using Abaqus suite (Dassault Systemes Simulia Corp., Providence, RI, USA). Since the FEA model only served as a benchmark for comparison performed in Chapter 6, the basic theory behind FEA is outlined here merely for the sake of completeness.

Finite Element Analysis (FEA) is a numerical method that enables finding approximative solutions of partial differential equations and integral equations associated with complex structures. The analysis starts by dividing the geometry of the object of interest into a collection of regions or "finite elements" that are connected by a set of nodes (see Figure 4.22). Certain boundary conditions can be prescribed to some of the nodes of the constructed FEA model, such as fixed displacements or prescribed loads. Thereafter, the solver assembles a system of equations governing the behaviour of the model and solves it:

$$\mathbf{K}_{ij}\mathbf{u}_j = \mathbf{f}_i, \tag{4.43}$$

where $\mathbf{u}$ is the displacement vector of the nodes, $\mathbf{f}$ is the vector of external loads on the nodes and $\mathbf{K}$ is the stiffness matrix. Finally, the resulting numerical output of displacements, stresses, etc., is visualised and analysed.

The basic principal of FEA can be illustrated on the example of a truss element.

[6] In collaboration with the Cardiovascular Unit, University College London, Institute of Child Health and Great Ormond Street Hospital for Children, London

2-D truss element. Consider a simple case of a 2-D truss element having two nodes i and j and building an angle θ with the horizontal axis, as illustrated in Figure 4.23 (a). The displacement of such an element can be described by the vector $\mathbf{u}$ in the following form:

$$\mathbf{u}^T = [u_i, v_i, u_j, v_j] \tag{4.44}$$

The elongation δ, expressed in the coordinate system of the element, can be linked to the displacement vector $\mathbf{u}$ by:

$$\delta = (u_j \cos\theta + v_j \sin\theta) - (u_i \cos\theta + v_i \sin\theta) \tag{4.45}$$

or in a matrix representation:

$$\delta = [-c \; -s \quad c \quad s] \begin{bmatrix} u_i \\ v_i \\ u_j \\ v_j \end{bmatrix}, \tag{4.46}$$

where $c = \cos\theta$ and $s = \sin\theta$.

According to Hook's law, the axial force P responsible for elongation δ is given by $P = (AE/L)\delta$ for linear elastic material, where A is the cross-sectional area, L is the length and E the modulus of elasticity of the given truss element (see Figure 4.23, b). Then, the corresponding force components are determined as:

$$\begin{bmatrix} f_{xi} \\ f_{yi} \\ f_{xj} \\ f_{yj} \end{bmatrix} = \begin{bmatrix} -c \\ -s \\ c \\ s \end{bmatrix} P = \begin{bmatrix} -c \\ -s \\ c \\ s \end{bmatrix} \frac{AE}{L}\delta = \begin{bmatrix} -c \\ -s \\ c \\ s \end{bmatrix} \frac{AE}{L} [-c \; -s \quad c \quad s] \begin{bmatrix} u_i \\ v_i \\ u_j \\ v_j \end{bmatrix} \tag{4.47}$$

After performing matrix multiplication, Equation (4.47) becomes:

$$\underbrace{\begin{bmatrix} f_{xi} \\ f_{yi} \\ f_{xj} \\ f_{yj} \end{bmatrix}}_{\mathbf{f}_i} = \underbrace{\frac{AE}{L} \begin{bmatrix} c^2 & cs & -c^2 & -cs \\ cs & s^2 & -cs & -s^2 \\ -c^2 & -cs & c^2 & cs \\ -cs & -s^2 & cs & s^2 \end{bmatrix}}_{\mathbf{k}_{ij}} \underbrace{\begin{bmatrix} u_i \\ v_i \\ u_j \\ v_j \end{bmatrix}}_{\mathbf{u}_j}, \tag{4.48}$$

where $\mathbf{k}_{ij}$ is the "element stiffness matrix", with each term representing the contribution of one of the displacements to one of the force components.

To capture contributions of all elements of the structure, the global system of equations has to be assembled by joining together the stiffness matrices of each truss element. This is done by taking into account the fact that at every vertex, forces exerted by neighbouring elements should be balanced by the external force at that vertex. That is, at static equilibrium, all forces arising from the neighbouring elements $\mathbf{f}_i^{elem}$ at a given vertex must sum to the external load applied at that vertex $\mathbf{f}_i^{ext}$ (see Figure 4.24):

$$\mathbf{f}_i^{ext} = \sum_{elem} \mathbf{f}_i^{elem} = \sum_{elem} \left(\mathbf{k}_{ij}^{elem} \mathbf{u}_j \right) = \left(\sum_{elem} \mathbf{k}_{ij}^{elem} \right) \mathbf{u}_j = \mathbf{K}_{ij} \mathbf{u}_j \tag{4.49}$$

To ensure the correct assembling, each element stiffness matrix $\mathbf{k}_{ij}^{elem}$ is placed at the corresponding position in the system stiffness matrix $\mathbf{K}_{ij}$.

Having assembled the system of equations, the FEA solver performs the analysis. At the beginning, every node of the mesh has to be sufficiently defined, meaning that either displacement or external load should be assigned to it, which provide the boundary conditions for the problem. With this information, the FEA solver computes the appropriate loads that correspond to prescribed displacements and the displacements for provided external loads.

4.5 GENETIC ALGORITHMS

Genetic algorithms (GAs) were used to optimise the performance of the novel virtual stent deployment method. Namely, the aim was to find the optimal stiffness values for the fast stent model. In general, stiffness settings have significant implications on the expansion process. Without any modification to other parts of the expansion algorithm, alterations to the stiffness setting can lead to substantial degradation or

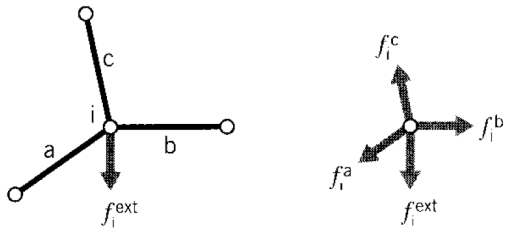

Figure 4.24: Contribution of neighbouring elements to the total nodal force (image from Roylance 2001).

even a complete loss of expanding properties of the modelled device. On the whole, instantiation of the stiffness values for spring models is not straightforward. Several attempts have been reported in literature, describing the way of finding the best stiffness parameters for spring models for different applications; for the most part, they are rather *ad hoc* (Louchet et al., 1995). Various optimisation techniques such as simulated annealing (Deussen et al., 1995), neural networks (Nurnberger et al., 1998), genetic algorithms (Bianchi et al., 2004), etc., have been employed for adapting the behaviour of a spring system, chosen depending on the concrete application and available resources.

Here, the framework of Genetic Algorithms (GAs) was utilised as a means to optimise stiffness setting. GAs draw inspiration from natural evolution (Goldberg and Holland, 1988). They simulate populations of individuals, each individual being represented by a certain number of *genes* that encode parameters of the investigated problem. The fitness of an individual was determined by a *cost* or *fitness function* that was formulated for a given problem setting (see Chapter 6). At the beginning of the optimisation process, the population was randomly initialised by assigning to individuals random values of genes that define them. In the course of an iteration, the fitness was assessed and the new population was formed based on the fitness/cost function and the *generic operators* of mutation and crossover applied to *selected* individuals. *Mutation* means that when copying the genes from the current to a new generation, random changes could occur with a certain probability. In contrast, *crossover* combined genes from selected individuals to form an offspring. The aim of the algorithm was to make the population converge to a final population in which the best performing individuals are as close as possible to the optimal solution of the problem. As a rule, GAs do not guarantee a convergence to the global optimum; however, they are able to find good approximative solutions by reaching local optima. In our case, the idea was to utilise the known FEA stent configurations and reported residual forces as a reference for optimising the stiffness parameters of the novel stent deployment method. Thus, the cost function for the GA formulation had to take into account the discrepancy between the fast method and FEA outcomes in terms of nodal distances and the value of forces. The goal was to find stiffness parameters resulting in better alignment between two methods.

Formally, the stiffness optimisation problem can be written in the following way. We aim at minimising the cost function $C(k)$ which is defined as a combination of

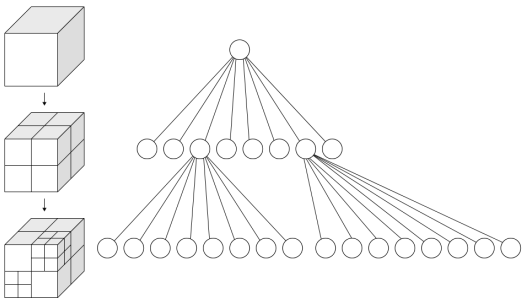

Figure 4.25: The recursive subdivision of a cell into 8 sub-cells and the corresponding octree data structure (image from `commons.wikimedia.org`).

errors from measured discrepancy in nodal position and force measurements between the fast and FEA method, which are dependent on the springs stiffness values k. The only constraint on the value of k is that it should be nonnegative:

$$\begin{aligned} \underset{k}{\text{minimize}} \quad & C(k) \\ \text{subject to} \quad & k \geq 0. \end{aligned} \tag{4.50}$$

The exact definition of $C(k)$, the rest of the GA setup and the results of the experiments are reported in Chapter 6.

4.6 OMNITREE

In order to perform the haemodynamic analysis of a vessel with Computational Fluid Dynamics (CFD), it is necessary to discretise the continuous fluid domain into a finite domain of grid cells (see workflow diagram in Figure 4.1). There are many software packages offering this functionality. This project used the package CFD-VisCART (ESI Group, France) which is linked to the CFD solver CFD-ACE+ (ESI Group, France).

CFD-VisCART is an adaptive Cartesian mesh generation system that is able to handle extremely complex geometries. It works with tree-based data structures generating Cartesian-based non-conforming grids. The Cartesian grid approach uses a recursive subdivision of grid cells and is very efficient in filling a space with a minimum number of cells, given a certain grid resolution.

CFD-VisCART offers both *octree* and *omni-tree* methods for subdividing cells. With octree (Mitchell and Vavasis, 1992), a cell is divided into eight sub-cells along

all 3 dimensions (see Figure 4.25). In some cases, octree may result in badly proportioned cells. This can occur, for example, when the cell size along one dimension is much larger than in the other two. In contrast, the omni-tree data structure supports anisotropic grid adaptation and can choose to split the cell along one, two or all three dimensions, avoiding thereby the aforementioned problem. The additional advantage of omni-tree (and anisotropic grid adaptation) is the dramatic reduction in the total number of cells needed to achieve a given level of solution accuracy.

During grid generation, CFD-VisCART requires specification of the maximum division level, which determines the maximum number of times (levels) a cell can be divided. The division starts from the bounding box of the domain, which is considered to be the first cell and is assigned level 0. Assuming the length of the bounding box is L in the X direction, it would then be split to $\frac{L}{2}$, $\frac{L}{4}$, $\frac{L}{8}$, $\frac{L}{16}$, etc., at every division level, respectively. Hence, the minimum cell size at level 1 would be $\frac{L}{2}$, at level 2 $\frac{L}{4}$, at level 3 $\frac{L}{8}$ and so on. In general, the minimum cell size at level n is calculated as $\frac{L}{2^n}$ (ESI, 2013b). For example, specifying the maximum division level in the Z direction as level 5, would split the bounding box along Z dimension in 32 cells.

This study used the "Projected Single Domain" mesh in which Cartesian cells were generated in most of the domain, whereas the mesh near the geometry surfaces was projected onto them to capture the geometry curvatures and thus obtain a body-fitted grid. With respect to cells located close to the boundaries of the geometry, the "Cell Size" method was utilised for their refinement. The method allowed cell sizes for boundary layers to be specified based on levels as explained above. Within each level of refinement, it was possible to specify the minimum number of layers to ensure a smooth transition from the fine boundary layers into more coarse inner parts of the mesh. Figure 4.26 shows an example mesh generated by CFD-VisCART which represents the cross section of a patient-specific aortic geometry. As can be seen, boundary layers near the vessel walls feature finer mesh.

After meshing, the resulting 3-D Cartesian grid was imported directly to the flow solver CFD-ACE+ for CFD computations (see Chapter 7).

4.7 Finite Volume Method

After the stent deployment procedure, the next step is to evaluate the alterations in the haemodynamic environment of the treated vessel (see workflow diagram in

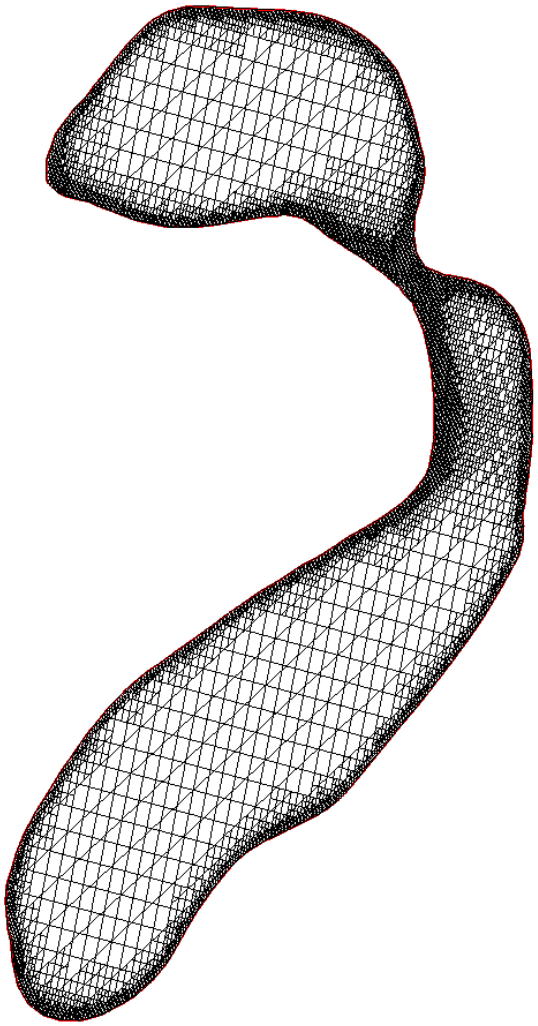

Figure 4.26: A cross section of the mesh generated by CFD-VisCART for a patient-specific aortic geometry, with gradual mesh refinements at boundary layers.

Figure 4.1). For that purpose, the established technique of Computational Fluid Dynamics (CFD) was utilised (as mentioned in Section 3.2). Because of the wide acceptance of the CFD method, this project capitalised on the already-established CFD methodology, and the contribution lies in the performed computational experiments (Chapter 7), rather than methodology. This section outlines the theory behind the CFD method merely for the sake of completeness.

There are many different CFD solvers available to carry out computations. In this project, the CFD-ACE+ suite (ESI Group, France) was employed, which solves the incompressible Naviér-Stokes equations using a finite volume formulation. Naviér-Stokes equations stem from mathematical formulations of the main conser-

vation laws (ESI, 2013a):

1. The mass of a fluid is conserved, meaning that there is no loss or gain of mass in the system. This requires that the time rate of change of mass in a control volume is balanced by the net mass flow into the same control volume, which formally written gives the conservation of mass equation:

$$\frac{\partial \rho}{\partial t} + \nabla \cdot \left(\rho \boldsymbol{U}\right) = 0, \tag{4.51}$$

   where ρ is the fluid density and $\boldsymbol{U}$ is the velocity vector. The first term on the left-hand side of the equation expresses the time rate of change of the density (mass per unit volume). The second term is referred to as the convective term and indicates the net mass flow across the boundaries of the control volume.

2. The time rate of change of momentum is equal to the sum of the forces acting on the fluid (Newton's second law)

$$\rho\left(\frac{\partial \boldsymbol{U}}{\partial t} + \boldsymbol{U} \cdot \nabla \boldsymbol{U}\right) = -\nabla P + \nabla \boldsymbol{\tau} + \boldsymbol{F}, \tag{4.52}$$

   where P indicates the pressure, $\boldsymbol{\tau}$ is the deviatoric stress tensor and $\boldsymbol{F}$ denotes external forces.

CFD-ACE+ employs the finite volume method (FVM) to approximate the solution of equations. To employ FVM, the solution domain is first divided into a set of cells known as control volumes (which are not necessarily the primary cells of the

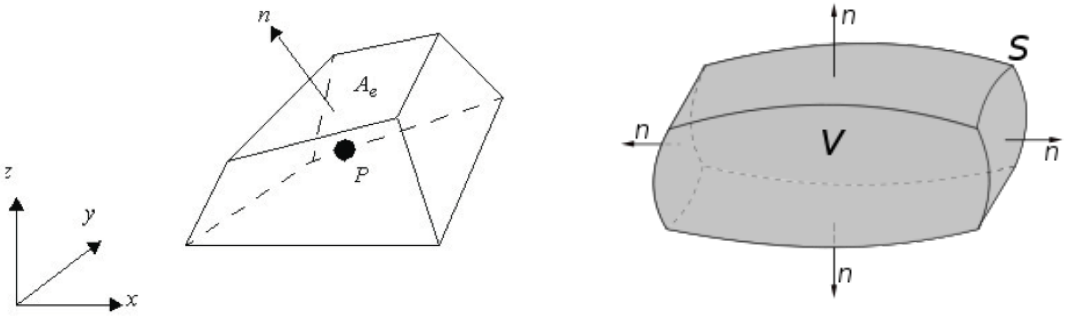

(a) (b)

Figure 4.27: (a) Example of a 3-D computational cell or control volume (image from ESI 2013a). (b) Boundary surface $S = \partial V$ of a computational cell V with the normal vectors n (image from ESI 2013a).

mesh), where the values of variables are stored at the center of the control volume (see Figure 4.27, a). Afterwards, the governing equations are numerically integrated over each of these computational cells. The values of the variables between cell centers are obtained through interpolation. The obtained discretisation equation captures the conservation principle for the variable inside the control volumes.

Discretisation. The majority of the governing equations can be written as a generalised transport equation for any conservable quantity ϕ:

$$\underbrace{\frac{\partial \rho\phi}{\partial t}}_{\text{transient}} + \underbrace{\nabla\cdot\left(\rho\boldsymbol{U}\phi\right)}_{\text{convection}} = \underbrace{\nabla\cdot\left(\Gamma\nabla\phi\right)}_{\text{diffusion}} + \underbrace{S_\phi}_{\text{sink/source}}, \tag{4.53}$$

where Γ is the diffusion coefficient and S is the sink or source term. For FVM, this equation can be integrated over each control volume Ω in the following way:

$$\int_\Omega \frac{\partial \rho\phi}{\partial t}\, d\Omega + \int_\Omega \nabla\cdot\left(\rho\boldsymbol{U}\phi\right)\, d\Omega = \int_\Omega \nabla\cdot\left(\Gamma\nabla\phi\right)\, d\Omega + \int_\Omega S_\phi\, d\Omega, \tag{4.54}$$

Each term of Equation (4.54) has to be discretised. The transient term is discretised using the first-order Euler method as follows:

$$\int_\Omega \frac{\partial \rho\phi}{\partial t}\, d\Omega = \frac{\rho^n\phi^n\Omega^n - \rho^{n-1}\phi^{n-1}\Omega^{n-1}}{\Delta t}, \tag{4.55}$$

where n denotes the current time step, $n-1$ is the previous time step and Δt is the time step, or using the second order Crank-Nicolson scheme to increase accuracy.

To discretise convection and diffusion terms, FVM uses the Gauss divergence theorem that converts volume integrals containing a divergence term ($\nabla\cdot$) into surface integrals. The theorem states that the rate of change of mass in the control volume is equal to the net mass flux through its boundary:

$$\int_V \nabla\cdot\boldsymbol{F}\, dV = \oint_{\partial V} \boldsymbol{F}\cdot\boldsymbol{n}\, dS, \tag{4.56}$$

where S indicates the surface boundary of volume V ($S = \partial V$) and $\boldsymbol{n}$ is the normal to the surface (see Figure 4.27, b). This way, the volume integral over the volume V on the left-hand side of the equation is translated into the surface integral over the surface S of the volume V on the right-hand side.

The Gauss theorem applied, for example, to the convection term of Equation (4.54) leads to:

$$\int_\Omega \nabla \cdot (\rho \boldsymbol{U} \phi)\, d\Omega = \oint_{\partial\Omega} \rho \boldsymbol{U} \phi \cdot \boldsymbol{n}\, dS \tag{4.57}$$

$$= \sum_e \left(\rho_e \phi_e \boldsymbol{U}_e^n\right) A_e \tag{4.58}$$

$$= \sum_e C_e \phi_e, \tag{4.59}$$

where the index e indicates one of the faces of the current computational cell, A_e is the area of the face e, $\boldsymbol{U}_e^n$ stands for the velocity components along the normal vector of the face and C_e can be described as the mass flux through the face.

Similar to the convection term, the diffusion term is also discretised with the help of the Gauss theorem, while the source term is linearised. The details are provided in ESI (2013a).

Interpolation. In FVM, the variable of interest ϕ is available only in the centers of the control volume, as mentioned before. Hence, to get the values at cell faces (ϕ_e) interpolation has to be performed. CFD-ACE+ offers several interpolation schemes that provide varying levels of numerical stability and accuracy.

The simplest interpolation method is the first-order *upwind* scheme. In this method, ϕ_e is taken to be the value of ϕ at the upstream grid point, i.e., ϕ_e equals either ϕ_P or ϕ_E of adjacent cells P or E, respectively, depending on the flow direction

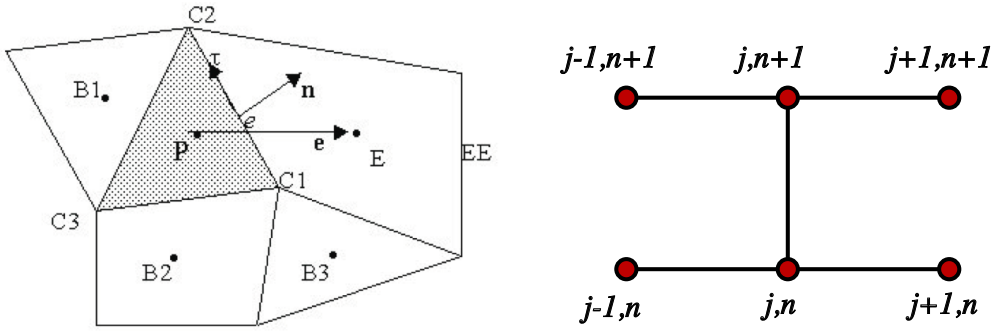

(a) (b)

Figure 4.28: (a) Illustration of interpolation schemes for the computational cell P with face e (image from ESI 2013a). (b) Working terms in the Crank-Nicolson scheme in 1-D (image from `source.ggy.bris.ac.uk`).

(see Figure 4.28 for schematic illustration):

$$\phi_e^{UP} = \begin{cases} \phi_P & \text{if } V_e^n > 0 \\ \phi_E & \text{if } V_e^n < 0 \end{cases} \tag{4.60}$$

The upwind scheme is numerically very stable but offers limited accuracy due to the first-order nature. Hence, to improve accuracy, second-order *central differencing* scheme is often used. This scheme assumes that ϕ varies linearly between the two adjacent centers (P and E) and calculates the value ϕ_e as the weighted average of ϕ_P and ϕ_E:

$$\phi_e^{CD} = \Upsilon_e \phi_P + (1 - \Upsilon_e)\phi_E, \tag{4.61}$$

where Υ_e is the weighting function.

The presented second-order central differences scheme is prone to numerical instabilities. Therefore, a combination of the central differencing and the upwind scheme is often utilised, with the weighting of each scheme determined by the blending factor α:

$$\phi_e = \alpha \phi_e^{UP} + (1 - \alpha)\phi_e^{CD} \tag{4.62}$$

In this work, the central differences method was employed using the blending coefficient 0.1.

Temporal discretisation. CFD-ACE+ gives two options for temporal discretisation: the backward Euler method and the Crank-Nicolson method.

The backward Euler method is a first-order implicit scheme, where the differencing is performed in the following way:

$$\frac{\phi_i^{n+1} - \phi_i^n}{\Delta t} + 0(\Delta t) = k \frac{\phi_{i+1}^{n+1} - 2\phi_i^{n+1} + \phi_{i-1}^{n+1}}{\Delta x^2} + 0(\Delta x^2), \tag{4.63}$$

where n is the time step, i is the current cell in which the computation is being performed for the variable of interest ϕ and k is the diffusion coefficient.

Crank-Nicolson is the combination of the forward (at n) and the backward Euler (at $n+1$) and can give an implicit or explicit scheme depending on the chosen blending factor (β). The Crank-Nicolson scheme works as follows:

$$\frac{\phi_i^{n+1} - \phi_i^n}{\Delta t} = k \left(\beta \frac{\phi_{i+1}^{n+1} - 2\phi_i^{n+1} + \phi_{i-1}^{n+1}}{\Delta x^2} + (1 - \beta) \frac{\phi_{i+1}^n - 2\phi_i^n + \phi_{i-1}^n}{\Delta x^2} \right) \tag{4.64}$$

β set to 0.5 results in pure Crank-Nicolson, while $\beta = 0$ produces the pure forward Euler and $\beta = 1$ pure backward Euler (see schematic representation in Figure 4.28, b). In this project, Crank-Nicolson which is second-order in time was used, with blending 0.6 (which is the default value).

Velocity-pressure coupling. The solution of the momentum equation (Equation 4.52) yields the velocity of the system. However, another important flow variable – pressure – is not directly specified in the remaining governing equation (continuity Equation 4.51). CFD-ACE+ determines the pressure field through pressure-velocity coupling and a pressure correction method, with the help of an iterative SIMPLEC algorithm (Semi-Implicit Method for Pressure-Linked Equations – Consistent) (Van Doormaal and Raithby, 1984). At first, the pressure field is guessed and provided as an input to the momentum equation, which is solved for velocity. The obtained velocity field has to satisfy both the momentum and continuity equations. Hence, using the linearised continuity equation, the pressure correction term can be calculated. Finally, this term is used to correct the values of velocity and pressure. This procedure is repeated until convergence is reached.

Solving the system. After the discretised equations have been assembled into a matrix system form, that system needs to be solved. For that purpose, CFD-ACE+ offers two iterative solvers: the Conjugate Gradient Squared (CGS) and the Algebraic Multigrid (AMG) solver (Ruge and Stüben, 1987). The conjugate gradient method seeks to solve the system $A\boldsymbol{\phi} = \boldsymbol{b}$ for $\boldsymbol{\phi}$ by minimising the following function

$$f(\boldsymbol{\phi}) = \frac{1}{2}\boldsymbol{\phi}^T A\,\boldsymbol{\phi} - \boldsymbol{\phi}^T \boldsymbol{b}, \tag{4.65}$$

whose gradient equals $A\boldsymbol{\phi} - \boldsymbol{b}$. Starting from the initial value of ϕ, in each iterative step, the direction where the function decreases most quickly is chosen, namely, the direction opposite the gradient. The minimum point along this direction becomes an improved approximation of the starting point, and the process is repeated until the convergence is reached.

In this project, the second method, AMG, was utilised. The idea behind AMG is to use a hierarchy of grids with different resolution to solve a system of equations. During one cycle, the residual is firstly obtained on the fine mesh, then iterations are performed on a coarser mesh, after which the corrections are interpolated and transferred to the fine grid, etc. More details are provided in ESI (2013a).

4.8 CONCLUDING REMARKS

This chapter described the methodology that was used to develop the novel fast virtual stent deployment method. The chapter started by outlining different preparatory stages for device modelling, from reconstructing of 3-D geometries, establishing the local coordinate system, crimping of devices and, finally, bringing them into the desired location inside the target vessel.

The core of the chapter was dedicated to modelling the mechanics of the expansion process. Different expansion methods were presented with the underlying theory and application to the stent deployment algorithms. In particular, the three spring analogy methods were investigated that are known for their simplicity and fast speed, which constitute the essential requirements for the envisioned virtual stent deployment system (see Section 1.2). The implementation started with the baseline version of the lineal spring analogy, which served as an inspiration for developing the stent expansion algorithm. Thereafter, the attention was turned to more sophisticated spring analogy methods, recognising that the process of stent expansion is mostly guided by restoring forces originating from the angular deformation in stent structure. Hence, implementing mechanisms that can capture and control angular deformation were relevant to explore, since we were interested in a mechanically feasible behaviour of the model. Thus, the more sophisticated semi-torsional and torsional spring analogy were employed which constituted the extensions of the baseline lineal version. The stent expansion methods based on all three versions were developed, which were able to bring the crimped device in its initial configuration in free expansion experiments.

The chapter continued with methods handling the vessel, from geometry reconstruction to modelling its contact with the stent. This part included the section on modelling the flexible vasculature which is of particular importance to be able to capture the potential vessel deformation (see Section 1.2). Additionally, the chapter briefly outlined the two established methods of Finite Element Analysis and Genetic Algorithms that will be employed in the coming Chapter 6 for the validation of the developed novel fast stent deployment method. Finally, techniques for computational grid generation and Finite Volume method for CFD were briefly described, which will be utilised in Chapter 7 for the pre- and post-procedural haemodynamic analysis of the vessel.

After introducing the concepts in this chapter, the next chapter investigates the performance of the three different spring analogy methods in a series of comparative experiments, with the aim of finding the most suitable method for virtual stent deployment.

CHAPTER 5

WHICH SPRING IS THE BEST? COMPARISON OF EXPANSION METHODS

This chapter reports the results of comparative experiments carried out to evaluate the performance of three different stent deployment methods, based on the lineal, the semi-torsional and the torsional spring analogy. To compare the different methods, stent deployment was performed in different vessel geometries with two different devices: a stent graft and a flow diverter. The primary goal of the comparison was to determine whether the use of the more computationally intensive version of stent deployment procedure would be eventually justified by the increasing precision of the results. This chapter has been published in an alternative form in Spranger and Ventikos (2014).

This chapter aims at evaluating the performance of the developed stent expansion methods (Section 4.2) in the context of the virtual stent deployment. For this purpose, a number of computational experiments were carried out using the expansion algorithms that were based on (1) the lineal spring analogy, (2) the semi-torsional spring analogy and (3) the torsional spring analogy. The comparison was based on the results of expansion of two different devices – a stent graft and a flow diverter – in four different scenarios: (1) in the case of free expansion, (2) in idealised straight vessels, (3) in idealised bent vessels and (4) in real patient's cases. The ultimate goal of the chapter was to find the most suitable method for virtual stent deployment, which is fast and sufficiently accurate. In assessing the precision, we were mostly interested in the final configuration of the deployed device (and not in the transient states) as this constitutes the clinically relevant component, especially with respect to the subsequent CFD analysis.

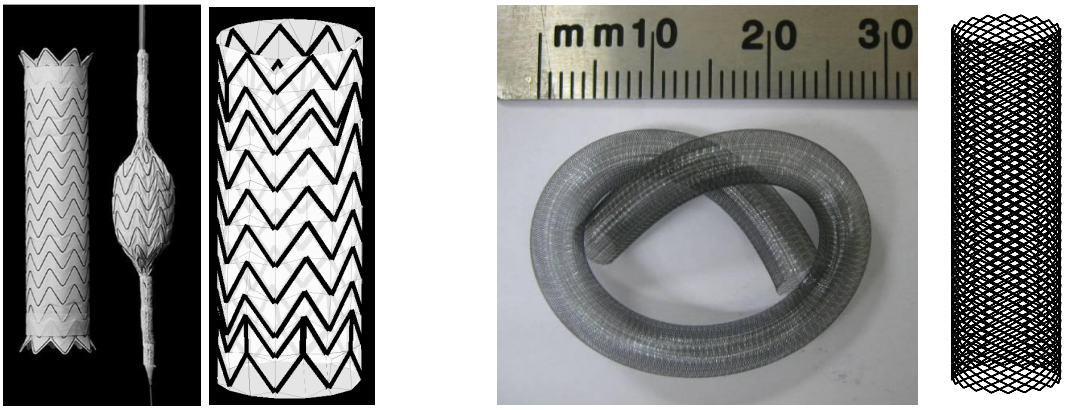

(a) (b)

Figure 5.1: Computational models of devices. (a) Gore TAG Thoracic Endoprosthesis (image from `www.goremedical.com`) and a reconstruction of the model TGT4010 that is similar in design but different in dimensions. (b) Pipeline Embolization Device (PED, ev3, Irvine, California, image from Pierot 2011) and the model of the PED device.

5.1 COMPUTATIONAL SETUP

In order to compare the methods, the stent deployment experiments were performed for 2 different devices in different vessel geometries. The two devices were chosen to represent a "typical" device used in the two distinct areas of radiological procedures of interest – thoracic and cerebral regions:

1. A **stent graft** (SG) corresponding to the Gore TAG Thoracic Endoprosthesis (model TGT4010) was utilised, with dimensions 4 cm in diameter (fully expanded) and 10 cm in length (see Figure 5.1, a). It is one of the most widely-used devices in radiological procedures to treat thoracic aneurysms as well as aortic dissections.

2. A **flow diverter** (FD) similar to the commercially available Pipeline Embolization Device (PED, ev3, Irvine, California) was employed, with a diameter of 3 mm and length of 14 mm (see Figure 5.1, b). PED is one of the three FD devices currently used in Europe to treat cerebral aneurysms.[1]

[1] next to the Silk stent (Balt Extrusion, Montmorency, France) and Surpass flow diverter (Stryker Neurovascular, Fremont, CA)

The stents were crimped to simulate their positioning in the catheter and aligned along the centerline of the target vessels at the relevant positions, as described in Section 4.1. For the SG device, the initial crimping was 20% of its labelled diameter, since in clinical practice the stent graft is compressed into a 24 FR[2] system, i.e., from 40 mm outer diameter to 8 mm (24×0.333 mm = 8 mm). With respect to the FD device, the PED is usually delivered via a 3 FR micro catheter (3×0.333 mm = 1 mm); hence, it was crimped to the 33% of its load-free diameter.

In all simulations, dimensionality parameters for the stent springs were set to $\kappa = \frac{1}{3\ell}$ for the semi-torsional method (Equation 4.26), where ℓ is the characteristic length of the device element, measured as an average length of a strut. For the torsional method, the scaling was with $\kappa = \frac{\ell}{3}$ (Equation 4.36). These settings were found experimentally to produce the best and most stable results.

To allow the focus on the process of stent expansion, the vessel was assumed rigid in order to eliminate possible interdependencies of device expansion and vessel deformation. Hence the rigid contact model described in Section 4.3.3 was used in all experiments reported in this chapter.

Comparison metrics. To compare the methods and evaluate the results, the following metrics of convergence were defined:

- *Mean nodal distance* between the load-free and the expanding stent: $\overline{\boldsymbol{d}} = \frac{1}{N}\sum_{i=1}^{N} \|n_i - n_i'\|$, where n_i is the position of the node i in the load-free stent and n_i' – in the current expanding stent.

- *Mean mesh point displacement* in one iteration due to restoring forces: $\overline{\boldsymbol{\delta}} = \frac{1}{N}\sum_{i=1}^{N} \|\boldsymbol{\delta}_i\|$, where $\boldsymbol{\delta}_i$ is the nodal displacement of the node i with i running from 1 to number of nodes N.

- *Mean angle difference* between the load-free and the expanding stent: $\overline{\boldsymbol{\theta}} = \frac{1}{M}\sum_{j=1}^{M} |\theta_j - \theta_j'|$, where θ_j is the value of the angle j in the load-free stent, θ_j' – in the current expanding stent and M stands for the number of angular elements in the stent structure.

[2] 1 FR = 0.333 mm

– *Mean strut length difference* between the load-free and the expanding stent: $\overline{L} = \frac{1}{S}\sum_{k=1}^{S} \frac{|l_k - l'_k|}{l_k}$, where l_k is the length of the strut k in the load-free stent, l'_k – in the current expanding stent and S stands for the number of struts.

– *Mean nodal force* in the expanding stent: $\overline{F} = \frac{1}{N}\sum_{i=1}^{N} \|\boldsymbol{F}_i\|$, where $\boldsymbol{F}_i$ is the reaction force at the node i with the index i running from 1 to number of nodes N.

Deployment cases. Deployment experiments in 4 different scenarios were conducted for SG and FD devices:

1. **free expansion** for both devices;
2. deployment in a **straight tube** for both devices;
3. deployment in a **bent tube** for both devices as well as in a **snake** geometry for SG and in a **torus** geometry for FD;
4. deployment in **real vessel geometries**: dissection case for SG and aneurysm case for FD.

All models were implemented in Matlab and executed on an Intel Core 2 Duo with CPU 2.66 GHz with 4 GB of memory and no parallelisation (e.g., multi-threading) was used.

5.2 RESULTS

5.2.1 Free expansion

SG device. From the initially crimped configuration (8 mm in diameter which is 20% of the labelled diameter), the SG device was subject to free expansion until it reached the load-free configuration. Figure 5.2 captures the evolution of the expansion process during 300 iterations. The four different convergence metrics were plotted for each of the springs methods: lineal springs in blue, semi-torsional springs in green and torsional springs in red. Since the released SG was going to spring back to the load-free configuration, the shape of which was also known, the clear way to demonstrate the expansion process was to track the distance to the target load-free stent. Hence, the average distance from the vertices of the current

expanding stent to their counterparts in the load-free device was measured (*mean nodal distance*), which is displayed in the first graph in the upper left corner. All 3 springs methods were able to reach the load-free configuration; however, they did so with different speed, with the lineal method being the fastest and the torsional method being the slowest (completely converges only after about 500 iterations).

The evolution of the angles is shown in the upper right corner as the *mean angle difference* between the load-free and the current expanding stent. This measure is very important since the difference in angles reveals the degree of crimping in the

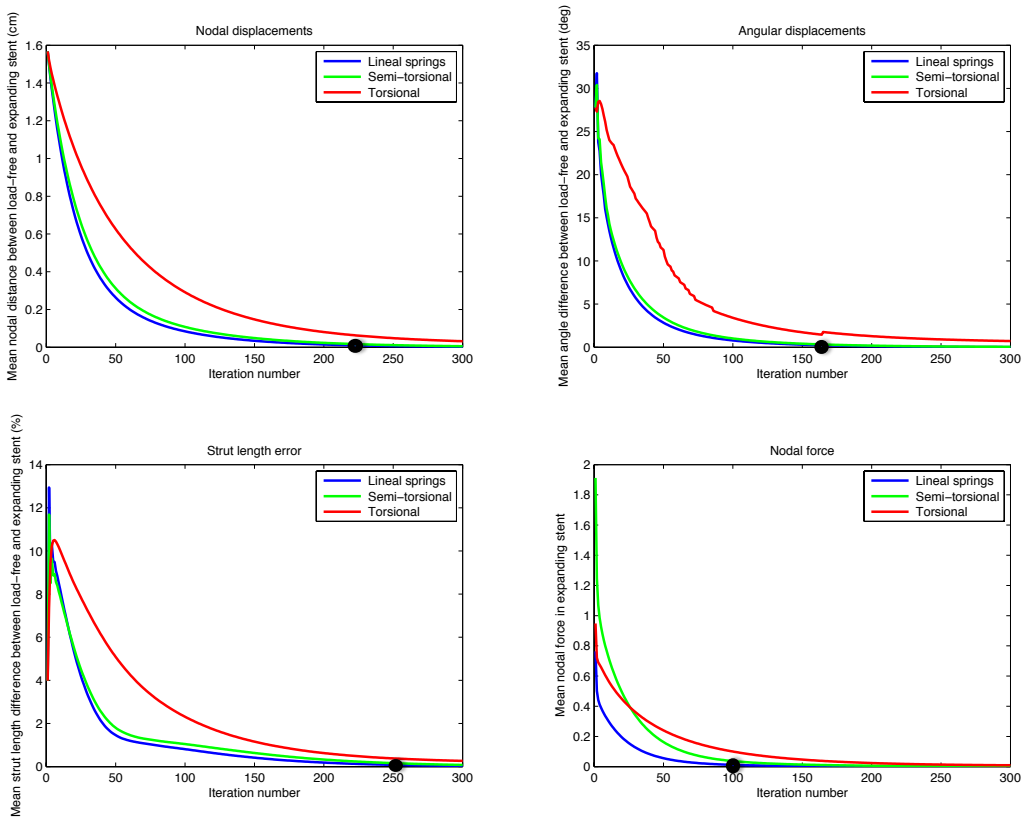

Figure 5.2: Free expansion of the SG for 300 iterations. Upper row: mean nodal distance and mean angle difference between the load-free and the expanding stent. Bottom row: mean strut length difference and mean nodal force in the expanding stent. All three methods were able to reach the load-free configuration. The lineal springs method (in blue) displayed the fastest convergence after about 190 iterations. The semi-torsional springs method (in green) was the second fastest, converging after about 200 iterations. The torsional springs method (in red) was the slowest, reaching convergence only after about 500 iterations. Black circle marks the point of first convergence in each of the corresponding metrics.

structure and indirectly shows the average angular displacement in every iteration. Again the lineal method displayed faster convergence, the semi-torsional was similarly fast and the torsional was the slowest. Equally, it was important to ensure the adequate struts' length evolution throughout the iterative process. This was done by measuring the *mean strut length difference* which gave the average error length as a relative percentage of the initial length. The bottom left graph displayed the behaviour of struts' lengths during the iterative process. The initial iterations corrupted the average length up to 14% (for the lineal springs method); however, it got corrected in the course of the expansion process.

Finally, the bottom right graph displays the *mean nodal force* in the expanding stent which gives account of the reaction forces guiding the expansion process. The fact worth mentioning is that the forces for the semi-torsional and the torsional methods included the lineal component, which resulted from the overlay of the semi-torsional and the torsional springs in the algorithms, respectively. Consequently, it was to expect that the lineal reaction forces were smaller in magnitude. On the other hand, the semi-torsional forces were much larger, even after the lineal component has been subtracted from them (almost three times the lineal value).

The device configuration during the free expansion experiment looked similar to that of a real nitinol stent (shown earlier in Figure 2.10), with a slight difference in timing to reach a certain state between different methods. Figure 5.3 shows the lineal expansion case.

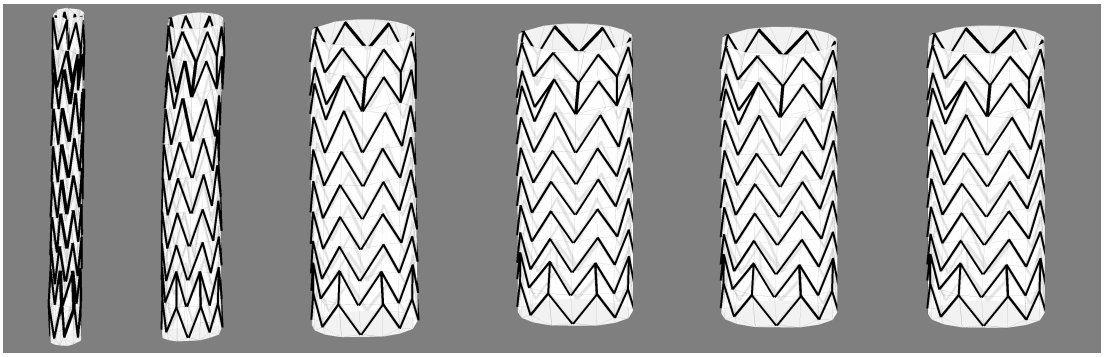

Figure 5.3: Free expansion of the SG device with the lineal springs. (a) Initial crimped stent, (b) result after 10 iterations, (c) 50, (d) 150, (e) 250, (f) 500 iterations.

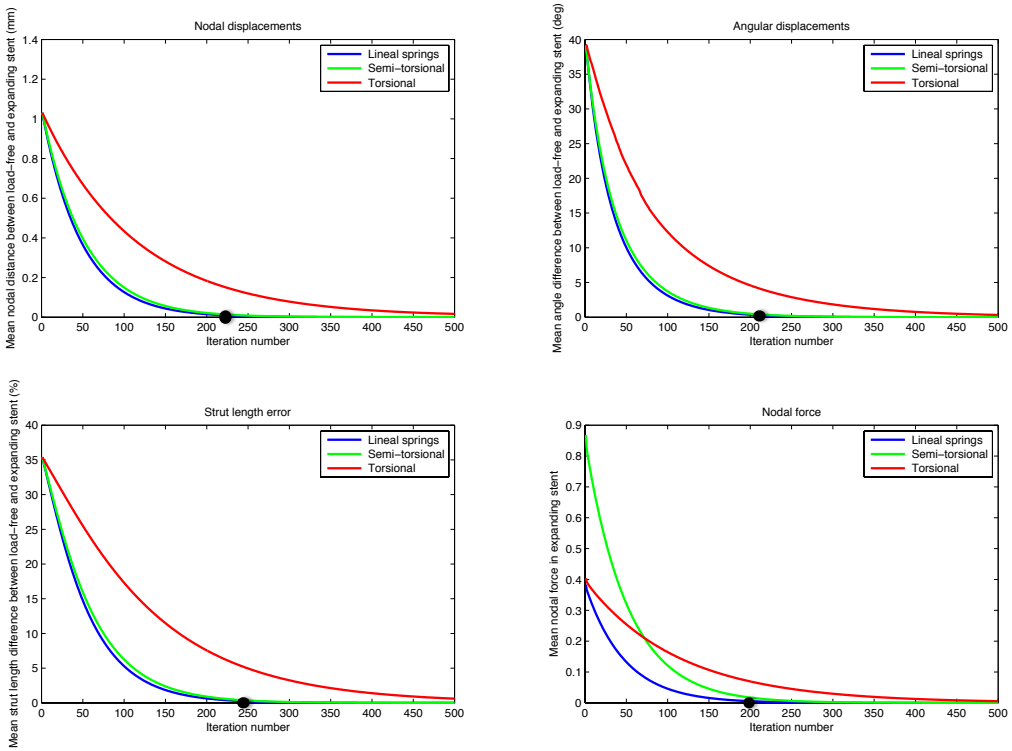

Figure 5.4: Free expansion of the FD device during 500 iterations. Upper row: mean nodal distance and mean angle difference between the load-free and the expanding stent. Bottom row: mean strut length difference and mean nodal force in the expanding stent. The lineal springs method displayed the fastest convergence, after about 200 iterations, followed by the semi-torsional springs. The torsional method converged fully after about 500 iterations. Black circle marks the point of first convergence in the corresponding metrics.

FD device. The FD device was initially crimped to the 33% of its labelled diameter and then underwent the free expansion test for 500 iterations. As was the case for the SG device, the lineal springs method displayed the fastest convergence, after about 200 iterations, closely followed by the semi-torsional springs. Again the torsional method converged only about 500 iterations (see Figure 5.4).

Interestingly, the semi-torsional forces in this device were not as large as in the SG device. However, they were still quite large, even without the lineal component. During the free expansion process, the device configuration looked similar for different methods with a slight difference in timing, as shown in Figure 5.5 for the lineal case.

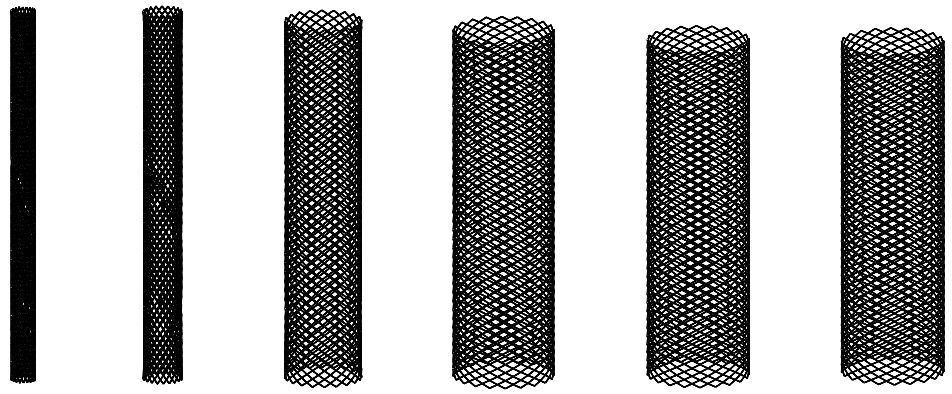

Figure 5.5: Free expansion of the FD device with the lineal springs method. (a) Initial crimped stent, (b) result after 10 iterations, (c) after 50 iterations, (d) after 150 iterations, (e) after 250 iterations, (f) after 500 iterations.

5.2.2 Deployment in straight tubes

SG device. In this set of experiments, the device was deployed inside an idealised vessel in the shape of a straight cylinder. The diameter of the cylinder was 34 mm, which is a usual vessel size for a 40 mm device diameter, because the grafts are always oversized in clinical practice for about 30%. As in the previous case, the device was crimped to 8 mm and then deployed, this time until it reached the vessel walls. The snapshots of the expansion with the semi-torsional method after a certain amount of iterations are captured in Figure 5.6. The other two methods displayed a comparable progression.

Figure 5.7 shows the convergence of parameters throughout the deployment process. The lineal springs method displayed the fastest convergence rate again, which was to expect. However, the torsional springs performed slightly better this time with respect to the final nodal displacement (see upper left graph), which was surprising given their earlier performance in the free expansion case. When the deployment was complete, after about 100 iterations on average, there was a very small but nonzero restoring force that remained due to the oversizing of the device. This force would help keeping the device placement intact after the intervention.

FD device. The FD was crimped to 1 mm and released into an idealised cylinder with the 2.3 mm diameter (in order to account for oversizing). As in the previous case, the deployment process continued until the device reached the vessel walls.

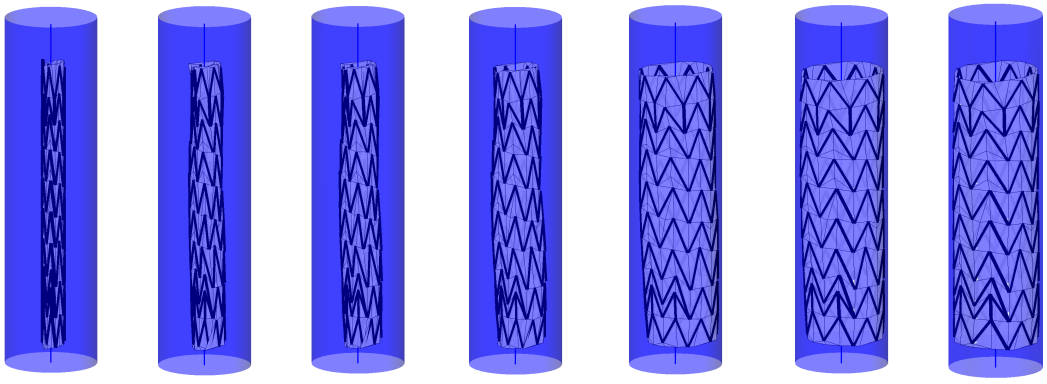

Figure 5.6: Deployment of the SG in a straight tube. Results after (a) initial crimping, (b) 3 iterations, (c) 5, (d) 10, (e) 30, (f) 50, (g) 200 iterations.

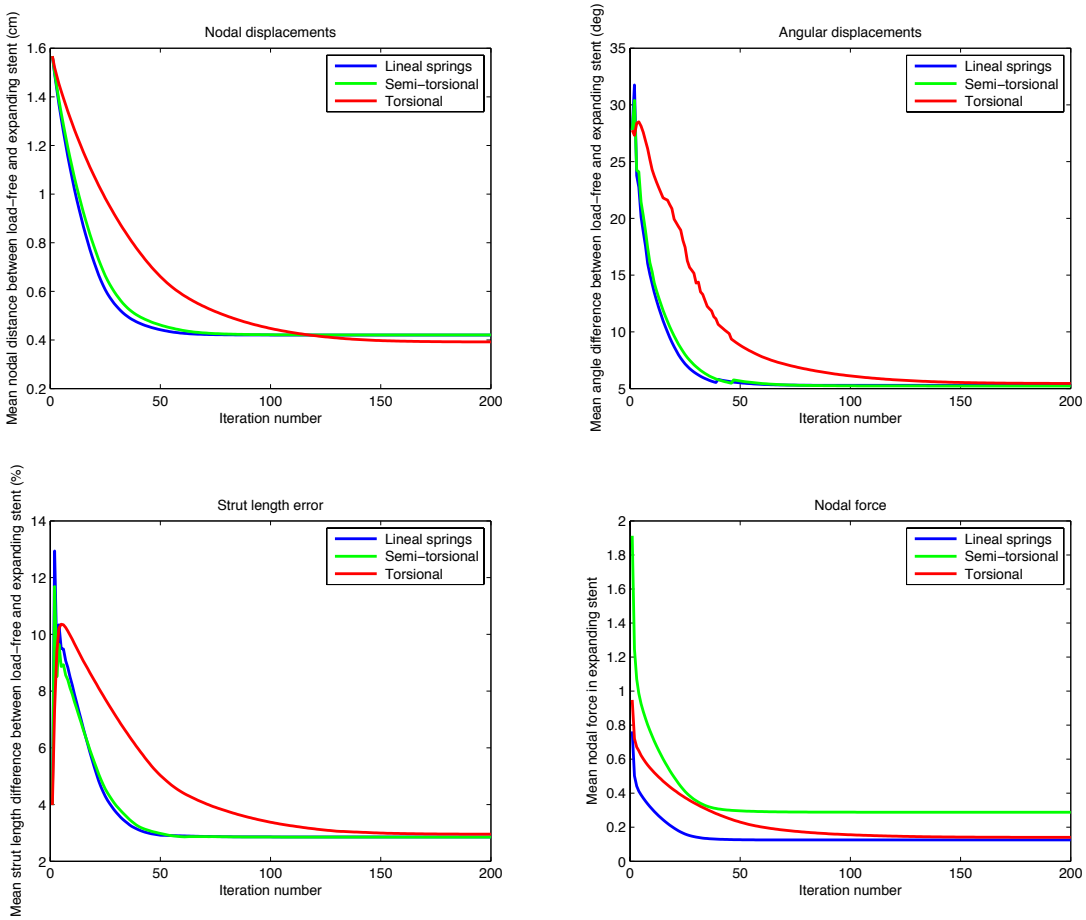

Figure 5.7: Deployment of the SG in a straight tube for 200 iterations.

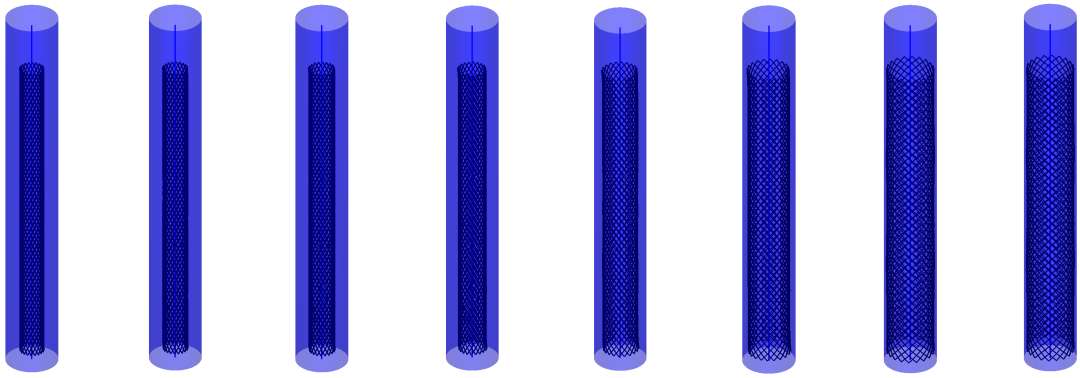

Figure 5.8: Deployment of the FD device in a straight tube. Results after (a) initial crimping, (b) 3, (c) 5, (d) 10, (e) 30, (f) 50, (g) 100, (h) 300 iterations.

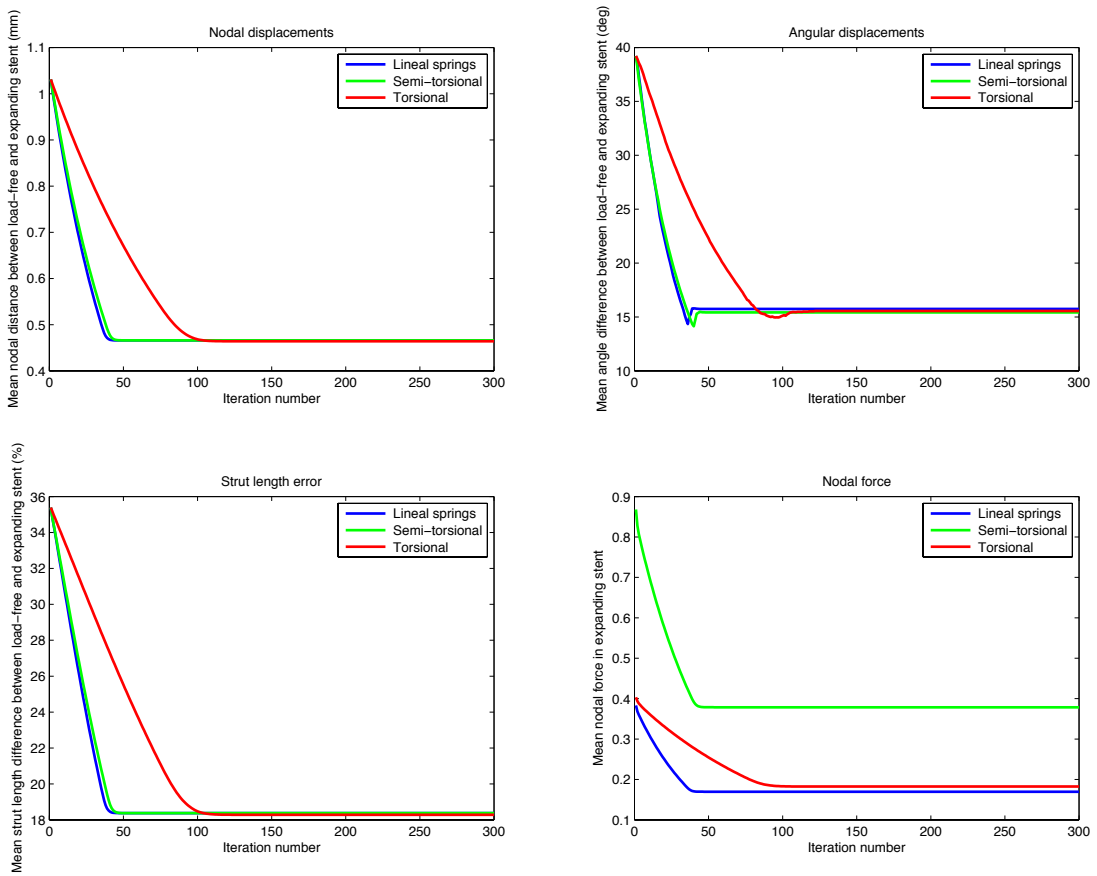

Figure 5.9: Deployment of the FD device in a straight tube for 300 iterations.

The snapshots of the expansion with the torsional method after a certain amount of iterations are captured in Figure 5.8. The other two methods displayed a comparable progression, but with a slightly faster convergence. The general convergence curve can be seen in Figure 5.9. The fact worth noting is that the struts' length difference remained substantial at the end of the deployment process (lower left graph). Also in reality, the FD struts are not fixed due to the woven design of the device. Hence, they can slide, changing the apparent struts' length, which could potentially be emulated by the flexible nature of the soft constraints imposed by the springs. However, whether the observed effect represents wire sliding in a realistic manner would require a detailed investigations and validation of the proposed springs method for flow diverters. Such validation would necessitate identifying the "gold standard" behaviour for that particular class of devices, information not available to us at this stage (see Chapter 8 for more).

5.2.3 Deployment in bent tubes

SG device. This time the geometry of the vessel was represented as a bent (rather than a straight) cylinder with a diameter of 34 mm. As in the previous case, the device of 40 mm in diameter was crimped to 8 mm and then deployed until it reached the vessel walls. The lineal springs method was applied in layers, starting from the center of the device, as performed in the clinical practice. Figure 5.10 displays snapshots of the layered lineal expansion.

The overall convergence behaviour is illustrated in Figure 5.11. Since the lineal springs method was applied in layers, it converged slower than the semi-torsional

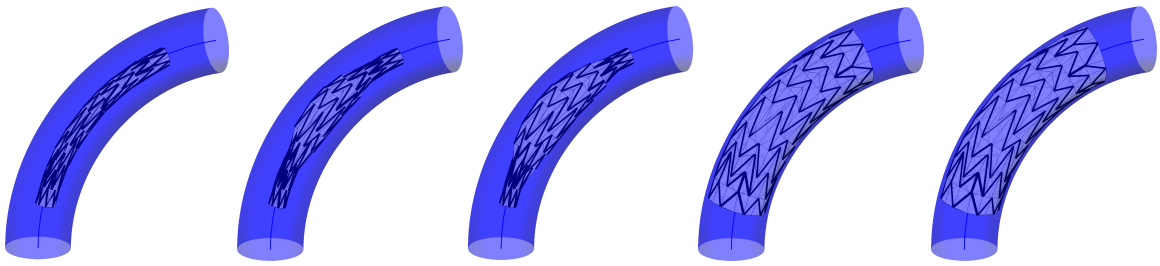

Figure 5.10: Deployment of the SG in a bent cylinder. Results after (a) crimping, (b) 20, (c) 30, (d) 100, (e) 200 iterations of the layered lineal springs method.

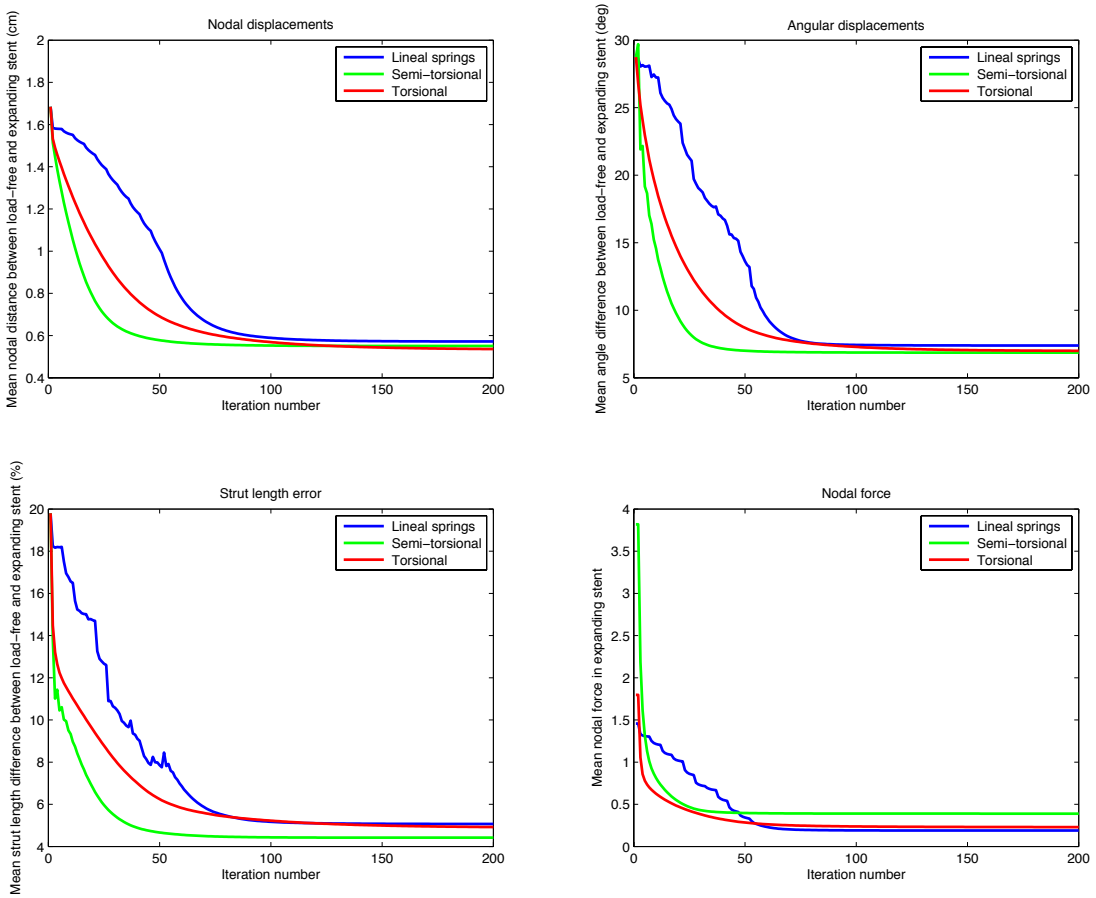

Figure 5.11: Deployment of the SG device in a bent vessel geometry during 200 iterations. The lineal springs method was applied in layers staring from the center; hence, it converged slower than the semi-torsional and the torsional method.

and the torsional method. The latter two methods displayed a progression comparable to the previous cases, although the torsional method was slightly more accurate with respect to the struts' lengths error. After the deployment completion, there was small nonzero restoring force that remained present due to the oversizing of the device and the geometry of the vessel. Note that the semi-torsional force was almost double at the beginning, compared to the straight tube case in Figure 5.7, while the angular displacements were comparable. In fact, all forces were almost double at the beginning of the expansion process. This was due to the larger strut length error, augmented through the alignment of the crimped vessel with the curved vessel centerline.

Another fact worth noting is that metrics used to evaluate the performance of

the methods were not all suitable for the bent (and more complicated) geometries. For example, the nodal displacements were calculated as the distance of the current expanding stent to the load-free configuration and did not represent a meaningful value in the bent vessel case, because the load-free configuration was not the target of the expansion process in this case. In fact, the target was unknown! Nevertheless, these familiar metrics were still employed for the reason of consistency, to compare the spring methods between themselves.

The conformity of the stent grafts to the vessel wall is an important parameter in assessing the outcome of the deployment procedure. Most modern grafts are specifically designed to account for potentially steep curvatures of the aortic arch. For example, Figure 5.12 (a) demonstrates the flexibility of the new Medtronic Valiant stent graft. To test the performance of the modelled SG in similar geometries, a slightly longer device (34 mm × 150 mm) was utilised. The new device was expanded in an "arch" vessel geometry and a "snake" vessel geometry with a 34 mm

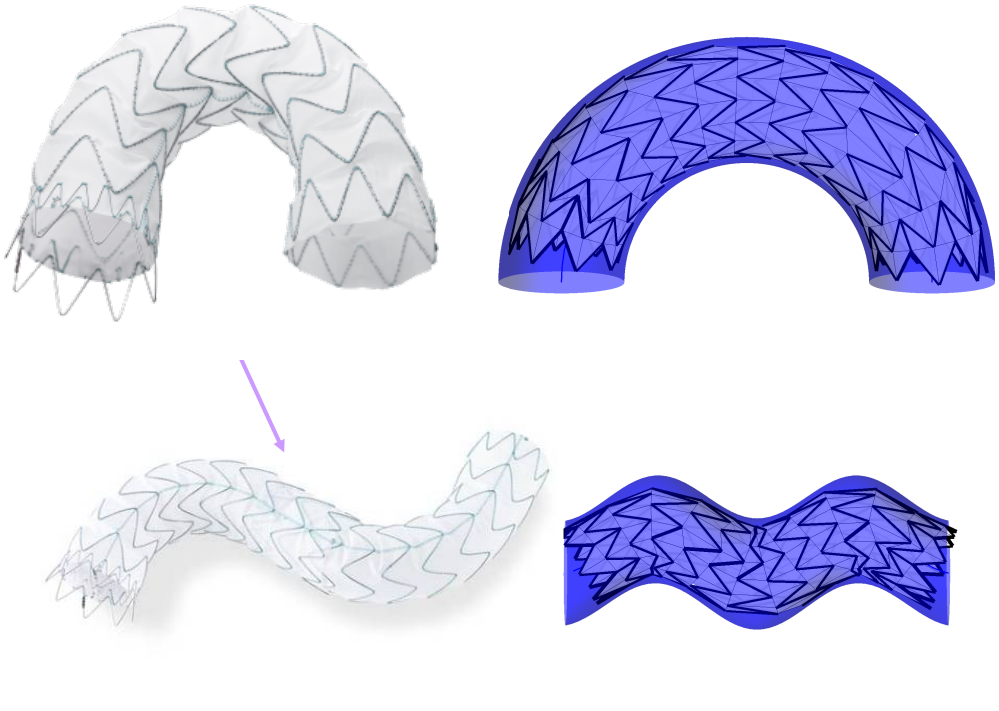

(a) (b)

Figure 5.12: Conformity in highly curved geometries. (a) Demonstration of the flexibility properties of the novel Medtronic Valiant stent graft (images from `www.cxvascular.com` and `www.bmctoday.net`). (b) Expansion of the modelled SG device (with different design) in similar vessel geometries.

diameter, which can be seen in Figure 5.12 (b) showing comparable conformity.

FD device. The FD was crimped to 1 mm and released in the idealised bent cylinder with the 2.6 mm diameter to account for the oversizing. This time, the semi-torsional method was applied in layers, the snapshots of which can be seen in Figure 5.14. The other two methods were applied simultaneously to all layers. The general convergence curve is depicted in Figure 5.13.

To illustrate the flexibility and conformity of the FD device, it was deployed in a

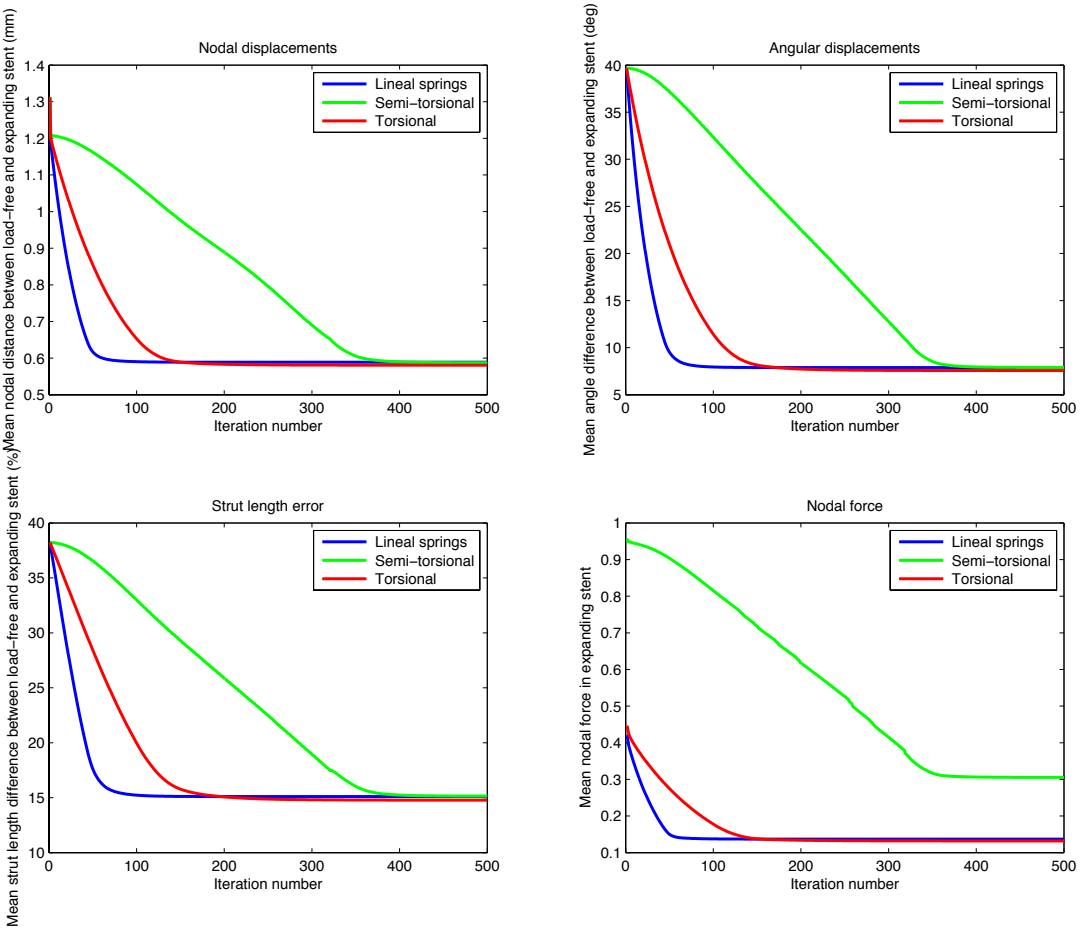

Figure 5.13: Expansion of the FD device in the bent vessel geometry during 500 iterations. The semi-torsional method was applied in layers which led to its slower convergence.

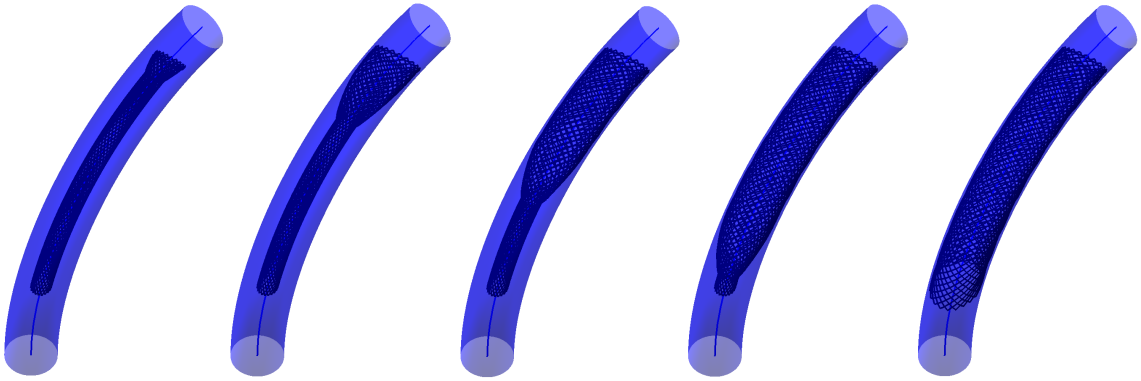

(a) (b) (c) (d) (e)

Figure 5.14: Stages of the expansion of the FD device in the bent vessel.

highly curved torus geometry, built by the parametric equation

$$\begin{cases} x &= \cos(t)(R + r\cos(u)) \\ y &= \sin(t)(R + r\cos(u)) \\ z &= r\sin(u) \end{cases} \tag{5.1}$$

where R is the major radius, r is the minor radius and the two parameters t and u both vary between 0 and 2π. The resulting device configuration is shown in Figure 5.15 (c) and featured similar bending properties as the real device represented in (a).

5.2.4 Deployment in real vessels

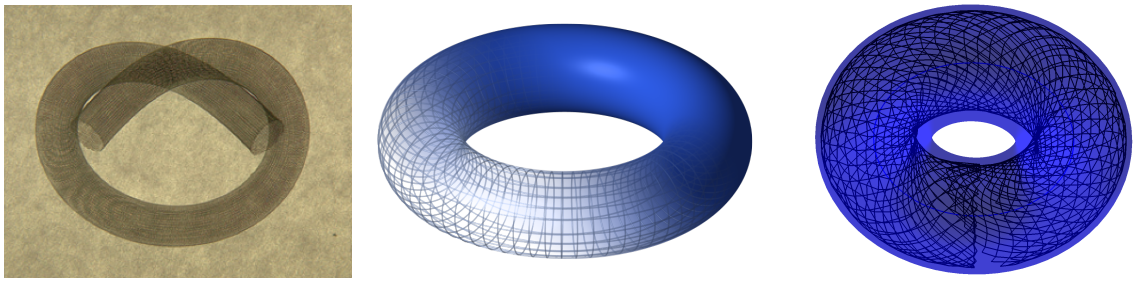

(a) (b) (c)

Figure 5.15: Flexibility of the FD device. (a) Bending of PED FD (image from Fiorella et al. 2009). (b) Reconstructed torus geometry. (c) Expansion of the modelled FD in the torus geometry.

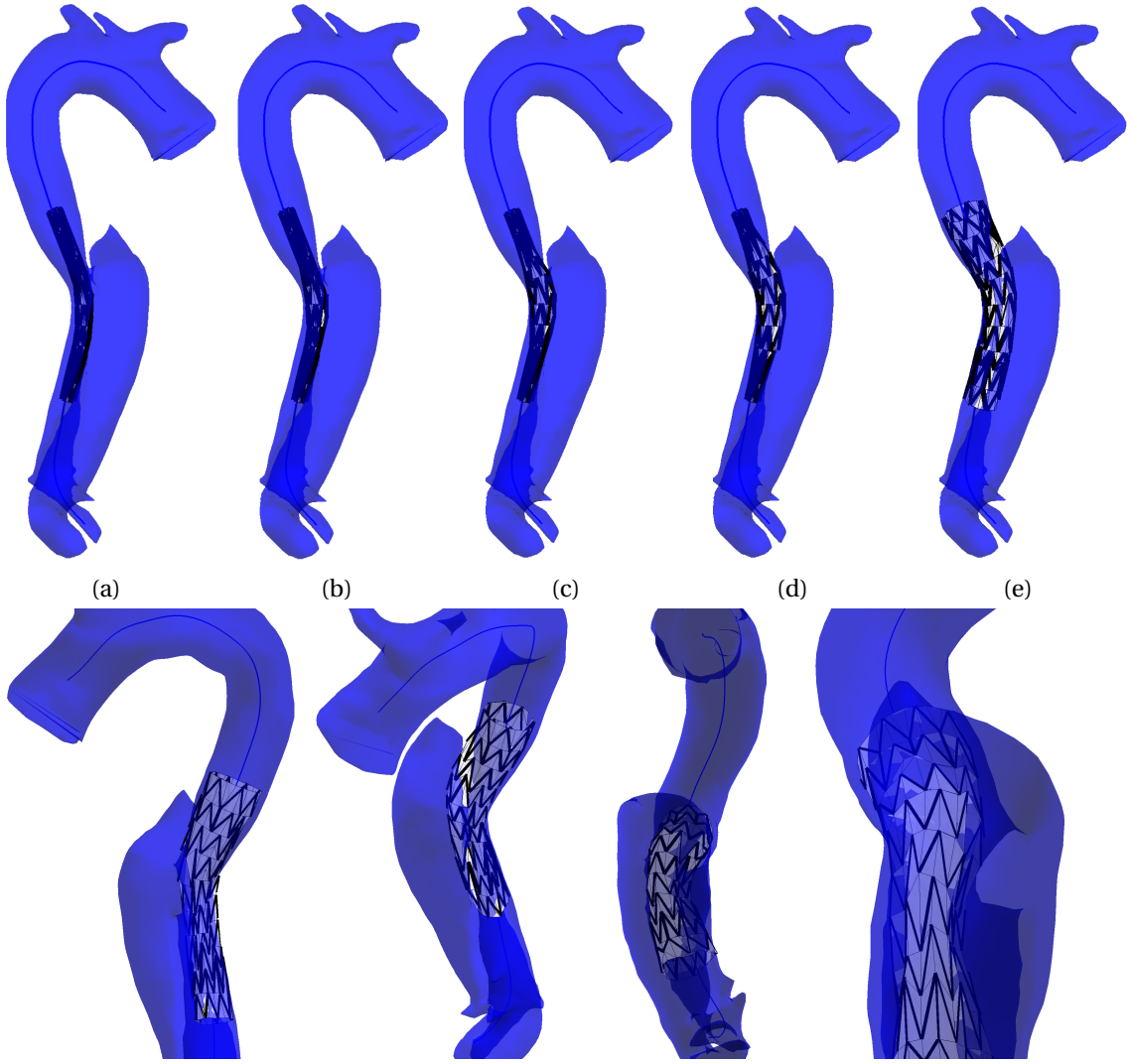

Figure 5.16: Upper row: stages of the virtual deployment process in patient's aorta. (a) 20%-crimped SG initially placed on the centerline of the target vessel at the site of the pathology; (b), (c), (d) after 10, 20 and 30 iterations of the expansion process with the semi-torsional springs method, respectively, starting from the central part of the device and propagating to its extremities; (e) configuration of the fully expanded device after 200 iterations. Lower row: final configuration of the deployed SG as in (e), displayed from different rotation angles.

SG device. The performance of the virtual deployment algorithm was tested in a case of aortic dissection. The vessel geometry was obtained by segmentation (see Section 4.3.1) and the SG device was deployed at the dissection site. As it would be done in clinical practice, the SG was placed inside the true lumen to cover the initial tear entry and prevent blood from flowing into the false lumen (see Section 2.2.1).

The vessel diameter varied at the deployment site and ranged between 3.2 and 2.7 cm in the distal and proximal location of the device in the true lumen. Therefore, the dimensions of the modelled SG had to be adjusted to match those that would be required in clinical practice. The modified device was 3.2 cm in diameter and 10 cm in length.

The opening of the SG was initiated in the center of the device, progressing to its extremities, as is common for this type of devices. Figure 5.16 shows the deployment snapshots at different time points during the deployment process with the semi-torsional springs method. The final configuration was obtained after approximately 90 iterations of the virtual deployment algorithm and required about 60 seconds. The opposition of the device to the vessel wall was good and covered the initial tear

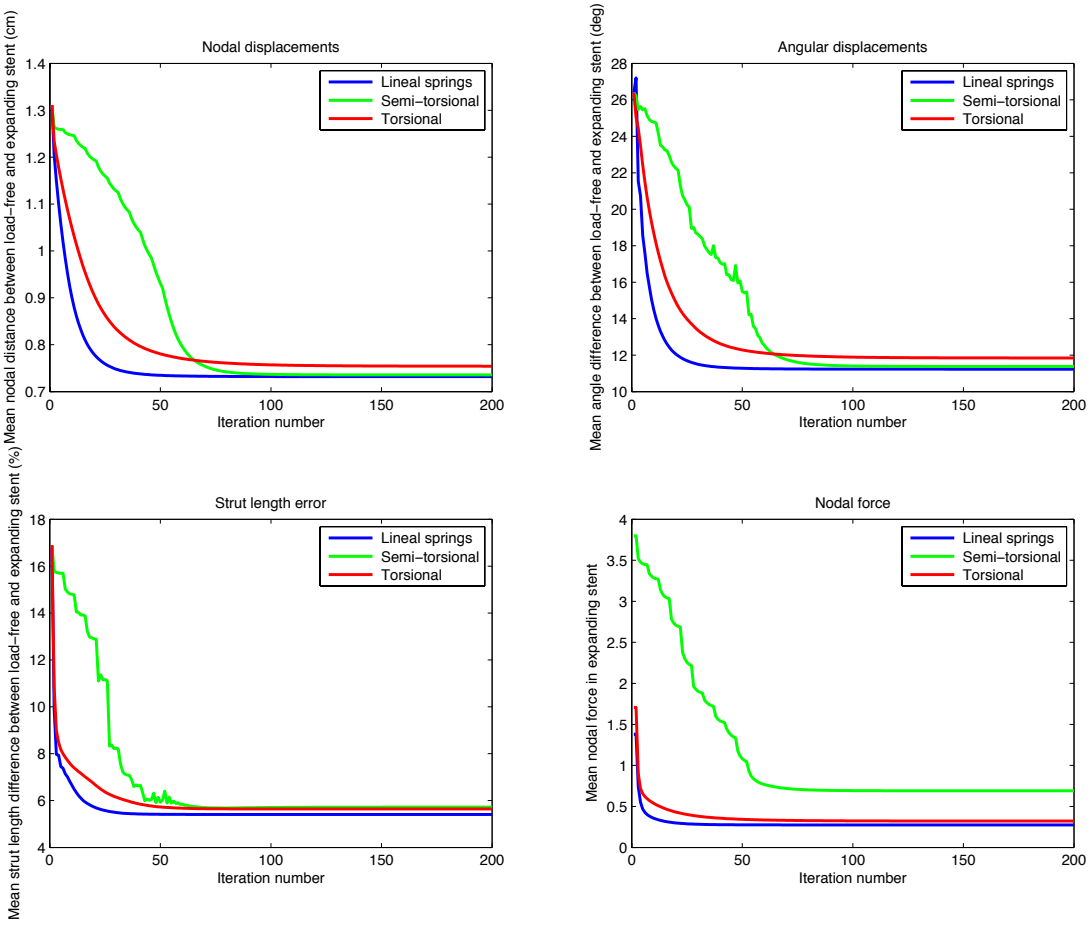

Figure 5.17: Expansion of the SG in the patient-specific vessel geometry during 200 iterations. The torsional method was applied in layers which led to its slower convergence.

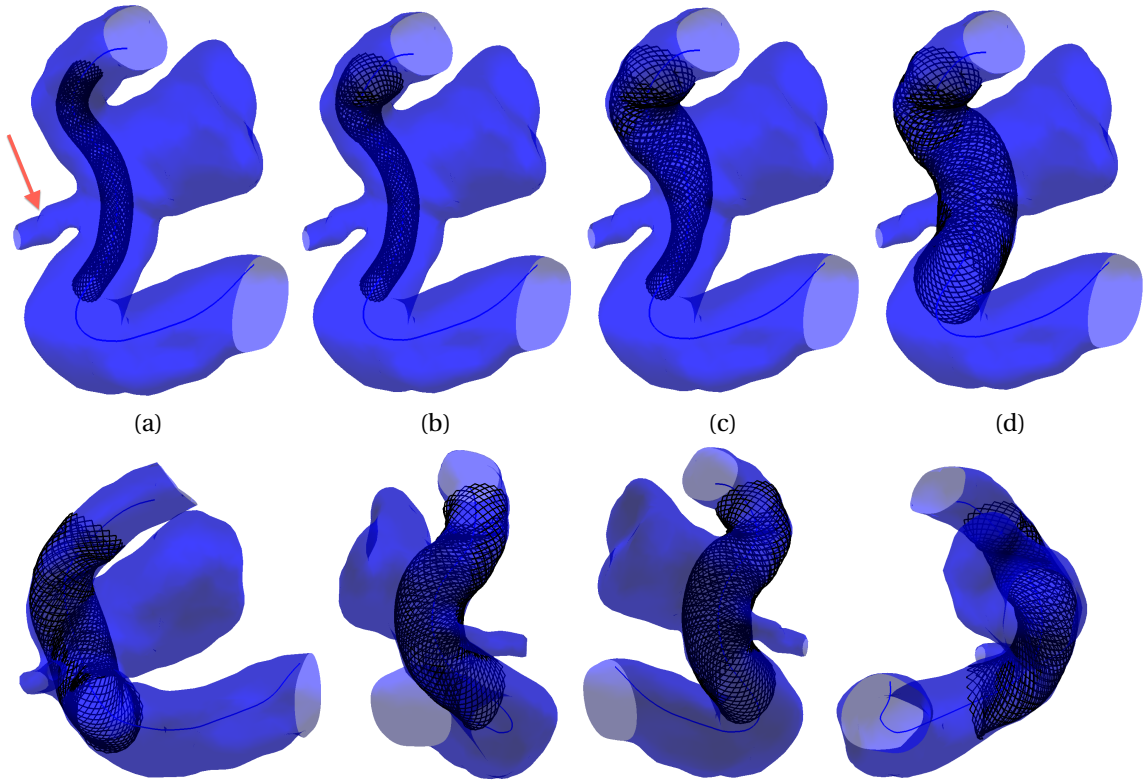

Figure 5.18: Upper row: stages of the virtual deployment process inside a patient's ICA. (a) 33%-crimped FD device initially placed on the centerline of the target vessel (red arrow indicates the opthalmic artery); (b) and (c) after 100 and 230 iterations of the expansion process, respectively, with the torsional springs method starting from the distal to proximal extremity of the device with respect to the aneurysm sac; (d) configuration of the fully expanded device after 400 iterations. Lower row: final configuration of the deployed FD as in (d), displayed from different rotation angles.

completely. Figure 5.17 shows the evolution of the convergence metrics. During the opening of the device, the struts' angles and lengths progressively approached the values corresponding to the load-free configuration.

FD device. The final deployment experiment involved a case of a giant aneurysm located in the left ICA artery of a patient (see Figure 5.18; note the small opthalmic artery originating on the opposite vessel wall with respect to the aneurysmal sac). The 3-D vessel geometry was obtained by the segmentation (see Section 4.3.1) and featured a variation in vessel diameter from 4.1 mm in the distal and 4.4 mm in the proximal location with respect to the aneurysm. For such dimensions of the vessel, a flow diverter of 4.5 mm diameter and 14 mm in length could be utilised in clinical

setting. Therefore, the modelled FD was adjusted, reconfiguring it to be 4.5 mm in diameter in order to account for both vessel geometry and oversizing. The device was deployed over the neck of the aneurysm. The torsional method was applied in layers this time.

As it would be the case in real interventions, the opening of the device was started from the proximal extremity of the device, progressing to its distal end, with respect to the aneurysm sac. Figure 5.18 shows the deployment snapshots at different time points during the deployment process with the torsional springs method. The final configuration was obtained after approximately 600 iterations of the virtual deployment algorithm and required about 2.5 minutes. The device was in a good opposition to the vessel wall. Figure 5.19 shows the evolution of the conver-

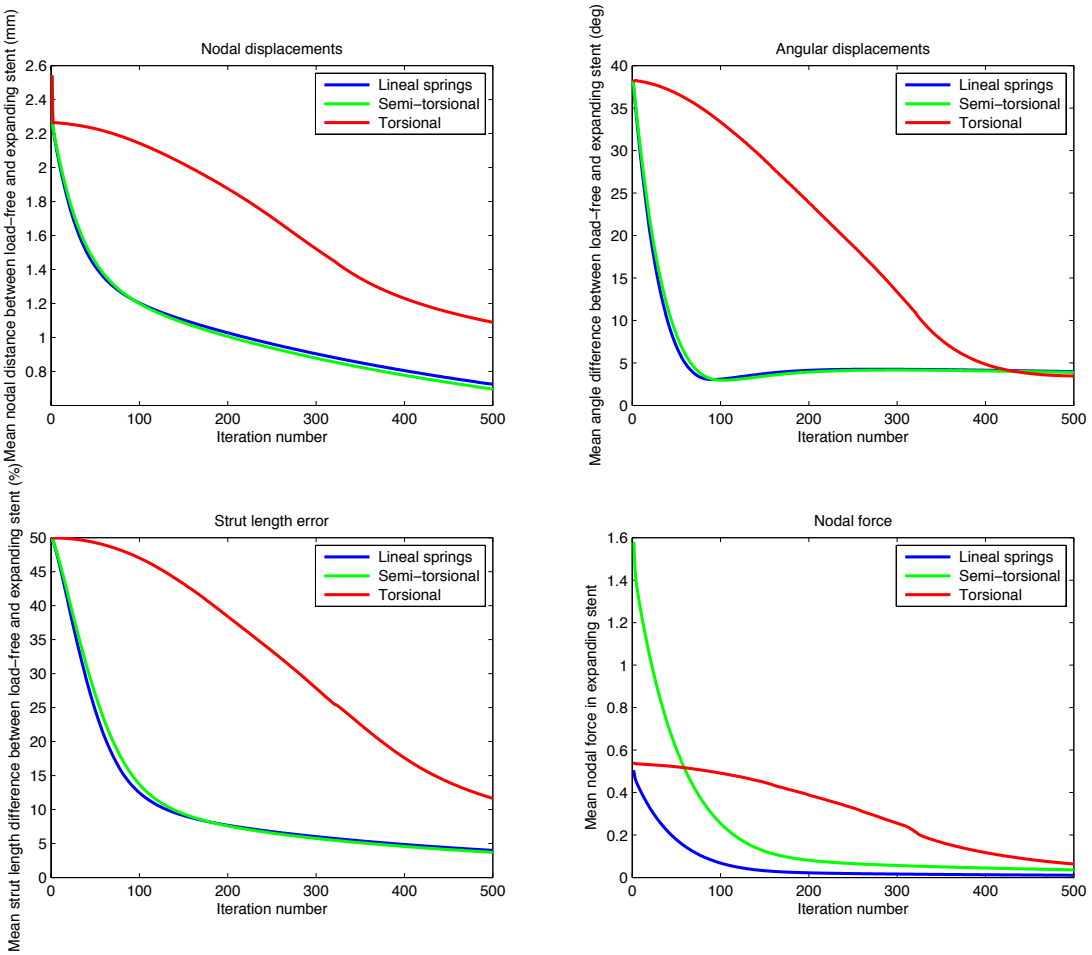

Figure 5.19: Expansion of the FD in the patient's ICA artery during 500 iterations. The torsional method was applied in layers which led to its slower convergence.

gence metrics. During the opening of the device, the struts' angles and lengths progressively approached the values corresponding to the load-free configuration.

5.3 CONCLUDING REMARKS

This chapter investigated the performance of the developed methods for virtual stent deployment. In particular, it compared the three different spring analogy algorithms featuring different properties of the springs and showed their performance in the given problem setting. The three spring analogy methods compared were (1) the lineal spring analogy, (2) the semi-torsional spring analogy and (3) the torsional spring analogy. The comparison was based on the results of expansion of two different devices – a stent graft and a flow diverter – in four different scenarios: (1) in the case of free expansion, (2) in idealised straight vessels, (3) in idealised bent vessels and (4) in real patient cases.

When applied to the stent deployment problem, all three spring analogy methods converged; however, they did so with different speed. The convergence was assessed by different metrics, measuring the displacement and force evolution as well as the evolution of angles between the struts and the struts' length. The end values of the convergence metrics for all cases are summarised in Table 5.1.

One of the interesting findings entailed the fact that lineal springs method displays faster convergence rate in all of the four metrics used. Additionally, it produced final results comparable with those obtained by its more sophisticated semi-torsional and torsional counterparts. This was surprising since the lineal method constituted the base for the other two springs methods and was associated with the simplest implementation. In the case of the first device, such outcome for the lineal version was facilitated by the presence of the background mesh, which served as an integrity-preserving element and simulated the angular elements indirectly. For the second device, the fine mesh of the struts effectively produced the effect of the "background" mesh, taking care of the torsional displacements and forces even in the lineal method.

Another characteristic that was similar to all three springs methods was the small residual error in the struts' lengths, even in the final stent configuration. This fact resulted from the accumulation of imprecisions along the entire deployment processing chain: the crimping, positioning along the centerline and the sequence

Simulation setup	it	time (s)	$\overline{d}$ (mm)	$\overline{\theta}$(°)	$\overline{\mathrm{L}}$ (%)	$\overline{\mathrm{F}}$
1) **SG: Free expansion: lin**	250	3	0	0	0	0
2) **SG: Free expansion: semi**	300	4	0	0	0	0
3) **SG: Free expansion: tors**	500	40	0	0	0	0
4) **FD: Free expansion: lin**	250	26	0	0	0	0
5) **FD: Free expansion: semi**	300	31	0	0	0	0
6) **FD: Free expansion: tors**	500	120	0	0	0	0
7) **SG: Straight tube: lin**	70	24	4.2	6	3	0.13
8) **SG: Straight tube: semi**	100	42	4.2	6	3	0.29
9) **SG: Straight tube: tors**	170	88	3.9	7	3	0.15
10) **FD: Straight tube: lin**	45	51	0.47	16	18.1	0.17
11) **FD: Straight tube: semi**	50	68	0.47	16	18.1	0.39
12) **FD: Straight tube: tors**	100	112	0.46	16	18	0.18
13) **SG: Bent tube: lin layers**	120	49	5.9	7	5	0.2
14) **SG: Bent tube: semi**	150	65	5.8	6.5	4.5	0.23
15) **SG: Bent tube: tors**	150	90	5.7	6.5	5	0.4
16) **FD: Bent tube: lin**	70	73	0.59	7	15	0.13
17) **FD: Bent tube: semi layers**	370	122	0.59	7	15	0.3
18) **FD: Bent tube: tors**	140	107	0.59	7	15	0.13
19) **SG: Aorta: lin**	50	12	7.4	11.3	5.8	0.3
20) **SG: Aorta: semi layers**	90	30	7.4	11.4	5.9	0.7
21) **SG: Aorta: tors**	80	24	7.5	12	5.9	0.3
22) **FD: ICA: lin**	500	126	0.5	4.5	4	0.1
23) **FD: ICA: semi**	500	130	0.4	4.5	4	0.15
24) **FD: ICA: tors layers**	600	150	1	4	10	0.2

Table 5.1: Values of convergence metrics at the end of the deployment process. Columns correspond to: **it** is the number of iterations required for convergence, $\overline{\boldsymbol{d}}$ is the mean nodal distance, $\overline{\boldsymbol{\theta}}$ is the mean angle difference, $\overline{\boldsymbol{L}}$ is the mean struts' length difference, $\overline{\boldsymbol{F}}$ is the mean nodal force.

of iterations based on the approximative methods.

With respect to the speed of the virtual simulation, it was sufficiently fast, the longest simulations lasting about 2.5 minutes for the case of the ICA cerebral

aneurysm with the high density FD device. Being implemented in MATLAB, with no parallelisation and on slow and antiquated hardware, the models are likely to obtain much higher speed when run on the more appropriate and powerful architectures. Achieving such fast running times was a very positive outcome, for high speed constitutes one of the top priorities for the development of the stent deployment method, as outlined in Section 1.2.

Overall, the presented results demonstrated that the lineal spring analogy method proved suitable for modelling the stent expansion in a fast way. Given the almost identical final device configurations obtained with the other two more sophisticated methods, it seemed that the employment of the complex torsional and semi-torsional springs did not add value in the problem of stent deployment modelling. Not only did they require more iterations to converge, but each iteration in itself was computationally more expensive, especially in cases of the torsional springs method. Therefore, from now on, the fast stent deployment algorithm will only use the stent expansion method based on the lineal spring analogy, putting aside the semi-torsional and torsional spring models.

To sum up, the results of this chapter demonstrated that the fast method based on the lineal springs model was able to bring the stent devices to expand. But how good is the algorithm in terms of assessing the final device configuration? Next chapter is dedicated to the validation of the lineal springs stent deployment method. It presents a study that compares the results reported here with the results of the finite element method for the SG device. The FEA method, being very slow but precise, can provide a validation benchmark for the fast springs method, assess the eventual divergence in the results and estimate the error.

From now on, the developed stent deployment method based on the lineal springs model will be referred to as simply the “fast method” or “FM”.

CHAPTER 6

VALIDATION OF DEPLOYMENT METHOD: COMPARISON TO FEA

This chapter presents a validation study for the newly developed fast virtual stent deployment method. To validate the new stenting method, its performance was compared to the gold standard of FEA in a number of *in silico* experiments. Given the results of the initial comparison, the fast method was further optimised by calibrating a set of parameters with the help of a genetic algorithm, which utilised the FEA outcomes as a learning base.
This chapter has been published in an alternative form in Spranger et al. (2014a).

The newly developed virtual stent deployment method featured fast computational times, which is a crucial characteristic for its future usefulness it clinical practice. However, the fast computational speed inevitably comes with a cost of reduced accuracy; therefore, the error has to be thoroughly estimated. On the other hand, a good candidate for modelling realistic stent behaviour is the FEA method, which has become a gold standard in mechanical simulations (as mentioned in Section 3.1.1). Although slow in speed, FEA can both simulate the process with high accuracy and provide a benchmark for estimation of the stiffness constants for the lighter spring method.

Hence, the goal of this chapter is to perform a comparative analysis of the results obtained by the new fast method (FM) with the FEA results. The SG device employed in the previous chapter was chosen to be the subject of comparison (see Section 5.1). Additionally, the stiffness setting for the spring model was investigated, using the FEA results as a learning base for fitting the stiffness parameters. For that pur-

pose, a number of *in silico* experiments of increasing complexity were conducted with the aim of evaluating the divergence in final device configurations and residual force estimation. To focus exclusively on the process of stent expansion and perform a valid comparison, the vascular wall was assumed rigid, using the rigid contact model (see Section 4.3.3).

First, the chapter describes the computational setup of validation experiments (Section 6.1), followed by the comparison report of the initial discrepancy in final device configurations and residual force estimation (Section 6.2). Thereafter, the optimisation step is reported, in which the parameters of the fast method were calibrated with the help of a genetic algorithm guided by the FEA results (Section 6.3). Finally, the post-calibration results are presented.

6.1 COMPUTATIONAL SETUP

FEA model. The theory behind the finite element analysis was presented in Section 4.4. The implementation of the FEA model for the FEA deployment experiments was done by my collaborators Claudio Capelli and Giorgia Bosi[1], who were also acknowledged at the beginning of the thesis.

All FEA simulations were performed using the FE code Abaqus 6.11/Explicit (Dassault Systemes Simulia Corp., Providence, RI, USA) on an Intel Xeon X5690 with 2 processors of 3.46 GHz and 24 GB of RAM. All simulations ran in parallel using 4 cores. The CAD model of the SG device was meshed with beam and shell elements to discretise the stent struts and the stent graft, respectively. Following sensitivity analysis, the average length of the beam elements was 0.9 mm with a final mesh resulting in 2,371 elements, while the average size of shell elements was 0.8 mm for a total of 13,004 elements. The constitutive models used to characterise both the nitinol stent struts and polyester graft were based on a previously validated study by Capelli et al. (2012). Each FEA deployment experiment consisted of three steps: crimping, positioning within the vessel model and deployment.

1. *Crimping.* The device was crimped to the size of the delivery catheter (8 mm diameter) by applying a radial displacement (15 mm) to a coaxial cylindrical surface. Such cylindrical surface mimicked the presence of a membrane

[1] Cardiovascular Unit, University College London, Institute of Child Health and Great Ormond Street Hospital for Children, London

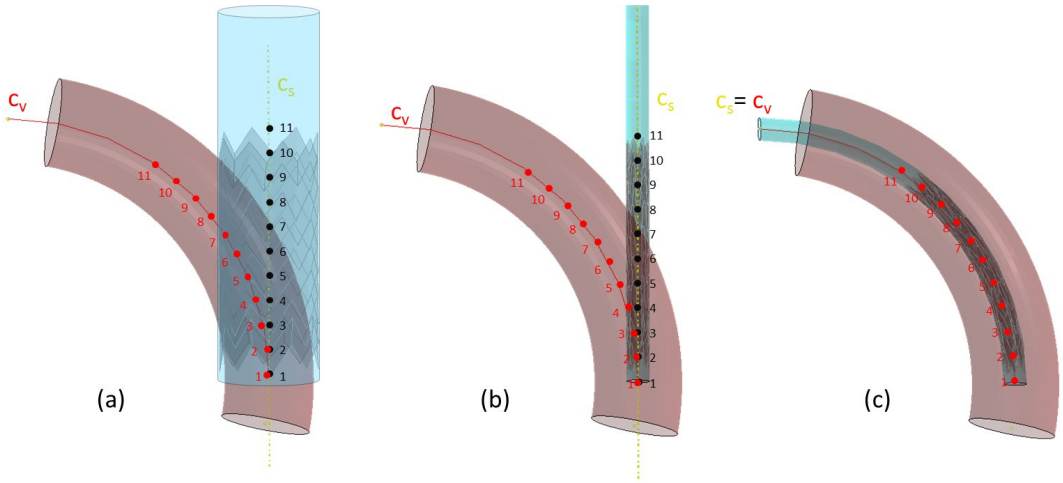

Figure 6.1: Crimping and initial positioning of the SG with FEA method. (a) The stent before crimping. C_v (in red) is the centerline of the vessel defined by 11 points. C_s (in yellow) is the centerline of the stent and the coaxial cylinder. (b) After the cylindrical surface crimped the stent, displacements and rotations were applied to the points of C_s, in order to make them reach the corresponding points of C_v and to position the stent inside the vessel (c).

sheath that constrains the stent into a delivery catheter (see Figure 6.1, a). Specific boundary conditions were assigned to the SG device, in order to avoid rigid translation during the analysis: the device was constrained in its terminal section in both circumferential and axial direction (see Figure 6.1, b).

2. *Positioning.* In order to position the crimped stent and its cylindrical sheath within each virtual implantation site, the respective centerlines were used. Since the stent and the sheath were coaxial, their centerline (C_s) was unique. Such centerline was then aligned to the vessel centerline (C_v). For that purpose, the lines were subdivided through a discrete number of points ($n = 11$). A kinematic constraint was applied between the points of C_s and the nodes of the cylinder lying on the plane passing through that point and cutting C_s perpendicularly. Hence, differences in coordinates between the points of C_s and C_v were calculated. The resulting displacements and rotations were applied onto the points of C_s, causing the bending of the device (see Figure 6.1, c).

3. *Deployment.* The deployment of the stent was achieved by replicating the release from the delivery catheter and was implemented by gradually retrieving the virtual membrane sheath.

Comparison experiments. The FM versus FEA comparison was based on the analysis of the expansion of the SG device under 6 different conditions:

1. Deployment within a 34 mm cylindrical vessel. This is a usual size for a 40 mm device diameter, since the grafts are always oversized in clinical practice by about 30% (Golzarian and Valenti, 2006).

2. Deployment within a 20 mm cylindrical vessel. This vessel is too small for a given graft size and would not be used in such a combination in clinical practice. However, the narrow vessel was utilised for the purpose of force juxtaposition measured with two compared methods, in order to investigate how the forces scale with a growing amount of crimping in the device.

3. Deployment within a bent vessel (diameter = 34 mm, curvature = 0.01)

4. Deployment within a C-shaped vessel (diameter = 34 mm, curvature = 0.02)

5. Deployment within an W-shaped vessel (diameter = 34 mm)

6. Deployment within an anatomical model of a patient-specific dissected aorta. As it would be done in clinical practice, the SG was placed inside the true lumen to cover the initial tear entry and prevent blood from flowing into the false lumen. The vessel diameter was varying at the deployment site: in the distal location (with respect to the dissection entry) it was approximately of a circular shape with 2.9 cm in diameter, whereas proximally the true lumen resembled an oval with dimensions of 1.3 and 2.8 cm. Hence, the geometry in the proximal end was quite irregular, exhibiting sharp corners that could be problematic to comply with for a stiff device. In both FM and FEA methods, the opening of the device was initiated at the distal end and was progressing to the proximal extremity, as common for this type of device.

Comparison metrics. In order to quantify the differences in outcomes of the two methods, the following parameters were measured:

1. Residual distance between the corresponding nodes of the deployed stent, expanded with the two different methods: FM and FEA. The difference was calculated by comparing these distances to the vessel diameters.

2. The distribution of residual forces in stent vertices in the two different methods: FM and FEA. While FM can directly output nodal forces, the residual forces (RF) in the FEA method can be calculated only if the structure is constrained in all directions. For this reason, the RF of the stent vertices were derived through the reaction forces measured at each node of the vessel, which is always fully constrained. For each stent vertex in contact with the vessel, it was possible to find the 4 closest nodes of the vessel with the help of a specifically implemented automated method. These 4 nodes belonged to the element of the vessel in contact with the vertex of the stent. The sum of these 4 RF was equal and opposite of the RF in the stent vertices (see Figure 6.2).

3. Relative error in struts' length, measured relative to the original length of struts, i.e., in the load-free stent configuration.

6.2 RESULTS

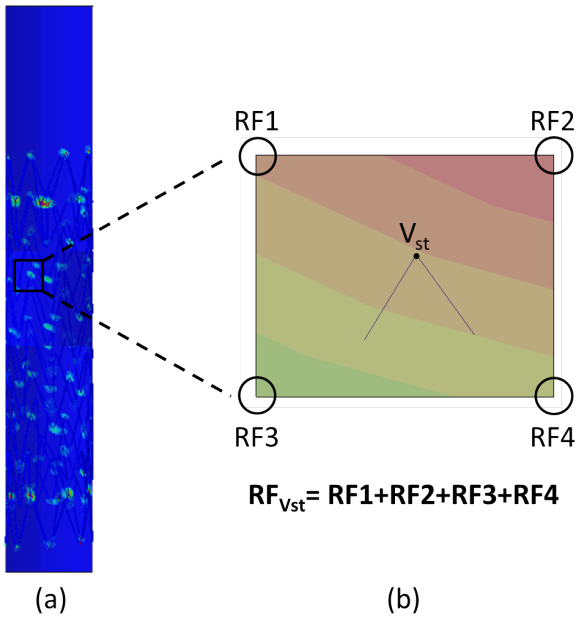

Figure 6.2: Measurement of reaction forces in FEA. (a) Reaction forces (RF) of the vessel are represented by a color map for the 20 mm cylindrical vessel. (b) The RF of the stent vertex V_{st}, which is in contact with the vessel, was calculated summing up the 4 RF of the 4 closest vessel nodes.

6.2.1 Free expansion

To test the validity of the models and their overall performance, free expansion experiments were first set up with both FM and FEA methods. From the initially crimped configuration (8 mm in diameter which is 20% of the labelled diameter), the SG device was subject to free expansion, under the subsequent release of constraints along the device, until it reached the load-free configuration. Analogous to the previous chapter, the dynamics of the FM expansion process was evaluated with the help of 4 metrics of convergence that were defined in Section 5.1. To set up the FEA free expansion, quasi-static conditions were used. These postulate that the contribution of the kinetic energy to the total energy should equal zero, assuming that there are no inertial effects. Therefore, to verify the convergence of the FEA model, the ratio *kinetic energy*/*internal energy* had to reach a value $< 5\%$.

Figure 6.3 highlights the phases of the free expansion process simulated with both numerical methods. In particular, results of FM simulations are presented as the snapshots of the obtained stent configurations after a certain number of iterations (upper row), while FEA models are shown throughout the time step (30 seconds) of the simulation (lower row). Dynamics of the expansion process are captured in Figure 6.4, where the four metrics of convergence (b) and the internal energy (a) were plotted for FM and FEA, respectively. The evolution of all plotted functions confirm the convergence of the results and the ability of both methods to bring the device to the load-free configuration.

Specifically for the FM case, the nodal displacement (Figure 6.4 b, upper left corner) converged completely after 200 iterations, while the measure of angular distance (Figure 6.4 b, upper right corner) and the measure of the residual nodal forces (Figure 6.4 b, bottom right corner) exhibited a slightly faster convergence, being almost zero during the last 100 iterations. The trend in the struts' length error (Figure 6.4 b, bottom left corner) showed a different tendency, with the error first increasing up to 20% after few iterations and then decreasing in the course of the iterative process, until complete convergence was reached.

The analysis of the ratio between internal and kinetic energies of the FEA model confirmed the absence of any dynamic processes at the end of the free expansion phase, when the stent graft completely recovered its original shape, as displayed in Figure 6.4 (a).

6.2.2 Deployment in idealised vessels

As in the free expansion case, the device was crimped to 8 mm and then deployed, this time until it reached the vessel walls.

Straight vessels. In this set of experiments, the device was deployed inside two idealised vessels in the shape of a straight cylinder. The diameter of the first vessel was 34 mm and of the second 20 mm. The deployment was performed in layers simulating the gradual release from a catheter, as can be seen in Figure 6.5 showing the snapshots of FM expansion after a certain amount of iterations. In the FM case, the

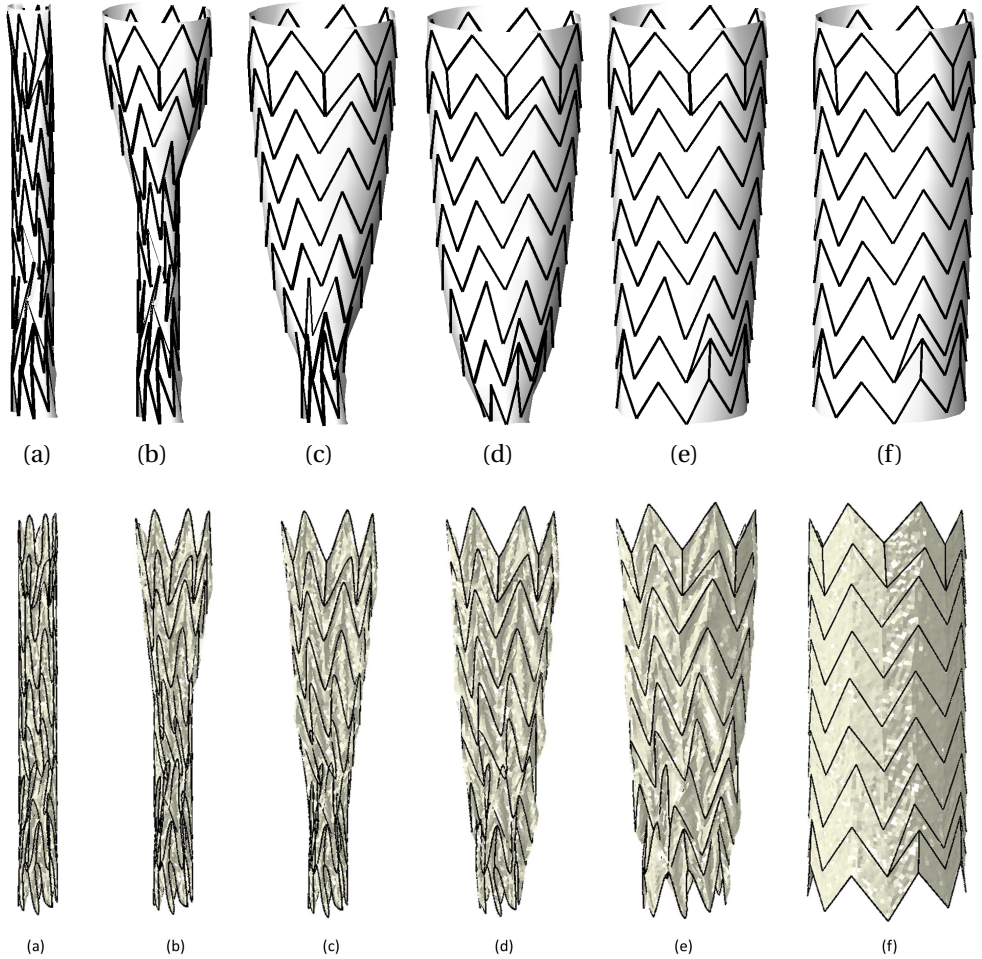

Figure 6.3: First row: free expansion of the SG device with FM: (a) initial crimped stent, (b) result after 10, (c) 50, (d) 150, (e) 250, (f) 500 iterations. Second row: free expansion of the SG device with the FEA method, whereby the crimped configuration was gradually released to the full expansion.

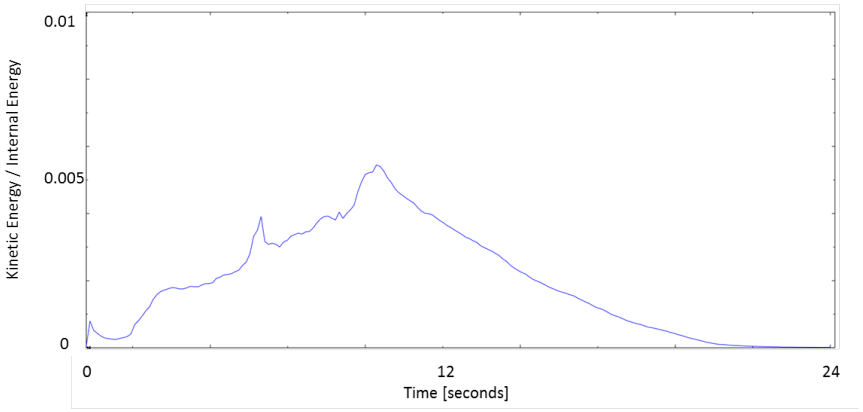

(a)

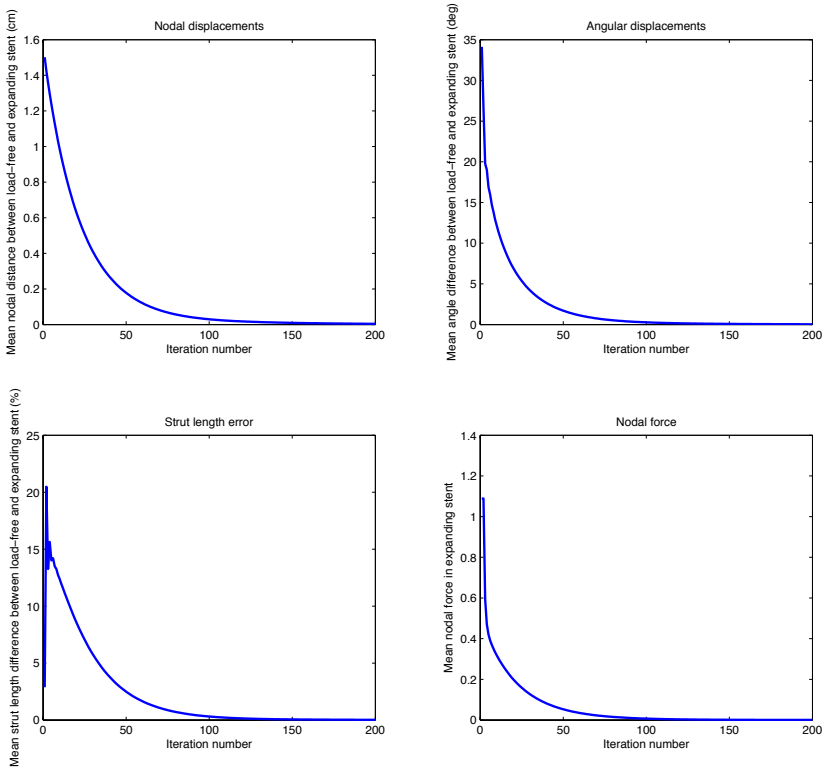

(b)

Figure 6.4: Convergence in the free expansion experiment. (a) The convergence of the FEA model in the free expansion experiment was achieved when the stent was fully deployed, and the ratio *kinetic energy*/*internal energy* was below 0.05. (b) Free expansion of the SG for 200 iterations with FM. Upper row: mean nodal distance and mean angle difference between the load-free and the expanding stent. Bottom row: mean strut length difference and mean nodal force in the expanding stent. FM reached convergence after about 200 iterations and 3 seconds of execution time.

convergence of parameters throughout the deployment process exhibited the same dynamics as in the free expansion case (Figure 6.4), with the only difference being that the device did not reach the load-free configuration because of the oversizing, which also happens in reality. Additionally, convergence was reached faster due to the contact with the vessel and the device oversizing, after about 200 iterations of layered expansion.

To visualise the difference between the two methods, Figure 6.6 illustrates the final deployed configuration for FM and the difference between the two methods by means of overlaying the two resulting devices. To quantify the results, Figure 6.7 (a) displays the residual nodal distances obtained with different methods for the deployment in two vessels, which is the equivalent of the *mean nodal distance* metrics employed in the free expansion case (see Figure 6.4, b). The distribution of differences between the load-free (LF) and the resulting FM configuration (FM) is summarised in the histogram in blue, the differences FEA vs LF in green, and finally, the difference between FM and FEA methods in red. The latter is the most interesting measure, showing for the 34 mm vessel the average difference in results of about 3.8% (mean μ = 2.73211%; percentage with respect to the vessel diameter) and the standard deviation σ = 1.20133%, when fitted to the normal distribution.

For the 20 mm vessel, the discrepancy between FM and FEA methods was more

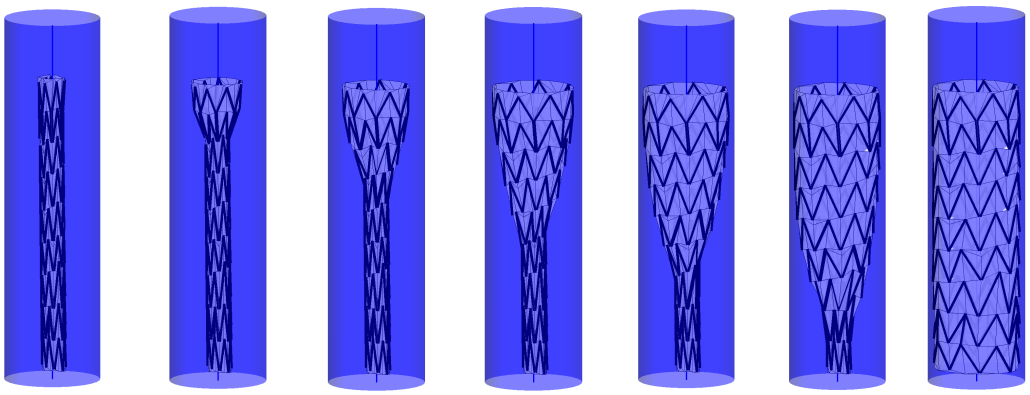

(a) (b) (c) (d) (e) (f) (g)

Figure 6.5: FM deployment of the SG device in a straight tube. Results after (a) initial crimping, (b) 20, (c) 45, (d) 65, (e) 85, (f) 110, (g) 200 iterations of the layered expansion.

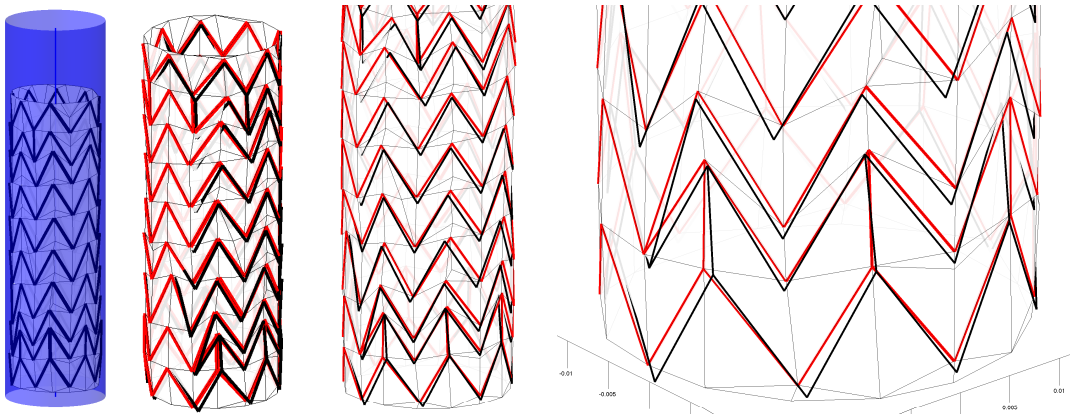

Figure 6.6: Deployment in straight vessels. Nodal distance between the resulting stent configurations, with FM in red and FEA in black (gradual zoom inside the structure from left to right).

pronounced: mean μ = 7.13367% and standard deviation σ = 2.59948%. The difference for the more narrow vessel was larger because the device did not have a chance to sufficiently open up before hitting the vessel wall and was still exhibiting a configuration very close to the crimped one. Since the crimping procedures in both methods were different (and hence different crimped configurations), the nodal difference effectively includes the difference in crimping as well. In a wider vessel, the difference in crimping was gradually elevated in the course of the expansion process, when the device was moving to its load-free configuration, resulting in a smaller difference.

Figure 6.7 (b) shows the relative error in struts length after the deployment in the two vessels, which is equivalent of the *mean strut length difference* metrics employed in the free expansion case (see Figure 6.4, b). In case of the 34 mm vessel, the majority of struts displayed an error of less than 3% of their original length; however, there were few struts exhibiting an error of 8%. As could be seen in the free expansion case, FM scrambled the struts length at the beginning of the iterative process, correcting it in the course of subsequent iterations (see Figure 6.4 (b), bottom left graph). This convergence dynamics was the reason for higher error rate in the narrower 20 mm vessel. Here, the average was around 6%. In contrary, the FEA method did not distort the struts length to such extent; however, for the 20 mm vessel there was a nonzero error of about 2%.

The distribution of residual forces is plotted in Figure 6.7 (c). The values of

forces measured by FM lay in the same order of magnitude as those reported by FEA method. Even in the case of the narrow 20 mm vessel, the relation remained the same, which means that the forces reported by FM scaled in a good way with the increase of the crimping in the device. The general trend was that the FEA forces were slightly smaller in value compared to those reported by FM.

Curved vessels. In this set of experiments, the vessel geometry was represented as a curved (rather than a straight) cylinder with a diameter of 34 mm, curved in three different ways: slightly bent, C-shaped and W-shaped vessel. Figure 6.8 displays the snapshots of the FM deployment inside the bent vessel after a certain amount of iterations. The overall convergence behaviour was similar to the free expansion case depicted in Figure 6.4. However, this time the SG did not reach the load-free configuration, as it was also the case for the straight vessels. Similarly, there remained a small nonzero restoring force after the deployment completion, which was the ex-

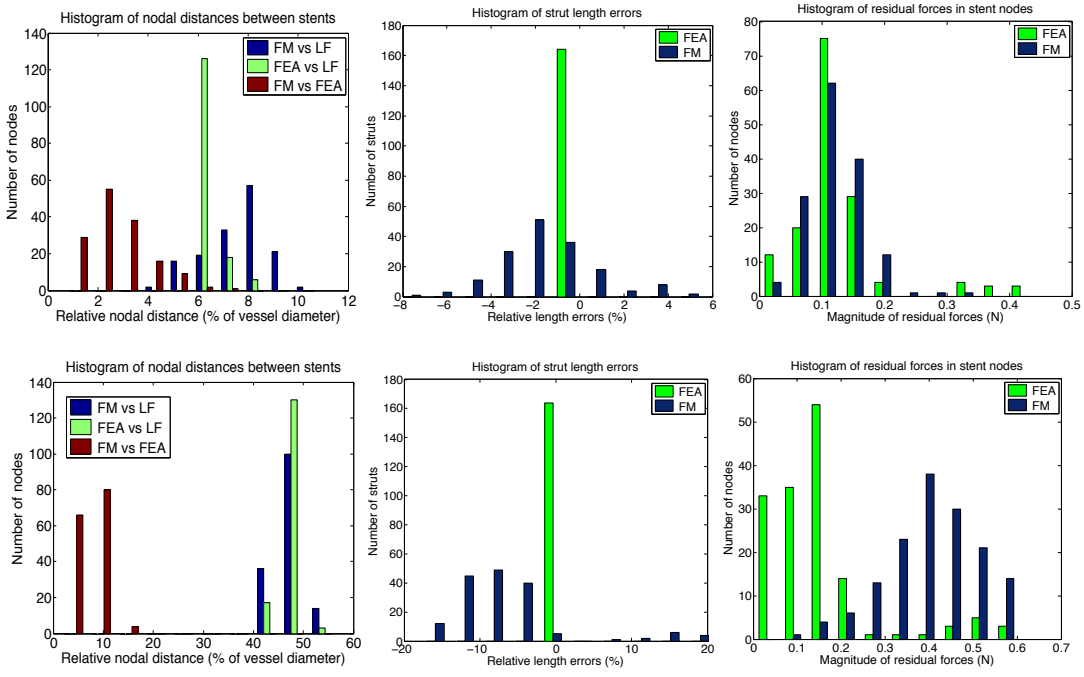

(a) (b) (c)

Figure 6.7: Difference between FM and FEA methods for straight vessels: top row shows results for 34 mm vessel; bottom row – for 20 mm vessel. (a) Residual nodal distances: (top) mean μ = 2.73211% (percentage with respect to the vessel diameter), standard deviation σ = 1.20133%; (bottom) μ = 7.13367%, σ = 2.59948%. (b) Relative error in struts' length. (c) Residual force distribution.

pected outcome due to the oversizing of the device and the geometry of the vessel.

The visual comparison of the resulting device configurations is illustrated in Figure 6.9. Here, for each of the three geometries, first the final configuration obtained with FM is shown inside the vessel and then overlaid with the FEA result (omitting the vessel for the sake of better visibility). It can be seen that the central part of the devices displayed good agreement between the two methods, while the extremities featured higher degree of discrepancy.

The quantitative difference between the methods is captured in Figure 6.10, that tracks the resulting values of the convergence metrics defined earlier. It is worth remembering that some metrics which were used to evaluate the performance of the methods are less meaningful on their own for the bent and more complicated geometries, as mentioned in the previous chapter. Nevertheless, these familiar metrics remain useful to compare the two methods relative to each other.

The general trend in the performance of FM was that there is an increase in discrepancy for the curved geometries, as compared to straight cases. The mean residual nodal distance (Figure 6.10, a) increased to approximately 9% relative to the diameter of the vessels (34 mm). As already mentioned, the errors seemed to be concentrated in the extremities of the device. In order to confirm this impression, the distribution of the nodal differences along the length of the device was additionally plotted (Figure 6.10, b). Indeed, the discrepancy was more pronounced at the ends of the devices.

Struts' length error was also slightly higher than in the straight cases, scattered

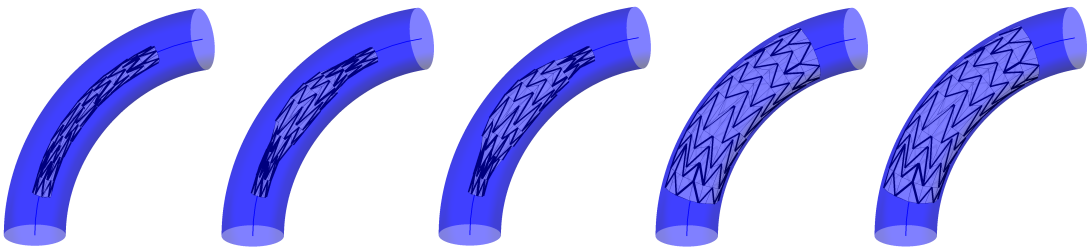

Figure 6.8: FM deployment of the SG in the bent vessel. Results after (a) crimping and initial positioning along the centerline, (b) after 20, (c) 30, (d) 100, (e) 200 iterations.

around 4%, but reaching as high as 15% for few exceptional nodal positions (Figure 6.10, c). Figure 6.10 (d) shows the distribution of the residual nodal forces, the values of which retained the same order of magnitude as those reported by the FEA method. In general, it can be seen that FM forces exhibited a slightly larger values than those of FEA.

6.2.3 Deployment in real vessels

The last experiment was performed on the patient-specific geometry of the aortic dissection. Figure 6.11 (a-e) shows the FM deployment snapshots at different phases during the iterative process. The final configuration was obtained after approximately 200 iterations of FM and required around 20 s. The device was in a reasonably good opposition to the vessel wall and entirely covered the initial tear. However, as compared to the FEA resulting configuration, the middle of the device was not complying to the vessel wall completely, which can be seen in Figure 6.11 (f-j) displaying the difference between the resulting configurations of the two methods. The reason for the lack of opposition in the FM device was the oval vessel geometry. In this geometry, FM detected the contact too soon in that part of the vessel circumference which had smaller radius of the oval. This led to termination of the device expansion, without further expansion in the part of the vessel circumference with larger radius of the oval. Such cases clearly show the limitation of the contact model employed (rigid contact).

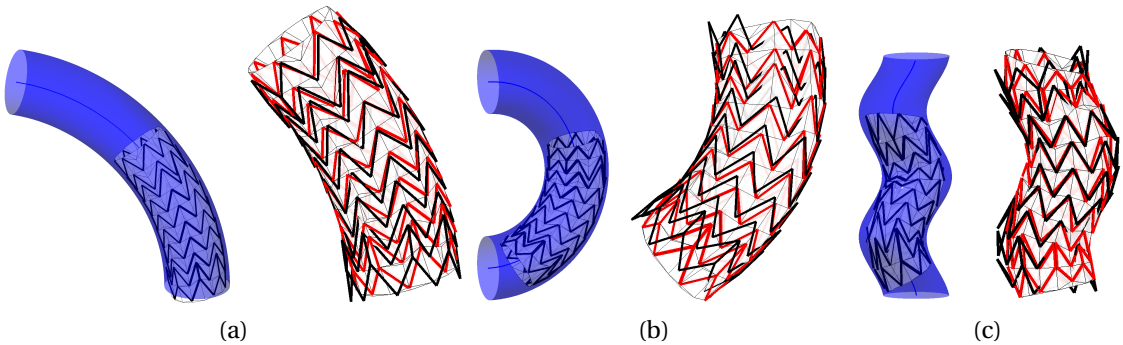

Figure 6.9: Resulting configurations after deployment in curved vessel geometries: (a) bent vessel, (b) C-shaped vessel, (c) W-shaped vessel. The resulting configuration obtained with FM is first presented inside the corresponding vessel, and afterwards displayed in red and overlaid with the FEA result in black.

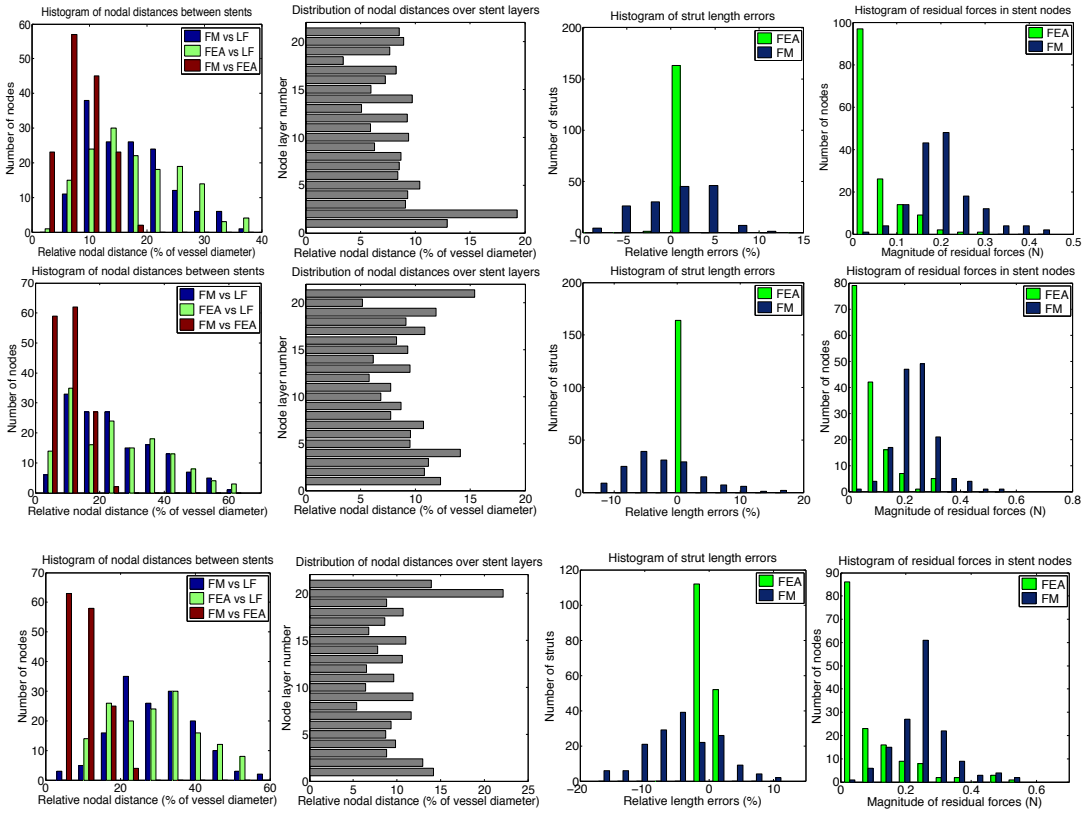

Figure 6.10: Difference between FM and FEA methods for curved vessels: first row shows results for the bent vessel; middle row – for the C-shaped and bottom row – for the W-shaped vessel. (a) Residual nodal distances: (top) mean μ = 8.31712% and standard deviation σ = 3.67111%; (middle) μ = 9.70638% and σ = 4.35756%; (bottom) μ = 9.58366% and σ = 4.36227%. (b) Distribution of the nodal differences along the length of the device. (c) Relative error in struts' length. (d) Residual force distribution.

Figure 6.12 sums up the metrics of the resulting differences. The important result was the mean residual nodal distance that lay around μ = 10.5% with respect to the vessel diameter (taken to be 2.5 cm as the result of averaging of the round distal and oval proximal diameters). The FM forces were again exhibiting slightly larger values compared to their FEA counterparts.

The summary of the comparative analysis is captured in Figure 6.13. In the simple straight geometries, the average nodal distance discrepancy was about 4%, but was larger in more complex geometries (Figure 6.13, a). Overall, the nodal difference tended to increase with the increasing complexity of the vessel model, reaching its

maximum in the case of dissected aorta (μ = 10.50% and and σ = 4.64%). With respect to residual forces, the average difference in forces between the two methods lay below 1 N and an absolute maximum was 4 N in the case of the curved C-shaped vessel (Figure 6.13, b). In all experiments, the forces of FM lay in the same order of magnitude as the FEA forces but displayed higher values. This outcome indicated that the stiffness of the springs in FM was set too high. With this in mind, the implications of the stiffness values are further investigated in the next section, with the motivation of finding a more appropriate setting and improving the performance of FM.

One of the most important outcomes of the comparative analysis was the fact that in all tested cases the use of FM was associated with a dramatic reduction in

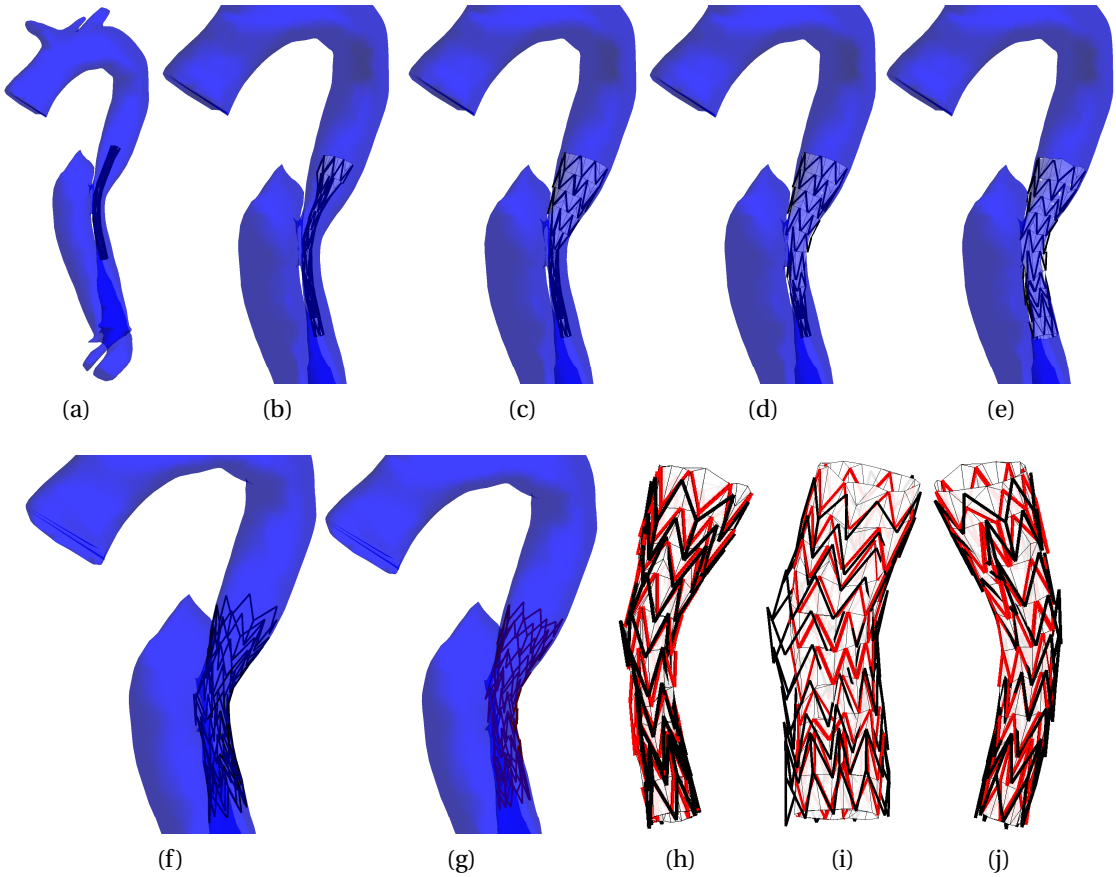

Figure 6.11: Placement of the SG over a dissection entry. Result after (a) 1, (b) 20, (c) 50, (d) 80, (e) 150 iterations of layered FM expansion. (f) Resulting FEA configuration inside the vessel. (g) Resulting FM configuration inside the vessel. (h-j) Overlay of FM (in red) with FEA (in black) final device configurations.

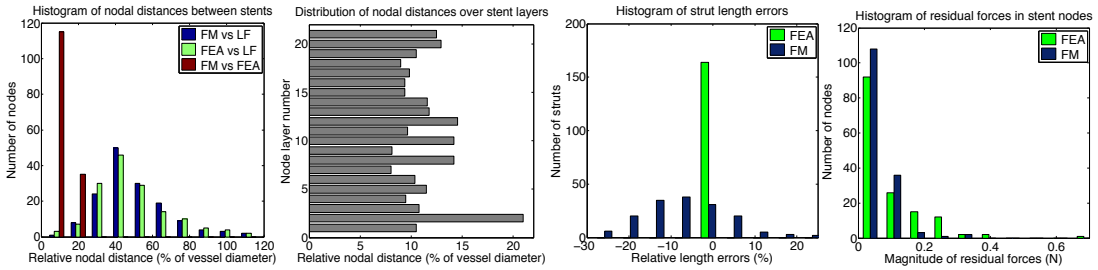

(a) (b) (c) (d)

Figure 6.12: Difference between FM and FEA methods for aortic geometry. (a) Residual nodal distances: mean μ = 10.4888% and standard deviation σ = 4.6468%; (b) Distribution of the nodal differences along the length of the device. (c) Relative error in struts' length. (d) Residual force distribution.

computational time when compared to FEA, generally being in the order of seconds for FM and in the order of hours for FEA. Table 6.1 reports the timings of the simulations for both methods. Free expansion was the fastest case, where FM reached the load-free configuration in just 3 seconds, while simulations inside the vessels with the diameter of around 30 mm took approximately 30 seconds. Most of the execution time of the FM deployment algorithm was spent on the contact check

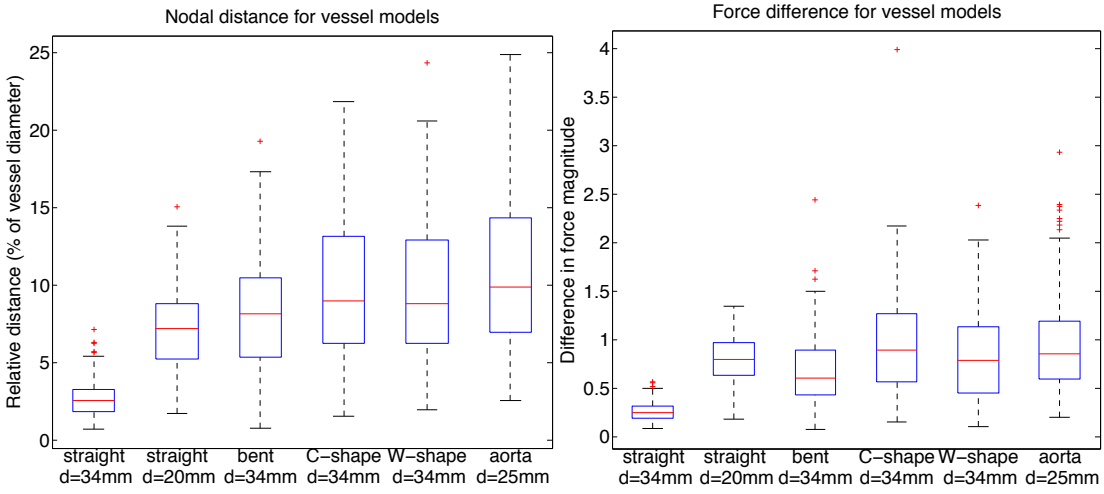

(a) (b)

Figure 6.13: Initial difference between the two methods FM and FEA for all vessel models. (a) Resulting nodal distance with the median value represented as a red line and the blue box outlining the 25th and 75th percentiles; the whiskers extend to the most extreme data points not considered outliers, and outliers are plotted individually. (b) Resulting difference in force magnitude between the two methods.

Simulation setup	Fast time (s)	$\overline{d}$ (%)	FEA time
1) **Free expansion**	2.01	0	2h 3 min
2) **Straight vessel: 34 mm**	28.60	2.73	1h 33 min
3) **Straight vessel: 20 mm**	8.55	7.13	7h 4 min
4) **Curved vessel: bent**	39.70	8.31	10h 15 min
5) **Curved vessel: C-shaped**	41.75	9.70	8h 9 min
6) **Curved vessel: W-shaped**	32.75	9.58	7h 28 min
7) **Aortic dissection**	19.44	10.50	4h 30 min

Table 6.1: Results of 7 stent deployment simulations with FM and FEA.

and calculations of the implications the vessel wall had on the stent structure when they were in contact. Interestingly, in both methods, the highest computational time (i.e., curved vessels) was not associated with the most complex geometry (i.e., patient-specific case of aortic dissection). Another fact worth mentioning is the relationship between the computational time and the diameter of the vessel in both methods. While the computational time for FM was directly related to the diameter of the vessel, the relation is reversed for the FEA case. The reason for this outcome was that FM employed a rather simple contact model, meaning that the expansion terminated when the vessel wall was encountered. In contrast to this, most of the execution time of FEA deployment was associated with the attempt to solve the interactions between stent structure and the vessel model.

Bearing in mind these initial results, the next section reports on the effect of modifying the FM stiffness setting, following stiffness calibrations with genetic algorithms.

6.3 Calibration with Genetic Algorithms

This section aims at finding more suitable stiffness values for the FM. On the whole, the stiffness setting has enormous implications for the expansion process. Without any modification to other parts of the expansion algorithm, alterations to the stiffness setting can lead to substantial degradation or even a complete loss of expanding properties of the modelled device. For example, when the stiffness of the springs was changed to arbitrary unsuitable values, all other things being equal, even the

simplest case of free expansion barely converged. Up until now, the stiffness of a spring was set to be inversely proportional to its length, which is a standard setting widely used in the literature (Batina, 1990). In the test below, this conventional value was scaled with a constant scalar. Additionally, it was differentiated between the scaling values for the background springs and the springs representing stent struts. More precisely, the stiffness was set to $0.1 \times \frac{1}{l}$ for springs of the background sheath and $5.1 \times \frac{1}{l}$ for the struts, where l was the length of the spring, with the intuition that the nitinol struts should be much stiffer than the sheath. The resulting convergence behaviour worsened considerably, as can be seen in Figure 6.14 (a). Compared to the previous setting with which the free expansion was completed after roughly 150 iterations (see Figure 6.4), the expansion with the new stiffness setting barely converged after 1,000 iterations! The resulting configuration after 150 iterations (which was previously enough to reach convergence) is displayed in Figure 6.14 (a) for illustration purposes. Figure 6.14 (b) shows the new convergence dynamics and (c) displays the result of another unsuitable stiffness setting ($0.03 \times \frac{1}{l}$ for springs of the

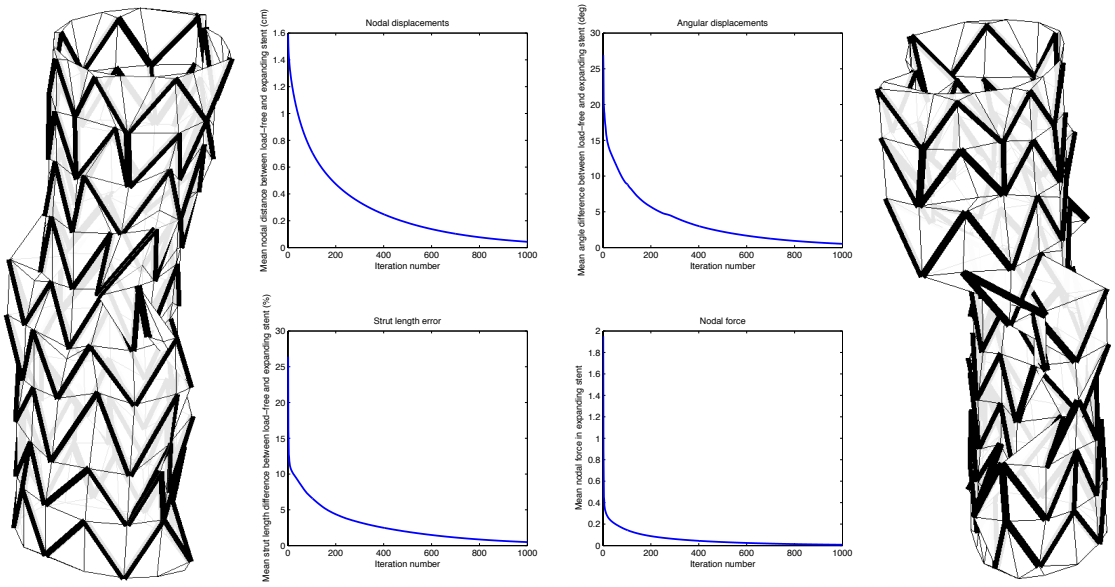

(a) (b) (c)

Figure 6.14: Deterioration of the convergence behaviour for the free expansion case due to the altered stiffness values. (a) Resulting configuration after 150 iterations with stiffness set to $0.1 \times \frac{1}{l}$ for springs of the background sheath and $5.1 \times \frac{1}{l}$ for the struts. (b) Convergence curves during 1,000 iterations with the stiffness setting in (a). (c) Resulting configuration after 150 iterations with stiffness set to $0.03 \times \frac{1}{l}$ for springs of the background sheath and $3.03 \times \frac{1}{l}$ for the struts.

background sheath and $3.03 \times \frac{1}{l}$ for the struts).

As reported in the previous section, FM forces were slightly higher than those reported by the FEA method but lay in the same order of magnitude. Therefore, the goal here was to find stiffness parameters resulting in better alignment between the two methods. The idea was to utilise the known final FEA configurations and reported residual forces as a reference for optimising the stiffness parameters of FM, using the framework of genetic algorithms (GAs). Hence, the cost function for GAs formulation should take into account the discrepancy between FM and FEA outcomes in terms of the nodal distances and the value of forces. The theory behind GAs was outlined in Section 4.5.

Setup. In theory, the spring constant of an "ideal" spring can be found as $k = \frac{EA_0}{L_0}$, where E is the Young's modulus of the material, A_0 is the unstretched cross sectional area and L_0 is the unstretched length of the spring. This indicates that, all else being equal, k is inversely proportional to the original length of the spring (L_0), scaled by EA_0. Therefore, in the FM model, the inverse relation to the length was kept, as was the case before, and the quest was set for finding the optimal scaling constant with the help of the GA. Additionally, it was differentiated between the scaling values for the background springs (*wBg*) and the springs representing stent struts (*wStr*). Hence, the space the GA was operating within can be visualised as a 3-D function defined by the two stiffness weights of interest: *wStr* and *wBg*. The springs constants were now calculated in the following way for a spring $(i-j)$ connecting vertices $\mathbf{v}_i = (x_i, y_i, z_i)'$ and $\mathbf{v}_j = (x_j, y_j, z_j)'$:

$$k_{ij}^{Bg} = \frac{wBg}{\|\boldsymbol{v}_i - \boldsymbol{v}_j\|} \quad \text{and} \quad k_{ij}^{Str} = \frac{wStr}{\|\boldsymbol{v}_i - \boldsymbol{v}_j\|} + k_{ij}^{Bg} = \frac{wStr + wBg}{\|\boldsymbol{v}_i - \boldsymbol{v}_j\|} \tag{6.1}$$

Figure 6.15 illustrates an approximative extract from this space for the case of the bent vessel (from the previous section) for the intervals $wBg = [0.1...1]$ and $wStr = [0...1]$ along abscissa and ordinate axis, respectively, and the corresponding cost value along the z-axis. The graph shows the behaviour of the nodal (a) and force (b) difference as parameters vary. The mean squared error of the nodal distance ranged between 80 (blue) and 170 (red), whereas the mean squared force error lay between 0.015 (blue) and 0.2 (red) in these intervals. Note the difference of more than 3 orders of magnitude between the error measures. To bring both values to the same order of magnitude, they will be redefined as dimensionless quantities for the later stiffness optimisation problem (see Equations 6.2 and 6.3).

All simulations in the initial comparison (previous section) were performed with the stiffness setting *wStr = 0* and *wBg = 1*, which was located at the bottom right corner of the error space, indicated by the red arrows in Figure 6.15. With the help of the graphs, it can be seen that this stiffness setting corresponded to a relatively low value with respect to the nodal difference; however, it mapped to a fairly high point on the force difference space, compared to other values of the analysed interval. More precisely, the baseline mean squared error values were $\overline{e}_{nodal}$ = 82.7447 and $\overline{e}_F$ = 0.1196.

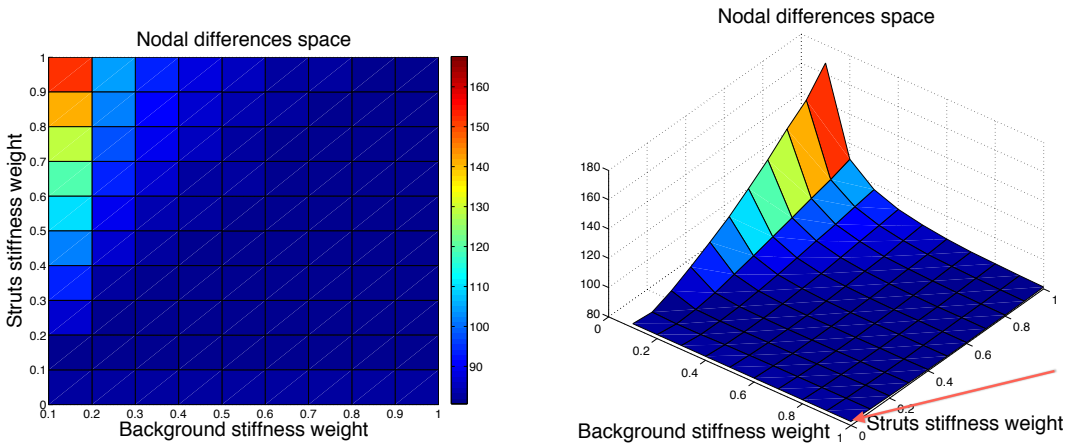

(a)

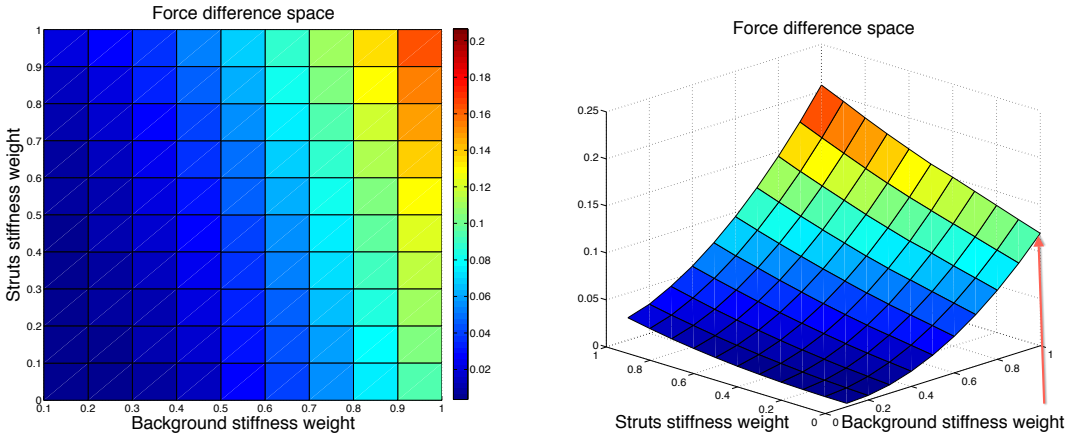

(b)

Figure 6.15: Variation of the error space as a function of stiffness scaling. (a) Space of nodal differences. (b) Space of force differences. Baseline values from the initial comparison (previous section) are indicated by red arrows: $\overline{e}_{nodal}$ = 82.7447 and $\overline{e}_F$ = 0.1196.

Implementation. As already mentioned, two classes of springs were distinguished: springs belonging to the stent struts and those of the background sheath.

Population: In each generation, there were 7 individuals in the population. Each individual was defined by a pair of genes that represented the two scalars of interest: the weight for the background sheath (*wBg*) and the (additional) weight for the struts stiffness (*wStr*), i.e., an individual was represented as a pair $ind_1 = [wStr,\ wBg]$. The population was randomly initialised and then evolved for roughly 100 generations using the genetic operators described below.

Cost function: Both the nodal distances and the force values were optimised simultaneously. Firstly, the mean squared errors of both values were computed, by calculating them from the convergence metrics used in the previous section. More precisely, the mean squared difference in residual force magnitude was measured

$$\overline{e}_F = \frac{1}{N}\left(\frac{1}{\boldsymbol{F}^{FE}_{max}}\right)^2 \sum_{i=1}^{N} (\|\boldsymbol{F}^{FE}_i\| - \|\boldsymbol{F}^{FM}_i\|)^2, \tag{6.2}$$

where $\boldsymbol{F}_i$ is the reaction force at the node i, with the index i running from 1 to number of nodes N. Note that to make the force measurement dimensionless, it was divided by $\boldsymbol{F}^{FE}_{max}$ squared. Similarly, the mean squared difference in nodal distance was calculated as

$$\overline{e}_{nodal} = \frac{1}{N}\left(\frac{100}{2R}\right)^2 \sum_{i=1}^{N} \|v^{FE}_i - v^{FM}_i\|^2, \tag{6.3}$$

where v_i is the position of the node i in the final stent obtained with FM (v^{FM}_i) and FEA (v^{FE}_i) method, respectively; R indicates the radius of the vessel wall, i.e., the error was estimated with respect to the vessel wall diameter. Thereafter, the two error measures were combined into a single cost function in the following way:

$$f_{cost} = \overline{e}_{nodal} + \overline{e}_F \tag{6.4}$$

to be able to optimise both metrics simultaneously. Note that both the nodal position values v^{FM}_i and the force measurements $\boldsymbol{F}^{FM}_i$ are dependent on the chosen parameter values *wStr, wBG*.

Therefore, the formal definition of the stiffness optimisation problem can be written in the following way (as defined in Equation 4.50):

$$\begin{aligned} \underset{wStr,wBG}{\text{minimize}} \qquad & f_{cost} = \frac{1}{N}\left(\frac{100}{2R}\right)^2 \sum_{i=1}^{N} \| v_i^{FE} - v_i^{FM}(wStr, wBG)\|^2 + \\ & + \frac{1}{N}\left(\frac{1}{\boldsymbol{F}_{max}^{FE}}\right)^2 \sum_{i=1}^{N} (\|\boldsymbol{F}_i^{FE}\| - \|\boldsymbol{F}_i^{FM}(wStr, wBG)\|)^2 \\ \text{subject to} \quad & wStr, wBG \geq 0. \end{aligned} \tag{6.5}$$

Selection: At each generation, all individuals were sorted according to their performance with respect to the cost function. Two best performing individuals were kept for the next generation without alterations. The rest of the population was subject to generic operators of mutation and crossover.

Mutations: At each generation, the 3 best performing individuals underwent random mutations when creating new offsprings. The mutation operator was adding a random variable from the interval $[-1.5...1.5]$ to each of the two genes. However, since stiffness could not be negative, the value was corrected if the result of the addition turned out to be negative, and the positive counterpart was taken instead.

Crossover: At each generation, the 2 fittest individuals were selected and crossed to create two offsprings by swapping the defining genes. To ensure the diversity in the population, at the end of the population forming, an additional check was performed to ensure that all individuals are different. This allowed to explore the space of possible solutions in a better way and speed up convergence.

The optimisation was performed once on the case of the bent vessel (diameter = 34 cm) to capture the bending behaviour, and the resulting stiffness values were subsequently used in all post-calibration comparisons.

6.3.1 Calibration results

Multiple runs of the GA were performed resulting in similar outcomes. On average, the convergence was achieved after 50 generations. The results of one typical run are reported here in detail. The very first, randomly assigned, population and the final population are captured in Table 6.2, together with the corresponding values of the cost function. The superscript ^{1} indicates the values in the first and the superscript * in the final population, respectively. As can be seen, the cost func-

tion fell from the initial best value of 275.6908 to 49.4124 during the simulation. All individuals that were sampled during the evolution process can be seen in Figure 6.16, which displays them as red crosses on the cost space (a) and as red circles on the nodal (b) and force (c) differences spaces. The evolution of the fittest individuals from each generation are plotted as a black line. The convergence towards the most optimal exemplar can be noticed by means of the increase in the concentration of red crosses and circles in the lowest interval of both parameters. In the course of the evolution, the fittest candidate emerged, defined by the pair [0.0688, 0.0874] with $\overline{f}_{cost}$ = 49.4124. Note that $wStr$ was defined as an additional stiffness weighting that would be added to the background stiffness weight (see Equation 6.1). Thus, the overall struts stiffness weight was the sum of the two values 0.0688 + 0.0874 = 0.1562, whereas the weight for the background stiffness remained 0.0874.

The optimal individual that emerged in the course of the GA was very sensitive to the definition of the presented cost function, in particular, to the weightings that indicate importance of the two error measures. The value of weightings employed in the presented cost function was found experimentally and seemed to result in both good simulation outcomes and stable convergence behaviour of the genetic algorithm.

Population	**wStr**[1]	**wBg**[1]	**cost**[1]	**wStr**[*]	**wBg**[*]	**cost**[*]
Individual 1	1.8147	0.5469	440.8714	0.7486	0.1202	98.3294
Individual 2	1.9058	0.9575	798.7505	0.0688	0.0874	49.4124
Individual 3	1.1270	0.9649	562.3603	0.0939	0.0137	74.6180
Individual 4	1.2785	0.4854	275.6908	0.9237	0.6537	295.5534
Individual 5	1.9134	0.1576	339.3775	0.1924	0.0399	63.0566
Individual 6	1.6324	0.9706	717.6938	0.4658	0.4898	146.7715
Individual 7	1.0975	0.9572	547.1314	0.2554	0.0205	110.6088

Table 6.2: Population evolution (values are rounded). The superscript [1] indicates the values in the first and the superscript [*] in the final population, respectively.

6.3.2 Post-calibration comparison

Figure 6.17 shows the results of the simulations with the new stiffness values obtained with the GA in the previous section, with the struts stiffness weight set to 0.1562 and the weight for the background stiffness set to 0.0874. Compared to the

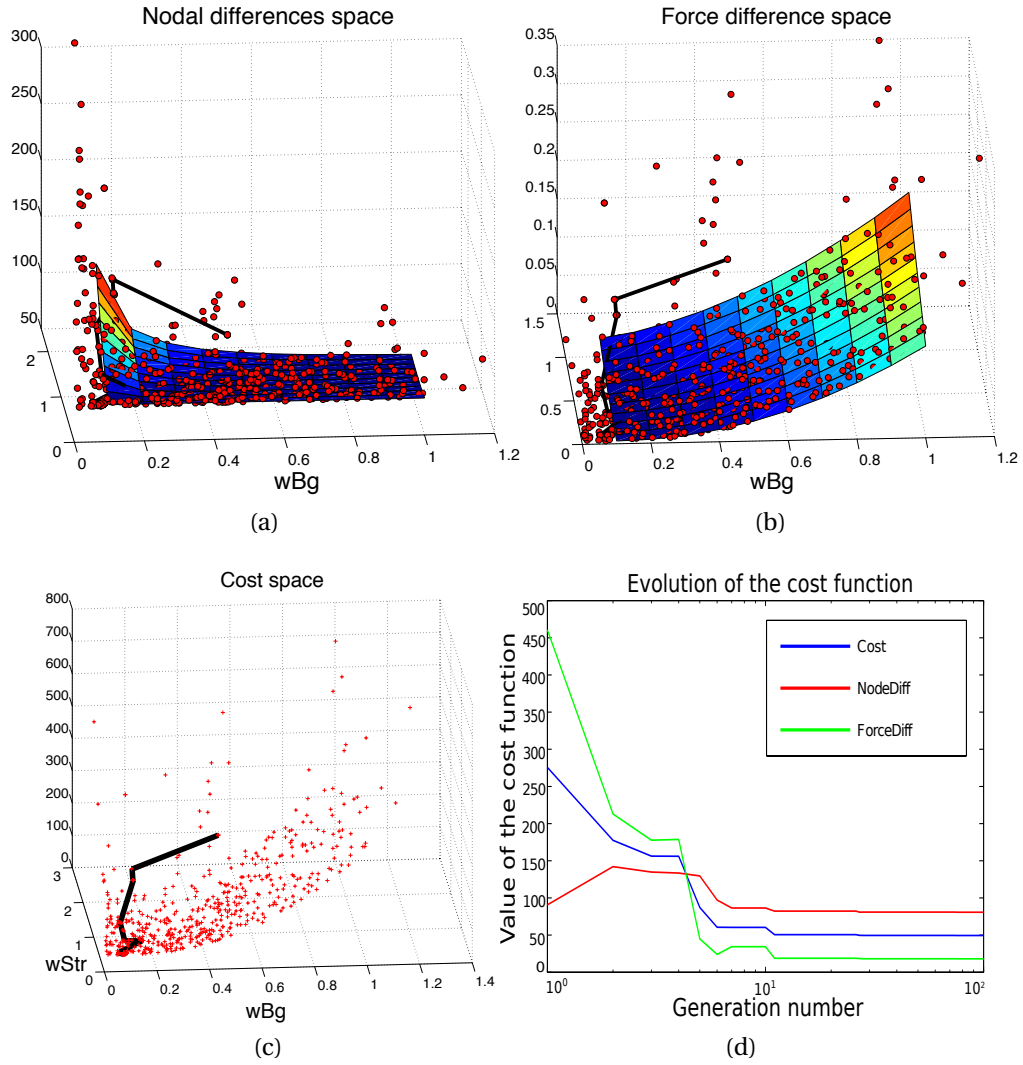

Figure 6.16: Example run of the GA visualised in the space of weighting parameters for (a) nodal difference function, (b) force difference function, and (c) the overall cost function. Red crosses and circles represent all individuals that happened to be instantiated during the 100 generations. The black line shows the evolution of the best fitted individuals from each generation, converging on the one defined by the pair [0.0688, 0.0874]. (d) Evolution of the cost function throughout 100 generations (abscissa is scaled logarithmically). Red, green and blue lines represent the evolution of nodal error, force error and the overall cost function, respectively.

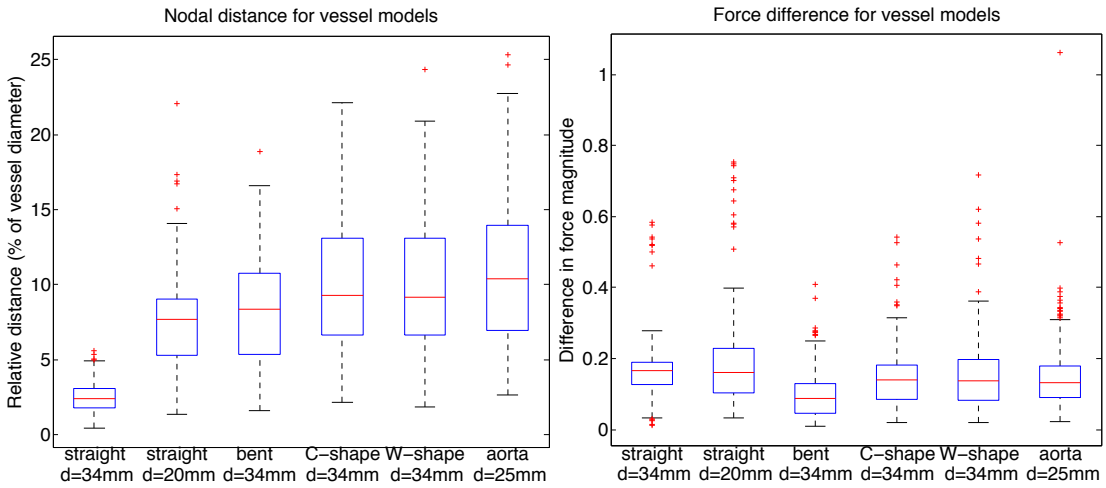

(a) (b)

Figure 6.17: Difference between the two methods FM and FEA for all vessel models, after stiffness learning. (a) Resulting nodal distance with the median value represented as a red line and the blue box outlining the 25th and 75th percentiles. (b) Resulting difference in force magnitude. This figure shall be compared to Figure 6.13 showing the same quantities before GA optimisation.

pre-calibration result (Figure 6.13), there was a considerable improvement in the force measurement: from the average difference in magnitude of 1 N to 0.18 N. However, the nodal distance exhibits only small change, with inconsistent tendency: in some cases there was a slight improvement, whereas others exhibited minor increase of the resulting discrepancy.

These results indicated that mere stiffness scaling was not sufficient to improve the FM nodal positioning and further increase in nodal accuracy should be approached by improving the contact model and possibly implementing a more sophisticated stiffness mechanisms, for example, 3-D stiffness or different settings for horizontal versus vertical components for the background mesh, which would require further investigations.

6.4 Concluding Remarks

This chapter preformed a validation study for the developed fast virtual stent deployment method. In particular, the chapter presented a comparative analysis of the new stenting method with respect to the widely-used finite element analysis.

For that reason, the set of six *in silico* experiments were conducted and evaluated, resulting in objective assessment of the novel FM. Further, using FEA results as a learning base, FM was optimised by calibrating stiffness parameters with the help of a genetic algorithm. The obtained stiffness setting substantially improved the force measures reported by the FM and reduced the force discrepancy between the two methods. Overall, the results of all performed experiments indicated a good agreement between the FM and FEA methods. More precisely, the mean difference in the nodal positions ranged between 4% and 10.5% depending on the complexity of the case, being the highest for the patient-specific case of aortic dissection with a very irregular geometry. Another quantitative measure of the validity of the FM was the mean force discrepancy, which after the calibration phase, lay below 0.2 N.

Another crucial point of comparison was the required computational speed of the two methods. Compared to FEA, FM was associated with a dramatic reduction in computational time, generally being in the order of seconds, while FEA times lay in the order of hours. As already mentioned in the previous chapter, such fast execution times constituted a very important result for the potential usability of FM in clinical practice.

The obtained results were quite promising, especially bearing in mind the numerous limitations of FM as it was implemented for now. With respect to limitations, the first to mention is the simplistic contact model, which gave raise to higher errors for the narrow vessels and when facing sharp corners of the analysed aorta. Improving the contact model would reduce the nodal difference; however, at the cost of more expensive computations and therefore longer execution time. Another limitation lay in the assumption of the rigid vessel wall. Although FM already features the capability to model the flexible vasculature, here the focus was on the process of stent expansion, in order to eliminate possible interdependencies. Hence, the modeling of the vessel deformation was postponed until the next chapter.

The next chapter is dedicated to the next and final step in modelling the virtual stent deployment, namely, investigation of the vessel haemodynamics after the stenting procedure.

CHAPTER 7

HAEMODYNAMICS AFTER STENTING: IMPLICATIONS OF TREATMENT OPTIONS

This chapter shows the next step in modelling of vascular interventions, namely, investigation of the haemodynamic conditions in the vessel after stent deployment. Using a real clinical case of an aortic dissection treated with endovascular repair, the chapter recreates the course of the treatment virtually. In addition to the real scenario, 3 variations of the performed intervention were conducted, in order to investigate the implications of different treatment options on the subsequent haemodynamic conditions of the vessel. In total, 6 computational experiments were performed for a given patient's case to compare the haemodynamic changes after treatments with the pre-procedural conditions.
This chapter has been submitted in an alternative form in Spranger et al. (2014b).

This chapter shows the next step in the modelling of vascular interventions, namely, investigation of the haemodynamic conditions of the vessel after stent deployment and comparing them with pre-procedural conditions. The chapter uses a clinical case of a patient that underwent a Thoracic Endovascular Aortic Repair (TEVAR) at the Department of Diagnostic and Interventional Radiology, University Hospital Heidelberg, Germany (Hoegen and von Tengg-Kobligk, June 2013, personal communication). The goal of TEVAR was to close the primary entry of the dissection to prevent blood from flowing into the false lumen. However, the initially performed TEVAR was unsuccessful, and the patient had to undergo 2 further interventions.

The effectiveness of endovascular repair is highly dependent on the configuration of the released stent graft (Böckler et al., 2006). In cases of unsuccessful repair, important complications such as device migration, formation of endoleaks and

fracture of the device can arise, that may result in secondary interventions or, in the worst-case scenario, morbidity and mortality of the patient. One reason a therapy can be unsuccessful is that not all dissection entries are covered by the stent graft, for example, when device is too short, and substantial flow into the false lumen is maintained. In general, however, shorter devices are preferred over the long ones in order to prevent spinal chord ischemia, which occurs when small arteries originating from the thoracic aorta (that supply the spinal chord with blood) are covered by the graft. Other reasons of unsuccessful repair may be the device's inability to withstand the haemodynamic loads of blood flow and to keep its originally intended post-operative position over time (Prasad et al., 2013).

Motivated by the long-term goal of improving vascular interventions, the aim of this chapter is to investigate the implications of different parameters of TEVAR on the subsequent haemodynamic conditions of the treated vessel. The parameters of interest were those that could be varied by a clinician in the course of the treatment, in order to optimise the planned intervention for a particular patient. These included the design, dimensions and stiffness of the stent graft as well as its placement position. Therefore, this study involves 4 computational experiments aiming to simulate different TEVAR scenarios for a given patient's aorta and to compare the haemodynamic changes they cause with the pre-procedural conditions. In particular, the difference in positioning of the stent graft was explored by virtually deploying the same device at different locations along the aorta. Further, the difference in device design and dimensions was investigated by deploying two different devices at the same location inside the vessel. Finally, the analysis looked into the implications of the device stiffness and vessel flexibility by setting the stiffness of the device to high values and allowing the vessel tissue to deform during the procedure. Each of the 4 TEVAR experiments included the virtual stent grafting with the newly developed FM and the subsequent CFD analysis, in order to show the implications of different TEVAR scenarios on the post-procedural haemodynamic conditions of the treated vessel. Given the results, the choice of which device and positioning is best for a particular patient should of course be left to the interventional radiologist. The contribution of the present study is to demonstrate the entire workflow, that enables the virtual investigation of different treatment options and thus provides additional information to the clinician treating the disease. The experiments served as a proof of concept at this stage.

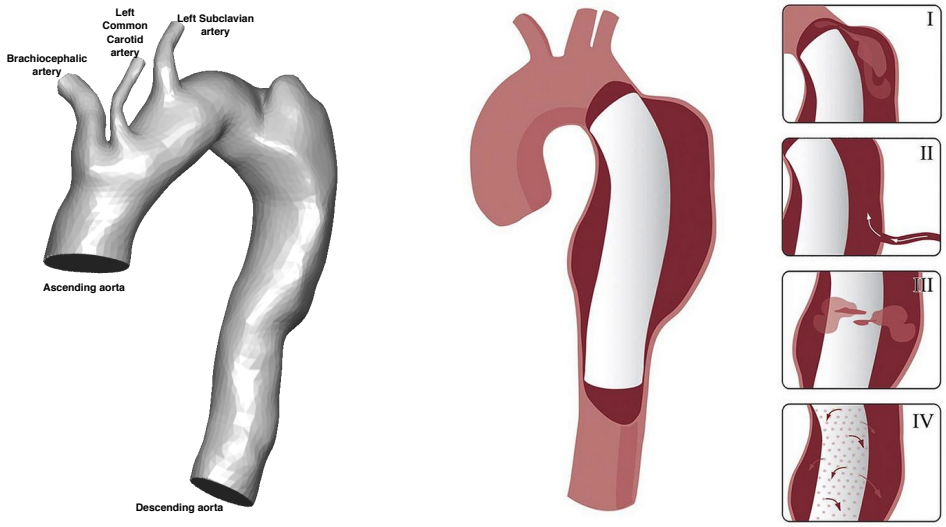

(a) (b)

Figure 7.1: (a) Analysed dissected aorta with three outgoing supra-aortic vessels: brachiocephalic artery, left common carotid artery and left subclavian artery. (b) Four types of possible endoleaks that can jeopardise the TEVAR procedure: Type I endoleak is caused by failure to achieve a circumferential seal at the ends of the device; Type II endoleak occurs because of the retrograde filling of the aneurysm from arteries; Type III endoleaks are due to a structural failure of the device; Type IV leaks result from the porosity of the graft fabric (Golzarian and Valenti 2006; image from `www.modernmedicaldictionary.com`)

The structure of the chapter is as follows. First the setup of computational experiments is described, namely, details on data acquisition, virtual stent grafting and the CFD analysis. Thereafter, the results of the FM stent deployment and 6 different CFD experiments are reported: 2 pre-TEVAR and 4-post TEVAR cases. The chapter finishes by discussing the limitations of the study.

7.1 Computational Setup

7.1.1 Clinical case

A female patient with a chronic expanding type B[1] aortic dissection was treated with a thoracic stent graft (Gore TAG 34/200) in 2006 at the age of 58. Prior to this, the dissection had persisted for three years and was treated pharmaceutically to control blood pressure. However, due to the enlargement of the dissection from 4.5 cm at

[1] Type B dissection involves the descending aorta or the arch (distal to the left subclavian artery).

primary diagnosis to 7.0 cm, the decision was made to treat the dissection by TEVAR in order to prevent rupture. Apart from that, the patient was asymptomatic. The most recent pre-interventional CT scan was acquired four months prior to TEVAR. In the pre-interventional CT scan, the dissection featured small length and dilated morphology, with the dissection membrane no longer visible, which made it look similar to an aneurysm, as can be seen in Figure 7.1 (a). During TEVAR, the left subclavian artery was overstented.

After the performed TEVAR, 2 complications were detected: minor remaining perfusion of the left subclavian artery and a type II endoleak from intercostal arteries (see Figure 7.1, b). Additionally, the patient showed symptoms (pain in the arm) arising from the reduced perfusion to the left subclavian artery due to the overstenting, but recovered after several days. However, six weeks after the primary intervention, a bypass from the left common carotid to the left subclavian artery was installed because the patient suffered from subclavian steal syndrome (whereby the arm is supplied by blood flowing in a retrograde direction). Six months after primary TEVAR, a second stent graft was implanted to extend the stent graft length distally. The latest follow-up examination in 2012 showed complete thoracic remodelling after false lumen thrombosis and did not reveal any aortic complications.

Vessel. The data of the dissection anatomy was acquired from the CT scans of the patient. Prior to the examination, a formal consent was granted by the patient. The 3-D representation of the aortic geometry was obtained by segmentation (see Section 4.3.1). Figure 7.1 (a) shows the resulting dissection anatomy with the three outgoing supra-aortic vessels. The dimensions of the aortic diameter at the proximal location were about 31.5 mm immediately downstream of the left subclavian artery and 30.0 mm upstream of it (the proximal landing zone of TEVAR). At the distal end, the descending aorta was about 27.0 mm in diameter (distal landing zone of TEVAR).

Some of the experiments performed in this chapter treated the vessel tissue as flexible. In those cases, the flexible contact model was employed, the details of which were described in Section 4.3.4. To instantiate Equation (4.40) that defined the stiffness of vessel springs, assumptions about the elastic properties and the thickness of the aortic wall had to be made, since these were not available from the clinical data. In previous studies, the Young's modulus of thoracic ascending aorta was reported to lie in the range of 2 – 6.5 MPa, decreasing in mid-abdominal aorta to 0.6 – 2 MPa (Mosora et al., 1993). With respect to the thickness of the aortic wall, Li

et al. (2004) found the mean thickness values to measure 2.32 mm for men and 2.11 mm for women, with values increasing with age. Hence, the aortic stiffness was set to 4 MPa and the wall thickness to 2.18 mm, considering gender and age of the analysed patient (female, 58 years old). This setting led to the average stiffness value of vessel springs of around 7,552 and the nodal stiffness of 43,860 in the created vessel model, for an average spring length of 2 mm.

Stent graft. The stent graft geometries were obtained with a high-resolution micro CT of unpacked, non-sterile stent graft samples. Segmentations and meshes of the implants were generated using medical post-processing software (Mimics, Materialise, Leuven, Belgium). Geometric parameters were measured both in these meshes and in the real stent graft samples to obtain exact values and create realistic SG models for virtual stent grafting. These models were created using commercial (CATIA, Dassault Systemes, France) and opensource (Blender, Stichting Blender Foundation, Amsterdam, Netherlands) computer aided design software (see Section 4.1.1 for more details). Figure 7.2 depicts an image of an example stent graft (a) and the resulting reconstructed Gore TAG 34/200 device (b), as well as the same SG model with the background mesh visible (c) and its zoomed element (d).

To set the stiffness of the stent springs in a way analogous to the vessel setting and ensure consistency of the two models, the Young's modulus of the entire stent had to be found, which was not straightforward due to the complex design and distribution of nitinol wires. However, Zahora and Hanus (2003) provided an approximative equation for the Young's modulus of the entire stent. They modelled a stent as chain of rings consisting of several semicircles and derived the stent stiffness formula based on geometrical parameters of strut wires and elasticity of the material. Assuming d is the diameter of the strut wire (m), r is radius of a semicircle, n is number of semicircles and E is the Young's modulus of elasticity of material (Pa), the Young's modulus of the stent E' could be calculated as:

$$E' = \frac{3Ed^4}{8\pi^2 nr^4} \tag{7.1}$$

In the stent model, the diameter of a strut wire was $d = 0.4$ mm, number of triangular elements in one layer $n = 16$ and the radius of the stent triangular element $r = 1$ mm (34mm/16/2). Assuming the elastic modulus of nitinol at body temperature to be $E = 83$ GPa, the Young's modulus of the entire stent could be estimated to 5 MPa. This estimated elastic modulus was fed into Equation (4.40) to calculate the

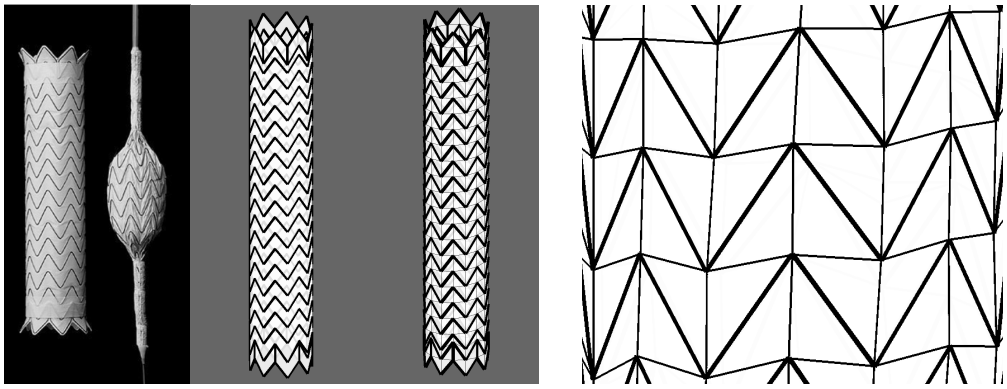

(a) (b) (c) (d)

Figure 7.2: Stent graft model. (a) Image of a Gore TAG Thoracic Endoprosthesis (image from `www.goremedical.com`). (b) Reconstruction of the stent graft. (c) Reconstructed SG model together with the background mesh. (d) Zoomed in element of the mesh with thick lines showing the struts and thin lines the background mesh.

stent springs stiffness which led to the average springs stiffness of 1,748 and nodal stiffness of 10,175, for an average stent springs length of 11 mm. Note the difference in stiffness values between the stent and vessels springs, which is inversely related to the spring length. This inverse relationship was in line with our earlier settings used in the previous chapters and the wider literature on springs modelling (Batina, 1990).

Deployment experiments. 4 different stent deployment scenarios were simulated:

1. TAG2 (34 mm × 200 mm) was deployed in the rigid vessel (rigid contact; Section 4.3.3), at the position reported in the medical records: the clinical intervention resulted in the overstenting of the left subclavian artery

2. TAG2 (34 mm × 200 mm) was deployed in the rigid vessel (rigid contact; Section 4.3.3) at a different position: further downstream and without the overstenting of the left subclavian artery

3. TAG (34 mm × 120 mm) was deployed in the rigid vessel (rigid contact; Section 4.3.3): this was a shorter device, which was different in design and dimensions and no overstenting occurred

4. TAG2 (34 mm × 200 mm) was deployed in the non-rigid vessel (flexible contact; Section 4.3.4) at the same position as in case 1

Comparison of cases 1 and 2 was performed to study consequences of different device positioning, since both utilised the same device deployed at two different locations along the vessel. Differences between the outcomes in cases 2 and 3 gave information about implications of device design and dimensions, by deploying two different devices at the same location site. Finally, cases 1 and 4 provided information about the implications of the stent graft stiffness and vessel flexibility, by setting the stiffness of the device to a substantial value and allowing the vessel tissue to deform during the procedure.

7.1.2 CFD model

All haemodynamic simulations were time-dependent and aimed at modelling transient flow under the assumption of rigid vessel wall with no-slip boundary conditions. The theory behind the CFD analysis was outlined in Section 4.7. It is worth remembering that the last deployment experiment simulated a flexible wall deformation; however, the subsequent CFD was run with a rigid wall assumption on the deformed vessel geometry. In the recent studies, the assumption of a rigid arterial wall was shown to have little effect on the flow patterns seen when compared to simulations with elastic compliant walls (Dempere-Marco et al., 2006). Therefore, the CFD with the rigid-wall setting was chosen for reasons of computational efficiency, which is of a paramount importance in a clinical setting where guidance is sought regarding haemodynamic features without the option of prolonged computation times.

Pre-TEVAR cases. 2 simulations of the pre-TEVAR case were performed in order to establish the baseline model for comparison with post-TEVAR cases. The objective of setting up two instead of just one pre-TEVAR simulation was to find a particular configuration of the boundary conditions (BCs) that was initially unavailable in the given clinical data. Thus, the first simulation was run with the given data, the so-called “forward” simulation. Its outcome was subsequently used to set up a second simulation with better-suited BC configuration – the so-called “reverse simulation”. In the sequel, the latter reverse simulation served as a baseline for comparisons with the post-TEVAR cases. More details on the reasons for the two different setups and their implementation are given in the later section describing the BC settings.

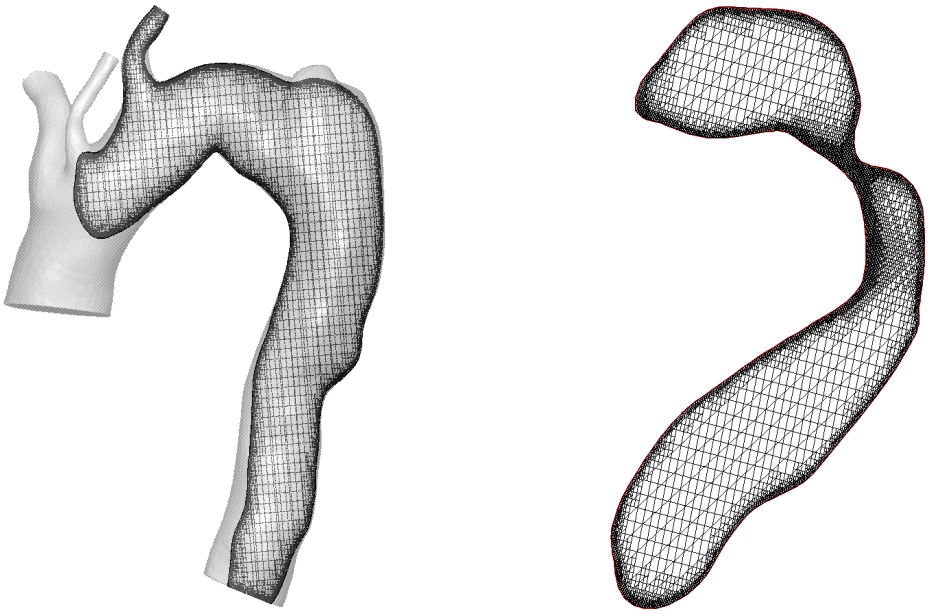

(a) (b)

Figure 7.3: (a) Resolution of the CFD grid for a plane cut inside the aortic geometry. (b) Illustration of the more fine-grid boundary layers at the vessel walls.

Volume Mesh Generation. The STL file containing the segmented and trimmed geometry was imported in CFD-VisCART (ESI Group, France) to generate a cartesian-based grid with omnitree structure (see Section 4.6 for details). The volumetric mesh contained around 2 million cell elements, of course depending on the experiment, with 3 near-wall Cartesian layers of fine resolution mesh and gradual coarsening towards the centre of the geometry, which gave a smooth and well-resolved boundary definition (see Figure 7.3). Thereafter, the generated mesh file was imported into the flow solver CFD-ACE+ (ESI Group, France) for computation.

To ensure the insensitivity of the results to resolution, grid independence analysis was conducted. A finer grid of around 8 million cells was employed in addition to the base grid of around 2 million cells. To compare the results of the two discretisations, the pressure and velocity magnitude distribution were measured in both solutions. The average and maximum difference in the velocity magnitude between the two grids measured 1.2% and 2% at the descending aortic outlet, respectively. With respect to pressure, the mean difference between values on boundaries measured 0.4% and max discrepancy lay under 2%. Therefore, for the purposes of the present study the base resolution of around 2 million cells was deemed adequate.

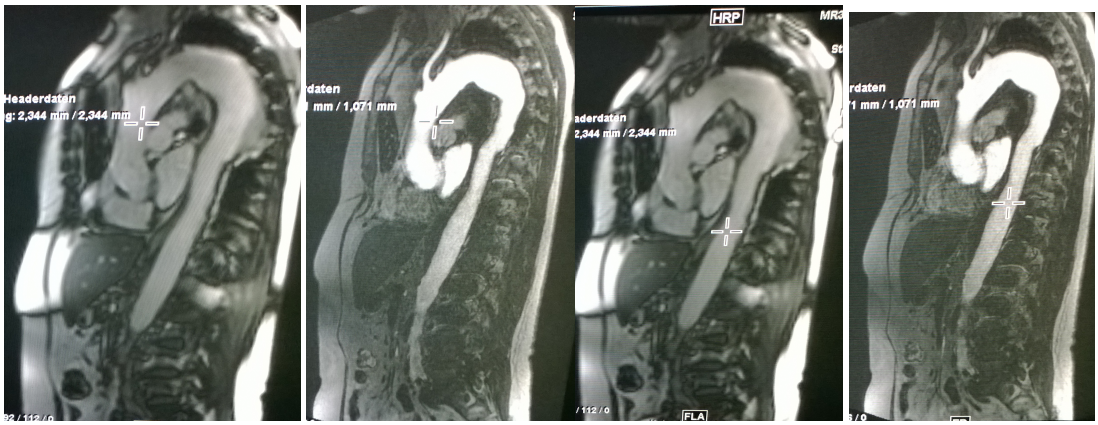

(a) (b)

Figure 7.4: Available patient-specific PC-MRI measurements taken at the ascending (a) and descending aorta (b) on the planes indicated by the crosses in the images.

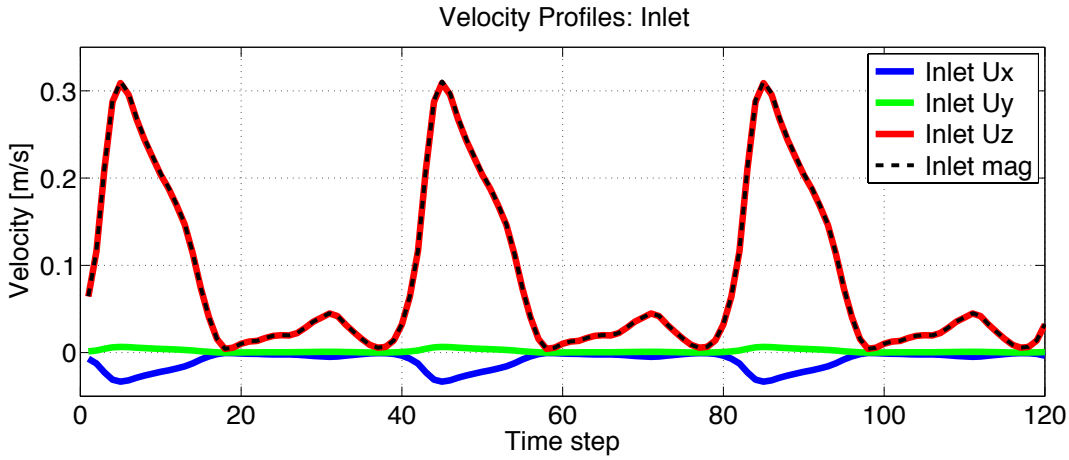

Figure 7.5: Patient-specific velocity profile at the ascending aorta used as a BC setting for the inlet.

Boundary conditions for the forward simulation. Patient-specific PC-MRI[2] measurements were available that could be used for setting the boundary conditions in the simulations. In particular, the patient's time-variant velocity profile at the ascending aorta was used as velocity-fixed BCs for the aortic inflow. The profile contained 40 averaged velocity values of the flow passing through a plane placed at the ascending aorta, as depicted in Figure 7.4 (a), during one cardiac cycle. It is worth mentioning that the aortic inlet and outlet were previously trimmed at the planes matching these planes of measurements and perpendicular to the centerline of the

[2]Phase Contrast Magnetic Resonance Imaging utilises phase differences to distinguish blood from static tissue.

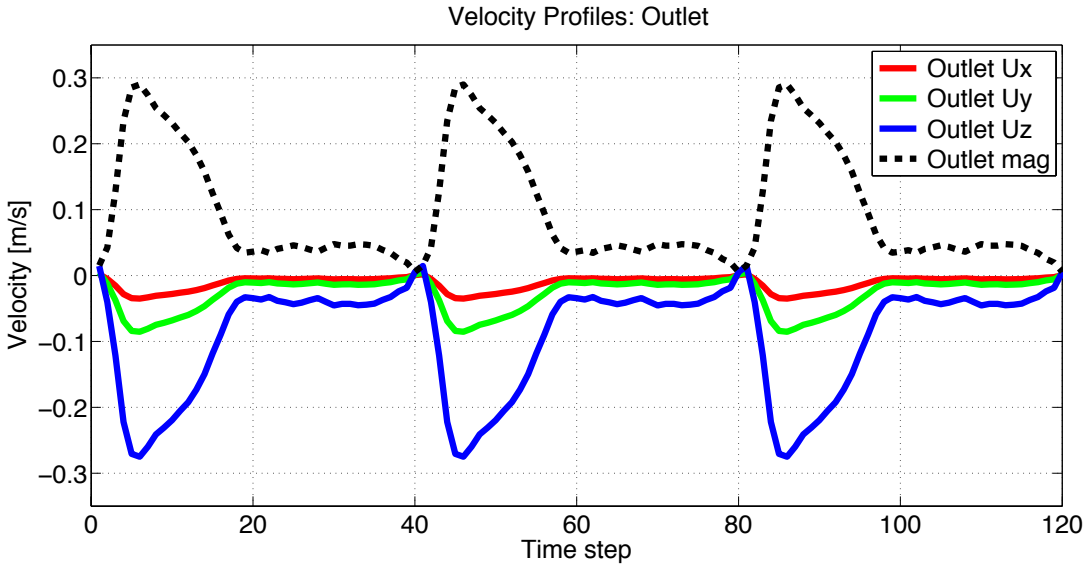

Figure 7.6: Velocity-fixed boundary conditions at the descending aortic outlet.

vessel, in order to be able to directly apply the recorded values as the BC. Since the heart beat rate of the patient was 69 beats per minute, each interval corresponded to 0.0217 s (60 sec / 69 beats / 40 points = 0.0217 sec). This velocity profile was cyclically repeated 3 times in order to obtain the BC settings for the aortic inlet during the 3 simulated cardiac cycles. The resulting waveform featured a systolic peak velocity of around 0.3 m/s, as shown in Figure 7.5.

Further, the phase data for the velocity profile was available at the descending aorta, recorded through the plane at the location in Figure 7.4 (b). However, neither the information about the magnitude of that velocity nor the data on the flow at the supra-aortic vessels was available. To compensate for this lack of information, values previously reported in the literature were used. In their paper, Gallo et al. (2012) reported that 13.4% of the aortic inflow is diverted into the brachiocephalic, 10.6% to the left common carotid and 12.0% to the left subclavian arteries. The percentages were computed as the ratio between the time-averaged flow rate measured at that outlet and the time-averaged flow rate measured at the inlet section. Hence, these ratios could be used to calculate the outflow at the descending aortic outlet. Assuming that 36% of the time-averaged inflow goes to the three supra-aortic vessels, the descending aortic phase profile was scaled in such a way that the outflow profile corresponded to the time-average of 64% of the inflow. From this calculated outflow, the velocity profile at the descending aorta was computed (see Figure 7.6).

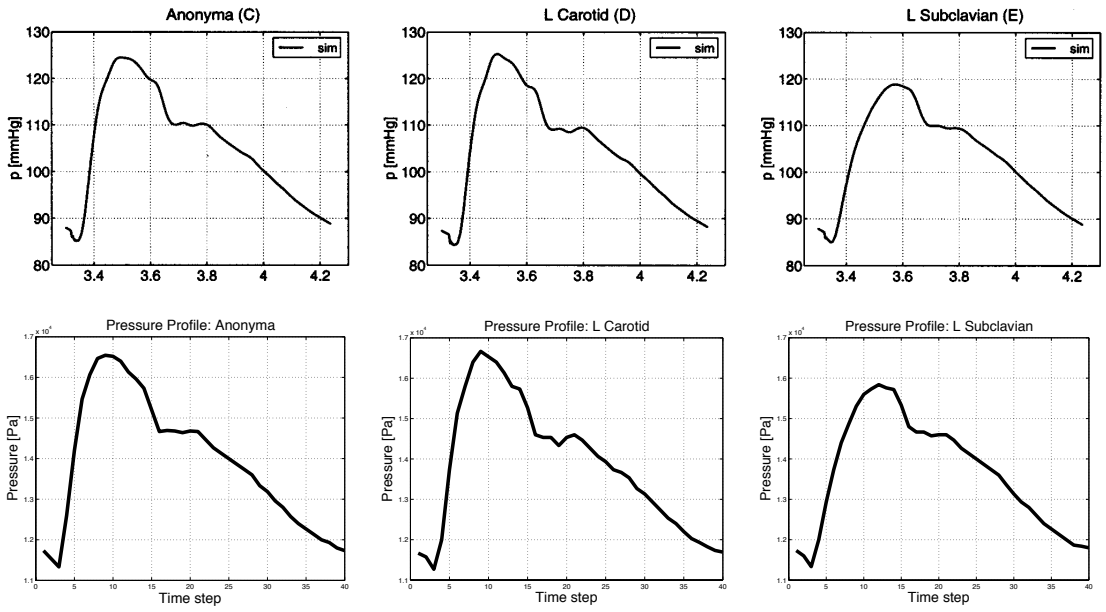

(a) (b) (c)

Figure 7.7: Upper row: pressure curves reported for 3 supra-aortic vessels (Olufsen et al., 2000). Bottom row: reconstructed pressure curves obtained by sampling of the reported above waveforms with 40 evenly distributed data points.

Because of the lack of data about the velocities of the supra-aortic vessels, it was decided to use pressure BC at these outlets in the forward simulation. This BC setting allowed to avoid the currently widely-used method of imposing the velocity profiles at the supra-aortic outlet sections as a scaled version of the inlet. The rationale behind the decision was that, firstly, the typical velocity profiles for the supra-aortic vessels look very different from the inlet velocity waveform. Secondly, it has been shown that this widely-used strategy leads to differences between measured and simulated flows at the descending outlet section of up to 49% (Gallo et al., 2012). Instead, the time-dependent pressure profiles were reconstructed for the three supra-aortic vessels from the study of Olufsen et al. (2000), by importing 40 regularly distributed data points from the reported profile curves. Figure 7.7 shows the reported curves from the study by Olufsen et al. (2000) and the reconstructed values for the 40 data points evenly distributed over one cardiac cycle (note the mmHg to Pa conversion).

In order to prescribe the obtained pressure profiles to the brachiocephalic (anonyma), left common carotid and left subclavian outlets, they had to temporally correspond to the velocity profiles of our patient. This was achieved by aligning the

systolic peaks of measurements for both patients' profiles: the systolic peak of our patient fell on the 5th time point (see Figure 7.5), whereas the systolic peak of the patient from the Olufsen et al. (2000) study corresponded to the 7th time point of the reconstructed inflow profile (see Figure 7.8, a). Therefore, the reconstructed pressure profiles were shifted by 2 time steps, i.e., the first two measured data points of Olufsen et al. (2000) were added to the end of the cycle (due to its circularity), resulting in the final pressure profiles depicted in Figure 7.8 (b).

The overall BC settings for the forward simulation are summarised in Figure 7.9 (a). This architecture of the simulation should result in physiologically realistic haemodynamic conditions, although not entirely patient-specific, but sufficient for the purposes of the present study, comparing pre- and post-TEVAR haemodynamics.

BCs for the reverse simulation. Since the study aimed at comparing the pre- and post-TEVAR cases, how the flow within the region develops and how it changes on the descending aorta, the BC setting should not be prescribing the same velocity profiles on the descending outlet as in the pre-TEVAR case. Especially in cases where the left subclavian artery was overstented, the flow on the outlet could not be assumed to remain unaltered. Moreover, in their study Gallo et al. (2012) found that in order to obtain realistic flow diversion patterns, measured flow rates need to be

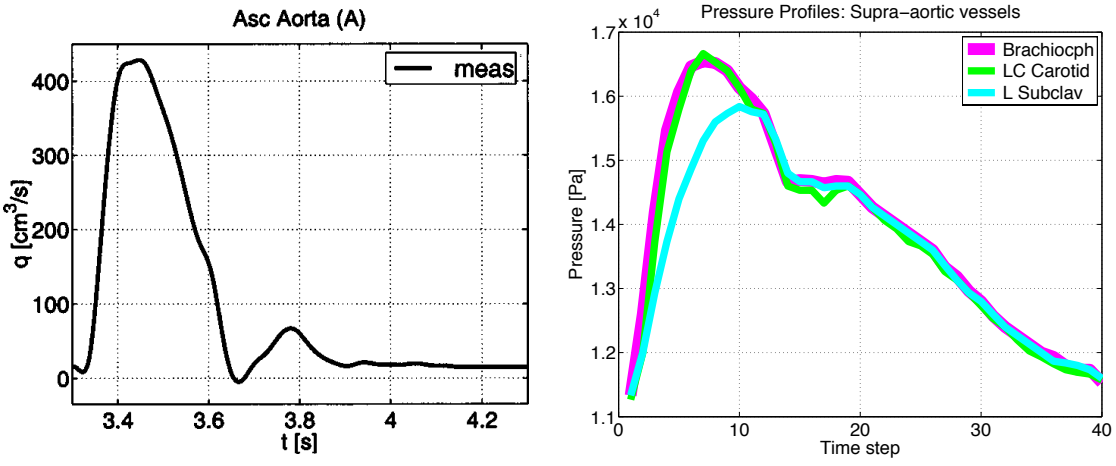

(a) (b)

Figure 7.8: (a) Inflow profile at the ascending aorta measured by Olufsen et al. (2000). (b) Final reconstructed pressure profiles for the three supra-aortic vessels used as pressure-fixed BC for the three corresponding outlets.

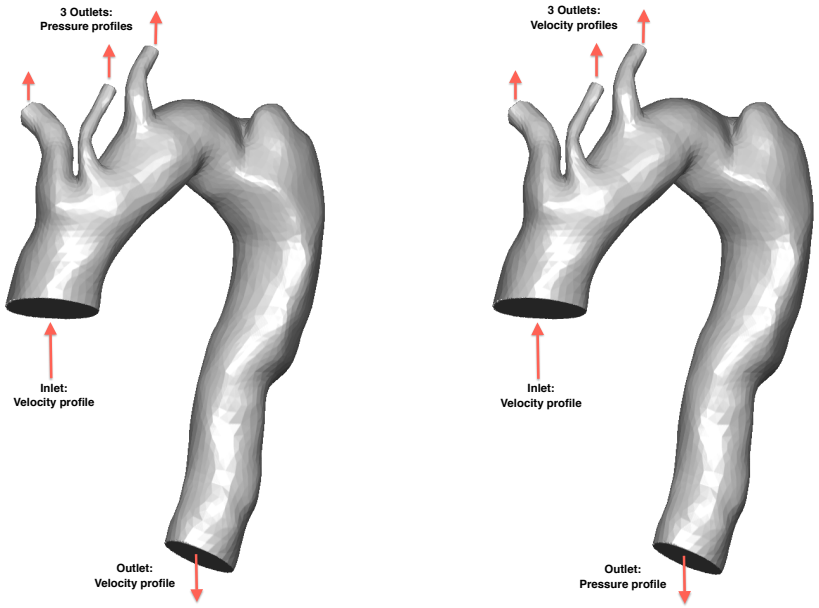

(a) (b)

Figure 7.9: Boundary conditions applied to the geometry in the forward (a) and reverse simulation (b) as well as in the post-TEVAR cases (b).

imposed as BCs at three of the four outlets of the CFD model. For this reason, a setup was sought which fulfilled the condition of prescribing the 3 of the 4 outlets and allowed to perform direct comparisons between the pre- and post-interventional cases. Since it was known from the clinical experiments (private communication with research clinicians) that the flow at the supra-aortic vessels undergoes insignificant changes after the TEVAR procedure, even in cases of overstenting (in the non-overstented arteries), a setup with velocity-fixed BCs on the supra-aortic outlets was chosen. For this purpose, the data for the supra-aortic velocity profiles was determined from the results of the forward simulation. Therefore, the new setup for the reverse simulation entailed the same velocity-fixed BCs on the ascending aortic inlet as in the forward simulation, velocity-fixed BCs on the 3 supra-aortic vessels and the pressure-fixed BC for the descending aortic outlet. The profiles for all outlets were determined from the results of the forward simulation. The necessary averaging had to be performed in order to obtain 40 data points of one cardiac cycle that had to be set as the BC profiles. Figure 7.9 (b) summarises the BC setup for the reverse simulation. The same setup was used for all post-TEVAR cases to enable a valid direct comparison.

Numerical Settings. A finite volume solver (CFD-ACE+, ESI CFD) was employed for the numerical solution of the Naviér-Stokes equations (see Section 4.7 for more details). Although in general blood is non-Newtonian, it has been shown that the non-Newtonian effects can be assumed secondary in arteries with a diameter greater than 0.5 mm (Perktold et al., 1991). Hence, since our study investigated the flow within large arteries, blood was treated as Newtonian and incompressible (Fung, 1997), with a density of $1044\frac{kg}{m^3}$ and a dynamic viscosity of 0.00365 $Pa \cdot s$.

The Reynolds Number (Re) is a measure of the ratio of inertial forces to viscous forces and can be determined as

$$Re = \frac{\rho v L}{\mu}, \tag{7.2}$$

where ρ is density of the fluid, v is mean sectional velocity, L is the vessel diameter and μ is the dynamic viscosity. Considering the inlet diameter of approximately 0.0357 m and the systolic peak velocity of blood when it enters the ascending aorta of 0.3 m/s, Re could be calculated to lie around 3,106 at systole ($1044 \cdot 0.3 \cdot 0.0357/0.00365$), indicating that the blood flow within the aorta was at a transitional state, with possible turbulent patches and laminar regions.

Post-TEVAR cases. After performing virtual stent grafting with FM, both the deployed stent and the (potentially deformed) vessel were exported from Matlab as STL files and imported into CFD-VisCART. There, the inner lumen of the stented vessel (which contains the inner lumen of the stent graft in the stented part of the vessel) was meshed building a single domain. The BC settings for all post-procedural CFD simulations were the same as in the reverse simulation case, which are depicted in Figure 7.9 (b).

CFD analysis metrics. To investigate the haemodynamic conditions of the vessel in pre- and post-procedural cases, the following flow metrics were evaluated in each of the experiments:

- Mass flow rates at all boundaries to capture the flow distribution across all outlets
- Lines tangential to the instantaneous velocity vector (called velocity streamlines) passing through the inlet plane and an additional plane at the dissec-

tion site during one computational time interval (0.0217 s), coloured by the velocity magnitude, in order to check the flow organisation

- Velocity contours and velocity vectors measured on the plane at the dissection site, in order to check the flow characteristics within the dissection lumen
- Vorticity contours at the plane passing through the center of geometry, in order to assess the flow organisation
- Pressure distribution and energy loss on the surface of the aortic geometry
- Wall shear stress (WSS) on the surface of geometry
- Pressure on boundaries and pressure drop at the ascending aortic inlet as compared to the descending aortic outlet
- Velocity profile at the descending aortic outlet

The measured metrics allowed to preform the qualitative and quantitative comparison of the pre- and post-TEVAR haemodynamic conditions.

7.2 RESULTS

This section reports the results of the virtual stent grafting with FM, followed by the CFD experiments.

7.2.1 Virtual stent grafting

The first three deployment cases were performed under the assumption of rigid vessel wall. Firstly, devices were crimped to 20% of their initial diameter, which simulated their positioning in the catheter of 24 FR ($24 \times 0.333 = 8$ mm). Subsequently, the crimped prostheses were placed along the centerline of the vessel at the relevant position for the start of the expansion procedure. Thereafter, the deployment process was initiated starting from the proximal end of the graft, gradually progressing to the distal layers (see Section 4.1 for more details). Because of the rigidity of the vessel wall and stent oversizing, the devices remained underexpanded, which is a desired effect since it ensures stability via higher forces. Figure 7.10 (first three rows) depicts the final configurations of deployed devices from different view angles.

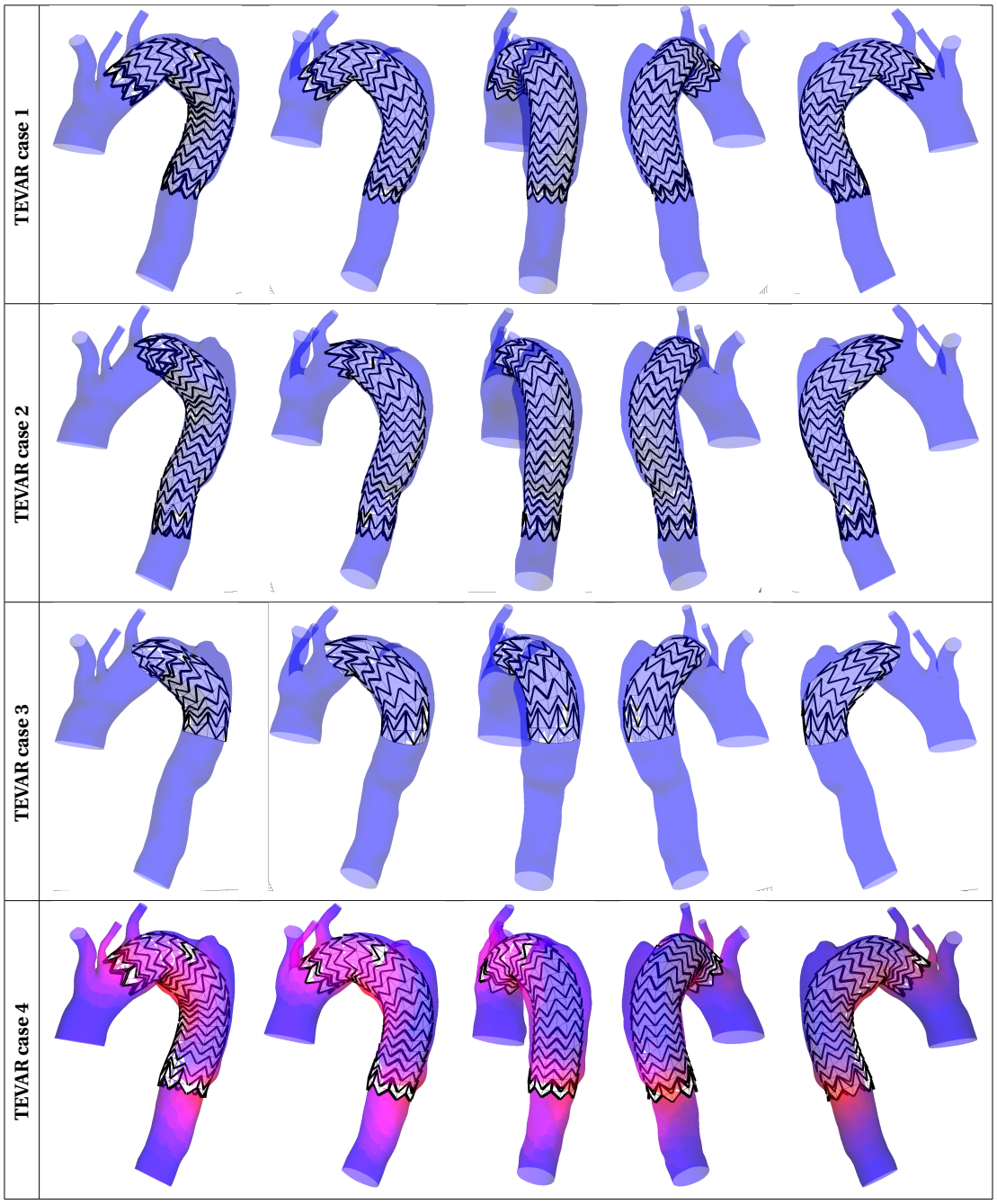

Figure 7.10: Virtual stent grafting with FM: final expanded configurations of devices and the vessel in 4 different TEVAR scenarios. In the last row (TEVAR case 4), the vessel geometry underwent substantial deformation, as shown on the surface in red.

The final deployment case modelled flexible vasculature. This time, the deployment process took longer than previously due to the more complex contact interactions. At the end of the deployment, the stent featured a more expanded configuration when compared to the previous cases. In particular, this case could be directly

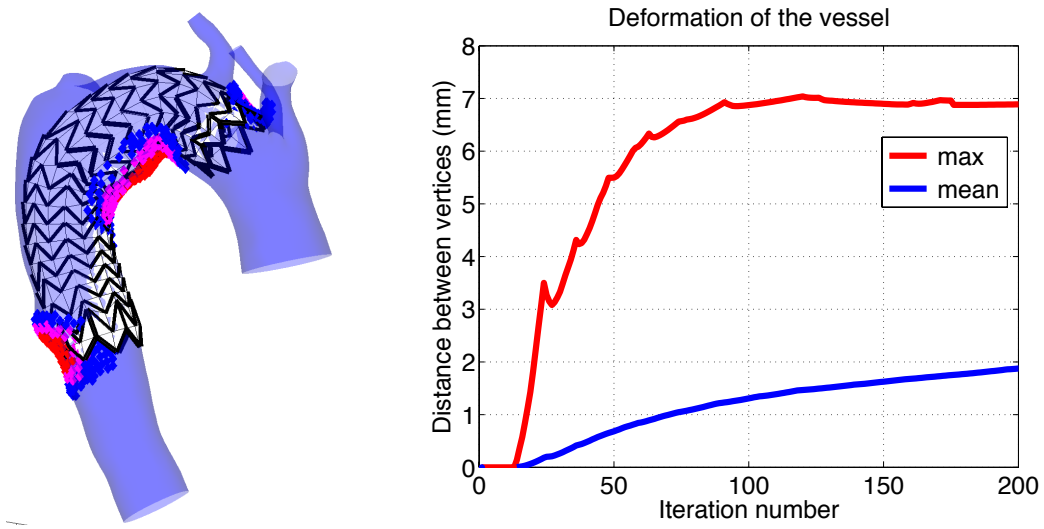

(a) (b)

Figure 7.11: Vessel deformation. (a) Vessel vertices with displacement of more than 6 mm are shown in red, vertices with displacement magnitude of more than 5 mm (< 6 mm) are shown in magenta and of more than 4 mm (< 5 mm) in deep blue. (b) Graph showing the maximum and mean displacement of vessel vertices during the stent expansion process.

compared with the first TEVAR case, which simulated exactly the same deployment conditions in terms of the device and its placement position; the two cases differed only in the vessel flexibility assumption. Figure 7.10 (last row) depicts the final configuration of the vessel and the graft. As can be seen, the vessel geometry underwent substantial deformation, shown on the surface in red colour. Maximum nodal displacement measured 7 mm and the mean displacement (among the displaced nodes) was 2 mm. This can be seen in Figure 7.11 (b) which displays the evolution of the vessel deformation during the expansion process. Figure 7.11 (a) shows the areas of major nodal displacement in the vessel. It can be observed that major vessel deformation concentrated at the inner curvature of the vessel and in areas of the device extremities.

7.2.2 Haemodynamic analysis

For each of the six analysed cases (2 pre-TEVAR and 4 post-TEVAR cases), a transient simulation was carried out for 3 full cardiac cycles, with a time step of 0.0217 seconds and 40 time steps per cycle, totaling 2.6 seconds. Time-step sensitivity studies at 0.01 and 0.005 seconds have produced similar results and hence a time step of

0.0217 seconds was deemed appropriate. The flow distribution was measured only in the third cycle, in order to remove as many initialisation effects of the pulsatile flow profile as possible. Hence, the results presented below are based on information output from the final third cardiac cycle. All simulations converged to a stable solution with a solution time for each time step of around 40 minutes when run on 8 Cores (3.40 GHz), depending on the mesh size. Each time step of the simulations typically converged to five orders of magnitude residual reduction in approximately 70 iterations.

Pre-TEVAR case: Forward simulation. The goal of the forward simulation was to obtain the missing velocity profiles for the three supra-aortic vessels as well as the pressure BC for the descending aorta.

Mass flow. In order to ensure the consistency of the results, the equality of the mass flow rates was checked on boundaries. The mass flow rate measures the mass of a substance passing through a given surface per unit of time and was computed as

$$\dot{m} = \rho \dot{V} = \rho v A, \tag{7.3}$$

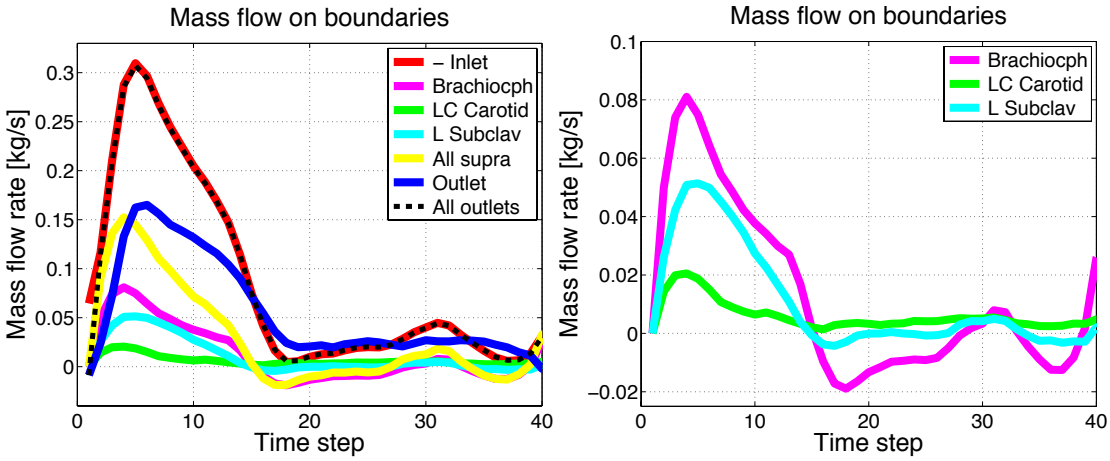

Figure 7.12: Forward simulation: total mass flow on boundaries. (a) Flow rates through the planes located at the boundaries during one cardiac cycle: flow at the inlet (red curve) was equal to the flow passing through all 5 outlets combined (dashed black line). (b) Flow profile curves for three supra-aortic vessels, with the peaks delayed in time as expected.

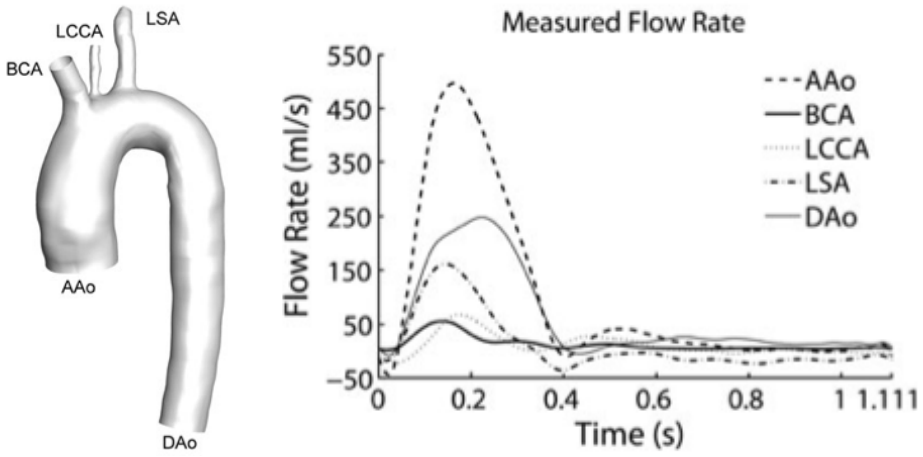

Figure 7.13: Patient-specific measurements of flow rates during one cardiac cycle from the study of Gallo et al. (2012).

where $\dot{m}$ denotes the mass flow rate in kg/s, ρ is the mass density of the fluid, $\dot{V}$ is the volume flow rate, v is the flow velocity and A is the cross-sectional vector area/surface.

At every time step of the simulation, the mass flow rates computed across all inflow boundaries should be equal to those across all outflow boundaries to satisfy the continuity condition, which was the case in our simulation. Figure 7.12 shows the mass flow rates on the inlet and all outlets, showing the equality of the inflow to the outflow by overlaying the flow at the inlet (red curve) with the flow passing through all 5 outlets combined (dashed black line). At systole, the inflow rate was slightly more than 310 mg of blood per second, that rushed from the heart into the ascending aorta at the systolic peak (Figure 7.12 (a) red curve). At the corresponding peaks, roughly 81 mg of blood per second (26% from total inflow) went to the brachiocephalic vessel (magenta curve), which is divided in the right common carotid artery and the right subclavian artery and supplies the entire right upper body. The other two branches – left common carotid and left subclavian – of the supra-aortic arteries both supply the left upper body and received 21 mg (7%, cyan curve) and 51 mg (16%, green curve) of blood per second at their peaks, respectively, which lay within the physiological range. The point to note is that slight reversal of the flow direction occurred in the brachiocephalic and left subclavian arteries at diastole, that can sometimes be observed in patients (see Figure 7.12 (b) magenta curve).

Although the flow and pressure profiles vary significantly even among healthy individuals, it was interesting to draw a comparison between the obtained results

and those reported by Gallo et al. (2012) for a healthy human, shown in Figure 7.13. As can be seen, the temporal sequence of the systolic peaks of different arteries of our results matched the experimental measurements of Gallo et al. (2012). The supra-aortic vessels experienced highest flow earlier or at the same time in the cycle as the inlet: the brachiocephalic and left common carotid arteries peaked at the 4th time point, whereas left subclavian at the 5th time step, together with the inlet. The descending aortic outlet peaked later than the three supra-outlets, at the 6th time step. Similarly, the patient from the Gallo et al. (2012) study experienced flow reversal in the left subclavian artery, similarly to our patient's case.

Calculation of Velocities. The spatially averaged velocity profiles were computed for the supra-aortic vessels from their mass flow measurements. From Equation 7.3, velocity was obtained from the flow rate, density and plane area, as follows:

$$v = \frac{\dot{m}}{\rho A} \tag{7.4}$$

Figure 7.14 depicts the average velocities through the plane (dotted black line) as well as the 3-D velocity components (red, green and blue lines). The 3-D velocity vectors were calculated by multiplying the velocity measured through the outlet plane with the normal of that plane. Velocities much higher than the peak inlet velocity could be observed, especially at the left subclavian artery, where the velocity magnitude reached 1.6 m/s, which was a fivefold increase compared to the 0.3 m/s peak on the inlet. Both brachiocephalic and left subclavian vessels experienced reversal in the flow direction at certain points during diastole.

Pre-TEVAR case: Reverse simulation. The goal of this simulation was to establish a baseline for the direct comparison with the post-TEVAR cases. To keep things *ceteris paribus*, a specific BC configuration was defined that would be used across all subsequent simulations that were subsequently compared. Since the velocities at the supra-aortic vessels were reported not to undergo substantial changes after the intervention, the velocity fixed BC were used at the supra-aortic outlets, in addition to the velocity-fixed inlet. Such a setup aimed at determining the change of the flow in the entire geometry, including at the descending aorta, in order to compare haemodynamic conditions in the pre- and post-procedural cases. Additionally, this setup prescribed flow profiles at 3 of the 4 outlets, which was a desired combination, as described earlier in the chapter. Therefore, the results of the forward simulation

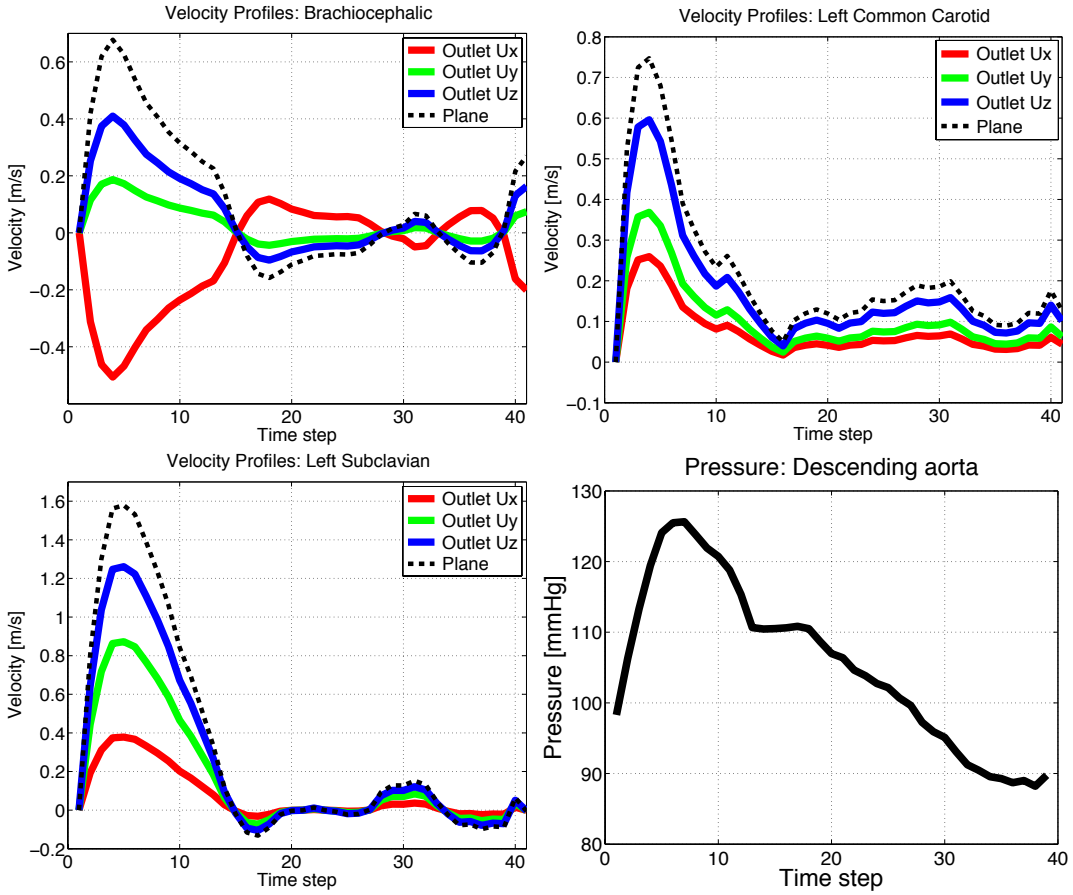

Figure 7.14: Simulated velocities at the supra-aortic vessels and pressure at the descending aortic outlet, used as BCs for the reverse and post-TEVAR simulations.

were used to obtain velocity profiles for the supra-aortic vessels as well as pressure profile for the descending aortic outlet (see Figure 7.14). These waveforms were prescribed as BCs at the corresponding boundaries.

Mass flow. As it was the case for the forward simulation, the mass flow rates across all inflow boundaries were equal to those across all outflow boundaries, as can be seen in Figure 7.15 (a). The flow at the inlet (red curve) matched the flow passing through all 5 outlets combined (dashed black line). This time, however, there was slightly less flow on the supra-aortic vessels and, consequently, more on the outlet than in the forward simulation case (compare to Figure 7.12 that shows the flows for the forward case). The overall shape of the waveforms remained the same. However, in the reverse simulation, approximately 69% of the inflow went to the descending aortic outlet, 14% was diverted to the brachiocephalic, 6% to the left common carotid and 11% to the left subclavian arteries. Recall that the initial

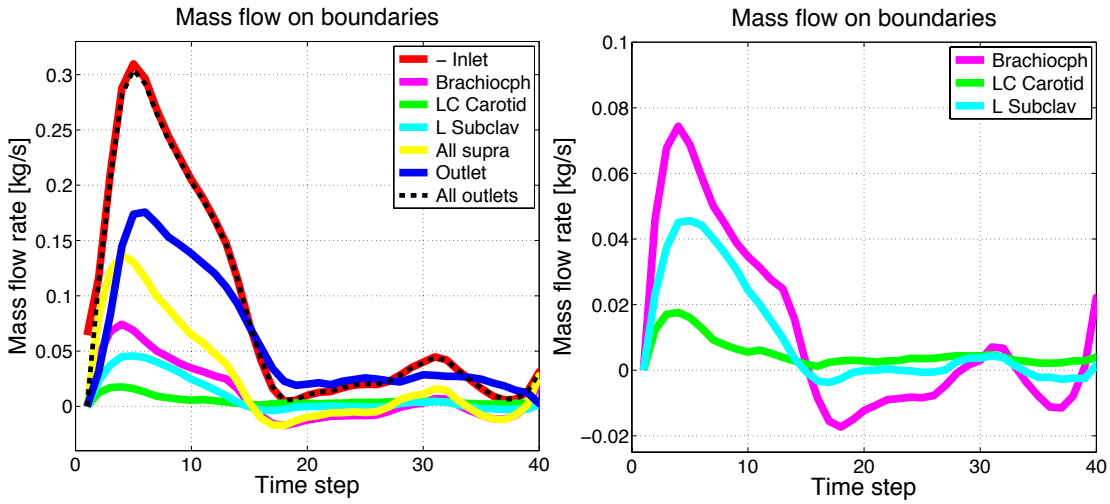

(a) (b)

Figure 7.15: Reverse simulation: total mass flow on boundaries. (a) Flow rates through the planes located at the boundaries during one cardiac cycle: flow at the inlet (red curve) was equal to the flow passing through all 5 outlets combined (dashed black line). (b) Flow profile curves only for the three supra-aortic vessels, with the peaks delayed in time as expected.

percentages of the forward setup, with which the outlet velocity profile was scaled: 64% was going into the aortic outlet and 36% to supra-aortic vessels. This discrepancy resulted from the averaging of the supra-aortic velocity profiles to derive a bulk velocity used as BCs for the reverse simulation.

Velocities. Figure 7.16 displays the flow patterns within the aorta by drawing lines tangential to the instantaneous velocity vector (that we shall call *streamlines* from now on, for brevity), coloured by velocity magnitude. At systolic peak (Figure 7.16, a), the flow was fairly well-organised within the entire aortic lumen, presenting few helical features at the dissection site. The blood entered the ascending aorta with a velocity of around 0.31 m/s, slowing down in the wider dissection area and accelerating thereafter into the descending aorta due to the narrower outlet.

The mid-systole (Figure 7.16, b) already exhibited more pronounced helical features, which became more and more aggravated in the sequel of the cycle. For example, in diastole (Figure 7.16, c), high velocities with respect to the inlet (0.15 m/s) and highly vortical features could be observed inside the dissection site. Additionally, substantial flow reversal occurred in the descending aorta close to the outlet.

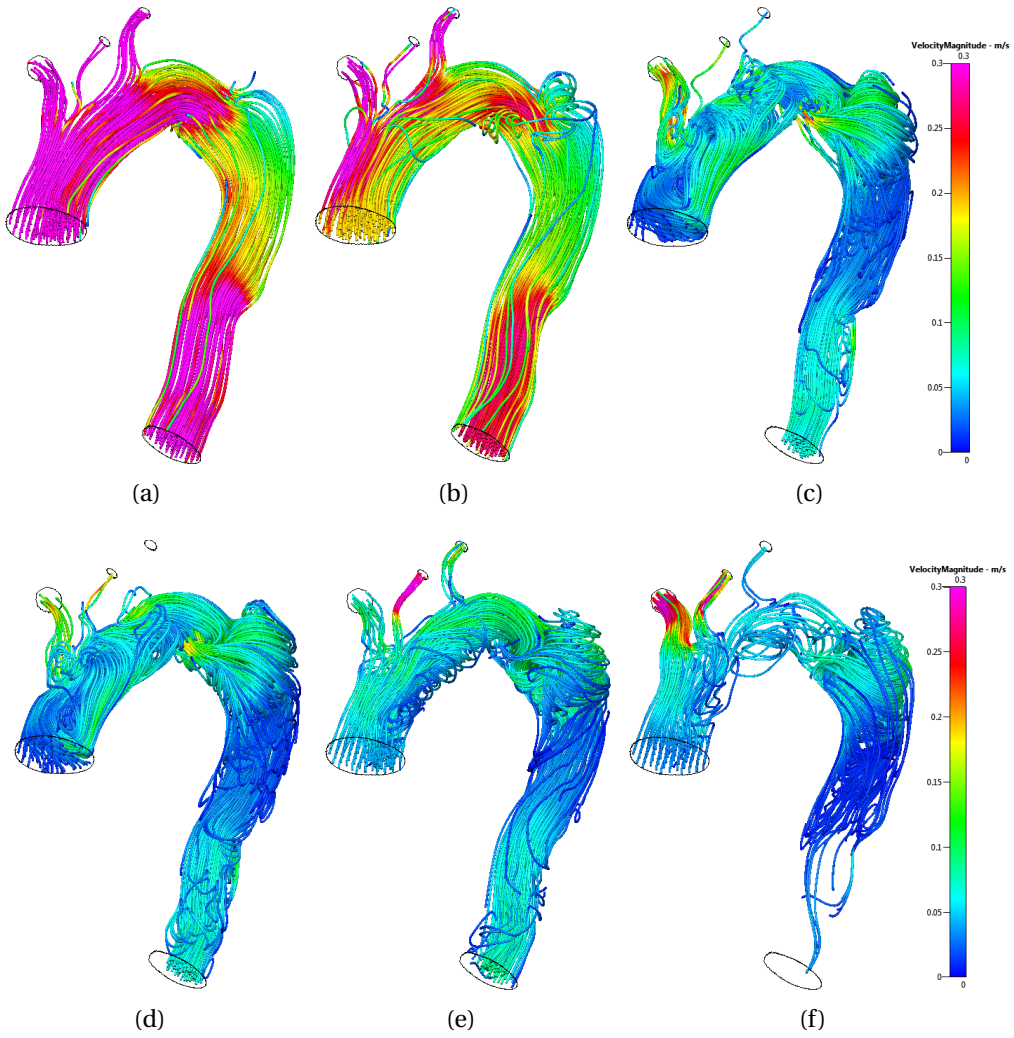

Figure 7.16: Flow patters within the aorta at 6 different time points during the 3rd cardiac cycle: (a) at the systolic peak (T = 1.8445 s), (b) middle of systole (T = 1.953 s), (c) diastole (T = 2.1266 s), (d) middle of the cycle (T = 2.17 s), (e) peak of diastole (T = 2.4087 s), (f) end of the cycle (T = 2.604 s). Streamlines were coloured according to the value of velocity magnitude.

The flow was far from being parallel to the boundaries or the centerline of the vessel along the entire aortic geometry. Similarly, in the rest of the cycle (Figure 7.16, d-f), the maximum velocity on the inlet was around 0.03 m/s (1/10 of the systolic peak), and the flow featured substantially more vortical pattern, as expected. At this stage, the flow presented highly helical features, and highest velocities (up to 0.15 m/s) could be observed within the dissection site, when the flow circulated inside the sac.

To examine the characteristics of the flow at the dissection site, an additional plane was placed cutting through the dissection area, as shown in Figure 7.17 (a-b), which enabled measuring the velocity magnitude and velocity direction on the plane. Figure 7.17 (c-e) depicts the plane coloured into velocity magnitude, with the velocity vectors on top, at three time points during the 3rd cardiac cycle. As can be seen, diastole displayed highly vortical features, with velocity vectors going in circles on the plane (d-e).

Further, another plane was placed across the entire lumen of the geometry, enabling to plot vorticity magnitude on top of it, as shown in Figure 7.18. Vorticity ($\boldsymbol{\omega}$) is defined as the curl or rotational of the velocity field ($\boldsymbol{u}$)

$$\boldsymbol{\omega} = \nabla \times \boldsymbol{u} \tag{7.5}$$

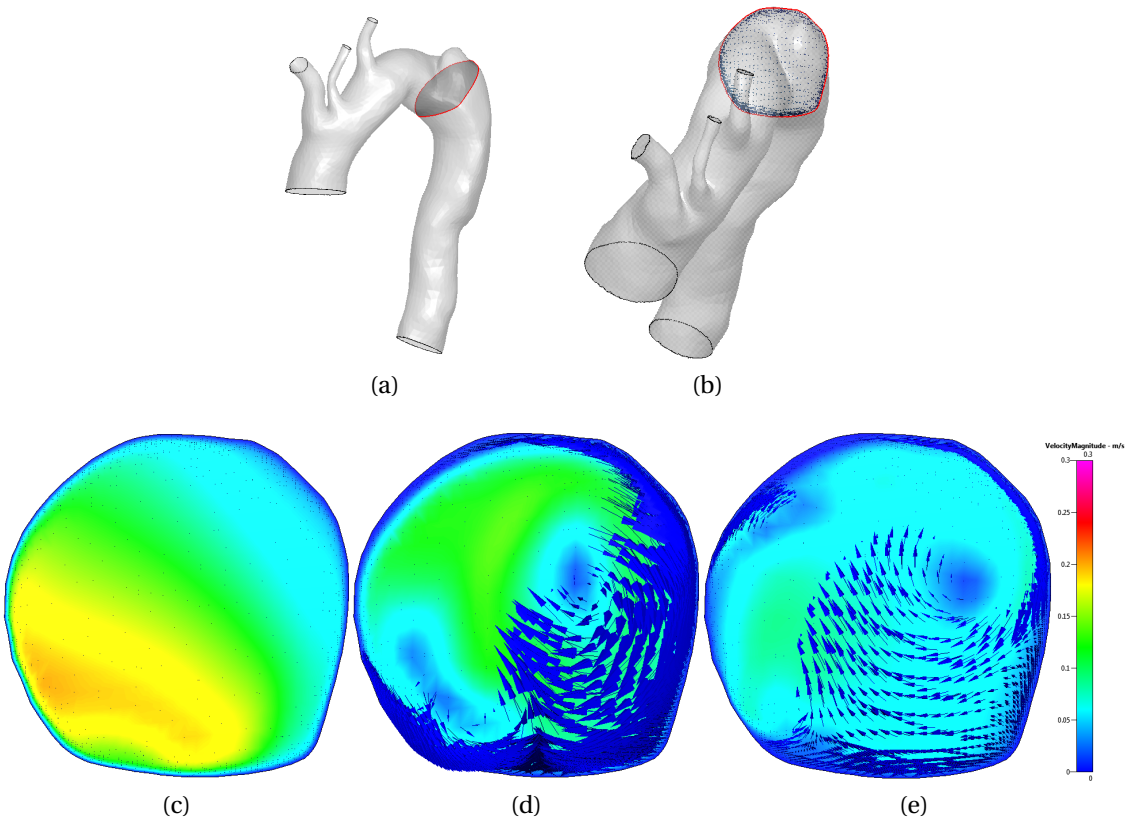

(a) (b)

(c) (d) (e)

Figure 7.17: (a) Plane through dissection. (b) Plane aligned with the viewer. Flow measured through the plane at the dissection site, aligned as in (b), coloured by velocity magnitude with velocity vectors during the 3rd cardiac cycle: (c) at the peak inlet velocity (T = 1.8445 s), (d) in the middle of the cycle (T = 2.17 s), (e) at the last time step (T = 2.604 s). Colourmap scale goes from 0 to 0.3 m/s.

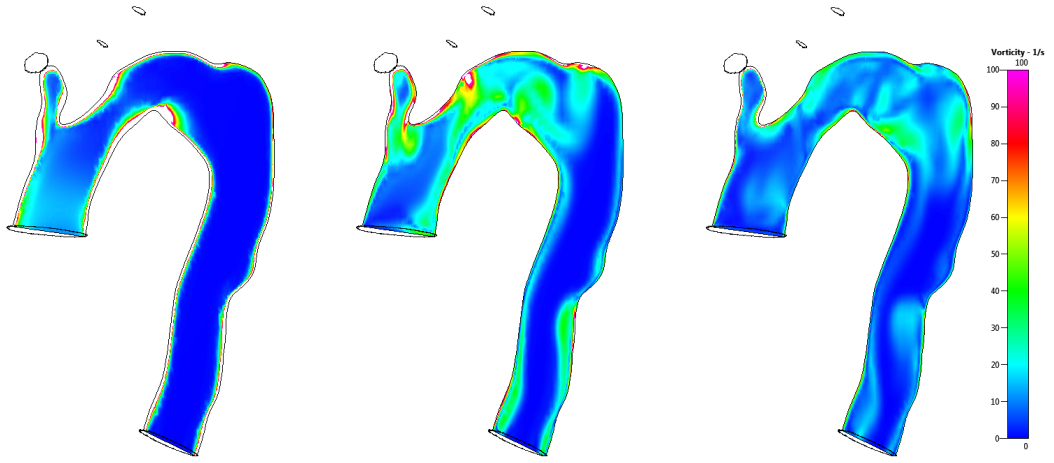

(a) (b) (c)

Figure 7.18: Plane through the entire lumen, coloured by vorticity magnitude value at 3 time points during the 3rd cardiac cycle: (a) at the peak inlet velocity (T = 1.8445 s), (b) in the middle of the cycle (T = 2.17 s), (c) at the last time step (T = 2.604 s).

and describes the local "spinning" motion of the fluid, as would be seen by an observer located at that point and traveling along with the fluid. Vorticity is indicative of high levels of energy spent on "spinning", which is then not available for further perfusion of organs, leading to higher pressure drop. One can see that vorticity was high in diastole, especially close to the dissection site and when approaching the descending aortic outlet. This confirms the overall flow characteristics displayed by the trajectories of velocity traces in Figure 7.16. In general, considering the highly dissorganised flow within the dissected aorta, the hope for the stent-grafting procedure is not only to close the dissection entry but also to align the flow more parallel to the boundaries.

Lastly, the simulated velocity profiles were plotted on the descending aortic outlet in Figure 7.19. The waveforms were almost the same as in the forward simulation (that were prescribed) but were of a slightly higher magnitude when compared to Figure 7.6. This discrepancy occurred due to the performed averaging of the velocity profiles for supra-aortic vessels, as previously pointed out.

Pressure. Figure 7.20 shows the pressure distribution along the aortic dissection at 3 points during the cardiac cycle: at the peak inlet velocity (T = 1.8445 s), in the middle of the cycle that is close to diastole (T = 2.17 s) and at the last time point of the cycle (T = 2.604 s). As can been seen from these snapshots, the pressure val-

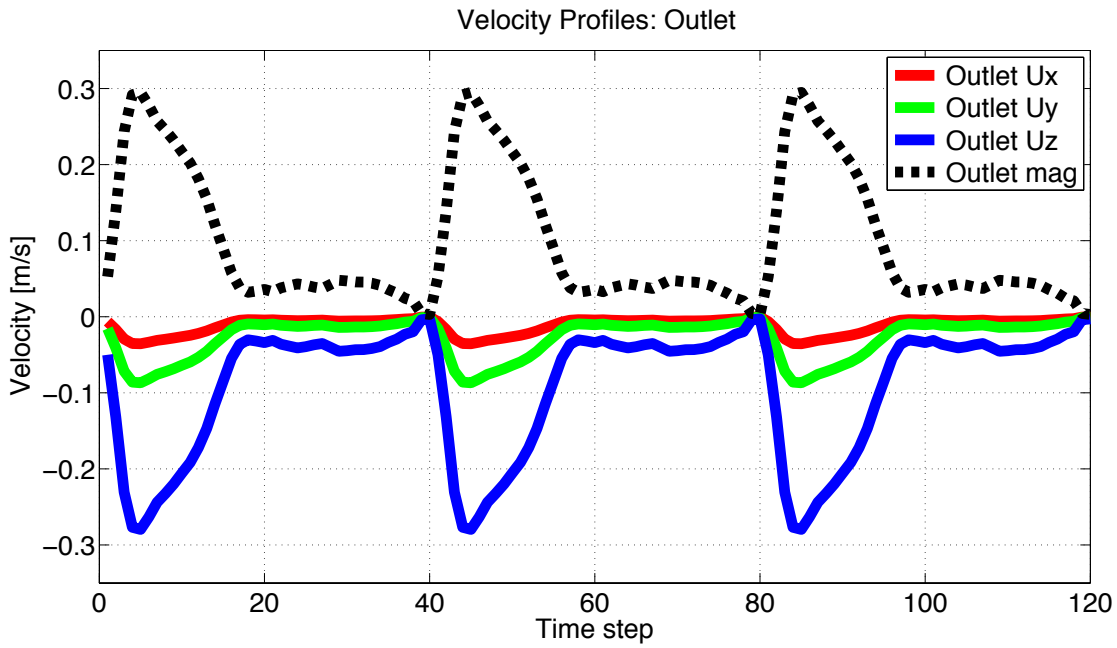

Figure 7.19: Simulated velocity profiles at the outlet in the reverse simulation.

ues varied from as high as 16,830 Pa (126 mmHg) to as low as 11,820 Pa (89 mmHg) along the aortic geometry.

On boundaries, the pressure variation was more pronounced. Figure 7.21 depicts the pressure profile curves on the ascending (inlet) and thoracic aorta (outlet)

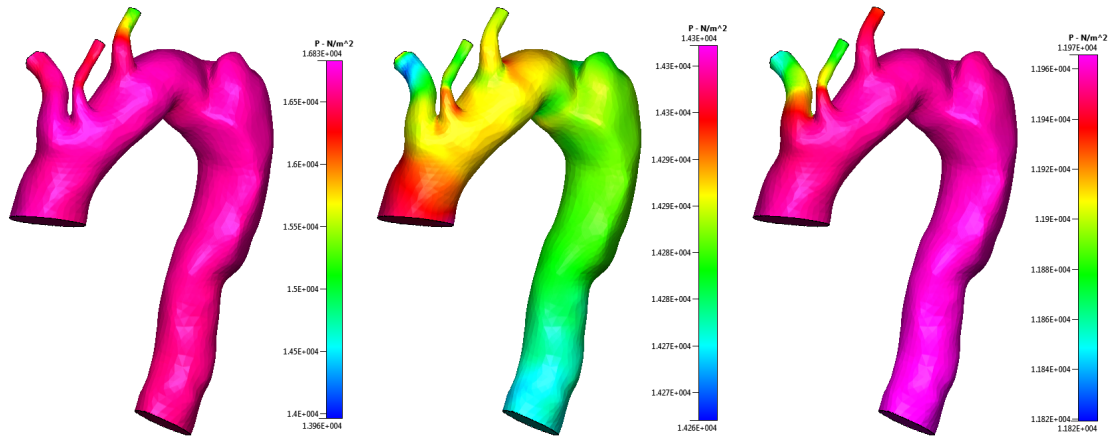

(a) (b) (c)

Figure 7.20: Pressure patterns on the aortic wall at three time points during the 3rd cardiac cycle: (a) at the peak inlet velocity (T = 1.8445 s), (b) in the middle of the cycle (T = 2.17 s), (c) at the last time step (T = 2.604 s).

and the corresponding pressure drop. At the inlet, the pressure peaked at the 86th time step, which lay after the peak systole (time step 85) and measured 16,683 Pa (126.2 mmHg), while the simultaneous pressure at the outlet was 16,538 Pa (124 mmHg). At the outlet, the peak pressure fell at the 88th time step and measured 16,749 Pa (125.6 mmHg), with the simultaneous 16,744 Pa (125.6 mmHg) measurement at the inlet. The measured pressure drop along the analysed aortic geometry was about 11.2 mmHg, which lay within the physiological range for the thoracic aorta (Bock et al., 2011). The point worth mentioning is that since the analysed data came from actual acquisition, the observed pressure drop is the combined effect of vessel distensibility and energy dissipation in flow. The highest pressure drop occurred at the time step 83, slightly before the systolic peak, as expected. Additionally, one could also observe the anticipated inverted pressure drop during early diastole.

In general, the blood pressure in our patient was slightly higher than normal: it measured 126.2 × 88 mmHg instead of the usual 120 × 80 mmHg, which could

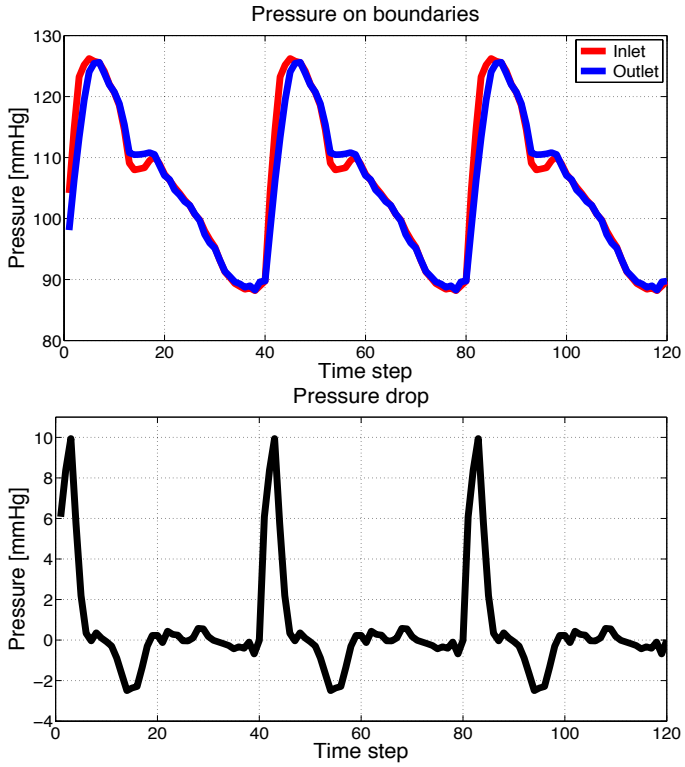

Figure 7.21: Upper row: pressure profile at the inlet and outlet during all 3 cardiac cycles. Lower row: pressure drop profile which corresponds to pressure difference between the ascending (inlet) and descending aorta (outlet).

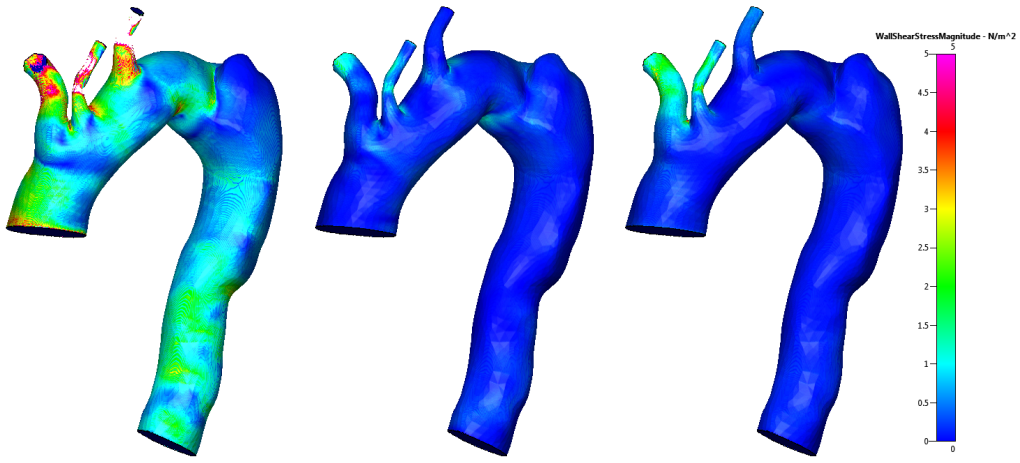

(a) (b) (c)

Figure 7.22: WSS distribution at 3 time points during the 3rd cardiac cycle: (a) at the peak inlet velocity (T = 1.8445 s), (b) in the middle of the cycle (T = 2.17 s), (c) at the last time step (T = 2.604 s). Note the scaling of the colour legend to increase visibility, with 5 Pa as the maximum value.

indicate an onset of the hypertension often found at the initial presentation of type-B aortic dissections (Hagan et al., 2000).

The importance of the Wall Shear Stress (WSS) metric for the healthy haemodynamics of the vessel has been widely discussed in the literature. Figure 7.22 represents the WSS distribution for the same 3 time points of the 3rd cardiac cycle. During systole, the studied aorta experienced relatively high WSS up to 58.97 Pa, which was concentrated mostly in regions of the supra-aortic vessels. In contrast, during diastole, the maximum values lay around 3.6 Pa, with wide area exhibiting values close to zero. To be able to compare the three snapshots, the colour map of the Figure 7.22 was scaled to feature the maximum WSS value of 5 Pa. Note that this scaling placed most of the area on the supra-aortic vessels out of the value range at systole (a).

Post-TEVAR cases.

Velocities. Figure 7.23 captures the difference in flow patterns in a table, which shows the streamlines coloured by velocity magnitude for all four post-TEVAR cases at three time intervals during the cardiac cycle: at systolic peak, in the middle of the cycle and at the last time point. At it was the case in the pre-TEVAR simulation

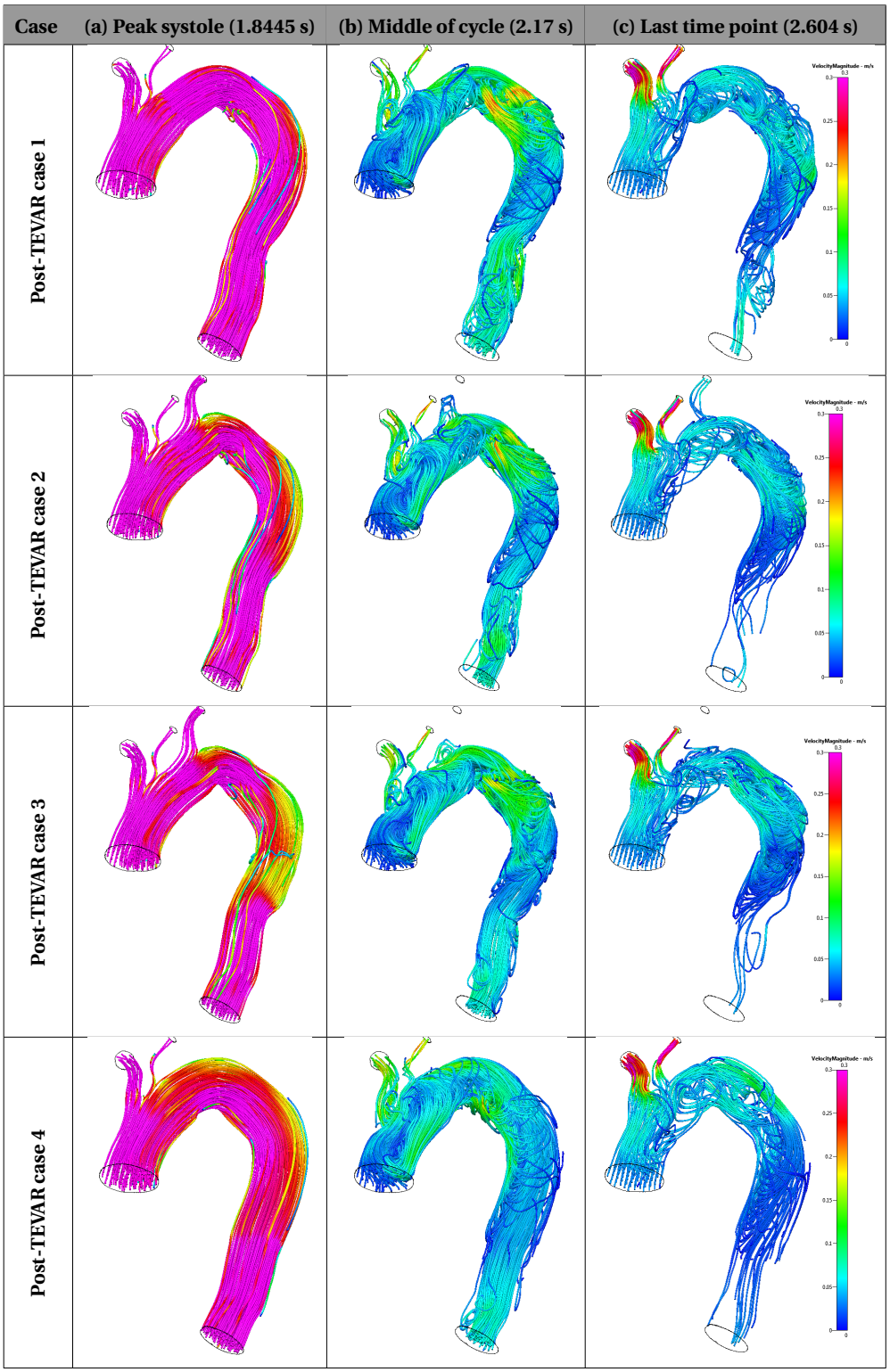

Figure 7.23: Velocity magnitude coloured streamlines with the colourmap scale running from 0 to 0.3 m/s.

(Figure 7.16), at the systolic peak, the flow was fairly organised within the entire aortic lumen, presenting few helical features at the inner curvature of the aorta, close to the dissection site (Figure 7.23, first column). Note that more helical elements were present in the 3rd post-TEVAR case at the distal extremity of the stent graft. This case employed the shorter device, indicating that it would be insufficient for the given aortic geometry. On the contrary, helical features were absent in the 4th post-TEVAR case, which featured wider aortic diameter due to the dilated vessel geometry after the stent grafting. The blood entered the ascending aorta with a velocity of around 0.31 m/s, slightly slowing down in the wider dissection area and accelerating thereafter into the descending aorta due to the narrower outlet.

Similarly to the pre-procedural case, mid-systole (Figure 7.23, second column) exhibited very pronounced helical features (compare to Figure 7.16, d). Additionally, mild flow reversal could be observed close to the descending aortic outlet. The flow was not parallel to the boundaries or the centerline of the vessel. Interestingly, however, case 4 exhibited relatively parallel flow, which was disrupted only close to the vessel wall boundaries, when compared to the other three cases. This fact can be possibly attributed to the passage expansion and the resulting wider cross section. Another fact worth mentioning is that in all post-procedural cases, the helical features were equally distributed along the entire geometry and were not mostly concentrated at the dissection site (since it was covered), as it was the case in the pre-procedural case. The last part of the cycle was characterised by slower flow, increased flow reversal and higher velocities in the supra-aortic vessels, compared to the mid-cycle.

The flow at the dissection site differed significantly among the 4 post-TEVAR cases – an observation that fully justifies this study and underpins the value of modelling for interventional planning. Figure 7.24 shows velocity magnitude vectors on top of the velocity magnitude contours. Both velocity magnitude values as well as vector trajectories varied in all cases and at all measured time points during the cycle. They were also very different from the pre-procedural case (compare to Figure 7.17). One can observe that the first three stent graft placements only covered the actual dissection entry, but did not result in reduction of vortical features in the remaining lumen at the dissection site. As before, diastole displayed highly vortical features, with velocity vectors forming circular patterns on the plane (2nd and 3rd column). However, the 4th post-TEVAR case substantially reduced vortical features

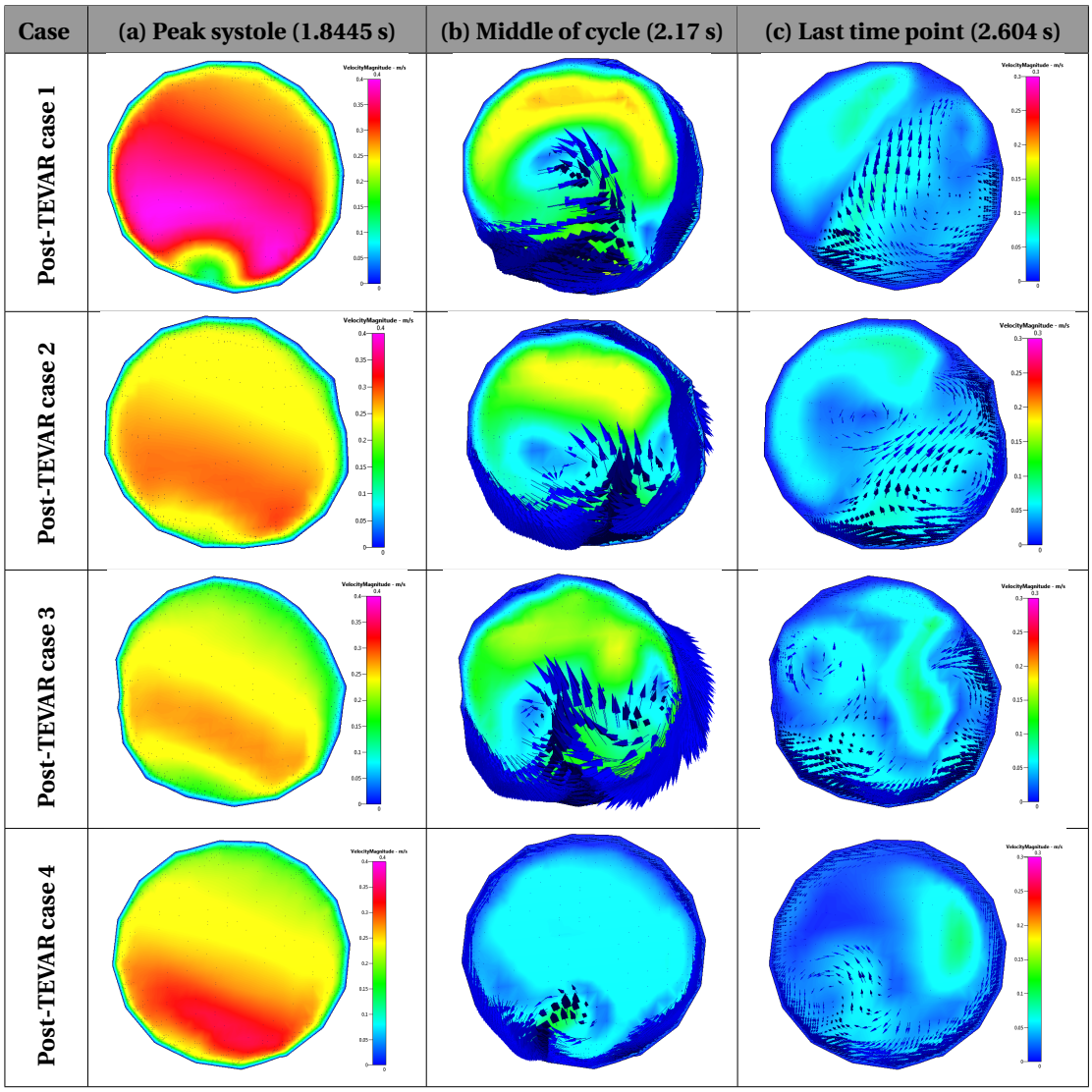

Figure 7.24: Velocity magnitude contours and velocity vectors at the plane cutting the dissection site. The colour scale in column (a) runs from 0 to 0.4 m/s, while in (b) and (c) from 0 to 0.3 m/s. The lack of smoothness on the contour of the in-stent lumen results from the stretching of the sheath in between the expanded struts.

in diastole, which was an interesting result, especially given the lack of reduction in the 1st case that differed only in flexibility of the vessel wall. Hence, it can be asserted that the difference in flow patterns between the 1st and 4th post-TEVAR cases illustrated the importance of simulating the distensible vasculature in order to capture the change in haemodynamics of the vessel after TEVAR.

Vorticity plots show further differences between the post-procedural cases. Figure 7.25 displays vorticity magnitude on the plane cutting through the entire aortic

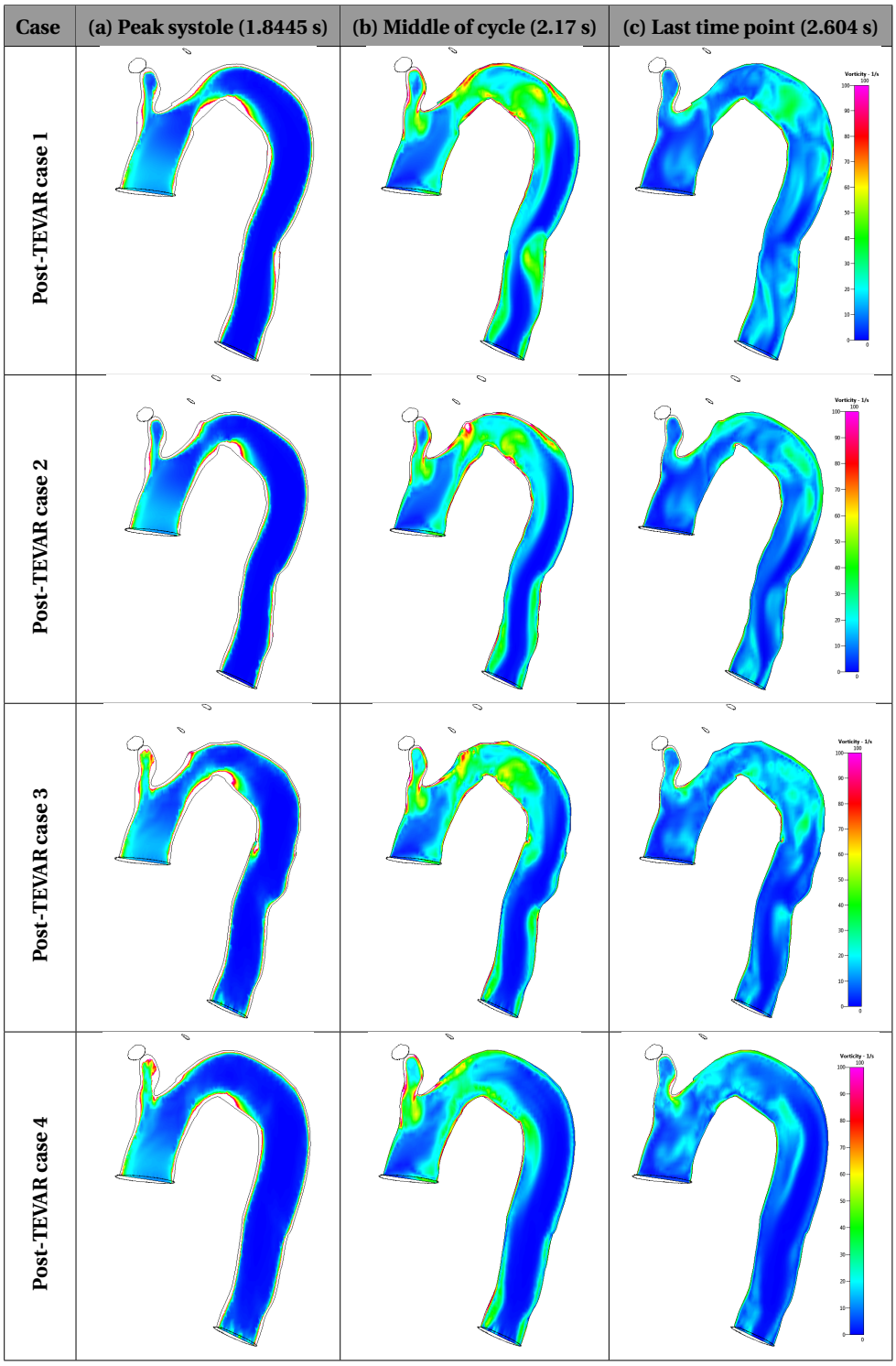

Figure 7.25: Vorticity contours on the plane cutting through the geometry with the colourmap running from 0 to 100 s^{-1}.

geometry. In general, vorticity was high in diastole, especially close to the dissection site and when approaching the descending aortic outlet, similar to the pre-procedural case (compare to Figure 7.18). However, one could notice the more pronounced vorticity features in the 3rd case, confirming the inappropriateness of the shorter device for the given patient's anatomy. As it was the case with velocity traces, vorticity patterns differed significantly between the 1st and 4th post-TEVAR cases, with the former exhibiting higher vorticity at the dissection site as well as in the descending aorta. This fact reaffirmed the earlier point about the importance of modelling the distensible vasculature.

Lastly, the simulated velocity profiles were plotted at the descending aortic outlet in Figure 7.28, second column. The 1st and the 4th post-TEVAR cases feature higher velocities, as compared to the pre-procedural case, due to the overstenting of the left subclavian artery. The peak outlet velocity in the 1st case measured 0.36m/s and in the 4th case 0.37 m/s. On the contrary, the 2nd and the 3rd post-TEVAR cases exhibited the velocity profiles very similar to the pre-TEVAR case with the peak of 0.29 m/s (see Figure 7.19). Analogously, the mass flow rates behaved in a similar way. The 1st and the 4th cases exhibited different flow profiles because of the remaining two supra-aortic arteries instead of the three, as can be seen in Figure 7.28 (first column), while the 2nd and the 3rd cases had similar profiles to the pre-procedural case (see Figure 7.15). Note the increase in flow rate resulting from the overstenting of the left subclavian artery. The mean flow at the descending aortic outlet increased from 69% in the pre-TEVAR case to 79% in the 1st and 4th post-TEVAR cases. Similarly, the peak outflow at the descending aortic outlet (time step 6) increased from 0.18 kg/s pre-procedurally to 0.22 kg/s in the 1st and 4th post-procedural cases.

Pressure. Figure 7.26 shows the pressure distribution along the aortic geometry in all four post-TEVAR cases and at 3 points during the cardiac cycle. As can been seen from the snapshots, the pressure values varied differently in each case. Note the difference in scaling of the colourmaps of the plots. Because the pressure on the outlet was fixed as a BC for all simulations, pressure drop provided a clear comparison between the cases, which can be seen in Figure 7.28, third column. Compared to the pressure drop in the pre-procedural case (which is depicted as a black dashed line), the most significant raise in the pressure drop peak could be observed in the 1st post-TEVAR case (red solid line). This simulation modeled the real positioning of the stent graft but without taking into account the distensibility of the vessel. In con-

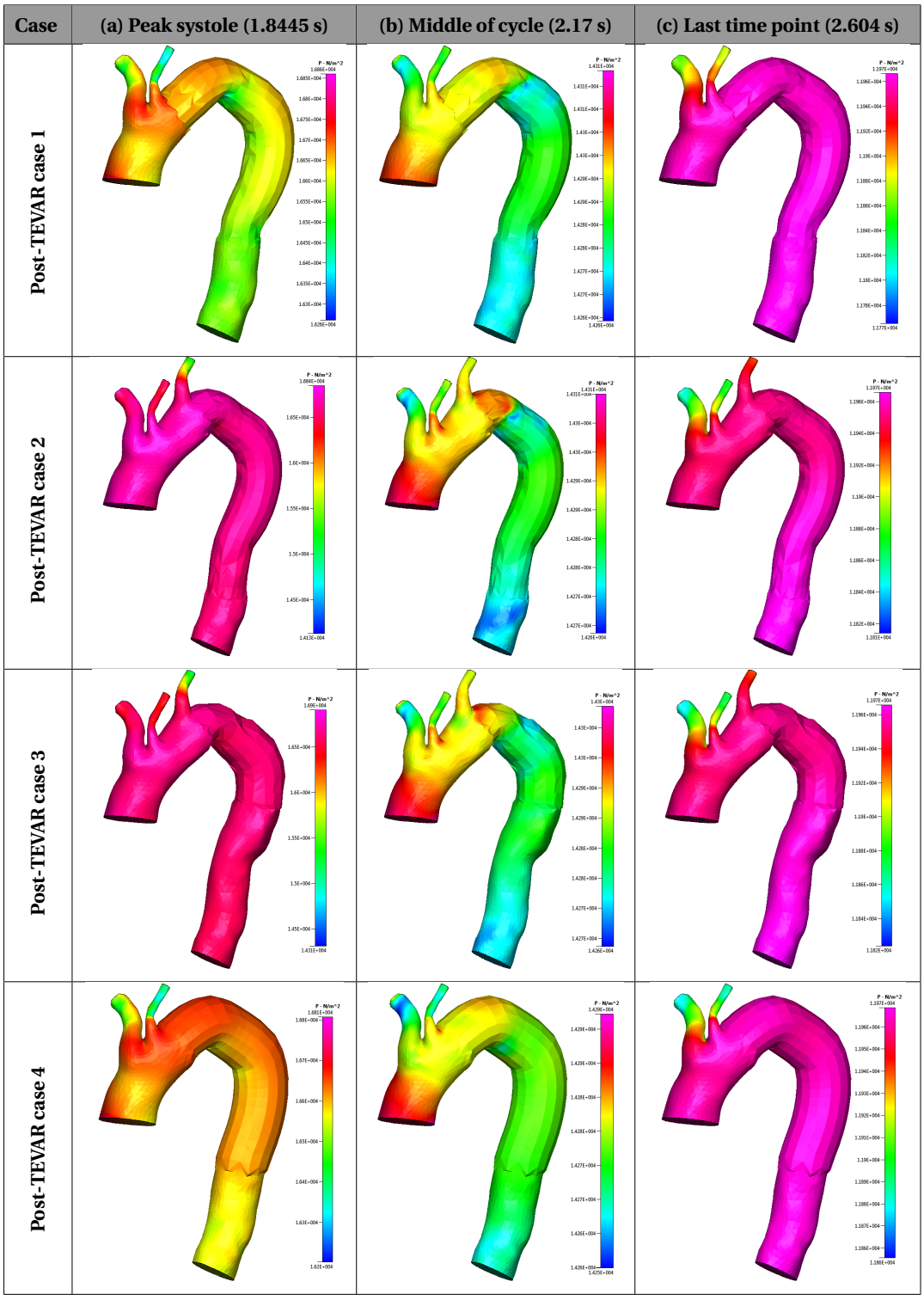

Figure 7.26: Pressure patterns within the stented aorta at three time points during the 3rd cardiac cycle. The lack of smoothness on the contour of the in-stent lumen results from the stretching of the sheath in between the expanded struts.

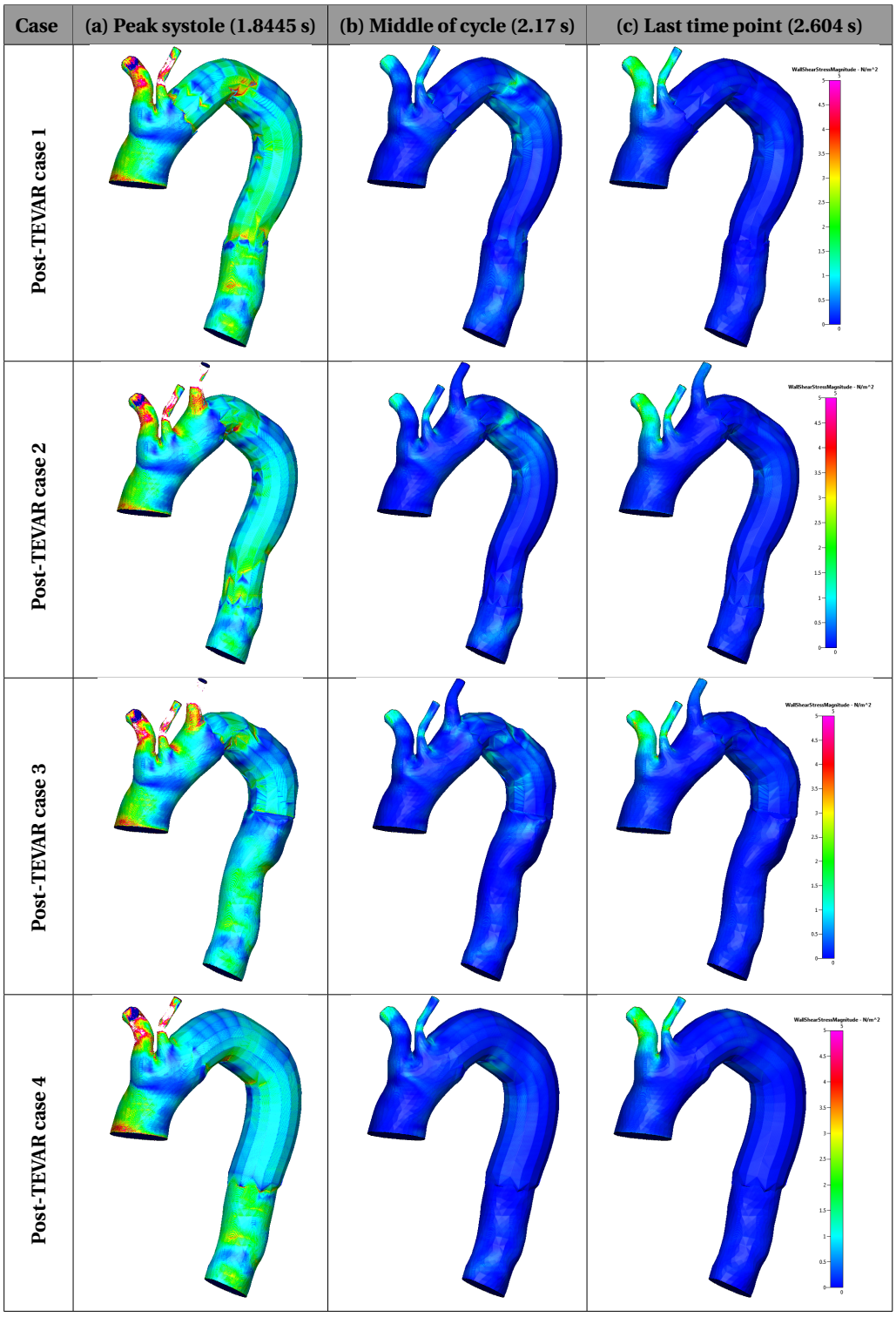

Figure 7.27: Wall shear stress distribution with the colourmap scaling running from 0 to 5 Pa. The lack of smoothness on the contour of the in-stent lumen results from the stretching of the sheath in between the expanded struts.

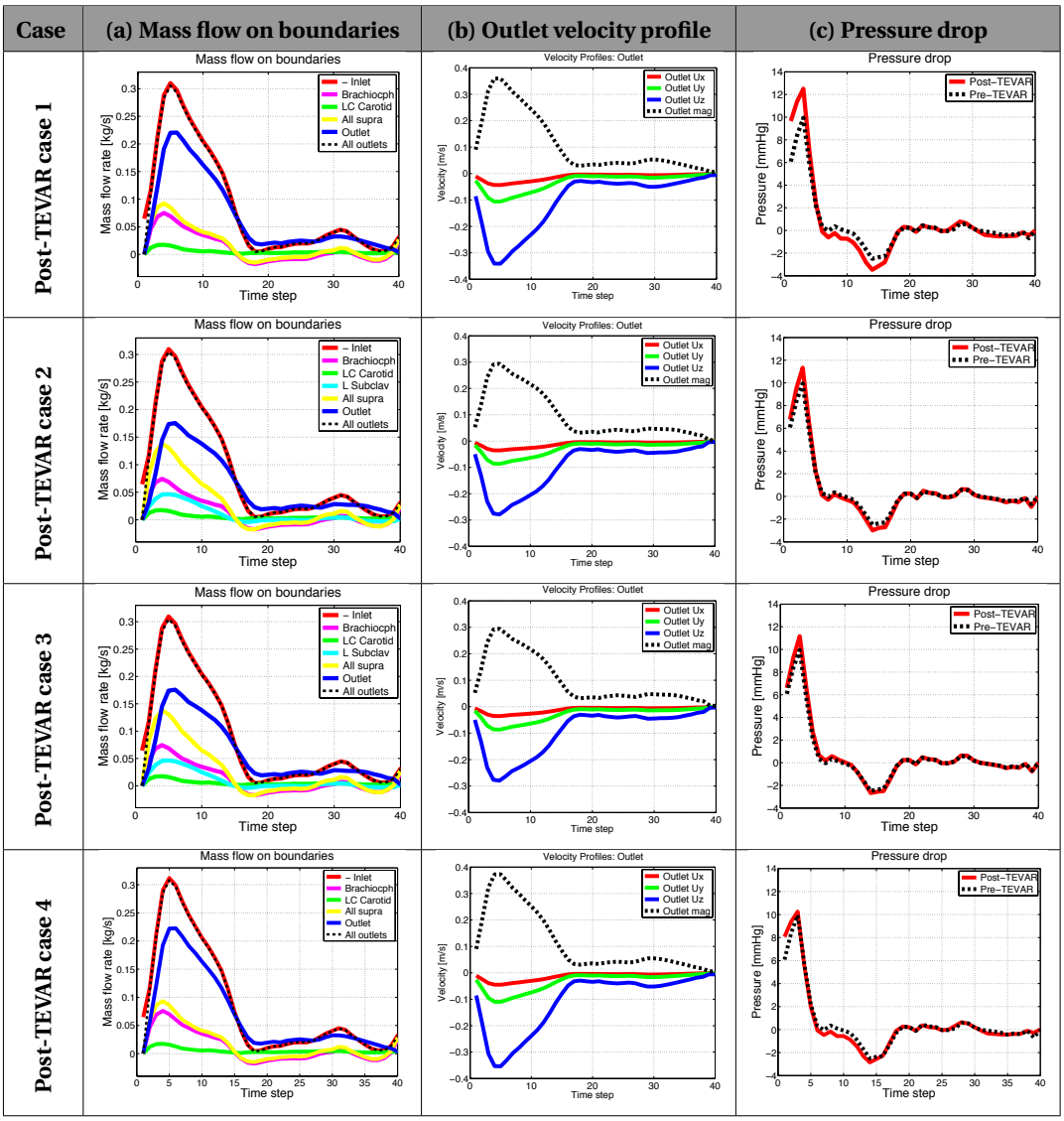

Figure 7.28: Flow features during the 3rd cardiac cycle: (a) mass flow rate through boundaries, (b) velocity profile of the descending aortic outlet, (c) pressure drop between the inlet and descending aortic outlet.

trast to that, the 4th simulation that also modeled the vessel dilation led to almost no change in the pressure drop peak. The least change in pressure drop resulted from the 3rd TEVAR deployment with the shorter device, showing the almost negligible contribution of the employed stent graft. In this case, the overall pressure drop profile remained very similar to the pre-procedural case. In general, all virtual TEVAR procedures resulted in almost no change in pressure drop and overall pressure values, which stayed slightly elevated also post-operatively. Such outcomes usually occur in cases in which the initial pre-procedural configuration presents relatively

low vorticity. This seemed to be the case in our patient due to the relatively regular geometry, more resembling a huge aneurysm rather than a dissection.

Finally, Figure 7.27 presents the WSS distribution in the four post-TEVAR cases. Similar trends as in the pre-procedural case could be observed (compare to Figure 7.22). Namely, the relatively high WSS up to 58.97 Pa prevailed during systole and concentrated mostly in regions of the supra-aortic vessels. On the contrary, low maximum values of around 3.6 Pa and wide area exhibiting very low WSS were present in diastole. In particular, the 4th post-TEVAR case (with the distensible aorta) experienced even lower values of the WSS, which was especially visible in diastole.

7.3 Concluding Remarks

This chapter presented the haemodynamic analysis of the post-treatment vessel, which constitutes the next step in modelling of vascular interventions after the phase of virtual stent deployment. In particular, the chapter reported the study demonstrating the implications of different stent grafts and their positioning on the post-procedural blood flow conditions of the treated vessel. Four different TEVAR scenarios were investigated, comparing the haemodynamic changes they induced to the pre-procedural case. The obtained results suggested that both device design, dimensions, stiffness and positioning have important implications on the post-TEVAR haemodynamic conditions of the vessel. With respect to device dimensions, the results indicated that a shorter device was insufficient for the given patient's anatomy, which became apparent from the comparison of the 2nd and 3rd TEVAR scenarios. Especially since this device introduced some additional vortical features at the site of the transition from the end of the graft to the vessel wall, that could introduce some adverse effects on the vessel remodelling after TEVAR.

Further, with respect to the device positioning, the presented experiments questioned the necessity of overstenting of the left subclavian artery that was performed during the real TEVAR. Firstly, by taking a closer look, the investigated geometry did not present obvious reasons for overstenting. Secondly, the overstenting triggered aggravated changes in flow conditions, such as elevated flow rate downstream the aorta and occlusion of the flow to the left arm supplied by the left subclavian artery. Hence, occlusion of an artery should only be pursued when clearly required by the

presented patient's pathophysiology. In addition, the investigation of the velocity and vorticity profiles in post-TEVAR cases 1 and 2 showed preference for positioning of the device further distally of the aorta, due to the accompanying relative decrease in vortical features. Therefore, it could be hypothesised that deploying the stent graft lower downstream in the initial intervention could possibly eliminate the need for the additional device, that was deployed during the secondary TEVAR to extend the length of the graft. Having said that, the final interpretation of the results and the judgement on the device choice and its deployment position should be made by the clinician.

With respect to the modelling aspect, this study showed the importance of taking the flexibility of the vessel into account. The performed experiments demonstrated that deformation of the vessel had significant implications on the flow patterns. This fact became clearly visible from the direct comparison of the two deployment cases that differed only in accounting (or not) for vessel deformations – case 1 and 4. The two cases featured notably different flow characteristics in all measured comparison metrics. Therefore, the obtained results point to including distensibility of the vessel tissue into a computational model of vascular interventions, as well as showing the implications of the stiffness of the device. On the other hand, it can be claimed that any computational model that assumes rigidity of the vessel when modelling the stent deployment and the subsequent CFD must be viewed as an approximation, since it is well known that vascular interventions in the abdominal and the thoracic area tend to deform the vessel geometry.

As expected, this study featured a number of limitations. Firstly, the velocities and pressure profiles used as BCs for the simulations were not entirely patient-specific. Using complimentary profiles from another patient and another study resulted in inevitable inaccuracies in the alignment of profiles. Difference in patients imply the discrepancies in systemic conditions, which have direct implications on the pressure profiles that were utilised. Also, assumptions about the flow distribution between the outlets had to be made due to the lack of velocity magnitude information for the descending aorta. All these assumptions could lead to imprecisions in resulting haemodynamic indicators, which cannot, therefore, be claimed to directly apply to our patient. However, since the primarily goal of the presented study was to perform a comparative analysis between the different TEVAR scenarios, this setup was deemed to be valid for our purposes.

Secondly, the CFD was performed on simplified aortic models. The initial inaccuracies stemming from the resolution of the CT-scanning device (which is often unable to capture small arteries), were aggravated by the segmentation procedure and subsequent smoothing of 3-D geometries. Thirdly, although the CFD simulations were transient, the aortic geometry was static during the whole cardiac cycle, which is not the case in reality. In reality, the vessel wall dilates during the cycle and accumulates fluid, which implies a reservoir effect connecting the inflow and outflow rates. This constitutes another limitation of the current CFD method that enforces the continuity constraint. The final limitation was the assumption regarding the rheological behavior of blood, which was treated as a Newtonian fluid.

The above limitations could lead to overall effects in the CFD models that cannot be neglected. However, since this study aimed at performing a comparative analysis, the differences between the models were of primary interest. Thus, no claim was being made about the validity of a single simulation; it was rather demonstrated that there were substantial discrepancies in post-procedural haemodynamic conditions of different TEVAR procedures. To sum up, it can be reiterated that both device choice and its positioning have important implications on the post-TEVAR haemodynamics. Therefore, it is crucial to carry out CFD studies of different deployment scenarios to evaluate the consequences of a stent deployment procedure. Hence, the present study constitutes an important proof of concept for demonstrating the necessity of computational modelling of vascular interventions in advance.

CHAPTER 8

CONCLUSIONS

Providing the best possible care for every individual patient necessitates patient-specific approaches. In treating cardiovascular diseases, the need for patient-specificity becomes exacerbated by the uniqueness of each patient's vascular geometry, especially at the diseased site, and by differences in mechanical properties of devices used in stent placement procedures. In this context, the inability of the clinician to predict the final shape of the deployed device inside a treated vessel and assess the potential vessel deformation, as well as the implications of the placement in terms of the haemodynamic changes, create the need for virtual pre-operative rehearsals. Providing a computational platform that enables pre-operative rehearsals constitutes an enormous technical challenge, which will continue to be the topic of multi-disciplinary research in the future. Nevertheless, this thesis aimed at making a sound step towards creating such a platform.

Summary. This thesis achieved several milestones:

- A computational platform that enables virtual deployment of stents inside patients vessels was developed. The framework allowed performing pre-operative rehearsals for the treatment of cerebral and aortic aneurysms as well as aortic dissections, in a user-friendly way for a clinician (see Appendix B).
- The stent deployment algorithm fulfilled the requirement of **fast** execution

times, delivering the results in the order of several minutes for real patient cases, which is of a paramount importance for its clinical usability.

- The results produced by the fast method have been **validated** for a stent graft device with the help of a "gold standard" FEA model, displaying reasonable accuracy in the final device configurations (mean nodal difference < 10.5%) and force measurements (mean force discrepancy < 0.2 N).

- It has been shown how to model a stent device in order to test its virtual deployment. All steps involved in the modelling pipeline have been demonstrated, starting from the reconstruction of device geometry to modelling its expansion process. Additionally, it was illustrated how to obtain a device-specific stiffness by means of parameter calibration with the help of GA and FEA.

- The FM deployment method included the possibility of modelling **flexible vasculature** and potential vessel deformation which might occur in the course of the stent deployment procedure. For that purpose, a novel contact model was implemented that influenced both the final shape of the expanded devices and the post-procedural vessel geometries due to the interplay of forces and strains of the two bodies in contact. The stiffness parameters for both the vessel and the stent were instantiated in a compatible way with values previously reported in the literature. Although not yet validated, this aspect of the model opened up a new array of possibilities and took the predictive capability of the stent deployment platform to a whole new level.

- The virtual stent deployment was linked to the subsequent **haemodynamic** analysis of the treated vessel. The CFD simulations of different treatment scenarios demonstrated the importance of modelling virtual stent deployment pre-operatively, showing significant variation in resulting flow patterns due to treatment differences. These differences in haemodynamics underpinned the value of modelling for interventional planning.

In conclusion, the developed virtual framework can be explored as an additional tool to facilitate clinical practice. It could contribute to assessing the risk of adverse effects of stent deployment and predict the stent behavior for each specific patient in an acceptable run time, thereby making an additional step towards bringing pre-operative computational modelling into the operating room.

Limitations. Inevitably, there were a number of overall limitations associated with the present study, in addition to those already listed at the end of the corresponding chapters.

Firstly, the FM deployment method included the possibility of modelling the vessel deformation resulting from the stent deployment procedure. However, the parameters for instantiating the stiffness of the stent and the vessel are yet to be investigated. Although the utilised values were taken from the literature, they were not validated for the given setup or for the employed device and the patient. Not to mention that the actual stiffness of the patient's aorta can differ substantially from the average values, especially due to anisotropy of the tissue or the presence of the disease. Further, the implemented flexible contact model was fairly simplistic, which while ensuring fast execution times of the model, inevitably introduced some compromises in accuracy.

Additionally, the proposed virtual model did not support the investigation of such important complications of stent placement procedures as occurrence of endoleaks or possible fracture of devices. The possible investigation of endoleaks was excluded due to the simple meshing strategy employed for the CFD analysis, which discretised the stent and the vessel as a single domain, disregarding any potential gaps between the device and vessel walls. With respect to the device fracture, it could only be indirectly investigated through measurements of residual forces.

Further, although the performance of FM was improved with GA, more complex stiffness mechanisms are needed to increase accuracy of the results. In particular, the FM method should be improved with respect to the struts length error. It is possible, however, that a special handling of the struts' length is necessary for the FM method, for example, incorporation of an additional constraint into the algorithm to preserve or correct the lengths.

Finally, the FM has to be validated for FD devices. The validation of the FM was performed only for the SG device, where obtaining the target for comparison was easy due to the existence of numerous established FEA methods for these types of devices. On the contrary, FEA models for FDs hardly exist due to the novelty and the braided design of these devices. Therefore, building the benchmark for comparison would be a substantial research endeavor in its own right.

Future work. The long-term success of stenting procedures largely depends on the fact that flow reduction or stagnation within the aneurysm sac (or false lumen of the dissection) leads to the formation of a stable thrombus. The hope is for the thrombus to eventually obliterate the lesion and restore normal blood flow within the parent vessel (Kulcsar et al., 2011). Thus, the next extension of the treatment planning model would be to account for the thrombus formation, especially since failure to produce a stably positioned clot often leads to secondary interventions.

Modelling of thrombosis in relation to local haemodynamics is an extremely challenging task, since its formation is a complex function of the underlying biochemistry, cell signaling, flow conditions, etc. Nevertheless, a tangible starting point could be, for example, to explore the thrombus growth alone through shear stress. Afterwards, the necessary comparisons between *in silico* simulations and *in vivo* data could be made, revealing the role of the shear stress. Following the work of Ventikos et al. (2009), the thrombus clot could be modelled as a porous medium, and its growth could be tracked through the use of a level set method.

A number of other possible extensions of the virtual stent deployment model can be envisioned. For example, based on the haemodynamic analysis of the post-treatment vessel, evaluation of the stent stability, possibility of endoleakage and endotension, or formation of hyperplasia could be incorporated into the model. These factors are of great importance with regards to recanalisation, subsequent regrowth at the neck of the aneurysm and overall success of the treatment.

Another possible research direction beyond the treatment planning lies in the investigation of aneurysm evolution following treatment. The evolution of the blood flow within the aneurysm determines the evolution of the WSS and spatial wall shear stress gradient (WSSG) distributions that act on the endothelial cell layer of the tissue. The challenge of the task would consist in incorporating the arterial micro-structure into the model and relating the local haemodynamic stimuli to tissue remodelling. For this purpose, conceptual models of aneurysm growth are currently being developed, for instance, where elastin degradation is linked to the local haemodynamics and collagen synthesis is linked to local stretching of the fibroblast cells (Watton et al., 2009).

Finally, I hope that the developed computational system becomes a useful tool in improving patient outcomes and advancing future research!

REFERENCES

The American Heritage® Medical Dictionary. Houghton Mifflin Company, 2007.

CFD-ACE V2013.3 Modules Manual. ESI Group, Huntville, Alabama, 2013a.

CFD-VisCART V2013.3 User Manual. ESI Group, Huntville, Alabama, 2013b.

ADRIAENSEN, M., BOSCH, J., HALPERN, E., MYRIAM HUNINK, M., AND GAZELLE, G. Elective endovascular versus open surgical repair of abdominal aortic aneurysms: Systematic review of short-term results. *Radiology*, 224(3):739–747, 2002.

ALFKE, K., STRAUBE, T., DORNER, L., MEHDORN, H., AND JANSEN, O. Treatment of intracranial broad-neck aneurysms with a new self-expanding stent and coil embolization. *American Journal of Neuroradiology*, 25(4):584–591, 2004.

ALLENDER, S., SCARBOROUGH, P., PETO, V., RAYNER, M., LEAL, J., LUENGO-FERNÁNDEZ, R., AND GRAY, A. European cardiovascular disease statistics 2008. *British Heart Foundation and University of Oxford*, 2008.

APPANABOYINA, S., MUT, F., LÖHNER, R., PUTMAN, C., AND CEBRAL, J. Simulation of intracranial aneurysm stenting: techniques and challenges. *Computer Methods in Applied Mechanics and Engineering*, 198(45-46):3567–3582, 2009.

APPANABOYINA, S., MUT, F., LÖHNER, R., PUTMAN, C., AND CEBRAL, J. Computational fluid dynamics of stented intracranial aneurysms using adaptive embedded unstructured grids. *International Journal for Numerical Methods in Fluids*, 57(5):475–493, 2008.

BARBER, D. C., OUBEL, E., FRANGI, A. F., AND HOSE, D. Efficient computational fluid dynamics mesh generation by image registration. *Medical Image Analysis*, 11(6):648–662, 2007.

BATINA, J. Unsteady euler airfoil solutions using unstructured dynamic meshes. *AIAA Journal*, 28(8): 1381–1388, 1990.

BERNARDINI, A., LARRABIDE, I., MORALES, H. G., PENNATI, G., PETRINI, L., CITO, S., AND FRANGI, A. F. Influence of different computational approaches for stent deployment on cerebral aneurysm haemodynamics. *Interface Focus*, 1(3): 338–348, 2011.

BIANCHI, G., SOLENTHALER, B., SZÉKELY, G., AND HARDERS, M. Simultaneous topology and stiffness identification for mass-spring models based on FEM reference deformations. In *Medical Image Computing and Computer-Assisted Intervention–MICCAI 2004*, pages 293–301. Springer, 2004.

BLOM, F. Considerations on the spring analogy. *International Journal for Numerical Methods in Fluids*, 32(6):647–668, 2000.

BOCK, J., FRYDRYCHOWICZ, A., LORENZ, R., HIRTLER, D., BARKER, A. J., JOHNSON, K. M., ARNOLD, R., BURKHARDT, H., HENNIG, J., AND MARKL, M. In vivo noninvasive 4D pressure difference mapping in the human aorta: phantom comparison and application in healthy volunteers and patients. *Magnetic Resonance in Medicine*, 66(4):1079–1088, 2011.

BÖCKLER, D., SCHUMACHER, H., GANTEN, M., VON TENGG-KOBLIGK, H., SCHWARZBACH, M., FINK, C., KAUCZOR, H.-U., BARDENHEUER, H., AND ALLENBERG, J.-R. Complications after endovascular repair of acute symptomatic and chronic expanding stanford type B aortic dissections. *The Journal of Thoracic and Cardiovascular Surgery*, 132(2): 361–368, 2006.

BOSE, A., HARTMANN, M., HENKES, H., LIU, H., TENG, M., SZIKORA, I., BERLIS, A., REUL, J., YU, S., FORSTING, M., ET AL. A novel, self-expanding, nitinol stent in medically refractory intracranial

atherosclerotic stenoses. *Stroke*, 38(5):1531–1537, 2007.

BOTTASSO, C., DETOMI, D., AND SERRA, R. The ball-vertex method: a new simple spring analogy method for unstructured dynamic meshes. *Computer Methods in Applied Mechanics and Engineering*, 194(39):4244–4264, 2005.

BRISMAN, J., SONG, J., AND NEWELL, D. Cerebral aneurysms. *New England Journal of Medicine*, 355 (9):928–939, 2006.

BROWN, P., ZELT, D., AND SOBOLEV, B. The risk of rupture in untreated aneurysms: The impact of size, gender, and expansion rate. *Journal of Vascular Surgery*, 37(2):280–284, 2003.

BYRNE, J., BELTECHI, R., YARNOLD, J., BIRKS, J., AND KAMRAN, M. Early experience in the treatment of intracranial aneurysms by endovascular flow diversion: a multicentre prospective study. *PloS One*, 5 (9):e12492, 2010.

CAPELLI, C., BIGLINO, G., PETRINI, L., MIGLIAVACCA, F., COSENTINO, D., BONHOEFFER, P., TAYLOR, A. M., AND SCHIEVANO, S. Finite element strategies to satisfy clinical and engineering requirements in the field of percutaneous valves. *Annals of Biomedical Engineering*, 40(12):2663–2673, 2012.

CEBRAL, J. AND LOHNER, R. Efficient simulation of blood flow past complex endovascular devices using an adaptive embedding technique. *Medical Imaging, IEEE Transactions on*, 24(4):468–476, 2005.

CEBRAL, J., MUT, F., RASCHI, M., SCRIVANO, E., CERATTO, R., LYLYK, P., AND PUTMAN, C. Aneurysm rupture following treatment with flow-diverting stents: computational hemodynamics analysis of treatment. *American Journal of Neuroradiology*, 32 (1):27–33, 2011.

CEBRAL, J. R., CASTRO, M. A., BURGESS, J. E., PERGOLIZZI, R. S., SHERIDAN, M. J., AND PUTMAN, C. M. Characterization of cerebral aneurysms for assessing risk of rupture by using patient-specific computational hemodynamics models. *American Journal of Neuroradiology*, 26(10):2550–2559, 2005.

CHEN, D., MÜLLER-ESCHNER, M., KOTELIS, D., BÖCKLER, D., VENTIKOS, Y., AND VON TENGG-KOBLIGK, H. A longitudinal study of Type-B aortic dissection and endovascular repair scenarios: Computational analyses. *Medical Engineering & Physics*, 35(9):1321–1330, 2013a.

CHEN, D., MÜLLER-ESCHNER, M., VON TENGG-KOBLIGK, H., BARBER, D., BÖCKLER, D., HOSE, R., AND VENTIKOS, Y. A patient-specific study of type-B aortic dissection: evaluation of true-false lumen blood exchange. *Biomedical Engineering Online*, 12 (1):65, 2013b.

CHENG, Z., TAN, F. P. P., RIGA, C. V., BICKNELL, C. D., HAMADY, M. S., GIBBS, R. G. J., WOOD, N. B., AND XU, X. Y. Analysis of flow patterns in a patient-specific aortic dissection model. *Journal of Biomechanical Engineering*, 132(5):051007, 2010.

CHUA, S., MACDONALD, B., AND HASHMI, M. Finite element simulation of stent and balloon interaction. *Journal of Materials Processing Technology*, 143:591–597, 2003.

COOK, S., WENAWESER, P., TOGNI, M., BILLINGER, M., MORGER, C., SEILER, C., VOGEL, R., HESS, O., MEIER, B., AND WINDECKER, S. Incomplete stent apposition and very late stent thrombosis after drug-eluting stent implantation. *Circulation*, 115(18):2426–2434, 2007.

CROWLEY, R. W., EVANS, A. J., KASSELL, N. F., JENSEN, M. E., AND DUMONT, A. S. Endovascular treatment of a fusiform basilar artery aneurysm using multiple in-stent stents. *Journal of Neurosurgery: Pediatrics*, 3(6):496–500, 2009.

DAKE, M., KATO, N., MITCHELL, R., SEMBA, C., RAZAVI, M., SHIMONO, T., HIRANO, T., TAKEDA, K., YADA, I., AND MILLER, D. Endovascular stent-graft placement for the treatment of acute aortic dissection. *New England Journal of Medicine*, 340(20): 1546–1552, 1999.

DE BOCK, S., IANNACCONE, F., DE SANTIS, G., DE BEULE, M., MORTIER, P., VERHEGGHE, B., AND SEGERS, P. Our capricious vessels: The influence of stent design and vessel geometry on the mechanics of intracranial aneurysm stent deployment. *Journal of Biomechanics*, 45(8):1353–1359, 2012.

DEGAND, C. AND FARHAT, C. A three-dimensional torsional spring analogy method for unstructured dynamic meshes. *Computers & Structures*, 80(3-4): 305–316, 2002.

DELINGETTE, H. General object reconstruction based on simplex meshes. *International Journal of Computer Vision*, 32(2):111–146, 1999.

DEMPERE-MARCO, L., OUBEL, E., CASTRO, M., PUTMAN, C., FRANGI, A., AND CEBRAL, J. CFD analysis

incorporating the influence of wall motion: application to intracranial aneurysms. In *Medical Image Computing and Computer-Assisted Intervention–MICCAI 2006*, pages 438–445. Springer, 2006.

DEUSSEN, O., KOBBELT, L., AND TÜCKE, P. Using simulated annealing to obtain good nodal approximations of deformable bodies. In *Computer Animation and Simulation '95*, pages 30–43. Springer, 1995.

DOENITZ, C., SCHEBESCH, K., ZOEPHEL, R., AND BRAWANSKI, A. A mechanism for the rapid development of intracranial aneurysms: a case study. *Neurosurgery*, 67(5):1213–1221, 2010.

D'URSO, P. I., LANZINO, G., CLOFT, H. J., AND KALLMES, D. F. Flow diversion for intracranial aneurysms a review. *Stroke*, 42(8):2363–2368, 2011.

EGGEBRECHT, H., HEROLD, U., KUHNT, O., SCHMERMUND, A., BARTEL, T., MARTINI, S., LIND, A., NABER, C., KIENBAUM, P., KÜHL, H., ET AL. Endovascular stent-graft treatment of aortic dissection: determinants of post-interventional outcome. *European Heart Journal*, 26(5):489–497, 2005.

FARHAT, C., DEGAND, C., KOOBUS, B., AND LESOINNE, M. Torsional springs for two-dimensional dynamic unstructured fluid meshes. *Computer Methods in Applied Mechanics and Engineering*, 163(1-4):231–245, 1998.

FIGUEROA, C. A., TAYLOR, C. A., YEH, V., CHIOU, A. J., AND ZARINS, C. K. Effect of curvature on displacement forces acting on aortic endografts: a 3-dimensional computational analysis. *Journal of Endovascular Therapy*, 16(3):284–294, 2009.

FIORELLA, D., ALBUQUERQUE, F., WOO, H., RASMUSSEN, P., MASARYK, T., AND MCDOUGALL, C. Neuroform stent assisted aneurysm treatment: evolving treatment strategies, complications and results of long term follow-up. *Journal of NeuroInterventional Surgery*, 2(1):16–22, 2010.

FIORELLA, D., LYLYK, P., SZIKORA, I., KELLY, M., ALBUQUERQUE, F., MCDOUGALL, C., AND NELSON, P. Curative cerebrovascular reconstruction with the pipeline embolization device: the emergence of definitive endovascular therapy for intracranial aneurysms. *Journal of NeuroInterventional Surgery*, 1(1):56–65, 2009.

FIORELLA, D., SADASIVAN, C., WOO, H., AND LIEBER, B. Regarding aneurysm rupture following treatment with flow-diverting stents: Computational hemodynamics analysis of treatment. *American Journal of Neuroradiology*, 32(5):E95–E97, 2011.

FLORE, E., LARRABIDE, I., PETRINI, L., PENNATI, G., AND FRANGI, A. Stent deployment in aneurysmatic cerebral vessels: Assessment and quantification of the differences between fast virtual stenting and finite element analysis. In *Proc. CI2BM09 - MICCAI Workshop on Cardiovascular Interventional Imaging and Biophysical Modelling*, volume 5242, pages 790–797. Springer, 2009.

FLÓREZ-VALENCIA, L., MONTAGNAT, J., AND ORKISZ, M. 3D graphical models for vascular-stent pose simulation. *Innovations Technol. Biol. Med.*, 28(2): 65–71, 2002.

FLÓREZ-VALENCIA, L., MONTAGNAT, J., AND ORKISZ, M. 3D models for vascular lumen segmentation in MRA images and for artery-stenting simulation. *IRBM*, 28(2):65–71, 2007.

FUNG, Y. Blood flow in arteries. In *Biomechanics*, pages 108–205. Springer, 1997.

GALLO, D., DE SANTIS, G., NEGRI, F., TRESOLDI, D., PONZINI, R., MASSAI, D., DERIU, M., SEGERS, P., VERHEGGHE, B., RIZZO, G., ET AL. On the use of in vivo measured flow rates as boundary conditions for image-based hemodynamic models of the human aorta: implications for indicators of abnormal flow. *Annals of Biomedical Engineering*, 40(3):729–741, 2012.

GAWENDA, M., JASCHKE, G., WINTER, S., WASSMER, G., AND BRUNKWALL, J. Endotension as a result of pressure transmission through the graft following endovascular aneurysm repair – an in vitro study. *European Journal of Vascular and Endovascular Surgery*, 26(5):501–505, 2003.

GIJSEN, F., MIGLIAVACCA, F., SCHIEVANO, S., SOCCI, L., PETRINI, L., THURY, A., WENTZEL, J., VAN DER STEEN, A., SERRUYS, P., AND DUBINI, G. Simulation of stent deployment in a realistic human coronary artery. *BioMedical Engineering OnLine*, 7 (1):23, 2008.

GOLDBERG, D. E. AND HOLLAND, J. H. Genetic algorithms and machine learning. *Machine Learning*, 3 (2):95–99, 1988.

GOLZARIAN, J. AND VALENTI, D. Endoleakage after endovascular treatment of abdominal aortic

aneurysms: diagnosis, significance and treatment. *European Radiology*, 16(12):2849–2857, 2006.

HAGAN, P., NIENABER, C., ISSELBACHER, E., BRUCKMAN, D., KARAVITE, D., RUSSMAN, P., EVANGELISTA, A., FATTORI, R., SUZUKI, T., OH, J., ET AL. The international registry of acute aortic dissection (IRAD). *JAMA: The Journal of the American Medical Association*, 283(7):897–903, 2000.

HALL, G. AND KASPER, E. Comparison of element technologies for modeling stent expansion. *Journal of Biomechanical Engineering*, 128(5):751–756, 2006.

HIRABAYASHI, M., OHTA, M., RÜFENACHT, D., AND CHOPARD, B. A lattice boltzmann study of blood flow in stented aneurism. *Future Generation Computer Systems*, 20(6):925–934, 2004.

HOLZAPFEL, G., GASSER, T., AND OGDEN, R. A new constitutive framework for arterial wall mechanics and a comparative study of material models. *Journal of Elasticity*, 61(1):1–48, 2000.

HUANG, Q., WU, Y., XU, Y., HONG, B., ZHANG, L., AND LIU, J. Vascular geometry change because of endovascular stent placement for anterior communicating artery aneurysms. *American Journal of Neuroradiology*, 32(9):1721–1725, 2011.

HUMPHREY, J. AND CANHAM, P. Structure, mechanical properties, and mechanics of intracranial saccular aneurysms. *Journal of Elasticity*, 61(1):49–81, 2000.

ISSELBACHER, E. Diseases of the aorta. In *Essential Cardiology*, pages 681–690. Humana Press, 2006.

JAMOUS, M., SATOH, K., MATSUBARA, S., SATOMI, J., NAKAJIMA, N., UNO, M., AND NAGAHIRO, S. Ischemic basilar artery dissecting aneurysm treated by stenting only. *Neurologia Medico-Chirurgica*, 44 (2):77–81, 2004.

JUVELA, S., PORRAS, M., AND POUSSA, K. Natural history of unruptured intracranial aneurysms: probability of and risk factors for aneurysm rupture. *Journal of Neurosurgery*, 93(3):379–387, 2000.

KARMONIK, C., BISMUTH, J., SHAH, D., DAVIES, M., PURDY, D., AND LUMSDEN, A. Computational study of haemodynamic effects of entry- and exit-tear coverage in a DeBakey type III aortic dissection: technical report. *European Journal of Vascular and Endovascular Surgery*, 42(2):172–177, 2011.

KARMONIK, C., STROTHER, C., CHEN, X., DEINZER, F., KLUCZNIK, R., AND MAWAD, M. Stent-assisted coiling of intracranial aneurysms aided by virtual parent artery reconstruction. *American Journal of Neuroradiology*, 26(9):2368–2370, 2005.

KIOUSIS, D., WULFF, A., AND HOLZAPFEL, G. Experimental studies and numerical analysis of the inflation and interaction of vascular balloon catheter-stent systems. *Annals of Biomedical Engineering*, 37(2):315–330, 2009.

KLEINSTREUER, C., LI, Z., BASCIANO, C., SEELECKE, S., AND FARBER, M. Computational mechanics of nitinol stent grafts. *Journal of Biomechanics*, 41 (11):2370–2378, 2008.

KULCSAR, Z., HOUDART, E., BONAFE, A., PARKER, G., MILLAR, J., GODDARD, A., RENOWDEN, S., GAL, G., TUROWSKI, B., MITCHELL, K., ET AL. Intra-aneurysmal thrombosis as a possible cause of delayed aneurysm rupture after flow-diversion treatment. *American Journal of Neuroradiology*, 32(1): 20–25, 2011.

LANZINO, G., KANAAN, Y., PERRINI, P., DAYOUB, H., AND FRASER, K. Emerging concepts in the treatment of intracranial aneurysms: stents, coated coils, and liquid embolic agents. *Neurosurgery*, 57 (3):449–459, 2005.

LARRABIDE, I., KIM, M., AUGSBURGER, L., VILLA-URIOL, M., RÜFENACHT, D., AND FRANGI, A. Fast virtual deployment of self-expandable stents: method and in-vitro evaluation for intracranial aneurysmal stenting. *Medical Image Analysis*, 16 (3):721–730, 2010.

LARRABIDE, I., RADAELLI, A., AND FRANGI, A. Fast virtual stenting with deformable meshes: Application to intracranial aneurysms. In *Medical Image Computing and Computer-Assisted Intervention–MICCAI 2008*, pages 790–797. Springer, 2008.

LASHERAS, J. The biomechanics of arterial aneurysms. *Annual Review of Fluid Mechanics*, 39(1):293–319, 2007.

LAWFORD, P., VENTIKOS, Y., KHIR, A., ATHERTON, M., EVANS, D., HOSE, D., CARE, C., WATTON, P., HALLIDAY, I., WALKER, D., ET AL. Modelling the interaction of haemodynamics and the artery wall: current status and future prospects. *Biomedicine & Pharmacotherapy*, 62(8):530–535, 2008.

LEE, R. Morphology of cerebral arteries. *Pharmacology & Therapeutics*, 66(1):149–173, 1995.

LI, A. E., KAMEL, I., RANDO, F., ANDERSON, M., KUMBASAR, B., LIMA, J. A., AND BLUEMKE, D. A. Using MRI to assess aortic wall thickness in the multiethnic study of atherosclerosis: distribution by race, sex, and age. *American Journal of Roentgenology*, 182(3):593–597, 2004.

LIEBER, B., LIVESCU, V., HOPKINS, L., AND WAKHLOO, A. Particle image velocimetry assessment of stent design influence on intra-aneurysmal flow. *Annals of Biomedical Engineering*, 30(6):768–777, 2002.

LLOYD, B. A., SZÉKELY, G., AND HARDERS, M. Identification of spring parameters for deformable object simulation. *Visualization and Computer Graphics, IEEE Transactions on*, 13(5):1081–1094, 2007.

LLOYD-JONES, D., ADAMS, R., CARNETHON, M., DE SIMONE, G., FERGUSON, T., FLEGAL, K., FORD, E., FURIE, K., GO, A., GREENLUND, K., ET AL. Heart disease and stroke statistics – 2009 update: a report from the American Heart Association Statistics Committee and Stroke Statistics Subcommittee. *Circulation*, 119(3):e21–e181, 2009.

LOUCHET, J., PROVOT, X., AND CROCHEMORE, D. Evolutionary identification of cloth animation models. In *Workshop on Computer Animation and Simulation (Eurographics '95)*, pages 44–54. Springer, 1995.

LYLYK, P., MIRANDA, C., CERATTO, R., FERRARIO, A., SCRIVANO, E., LUNA, H. R., BEREZ, A. L., TRAN, Q., NELSON, P. K., AND FIORELLA, D. Curative endovascular reconstruction of cerebral aneurysms with the pipeline embolization device: the buenos aires experience. *Neurosurgery*, 64(4):632–643, 2009.

MA, D., DARGUSH, G. F., NATARAJAN, S. K., LEVY, E. I., SIDDIQUI, A. H., AND MENG, H. Computer modeling of deployment and mechanical expansion of neurovascular flow diverter in patient-specific intracranial aneurysms. *Journal of Biomechanics*, (45):2256–2263, 2012.

MA, J., YOU, Z., AND BYRNE, J. A novel flow diverter for direct treatment of cerebral aneurysms. In *ASME 2013 Summer Bioengineering Conference*, pages V01AT12A001–V01AT12A001. American Society of Mechanical Engineers, 2013.

MARKS, M., MARCELLUS, M., DO, H., SCHRAEDLEY-DESMOND, P., STEINBERG, G., TONG, D., AND ALBERS, G. Intracranial angioplasty without stenting for symptomatic atherosclerotic stenosis: long-term follow-up. *American Journal of Neuroradiology*, 26(3):525–530, 2005.

MAS, J., CHATELLIER, G., BEYSSEN, B., BRANCHEREAU, A., MOULIN, T., BECQUEMIN, J., LARRUE, V., LIÈVRE, M., LEYS, D., BONNEVILLE, J., ET AL. Endarterectomy versus stenting in patients with symptomatic severe carotid stenosis. *New England Journal of Medicine*, 355(16):1660–1671, 2006.

MEIER, U., LÓPEZ, O., MONSERRAT, C., JUAN, M. C., AND ALCANIZ, M. Real-time deformable models for surgery simulation: a survey. *Computer Methods and Programs in Biomedicine*, 77(3):183–197, 2005.

MIGLIAVACCA, F., PETRINI, L., MASSAROTTI, P., SCHIEVANO, S., AURICCHIO, F., AND DUBINI, G. Stainless and shape memory alloy coronary stents: a computational study on the interaction with the vascular wall. *Biomechanics and Modeling in Mechanobiology*, 2(4):205–217, 2004.

MIGLIAVACCA, F., PETRINI, L., MONTANARI, V., QUAGLIANA, I., AURICCHIO, F., AND DUBINI, G. A predictive study of the mechanical behaviour of coronary stents by computer modelling. *Medical Engineering & Physics*, 27(1):13–18, 2005.

MITCHELL, S. A. AND VAVASIS, S. A. Quality mesh generation in three dimensions. In *Proceedings of the 8th Annual Symposium on Computational Geometry*, pages 212–221. ACM, 1992.

MOLYNEUX, A. ET AL. International subarachnoid aneurysm trial (ISAT) of neurosurgical clipping versus endovascular coiling in 2143 patients with ruptured intracranial aneurysms: a randomised trial. *The Lancet*, 360(9342):1267–1274, 2002.

MONTAGNAT, J. AND DELINGETTE, H. 4D deformable models with temporal constraints: application to 4d cardiac image segmentation. *Medical Image Analysis*, 9(1):87–100, 2005.

MOORE, J. AND BERRY, J. Fluid and solid mechanical implications of vascular stenting. *Annals of Biomedical Engineering*, 30(4):498–508, 2002.

MOSORA, F., HARMANT, A., BERNARD, C., FOSSION, A., POCHET, T., JUCHMES, J., AND CESCOTTO, S. Modelling the arterial wall by finite elements. *Archives of Physiology and Biochemistry*, 101(3):185–191, 1993.

MOYLE, K. R. AND VENTIKOS, Y. Local remeshing for large amplitude grid deformations. *Journal of Computational Physics*, 227(5):2781–2793, 2008.

NURNBERGER, A., RADETZKY, A., AND KRUSE, R. A problem specific recurrent neural network for

the description and simulation of dynamic spring models. In *Neural Networks Proceedings, 1998. IEEE World Congress on Computational Intelligence. The 1998 IEEE International Joint Conference on*, volume 1, pages 468–473. IEEE, 1998.

OLUFSEN, M. S., PESKIN, C. S., KIM, W. Y., PEDERSEN, E. M., NADIM, A., AND LARSEN, J. Numerical simulation and experimental validation of blood flow in arteries with structured-tree outflow conditions. *Annals of Biomedical Engineering*, 28(11): 1281–1299, 2000.

PERKTOLD, K., RESCH, M., AND FLORIAN, H. Pulsatile non-newtonian flow characteristics in a three-dimensional human carotid bifurcation model. *Journal of Biomechanical Engineering*, 113(4):464–475, 1991.

PHATOUROS, C., HIGASHIDA, R., MALEK, A., MEYERS, P., LEMPERT, T., DOWD, C., AND HALBACH, V. Carotid artery stent placement for atherosclerotic disease: Rationale, technique, and current status. *Radiology*, 217(1):26–41, 2000a.

PHATOUROS, C., HIGASHIDA, R., MALEK, A., MEYERS, P., LEMPERT, T., DOWD, C., AND HALBACH, V. Endovascular stenting for carotid artery stenosis: preliminary experience using the shape-memory-alloy-recoverable-technology (SMART) stent. *American Journal of Neuroradiology*, 21(4): 732–738, 2000b.

PIEROT, L. Flow diverter stents in the treatment of intracranial aneurysms: Where are we? *Journal of Neuroradiology*, 38(1):40–46, 2011.

PRASAD, A., XIAO, N., GONG, X.-Y., ZARINS, C. K., AND FIGUEROA, C. A. A computational framework for investigating the positional stability of aortic endografts. *Biomechanics and Modeling in Mechanobiology*, 12(5):869–887, 2013.

PRINSSEN, M., VERHOEVEN, E., BUTH, J., CUYPERS, P., VAN SAMBEEK, M., BALM, R., BUSKENS, E., GROBBEE, D., AND BLANKENSTEIJN, J. A randomized trial comparing conventional and endovascular repair of abdominal aortic aneurysms. *New England Journal of Medicine*, 351(16):1607–1618, 2004.

REBELO, N., FU, R., AND LAWRENCHUK, M. Study of a nitinol stent deployed into anatomically accurate artery geometry and subjected to realistic service loading. *Journal of Materials Engineering and Performance*, 18(5):655–663, 2009.

ROYLANCE, D. Finite Element Analysis - Lecture Notes. 2001.

ROZANSKI, A., BLUMENTHAL, J., AND KAPLAN, J. Impact of psychological factors on the pathogenesis of cardiovascular disease and implications for therapy. *Circulation*, 99(16):2192–2217, 1999.

RUGE, J. W. AND STÜBEN, K. Algebraic multigrid. 1987.

SAAD, C. P., MURTHY, S., KRIZMANICH, G., AND MEHTA, A. C. Self-expandable metallic airway stents and flexible bronchoscopylong-term outcomes analysis. *CHEST Journal*, 124(5):1993–1999, 2003.

SCHIEVINK, W. Intracranial aneurysms. *New England Journal of Medicine*, 336(1):28–40, 1997.

SCHWARTZ, R. AND HENRY, T. Pathophysiology of coronary artery restenosis. *Reviews in Cardiovascular Medicine*, 3:S4–9, 2001.

SCOTT, R., TISI, P., ASHTON, H., AND ALLEN, D. Abdominal aortic aneurysm rupture rates: a 7-year follow-up of the entire abdominal aortic aneurysm population detected by screening. *Journal of Vascular Surgery*, 28(1):124–128, 1998.

SEHNERT, A. AND STAINIER, D. A window to the heart: can zebrafish mutants help us understand heart disease in humans? *Trends in Genetics*, 18(10):491–494, 2002.

SHADWICK, R. Mechanical design in arteries. *Journal of Experimental Biology*, 202(23):3305–3313, 1999.

SHOJIMA, M., OSHIMA, M., TAKAGI, K., TORII, R., HAYAKAWA, M., KATADA, K., MORITA, A., AND KIRINO, T. Magnitude and role of wall shear stress on cerebral aneurysm computational fluid dynamic study of 20 middle cerebral artery aneurysms. *Stroke*, 35(11):2500–2505, 2004.

SINGH, K., BØNAA, K., JACOBSEN, B., BJØRK, L., AND SOLBERG, S. Prevalence of and risk factors for abdominal aortic aneurysms in a population-based study. *American Journal of Epidemiology*, 154(3): 236–244, 2001.

SINGH, P., MARZO, A., COLEY, S., BERTI, G., BIJLENGA, P., LAWFORD, P., VILLA-URIOL, M., RUFENACHT, D., MCCORMACK, K., FRANGI, A., ET AL. The role of computational fluid dynamics in the management of unruptured intracranial aneurysms: a clinicians' view. *Computational Intelligence and Neuroscience*, 2009(760364):1–12, 2009.

SPRANGER, K., CAPELLI, C., BOSI, G., SCHIEVANO, S., AND VENTIKOS, Y. Comparison and calibration of a real-time virtual stenting algorithm using Finite Element Analysis and Genetic Algorithms. *Computer Methods in Applied Mechanics and Engineering (in press)*, 2014a.

SPRANGER, K., HOEGEN, P., VON TENGG-KOBLIGK, H., AND VENTIKOS, Y. Implications of stent graft choice and placement position on the haemodynamics of the aorta: Case study with aortic dissection type B. *(in review)*, 2014b.

SPRANGER, K. AND VENTIKOS, Y. Which spring is the best? Comparison of methods for virtual stenting. *IEEE Transactions on Biomedical Engineering*, 61 (7):1998–2010, 2014.

STEINMAN, D. A., HOI, Y., FAHY, P., MORRIS, L., WALSH, M. T., ARISTOKLEOUS, N., ANAYIOTOS, A. S., PAPAHARILAOU, Y., ARZANI, A., SHADDEN, S. C., ET AL. Variability of computational fluid dynamics solutions for pressure and flow in a giant aneurysm: the ASME 2012 Summer Bioengineering Conference CFD Challenge. *Journal of Biomechanical Engineering*, 135(2):021016, 2013.

STOECKEL, D., BONSIGNORE, C., AND DUDA, S. A survey of stent designs. *Minimally Invasive Therapy & Allied Technologies*, 11(4):137–147, 2002.

TARDY, Y., MEISTER, J., PERRET, F., BRUNNER, H., AND ARDITI, M. Non-invasive estimate of the mechanical properties of peripheral arteries from ultrasonic and photoplethysmographic measurements. *Clinical Physics and Physiological Measurement*, 12(1): 39–54, 1991.

THERIAULT, P., TERRIAULT, P., BRAILOVSKI, V., AND GALLO, R. Finite element modeling of a progressively expanding shape memory stent. *Journal of Biomechanics*, 39(15):2837–2844, 2006.

VAN DOORMAAL, J. AND RAITHBY, G. Enhancements of the SIMPLE method for predicting incompressible fluid flows. *Numerical Heat Transfer*, 7(2):147–163, 1984.

VAN GIJN, J. AND RINKEL, G. Subarachnoid haemorrhage: diagnosis, causes and management. *Brain*, 124(2):249–278, 2001.

VENTIKOS, Y., BOWKER, T., WATTON, P., KAKALIS, N., AND BYRNE, J. Risk evaluation and interventional planning for cerebral aneurysms: computational models for growth, coiling and thrombosis. *International Journal of Computational Fluid Dynamics*, 23(8):595–607, 2009.

VITEK, J., ROUBIN, G., AL-MUBAREK, N., NEW, G., AND IYER, S. Carotid artery stenting: technical considerations. *American Journal of Neuroradiology*, 21(9):1736–1743, 2000.

WATTON, P., RABERGER, N., HOLZAPFEL, G., AND VENTIKOS, Y. Coupling the hemodynamic environment to the evolution of cerebral aneurysms: computational framework and numerical examples. *Journal of Biomechanical Engineering*, 131(10):101003, 2009.

WEBER, W., MAYER, T., HENKES, H., KIS, B., HAMANN, G., HOLTMANNSPOETTER, M., BRUECKMANN, H., AND KUEHNE, D. Efficacy of stent angioplasty for symptomatic stenoses of the proximal vertebral artery. *European Journal of Radiology*, 56(2):240–247, 2005.

WENTZEL, J., GIJSEN, F., STERGIOPULOS, N., SERRUYS, P., SLAGER, C., AND KRAMS, R. Shear stress, vascular remodeling and neointimal formation. *Journal of Biomechanics*, 36(5):681–688, 2003.

WHEATLEY, G., GURBUZ, A., RODRIGUEZ-LOPEZ, J., RAMAIAH, V., OLSEN, D., WILLIAMS, J., AND DIETHRICH, E. Midterm outcome in 158 consecutive Gore TAG thoracic endoprostheses: single center experience. *The Annals of Thoracic Surgery*, 81(5): 1570–1577, 2006.

WU, W., QI, M., LIU, X., YANG, D., AND WANG, W. Delivery and release of nitinol stent in carotid artery and their interactions: a finite element analysis. *Journal of Biomechanics*, 40(13):3034–3040, 2007a.

WU, W., WANG, W., YANG, D., AND QI, M. Stent expansion in curved vessel and their interactions: A finite element analysis. *Journal of Biomechanics*, 40 (11):2580–2585, 2007b.

WU, W., YANG, D., QI, M., AND WANG, W. An FEA method to study flexibility of expanded coronary stents. *Journal of Materials Processing Technology*, 184(1-3):447–450, 2007c.

XIONG, G., CHOI, G., AND TAYLOR, C. A. Virtual interventions for image-based blood flow computation. *Computer-Aided Design*, 44(1):3–14, 2012.

XIONG, G. AND TAYLOR, C. A. Virtual stent grafting in personalized surgical planning for treatment of aortic aneurysms using image-based computational fluid dynamics. In *Medical Image Computing and Computer-Assisted Intervention–MICCAI 2010*, pages 375–382. Springer, 2010.

YUSUF, S., REDDY, S., OUNPUU, S., AND ANAND, S. Global burden of cardiovascular diseases; part 1: general considerations, the epidemiologic transition, risk factors, and impact of urbanization. *Circulation*, 104(22):2746–2753, 2001.

ZAHORA, J. AND HANUS, J. Model of mechanical properties of nitinol stent. In *Proceedings of XVII IMEKO World Congress*, volume TC13, pages 1757–9, 2003.

ZENG, D. AND ETHIER, C. A semi-torsional spring analogy model for updating unstructured meshes in 3D moving domains. *Finite Elements in Analysis and Design*, 41(11-12):1118–1139, 2005.

ZHOU, X. *Design of Stents for the Direct Treatment of Intracranial Aneurysms*. PhD thesis, the University of Oxford, 2009.

ZHOU, X. AND YOU, Z. A new stent for direct treatment of intracranial aneurysms. In *ASME 2009 Summer Bioengineering Conference*, pages 1013–1014. American Society of Mechanical Engineers, 2009.

ZHU, H., WARNER, J., GEHRIG, T., AND FRIEDMAN, M. Comparison of coronary artery dynamics pre- and post-stenting. *Journal of Biomechanics*, 36(5):689–698, 2003.

APPENDIX A

DERIVATIONS FOR TORSIONAL SPRING ANALOGY

This appendix provides additional derivations for the torsional spring analogy method, described in Section 4.2.3. The derivations are based on Farhat et al. (1998).

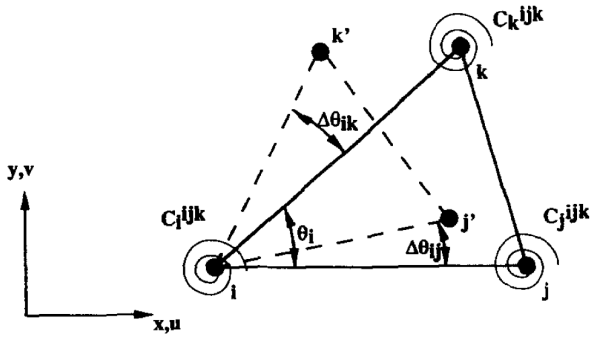

Figure A.1: Graphical interpretation of the torsional spring analogy, where each vertex is attached to a torsional spring that resists the change of the angle at the vertex. The moments generated by these torsional springs are proportional to the torsional stiffness and the angular displacement (image from Farhat et al. 1998).

A.1 KINEMATICS

Figure A.1 shows a reference position of a triangle Δ_{ijk} in solid line and the position of this triangle after its j and k vertices have been displaced by the vector q in dashed line.

At vertex i, the rotation increment $\Delta\theta_{ik}^{ijk}$ due to the relative motion of vertex k with respect to vertex i is given by

$$\sin\Delta\theta_{ik}^{ijk} = \frac{|\boldsymbol{\xi}_{ik} \times \boldsymbol{\xi}_{ik'}|}{l_{ik} l_{ik'}}, \tag{A.1}$$

where $\boldsymbol{\xi}_{ik} = \boldsymbol{\xi}_k - \boldsymbol{\xi}_i$ and $\boldsymbol{\xi}_{ik'} = \boldsymbol{\xi}_{k'} - \boldsymbol{\xi}_i = \boldsymbol{\xi}_{ik} + \mathbf{q}_k$.

The equation A.1 is derived from the definition of the cross product of two vectors $\mathbf{a} \times \mathbf{b}$, the magnitude of which can be geometrically interpreted as the area of the parallelogram with sides $\mathbf{a}$ and $\mathbf{b}$. That is,

$$|\mathbf{a} \times \mathbf{b}| = |\mathbf{a}| \cdot |\mathbf{b}| \cdot \sin\theta,$$

where θ is the corresponding (smallest) angle between them. Taking $\boldsymbol{\xi}_{ik}$ as $\mathbf{a}$ and $\boldsymbol{\xi}_{ik'}$ as $\mathbf{b}$, we get

$$|\boldsymbol{\xi}_{ik} \times \boldsymbol{\xi}_{ik'}| = |\boldsymbol{\xi}_{ik}| \cdot |\boldsymbol{\xi}_{ik'}| \cdot \sin\Delta\theta_{ik}^{ijk}$$

Hence, denoting $|\boldsymbol{\xi}_{ik}| = l_{ik}$ and $|\boldsymbol{\xi}_{ik'}| = l_{ik'}$, results in the expression for sine shown in Equation A.1.

The following derivation was proposed by Farhat et al. (1998) and assumes that the increment of mesh motion between two time-steps is sufficiently small. The assumption of small displacements and small rotations is needed for obtaining a linearised formulation. This assumption enables substitution of $\sin\Delta\theta_{ik}^{ijk} \approx \Delta\theta_{ik}^{ijk}$ (small angle approximation) and equation of $l_{ik'} \approx l_{ik}$. Then $\Delta\theta_{ik}^{ijk}$ can be computed from Equation A.1 as

$$\Delta\theta_{ik}^{ijk} = a_{ik} v_k - b_{ik} u_k,$$

where

$$a_{ik} = \frac{x_{ik}}{l_{ik}^2}, \quad b_{ik} = \frac{y_{ik}}{l_{ik}^2}$$

Similarly, at vertex i, the rotation increment $\Delta\theta_{ij}^{ijk}$ due to the relative motion of vertex j with respect to vertex i can be computed as

$$\Delta\theta_{ij}^{ijk} = -a_{ij} v_j + b_{ij} u_j,$$

where

$$\boldsymbol{\xi} = \begin{bmatrix} x \\ y \end{bmatrix}, \quad \mathbf{q} = \begin{bmatrix} u \\ v \end{bmatrix}$$

and

$$a_{ij} = \frac{x_{ij}}{l_{ij}^2}, \quad b_{ij} = \frac{y_{ij}}{l_{ij}^2}$$

The total rotation increment at vertex i is

$$\Delta\theta_i^{ijk} = \Delta\theta_{ii}^{ijk} + \Delta\theta_{ij}^{ijk} + \Delta\theta_{ik}^{ijk}$$

The remaining $\Delta\theta_{ii}^{ijk}$ can be determined by analogously decomposing it as

$$\Delta\theta_{ii}^{ijk} = \gamma v_i + \beta u_i$$

The two unknowns γ and β can now be determined by stating that for a rigid body motion characterised by $u_i = u_j = u_k = u$ and $v_i = v_j = v_k = v$, the total rotation increment at vertex i must be zero. Hence, γ and β must satisfy

$$\forall u, v \quad (\gamma - a_{ij} + a_{ik})\, v + (\beta + b_{ij} - b_{ik})\, u = 0$$

It follows that

$$\begin{aligned} \gamma - a_{ij} + a_{ik} = 0 \quad &\Rightarrow \quad \gamma = a_{ij} - a_{ik} \\ \beta + b_{ij} - b_{ik} = 0 \quad &\Rightarrow \quad \beta = -b_{ij} + b_{ik} \end{aligned}$$

Substitution gives the final expression of the total rotation increment at vertex i. The expressions of the total rotation increments at vertices j and k can be analogously deduced by cyclic permutation.

The final matrix form looks in the following way

$$\boldsymbol{\Delta\theta}^{ijk} = \boldsymbol{R}^{ijk} \boldsymbol{q}^{ijk}, \tag{A.2}$$

where

$$\boldsymbol{\Delta\theta}^{ijk} = \begin{bmatrix} \Delta\theta_i \\ \Delta\theta_j \\ \Delta\theta_k \end{bmatrix}, \quad \boldsymbol{q}^{ijk} = \begin{bmatrix} u_i \\ v_i \\ u_j \\ v_j \\ u_k \\ v_k \end{bmatrix}$$

$$\boldsymbol{R}^{ijk} = \begin{bmatrix} b_{ik} - b_{ij} & a_{ij} - a_{ik} & b_{ij} & -a_{ij} & -b_{ik} & a_{ik} \\ -b_{ji} & a_{ji} & b_{ji} - b_{jk} & a_{jk} - a_{ji} & b_{jk} & -a_{jk} \\ b_{ki} & -a_{ki} & -b_{kj} & a_{kj} & b_{kj} - b_{ki} & a_{ki} - a_{kj} \end{bmatrix}$$

A.2 EQUILIBRIUM

To determine the contribution of the proposed torsional springs to the fictitious elastic forces acting on the dynamic mesh, we consider the moments generated by these springs that can be written in matrix form as

$$\boldsymbol{M}^{ijk} = \boldsymbol{C}^{ijk} \boldsymbol{\Delta\theta}^{ijk},$$

where

$$\boldsymbol{M}^{ijk} = \begin{bmatrix} \boldsymbol{M}_i \\ \boldsymbol{M}_j \\ \boldsymbol{M}_k \end{bmatrix}; \quad \boldsymbol{C}^{ijk} = \begin{bmatrix} \boldsymbol{C}_i^{ijk} & 0 & 0 \\ 0 & \boldsymbol{C}_j^{ijk} & 0 \\ 0 & 0 & \boldsymbol{C}_k^{ijk} \end{bmatrix}$$

Substituting the expression for $\boldsymbol{\Delta\theta}^{ijk}$ defined in the Equation A.2, we get

$$\boldsymbol{M}^{ijk} = [\boldsymbol{C}^{ijk} \boldsymbol{R}^{ijk}] \boldsymbol{q}^{ijk}$$

We convert the moments $\boldsymbol{M}^{ijk}$ into a set of equivalent forces at each vertex gathered in vector $\boldsymbol{F}_{torsion}^{ijk}$

$$\boldsymbol{F}_{torsion}^{ijk} = \begin{bmatrix} F_{i_x} \\ F_{i_y} \\ F_{j_x} \\ F_{j_y} \\ F_{k_x} \\ F_{k_y} \end{bmatrix}_{torsion}$$

$\boldsymbol{F}_{torsion}^{ijk}$ can be deduced from moments $\boldsymbol{M}^{ijk}$ by a linear transformation of the form

$$\boldsymbol{F}_{torsion}^{ijk} = \boldsymbol{T}^{ijk} \boldsymbol{M}^{ijk}$$

and requiring that the work done by the forces $\boldsymbol{F}^{ijk}_{torsion}$ is equal to the work done by the moments $\boldsymbol{M}^{ijk}$

$$\boldsymbol{F}^{ijk^T}_{torsion}\boldsymbol{q}^{ijk} = \boldsymbol{M}^{ijk^T}\boldsymbol{\Delta\theta}^{ijk}$$

where superscript T indicates a transpose. Substituting the expression for the forces $\boldsymbol{F}^{ijk}_{torsion}$ and rotation increments $\boldsymbol{\Delta\theta}^{ijk}$, we get

$$\boldsymbol{M}^{ijk^T}\boldsymbol{T}^{ijk^T}\boldsymbol{q}^{ijk} = \boldsymbol{M}^{ijk^T}\boldsymbol{R}^{ijk}\boldsymbol{q}^{ijk}$$

which implies

$$\boldsymbol{T}^{ijk^T} = \boldsymbol{R}^{ijk}$$

Hence, in each triangle $\boldsymbol{\Delta}^{ijk}$, the contribution of the torsional springs connected to nodes of the triangular mesh elements can be expressed by discrete forces acting on these elements:

$$\boldsymbol{F}^{ijk}_{torsion} = [\boldsymbol{R}^{ijk^T}\boldsymbol{C}^{ijk}\boldsymbol{R}^{ijk}]\boldsymbol{q}^{ijk} = \boldsymbol{K}^{ijk}_{torsion}\boldsymbol{q}^{ijk}$$

APPENDIX B

VIRTUAL STENT DEPLOYMENT SYSTEM

This appendix illustrates an example of a rehearsing session of a minimally invasive stent deployment. The developed virtual deployment system is used to deploy a stent graft in an aorta of a patient with a dissection pathology.

The geometry of a patient's vessel obtained by segmentation of CT images (Figure B.1, a) has to first be discretised, i.e., meshed with an appropriate resolution to enable computations (Figure B.1, b). This 3-D mesh serves as an input to the Virtual Stent Deployment system, after which a sequence of deployment steps is performed, as illustrated in Figures B.2-B.9.

The concluding step of the clinical workflow is the haemodynamic analysis of the performed deployment. For that, the final vessel and stent geometries are exported from the Virtual Stent Deployment system (Figure B.9) and imported into a flow solver, e.g., CFD-ACE+ (ESI Group). Haemodynamic parameters in the focus of attention are flow exchange between true and false lumen, blood velocity and blood flow patterns, pressure distribution and WSS in the vessel wall. These measurements indicate whether the introduction of the stent graft results in an obliteration of the flow into the false lumen and hence, predict the outcome of the intervention.

If after the haemodynamic analysis, the virtual intervention does not bring desired outcomes, an alternative stenting scenario, e.g., with another graft or changed dimensions, should be tried out and the workflow repeated until the most optimal patient-specific procedure is identified.

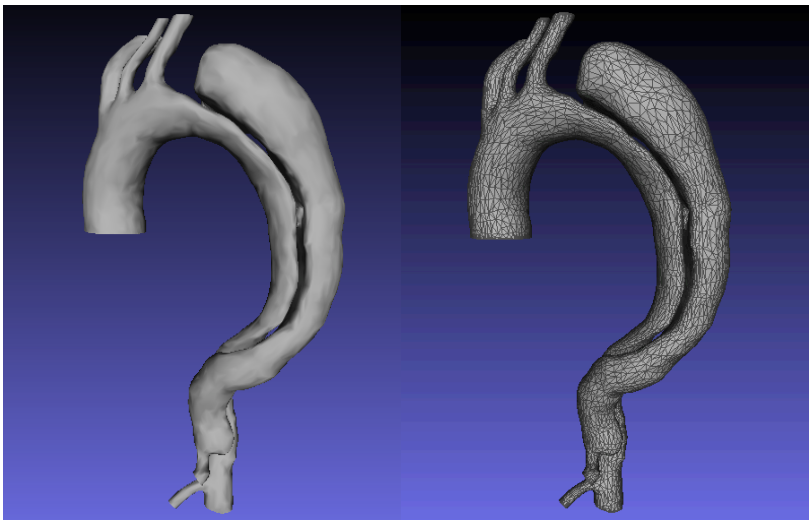

(a) (b)

Figure B.1: The configuration of the patient's aorta is obtained from medical images by segmentation and saved as a 3-D geometry (a), which is meshed for computations with the appropriate resolution (b).

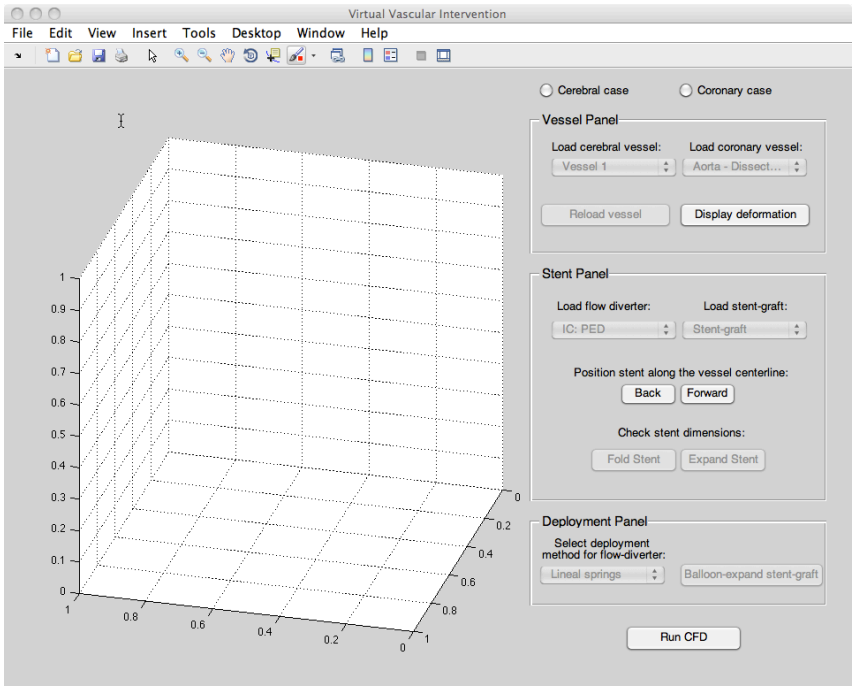

Figure B.2: Initial screen of the Virtual Stent Deployment tool.

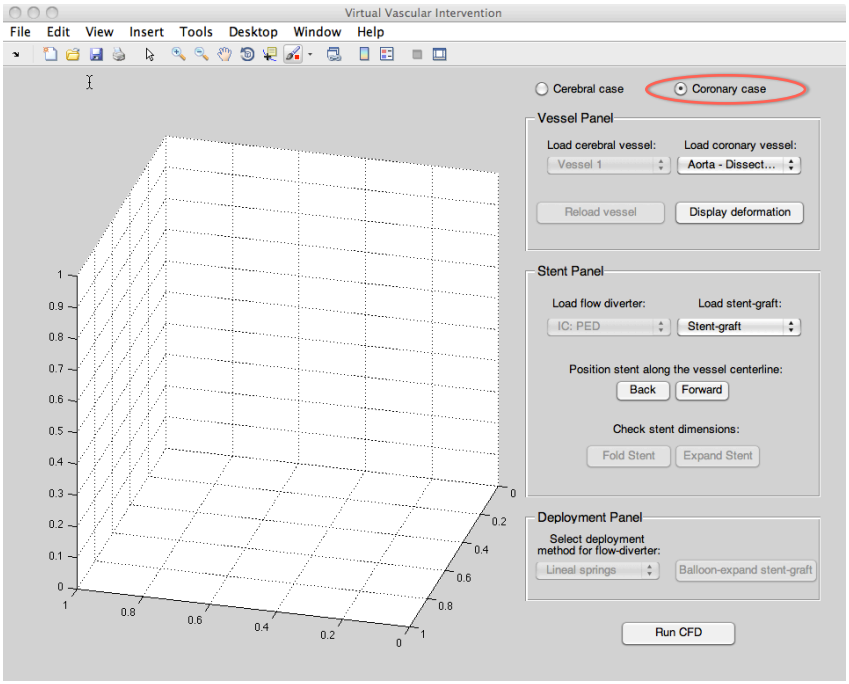

Figure B.3: Choose either “Cerebral case” or “Aortic case” in the right panel on the top (indicated by a red oval).

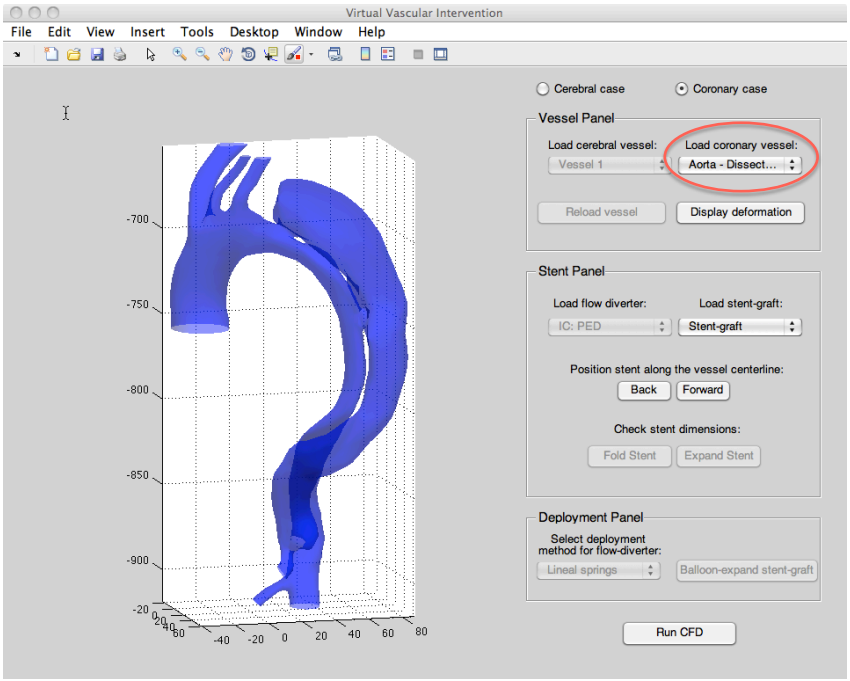

Figure B.4: In the vessel panel, choose the desired medical case (indicated with the red oval). The 3-D geometry of the patient is loaded on the left.

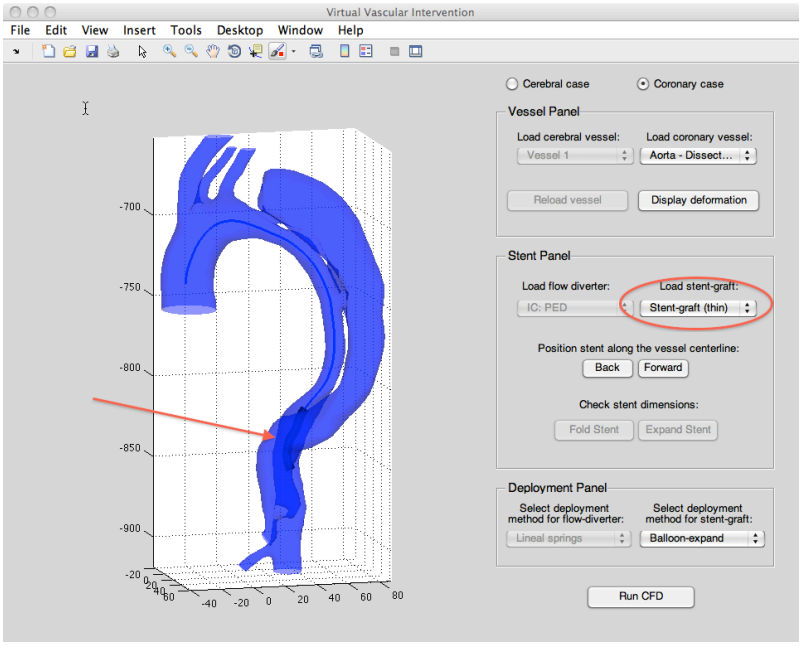

Figure B.5: In the stent panel, choose the desired device (red oval). The stent graft is loaded in a folded state inside a micro catheter and placed along the centerline of the vessel initiating the minimally invasive stent deployment (red arrow).

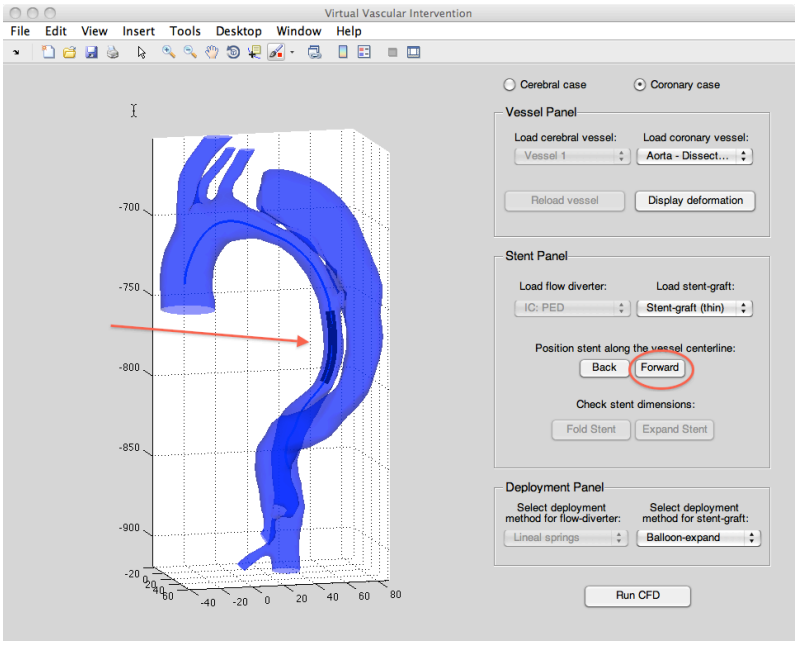

Figure B.6: In the stent panel, advance the stent graft along the centerline to the desired location by pushing the “Forward” button (red circle). You can go back by clicking the “Back” button.

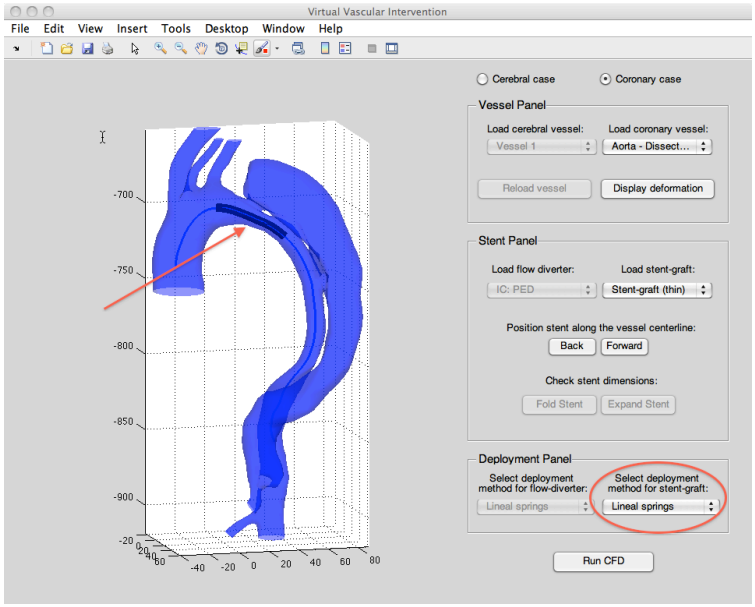

Figure B.7: When the stent reaches the desired location along the centerline (red arrow), choose the deployment method in the stent panel (red circle). You can choose either the ballon-expansion of the device or the self-expansion with lineal springs, depending on the type of the endograft. The deployment process starts, showing the outcome after every iteration.

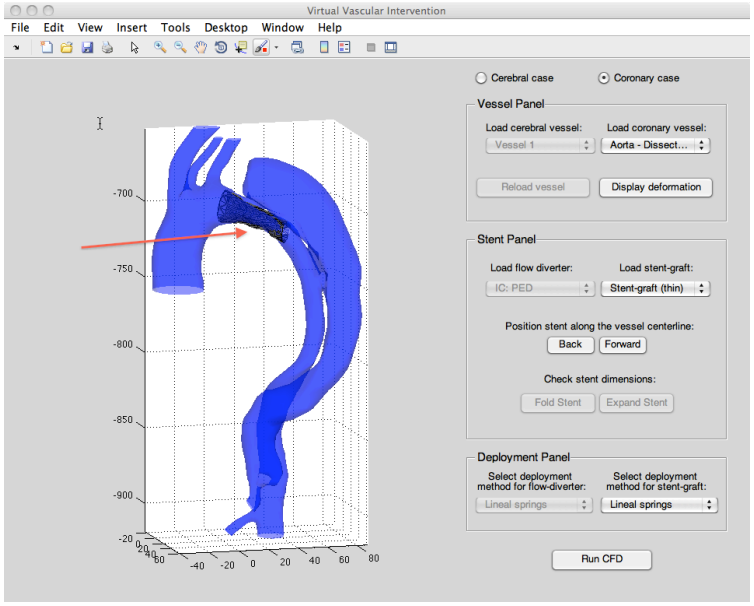

Figure B.8: The stent is iteratively expanding which allows to observe the deployment process. The final configuration of the device is indicated by the red arrow.

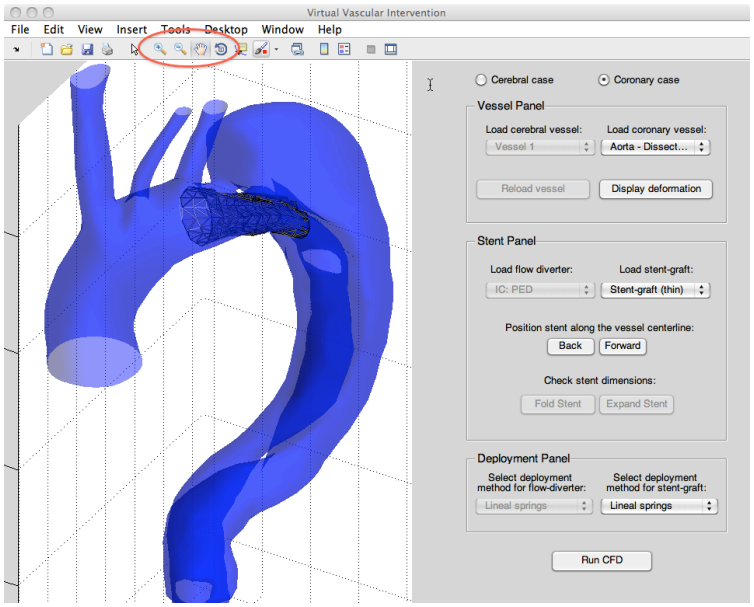

Figure B.9: It is possible to zoom in and out and to rotate the 3-D model by manipulating the toolbar (red circle) in order to inspect the final configuration of the deployed device. Additionally, the vessel deformation can be displayed by pressing the button “Display deformation” in the vessel panel. If the deployment result is satisfactory, the configurations of the vessel and the stent can be submitted to the CFD solver by pressing the button “Run CFD” at the bottom of the window.